

Everything flows...

Two-phase flow experimental studies in micro-models

Nikolaos Konstantinou Karadimitriou

Utrecht Studies in Earth Sciences 034

Everything flows ...

**Two-phase flow experimental studies in micro-
models**

Nikolaos K. Karadimitriou

Utrecht 2013

ISBN: 978-90-6266-326-2

NUR-code: 934

NUR-description: Hydrogeology

Cover Illustration: ©Nikolaos Karadimitriou

Cover lay-out: Margot Stoete, Faculty of Geosciences, Utrecht University

Printed by: Proefschriftmaken.nl || Uitgeverij BOXPress

Copyright © 2013 Nikolaos Karadimitriou

All rights reserved. No part of this publication may be reproduced in any form, by print or photo print, microfilm or any other means, without written permission by the publishers.

Everything flows ... Two-phase flow experimental studies in micro-models

Alles stroomt ... Twee-fase stroming experimentele studies in micro-modellen

(met een samenvatting in het Nederlands)

Proefschrift

ter verkrijging van de graad van doctor aan de Universiteit Utrecht op gezag van de rector magnificus, prof.dr. G.J. van der Zwaan, ingevolge het besluit van het college voor promoties in het openbaar te verdedigen op dinsdag 14 mei 2013 des middags te 4.15 uur

door

Nikolaos Karadimitriou

geboren op 21 februari 1978 te Athene, Griekenland

Promotor: Prof. dr. ir. S. M. Hassanizadeh

The Reading Committee

Prof. M. A. Celia, Princeton University

Prof. T. H. Illangasekare, Colorado School of Mines

Prof. M. T. Kreutzer, TU Delft

Prof. W. R. Rossen, TU Delft

The Examining Committee

Prof. M. A. Celia, Princeton University

Prof. T. H. Illangasekare, Colorado School of Mines

Dr. V. Joekar-Niasar, Shell B. V.

Prof. M. T. Kreutzer, TU Delft

Dr. M. Oostrom, Pacific Northwest National Laboratory

Acknowledgements

I would like to acknowledge the contribution to this work of a number of people, whose support and assistance played a key role in my research in the past years.

I would like to express my gratitude and respect to my supervisor, Majid Hassanizadeh. Majid trusted me with his decision to hire me as a Ph.D. candidate, while two-phase flow was a new scientific field for me at this time. And I did my best to stand up for his choice of trust. He made sure that I will learn well the fundamentals in theory, as we had regular weekly meetings with presentations on relevant topics. He was always there to give answers to questions, and pose new ones, so as to make everything physically justified in a simple way. He was always encouraging me to attend conferences so as to enrich my perspective regarding our work. He was also a tireless and precise editor of our scientific papers, and this is not an easy task at all. But, his main characteristic that I appreciated the most is that he never prohibited me from exploring new ideas and ways of treating a question, or a practical experimental issue. I was free to try and see. I will always be grateful to you, Majid, for crediting me with your trust, and for giving me the freedom to explore new ideas in our research. Because this is not only a way of doing science, it is a way of living.

I would also like to express my gratitude to Ruud Schotting for letting me know of the Ph.D. position, and bringing me in contact with Majid, but not only for this. Apart from the scientific issues, Ruud is always there to discuss issues that bother you, suggest solutions, and he will do his best to do anything that passes by his hand to make things easier for you. Thank you very much for everything Ruud.

The first person that I saw when I got into the Earth Sciences building on the 3rd of November, 2008, was a very friendly guy, with a characteristic smile. And this guy would prove to be one of my best collaborators and friends. It was Vahid Joekar-Niasar. His clear character, along with his excellent insight on the physical processes that occur in two-phase flow makes him an excellent collaborator and teacher. And this is why Vahid has an overall contribution to this work. I truly hope that in the future we will have the opportunity to work together again.

There is a person that everyone who is doing experimental work would appreciate his contribution. And this person is Pieter J. Kleingeld. Without him, everything would have been much more difficult, if not impossible. Pieter is not only a technician. He is

definitely a person with technical skills, but he also has a very strong background on numerous aspects of physics. He is the kind of guy that you have a long and intense discussion about things that come up regarding the experimental setup, you disagree, you exchange ideas, you disagree again, and in the end, something wonderful comes out of it. Pieter, it was a pleasure working with you.

I cannot help thinking what would be the future of this work, if Michiel Kreutzer from TU Delft has not shared his expertise in making micro-fluidic devices with us. Michiel made the fabrication process of micro-fluidic devices seem an easy task. Under his guidance, and with his Ph.D. student Michiel Musterd being my mentor in Kavli Institute of NanoScience, I managed to reach to the point of making high quality PDMS micro-models. And that was crucial in the fulfillment of this work. I am truly grateful to both of you.

I would like to acknowledge NUPUS International Research Training Group contribution to this work. With the regular meeting that we had, I had the opportunity to meet with people working in the same field, and exchange ideas, or even initiate collaborations.

I would like to thank Prof. Sushanta Mitra from the University of Alberta, Canada, for our collaboration in the construction of a silicon-glass micro-model, which led to a cover article in Lab on Chip journal. I also would like to thank Prof. Hans Bruining from TU Delft, Prof. Michael Celia from Princeton University, and Prof. Rainer Helmig from Stuttgart University, for the very fruitful discussions we had during meetings and conferences. I would like to express my gratitude to Prof. Laura J. Pyrak-Nolte for her hospitality during my visit to Purdue University, and her collaboration in the fabrication procedure of a glass micro-model which led to a publication on Lab on Chip journal. I would also like to thank Prof. Martyn Drury for providing us with the necessary space in his lab, and for his tolerance when the lights had to be out for days.

In my daily work I had the opportunity to meet and work with a friendly and supportive group of colleagues. First of all I should thank Margreet for her help in administrative tasks, and in organizing the conference in Poros. Not to mention her support under difficult circumstances that was priceless. I would like to thank my former and current office mates, Simona Bottero, Amir Raoof, and Mojtaba Mahmoodlu for their feedback in the early stages of my research, but also for all the nice times we had together. I would also like to thank my friends, and my former and current colleagues, like Imran, Qiu, Shuai, Reza, Wouter, Eric, Alexandros, Romina, Nikos, Giorgos, Kostas, Kostis, Milica, Maya, and many others.

I feel the need to express my gratitude to Alexandros Papadopoulos for making me aware of the Ph.D. position announcement, and not only for this. He has been a major source of inspiration with his interest in the progress of our work, with his assistance during the conference in Poros, and with his support in difficult times. I think that he played the key role for everything to happen, since he managed to drastically change my life in the best possible way.

In Greece we say that if a tree does not honor its own roots, it will eventually fall. My mother, Matoula, even though she does not really understand what I am doing, she always has an encouraging word. She and my sisters, Nectaria and Katerina, my brother in law, Tassos, and my nephews Dimitris, Iasonas, and Konstantinos, made sure that I can count on them, even under the worst circumstances.

There is no known way of being effective and productive in any way, if you do not have support and understanding in your own house. And this was made sure by my wife, Dionysia. Her understanding to long days and short weekends, and her support in difficult times kept me strong and focused enough to fulfill this task. It is her smile that makes difficulties to fade away. I consider myself blessed for having her adding color in my life, every day.

There is a special group of people, which I consider to be family. These people, I know them for my whole life and when I go back, it is impossible to find a time where they were not there for me. Thanassis, Makis, Leandros, there is no way to express my gratitude to all of you. Thank you.

Finally, I would like to express my gratitude to a person that I have the honor to know. And this person is my father, Konstantinos Karadimitriou. He is the source of inspiration in my life, and every past or future achievement, minor or major, in my life will be because of him. This person has been my tutor in my whole life, and he managed to make honesty, altruism, responsibility, patience, hard work and to never give up, basic principles in my life. And I think that he is proud of his son. And nothing could satisfy me more.

Closing, I would like to point out that the outcome of this Ph.D. research is a combined contribution of many persons, in many different ways, which gives a harmonic outcome. I consider myself lucky for being able to live this experience.

Nikolaos K. Karadimitriou

May 2013.

Table of contents

Chapter 1.

Introduction

1.1 Theory	1
1.2 Research objectives	3
1.3 Thesis outline	3
1.4 References	5

Chapter 2.

A review of micro-models and their use in two-phase flow studies

2.1 Introduction	7
2.2 The micro-model geometry	8
2.2.1 Perfectly-regular model	9
2.2.2 Partially-regular models	9
2.2.3 Fractal patterns	10
2.2.4 Irregular patterns	10
2.3 Fabrication of micro-models	11
2.3.1 Hele-Shaw and glass-beads models	11
2.3.2 Optical lithography	13
2.3.3 Etching method	16
2.3.4 Stereo-lithography	21
2.3.5 Soft lithography	23
2.3.6 Micro-model materials	26
2.4 Micro-models visualization methods	28
2.4.1 Basic issues	28
2.4.2 A microscope-camera visualization setup	29
2.4.3 Direct visualization with a camera	30
2.4.4 Photo-luminescent Volumetric Imaging (PVI) – Confocal microscopy	31
2.5 Applications of micro-models in studies of flow and transport in porous media	35
2.5.1 Studies of two-phase displacement processes	35
2.5.2 Measurements of interfacial area and phase saturation	37
2.5.3 Measurements of relative permeability	38
2.5.4 Enhanced oil recovery	40
2.6 Summary and Discussions	42
2.7 References	44

Chapter 3.

Quasi-static, two-phase flow pore network model

3.1 Introduction	61
3.2 Model description	63
3.2.1 Structure	63
3.2.2 Numerical experiments	66
3.2.3 Drainage-imbibition	67
3.2.4 Relative permeability	68
3.2.5 REV determination	69
3.3 Numerical results	71
3.3.1 Pc-S curves	71
3.3.2 a^{wn} -S curves	71
3.3.3 Relative permeability	72
3.3.4 Pc-S ^w - a^{wn} surfaces	73
3.4 References	74

Chapter 4.

Part 1. Reservoir-on-a-Chip (ROC): A new paradigm in reservoir engineering

4.1.1 Introduction	77
4.1.2 Reservoir-on-a-chip: ROC	80
4.1.2.1 Introduction	80
4.1.3 Experimental section	81
4.1.3.1 Pore network design	81
4.1.3.2 Fabrication and characterization of ROC	82
4.1.3.3. Water-flooding experiments	84
4.1.4 Results and discussion	86
4.1.5 Conclusion	90
4.1.6 References	90

Part 2. A novel Deep Reactive Ion Etched (DRIE) glass micro-model for two-phase flow experiments

4.2.1 Introduction	95
4.2.2 Pore-network model description	96
4.2.3 Experimental setup and procedure	98
4.2.4 Two-phase displacement experiments	103
4.2.5 Results	104

4.2.6	Discussion and Conclusions	105
4.2.7	References	107

Chapter 5.

In situ surface treatment of PDMS to enhance natural hydrophobicity

5.1	Introduction	111
5.2	Silanization process	113
5.3	Post-treatment observations	115
5.4	Discussion	117
5.5	Summary and conclusion	121
5.6	References	121

Chapter 6.

On the fabrication of PDMS micro-models by rapid prototyping, and their use in two-phase flow studies

6.1	Introduction	123
6.2	Construction of the Micro-model	126
6.2.1	Main steps	126
6.2.2	Design of the flow network and the reservoirs.	126
6.2.3	Preparation of a patterned silicon wafer with photo-lithography.	129
6.2.4	Fabrication of a PDMS micro-model	130
6.3	Issues with PDMS models	134
6.3.1	Wettability issues	134
6.3.2	Deformation of micro-model	137
6.4	Experimental setup	137
6.4.1	Visualization setup	137
6.4.2	Pressure measurement and control	141
6.5	Quasi-static experiments	141
6.6	Results	142
6.7	Discussion	145
6.8	Conclusions	146
6.9	References	147

Chapter 7.

Micro-model study of Specific interfacial area - Capillary pressure - Saturation relationship under transient conditions in two-phase flow

7.1	Introduction	153
7.1.1	Specific interfacial area and two-phase flow	153
7.1.2	Micro-models and two phase flow	155
7.2	Experimental setup	156
7.3	Dynamic experiments	157
7.3.1	Experimental process	157
7.3.2	Data processing	157
	7.3.2.1 $P^c-S^w-A^{wn}$	157
	7.3.2.2 Interfacial area production term and velocity	159
7.4	Results	160
7.4.1	P^c-S-A^{wn} surface	160
7.4.2	Production term and interfacial velocity	161
7.5	Discussion	163
7.6	Conclusion	168
7.7	Suggested future work	168
7.8	References	168

Chapter 8.

Visualization of pore-scale two-phase displacement mechanisms

8.1	Introduction	173
8.2	Experimental setup	175
8.3	Mechanisms during drainage	
	8.3.1 Haines jump	175
	8.3.2 Capillary end effects	175
	8.3.3 Local imbibition-mobilization of the non-wetting phase	177
8.4	Mechanisms during imbibition	
	8.4.1 Snap-off	179
	8.4.2 Cooperative filling	180
	8.4.3 Capillary end effects	181
	8.4.4 Local drainage	182
8.5	Relative permeability	182
8.5	References	185

Chapter 9. Summary and conclusions

9.1 Background	187
9.2 Theory validation	188
9.3 Innovation - Technical developments	190
9.4 Suggestions for future work	191

Samenvatting	193
---------------------	-----

List of publications	195
-----------------------------	-----

Chapter 1.

Introduction

1.1 Theory

Darcy's law is an empirical formula, established by Henry Darcy in 1856. Darcy's law for single phase flow assumes that the only driving forces for flow are the gradient in pressure and the gravitational force. It is assumed that the flow velocity is linearly proportional to these driving forces. The same stands for multiphase flow, where it is assumed that Darcy's law is valid as in single phase flow, only that the proportionality coefficient should depend on fluid saturation. Even intuitively, one may expect that there should be more factors affecting the flow of a fluid in a porous medium than those accounted for in Darcy's law.

Hassanizadeh and Gray (1990, 1993a), developed an extended theory for two-phase flow. In their work, which was based on rational thermodynamics, interfaces between phases in two-phase flow were accounted for as separate entities. They proposed that these interfaces affect the flow of each phase in a porous medium, based on energy and momentum balance equations. They concluded that specific interfacial area should be accounted for as a separate variable in two-phase flow. They showed that the driving forces in multiphase flow are the gradient of Gibbs free energy, as well as gravity. They also showed that in single-phase flow, the gradient of Gibbs free energy is reduced to the gradient of pressure, so that Darcy's law is obtained. But, in two-phase flow, because the Gibbs free energy of each phase is a function of phase saturation and specific interfacial area, as well as the mass density, a more complex form of Darcy's law is obtained (Hassanizadeh and Gray, 1990):

$$\vec{q}^a = -\frac{k_r^a \cdot \vec{K}}{\mu^a} \cdot (\nabla P^a - \rho^a \vec{g} - \lambda_1 \nabla \alpha^{wn} - \lambda_2 \nabla S^a), \quad a = w, n \quad (1)$$

In equation 1, q is the phase flow velocity, k_r^a is phase relative permeability, \mathbf{K} is the intrinsic permeability tensor, μ^a is phase viscosity, P^a is phase pressure, ρ^a is phase density, \mathbf{g} is gravity vector, λ_1 and λ_2 are material coefficients, α^{wn} is the specific interfacial area between fluid phases, and S^a is phase saturation.

Another central equation in theories of two-phase flow is the so-called capillary pressure – saturation relationship. This relationship is formulated as follows:

$$P^n - P^w = P^c(S^w) \quad (2)$$

In equation 2, there are two major implicit assumptions. First, capillary pressure is assumed to be a function of saturation only. Second, the fluids pressure difference is assumed to be equal to capillary pressure under any conditions and at all times.

It is well known that the relationship between capillary pressure and wetting phase saturation is not unique. It depends not only on saturation but also on the history of the distribution of the two phases in the network. Hassanizadeh and Gray (1993b) proposed that the non-uniqueness of the relationship between capillary pressure and saturation is because of the absence of the interfacial area from the capillarity theory. They proposed the following equation to describe the macroscopic capillary pressure:

$$P^c(S^w) = P^c(S^w, \alpha^{wn}) \quad (3)$$

Various computational and experimental works have shown that under quasi-static conditions, and under a wide range of drainage and imbibition histories, $P^c-S^w-\alpha^{wn}$ surfaces for drainage and imbibition more or less coincide (e.g. Reeves and Celia, 1996; Cheng et al., 2004; Joekar-Niasar et al., 2008, 2010b; Porter et al., 2009; Karadimitriou et al., 2012). This is direct evidence that the inclusion of specific interfacial area leads to the removal, or at least to a significant reduction of hysteresis in the capillary pressure – saturation relationship. This means that under quasi-static conditions, there is one unique surface that fully characterizes drainage and imbibition in two-phase flow.

As far as the limitation in equation 2 is concerned, it is now established that P^n-P^w is equal to capillary pressure only under static conditions (see Hassanizadeh et al., 2002, for an extended review of experimental evidences). Under transient conditions, the difference in phase pressures is equal to the following equation (Stauffer, 1978; Entov, 1980; Kalaydjian and Marle, 1987; Hassanizadeh and Gray, 1990):

$$P^n - P^w = P^c - \tau \frac{\partial S^w}{\partial t} \quad (4)$$

where τ , the non-equilibrium capillarity coefficient, is a material property that may still be a function of saturation and specific interfacial area.

Equations 2 and 3 have been studied experimentally with the use of micro-models, only under equilibrium conditions, and only for square, or nearly square flow networks. Micro-models have never been used to study these equations under transient conditions, and for elongated flow networks.

1.2 Research objectives

The main objective of this research is to investigate pore-scale physics of two-phase flow. The significance of the inclusion of interfacial area as a separate variable in two-phase flow models will be investigated. This is accomplished through the following specific objectives:

1. Constructing a quasi-static numerical model and performing numerical experiments to investigate the significance of incorporating interfacial area in the theories of two-phase flow.
2. Manufacturing transparent elongated micro-models, as representations of natural porous media, with very well controlled wetting properties that bear flow networks which correspond to the ones used in the numerical simulations.
3. Designing and materializing an optical setup that allows the visualization of flow in elongated micro-models.
4. Designing and performing physical experiments where interfacial area is measured under quasi-static and dynamic flow conditions.
5. Investigating the validity of the extended theories with the aid of the experimental results.

1.3 Thesis outline

This thesis is organized as follows.

In Chapter 2, an extensive and comprehensive review of micro-models materials and manufacturing processes, visualization setups used, and their applications in two-phase flow studies is presented. Based on this review, the manufacturing material for our micro-model studies was chosen. In addition to this, the lack of an optical setup that can visualize flow in elongated micro-models is discussed.

In Chapter 3, a quasi-static pore network model is presented. A flow network based on Delaunay triangulation was used to simulate drainage and imbibition under quasi-static conditions. Calculations for capillary pressure, wetting phase saturation, and interfacial area were used to construct the relevant surfaces, for various configurations of the flow

network. Intrinsic permeability of the flow network, as well as relative permeability for both phases, were calculated for drainage. Typical flow rates were also calculated, so as to be later compared to experimental values.

In Chapter 4, we describe studies involving prototype micro-models, having the flow network designed in Chapter 3. First, the construction and use of a micro-model made of silicon and sealed with a glass plate are explained and its use to study oil recovery in natural rocks is explained. Then, the construction and use of a novel all-glass micro-model are described. This micro-model is used to compare the experimental results to those from the numerical model, under quasi-static conditions, during drainage. A novel optical setup which would allow the dynamic observation of pore scale flow processes in an elongated micro-model was designed and materialized for this purpose.

In Chapter 5, a novel procedure to treat PDMS in order to obtain wetting properties stable in time and uniform in space, is presented. PDMS micro-models are treated in a way that they become stable and uniformly hydrophobic. This is crucial for performing well-defined and well-controlled two-phase flow studies.

In Chapter 6, the process of manufacturing PDMS micro-models with very well controlled geometrical features and chemical properties is described and the experimental results obtained with the use of such models for two-phase flow are presented. Quasi-static experimental data for capillary pressure, wetting phase saturation, and specific interfacial area, extracted from acquired images are shown. Data from drainage, imbibition, and scanning curves are used to test the validity of the new capillarity equation for two-phase flow (equation 3).

In Chapter 7, results from dynamic experiments are presented. With the use of PDMS micro-models, equations 2 and 3 are evaluated for their validity. During the experiments, the flow rate of the wetting phase was measured, and from the images acquired, local capillary pressure, saturation of the wetting phase, and interfacial area were calculated. We evaluate the validity of equation (3) under dynamic conditions by comparing $P_c-S^w-\alpha^{wn}$ surfaces to the corresponding surfaces under equilibrium conditions.

In Chapter 8, some experimental observations during displacement experiments are presented. Effects like Haines jump, snap-off, capillary end effects etc., are shown in pictures taken from the micro-model. These side-observations come to fill the gap between assumptions used in numerical models, and the actual case in real porous media. Relative permeability for the wetting and the non-wetting phase during drainage is experimentally measured.

In Chapter 9, the concluding remarks from the experimental work are presented.

1.4 References

Cheng, J. T., L. J. Pyrak-Nolte, and Nolte, D. D., (2004), Linking pressure and saturation through interfacial area in porous media, *Geophysical Research Letters*, **31**, L08,502, doi:10.1029/2003GL019282.

Entov, V. M., (1980), Theory of nonequilibrium effects associated with the flow of nonuniform fluids in porous media, *Fluid Dynamics*, **15**(3), pp. 365–369, doi:10.1007/BF01089969.

Hassanizadeh, S.M., Gray,W.G., (1990), Mechanics and thermodynamics of multiphase flow in porous media including interphase boundaries, *Adv. Water Resour.*, **13**, pp. 169–186.

Hassanizadeh, S.M., Gray,W.G., (1993a), Thermodynamic basis of capillary pressure in porous media. *Water Resour. Res.*, **29**, pp. 3389–3405.

Hassanizadeh, S.M., and Gray, W. G., (1993b), Toward an improved description of the physics of two-phase flow, *Advances in Water Resources*, **16**, pp. 53–67.

Hassanizadeh, S.M., M.A. Celia, and H.K. Dahle, (2002), Dynamic effects in the capillary pressure-saturation relationship and their impacts on unsaturated flow, *Vadose Zone Journal*, **1**, pp. 38-57, 2002

Joekar-Niasar, V., S. Hassanizadeh, and Leijnse, A., (2008), Insights into the relationships among capillary pressure, saturation, interfacial area and relative permeability using pore network modeling, *Transport in Porous Media*, **74**(2), pp. 201–219.

Joekar-Niasar, V.,M. Prodanovi'c, D.Wildenschild, and Hassanizadeh, S.M., (2010b), Network model investigation of interfacial area, capillary pressure and saturation relationships in granular porous media, *Water Resources Research*, doi:10.1029/2009WR008585.

Kalaydjian, F., and C. M.Marle (1987), Thermodynamic aspects of multiphase flow in porous media, *Collection colloques et s'eminaires - Institut francais du petrole*, **45**, pp. 513–531.

Karadimitriou, N. K., and Hassanizadeh, S. M., 2012, A Review of Micro-models and their Use in Two-Phase Flow Studies, *Vadose Zone Journal*, doi:10.2136/vzj2011.0072.

Karadimitriou, N. K., Musterd, M., Kleingeld, P. J., Kreutzer, M. T., Hassanizadeh, S. M., and Joekar-Niasar, V., (2013), On the fabrication of PDMS micro-models by rapid prototyping, and their use in two-phase flow studies, *Water Resources Research*.

Porter, M. L., M. G. Schaap, and Wildenschild, D. , (2009), Lattice-boltzmann simulations of the capillary pressure-saturation-interfacial area relationship for porous media, *Advances in Water Resources*, **32**(11), pp. 1632 - 1640, doi:DOI: 10.1016/j.advwatres.2009.08.009.

Reeves, P. C., and Celia, M. A., (1996), A functional relationship between capillary pressure, saturation, and interfacial area as revealed by a pore-scale network model, *Water Resources Research*, *32*, pp. 2345-2358.

Stauffer, F. (1978), Time dependence of the relations between capillary pressure, water content and conductivity during drainage of porous media, IAHR, pp. 3.35-3.52, Thessaloniki.

Chapter 2

A review of micro-models and their use in two-phase flow studies

Abstract

Over the last 25 to 30 years, micro-models have been increasingly used to study the behavior of fluids inside micro-structures in various research areas. Studies have included chemical, biological, and physical applications. Micro-models have been proven to be a valuable tool in the field of porous media by enabling us to observe the flow of fluids and transport of solutes within the pore space. They have helped to increase our insight of flow and transport phenomena on both micro- and macro-scales. In this review, first we present various methods for generating patterns used in micro-models. Then, fabrication methods and materials are described. Next, visualization setups used for the study of fluid flow and transport processes are explained. Finally, various applications of micro-models are discussed.

Keywords: micro-models, two-phase flow, pore network, percolation, interfacial area, capillary pressure, saturation, microscopy, porous media.

2.1 Introduction

Micro-models are commonly used to investigate and visualize small-scale physical, chemical, and biological processes. One of the earliest micro-models was developed and used by Chatenever and Calhoun (1952), for investigating micro-scale mechanisms of fluid behavior in porous media. Since then, micro-models have been used to study many processes and applications involving two-phase flow. Examples include the capillary fingering effect, the percolation dimension (van der Marck and Glas, 1997), the fractal dimension (Lenormand and Zarcone, 1985; Lenormand, 1989; Lenormand et al., 1988), fluid flow through a nanometer-scale channel (Cheng and Giordano, 2002), and the labyrinth patterns in confined granular-fluid systems (Sandnes et al., 2007).

Strictly speaking, no clear definition of a micro-model in terms of two-phase flow in porous media has been articulated. A micro-model is an idealized, usually two-

dimensional representation of a porous medium; a network of connected pores, measuring in the (tens) of microns, through which fluids flow and solutes spread. Moreover, visual observation of the flow of fluids and movement of colloids or solutes should be possible in a micro-model. Accordingly, a micro-model is typically made of a transparent material that enables visual observation, such as glass, or quartz, but it could also be polymeric. The requirement of small pores (less than a millimeter) is essential for two-phase flow studies, because the capillary effects will be otherwise irrelevant. The overall size of a micro-model is typically on the centimeter scale. There must be also an inlet and an outlet area for the introduction and removal of the wetting and non-wetting phases. In summary, a micro-model will be defined here as an artificial representation of a porous medium, made of a transparent material. This fluidic device bears a flow-network, with features on the micro-scale, and an overall size of up to a few centimeters.

Most micro-models have been considered as two-dimensional porous media. However, examples of a three-dimensional micro-model can be found in the work of Montemagno and Gray (1995) and Avraam and Payatakes (1999). The difference between two-dimensional and three-dimensional micro-models relates to the limitations of the visualization setup. In principle, optical methods cannot be used for visualization over the depth of the model.

This paper presents an overview of micro-models used in studying two-phase flow and transport in porous media. This paper describes methods for generating the network of pores, as well as the means of manufacturing a micro-model. The focus then shifts to the various visualization setups used. We conclude by describing the applications of micro-models in the field of two-phase flow in porous media.

2.2 The micro-model geometry

The early micro-models (Chatenever and Calhoun, 1952; Nuss and Whiting, 1947) had a simple and regular geometry. Later, micro-models were constructed with a more complicated geometry. Since the 1980s, the flow pattern of micro-models has been computer generated. The following sections outline a general classification of micro-models based on the geometry and topology of the porous medium. Four main categories are identified and described below.

2.2.1 Perfectly-regular models

In perfectly-regular models, all pores have the same geometry—for instance, a square or rectangular cross-section throughout the entire domain. The pore depth and width, and the distance between pores are constant throughout the whole network. Of course, some small variations may exist resulting from the manufacturing process. Examples of perfectly-regular micro-models are those by Corapcioglu et al (1997) used to visualize and quantify solute transport in porous media (see Figure 1); and by Chen and Wilkinson (1985) used to examine viscous fingering.

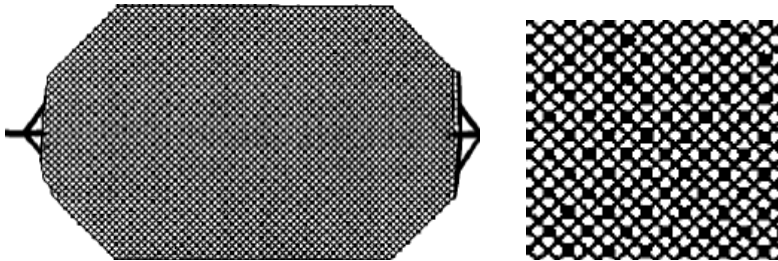


Figure 1. Left: Example of micro-model with a perfectly regular pattern. Right: A magnified part of the left figure (Corapcioglu et al. 1997).

2.2.2 Partially-regular models

In partially-regular micro-models, pore bodies and pore throats form a regular lattice and have the same cross-sectional shape. However, the pores' dimensions are variable. Pore sizes are chosen from a statistical distribution and may be correlated or uncorrelated. This pore size distribution determines the permeability of the network as demonstrated by Tsakiroglou and Avraam (2002) (Figure 2); Sbragaglia et al. (2007); and Chen and Wilkinson (1985).

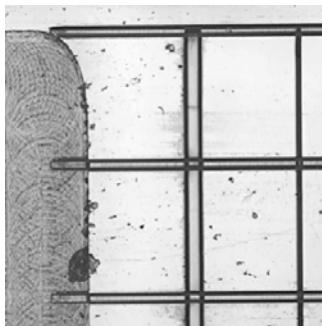


Figure 2. Image of micro-model with a partially regular pattern. (Tsakiroglou and Avraam 2002)

2.2.3 Fractal patterns

In some micro-models developed during the last few decades, the representation of the porous medium is based on fractals. The fractal patterns can be spatially correlated or not. A fractal micro-model may appear to have a completely irregular pattern but actually it does not. Examples of such fractal patterns in natural rocks or flow networks in micro-models can be found in the works of Cheng et al. (2004), shown in Figure 3, Nolte and Pyrak-Nolte (1991), Nolte et al. (1989), and Pyrak-Nolte et al. (1988). Flow networks that are generated in this way follow the rules of percolation theory. For flow to occur, its porosity has to be at least 50 per cent for a correlated network and 60 per cent for the uncorrelated network. If porosity is lower than these limits, then there is no connected path across the micro-model.

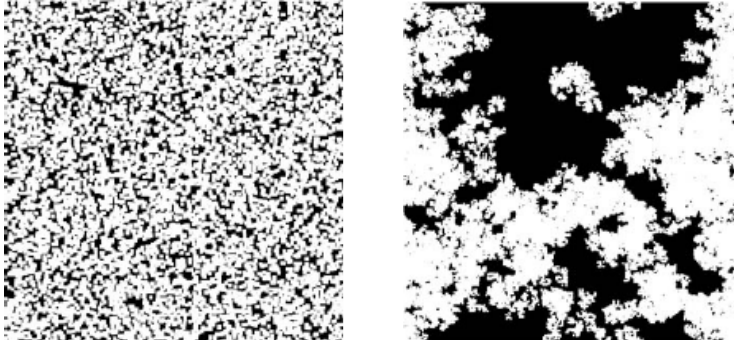


Figure 3. Examples of micro-models with fractal patterns: spatially uncorrelated (left) and correlated (right) (Cheng et al, 2004).

2.2.4 Irregular patterns

For this category of networks, the main feature of the pattern and its geometry is a lack of spatial correlation. Pores are randomly placed in the network while their sizes are chosen from a single statistical distribution (see Figure 4 from Sandnes et al., 2007). Use of Delaunay triangulation for generating the pattern can reproduce patterns that have properties that correspond well to real porous media, as shown by Heiba et al. (1992), and Blunt and King (1991). Delaunay triangulation requires that the connections between network nodes not intersect and that the triangular pattern of connections be as equilateral as possible.

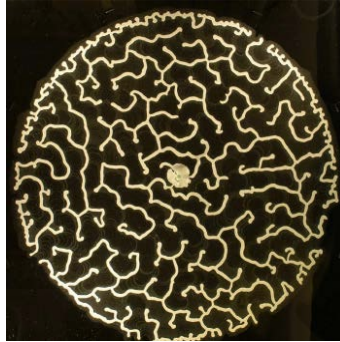


Figure 4. Example of an irregular pattern micro-model. (Sandnes et al. 2007)

2.3 Fabrication of micro-models

This section discusses various techniques in the fabrication of a micro-model. As mentioned earlier, the material that can be used to make a micro-model should be transparent. In this way, direct optical visualization of the flow and the distribution of fluids in the flow network is possible. Such materials are glass, quartz, PMMA (Poly-methyl-meth-acrylate), and PDMS (Poly-di-methyl-siloxane). Another material that can be used is silicon. Later, in section 3.6 we briefly describe the features and potential limitations of each material. The fabrication procedure needs to be accurate and efficient. New fabrication techniques have been introduced as micro-models have been increasingly used to study the behavior of fluids on a very small scale. For the sake of brevity, reported here are not all methods of fabrication but only those that are widely used.

2.3.1 Hele-Shaw and glass-beads models

Chuoque et al. (1959) conducted one of the first studies of two-phase flow with a Hele-Shaw micro-model. Their work presented theoretical and experimental evidences for the existence of macroscopic instabilities in displacement of a fluid by another immiscible fluid through a uniform porous medium. Hele-Shaw models are very simple in principle. They are made of two parallel transparent plates, with the flow taking place in the gap between them. The flow between two parallel plates is mathematically analogous to the flow through pores. This model is called a glass-beads model when glass or quartz beads or spheres are inserted between the two plates. The very first micro-model made by Alfred Chatenever and John C. Calhoun in 1952 at the University of Oklahoma is an example of a glass-beads model.

Chatenever and Calhoun's micro-model consisted of an observation cell, as they called it, which was a single layer of glass spheres sandwiched between two flat plates. They found that using two or more layers would make it difficult, given the available means of visualization, to distinguish one phase from the other. The observation of flow phenomena was extremely complicated. Chatenever and Calhoun used different flow cells. One of the flow cells is shown in Figure 5.

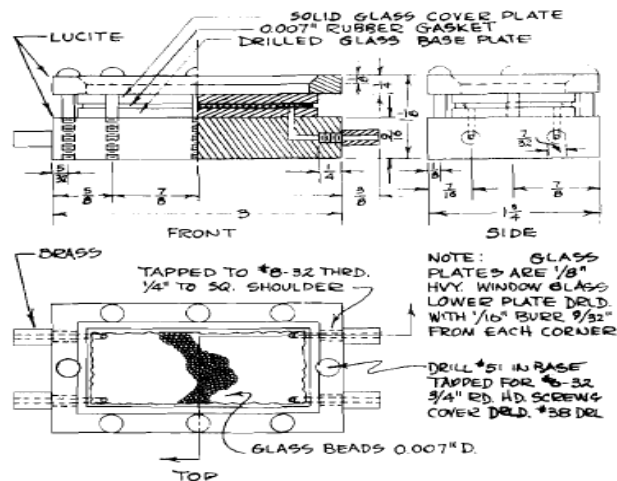


Figure 5. Sketch of type 'C' cell by Chatenever and Calhoun (1952).

This micro-model was comprised of a Lucite base, a compression cover, an observation window, and a gasket. A glass plate was molded into the Lucite base in a press to make an all-glass matrix composed of a glass top, glass spheres, and a glass base. The observation window was, in fact, the top cover of the cell. The spheres that were packed inside the cell formed a single-layered rhombic pattern of pore network.

In Hele-Shaw and glass beads micro-models, fluids were introduced into the model through a hole in the center of one plate (Sandnes et al., 2007), or at the ends of the parallel plates (Corapcioglu and Fedirchuk, 1997; 1999; Tóth et al., 2007, Lovoll et al., 2005, 2010; Tallakstad et al., 2009). Figure 6 shows the side view of a glass bead micro-model from Corapcioglu and Fedirchuk (1999).

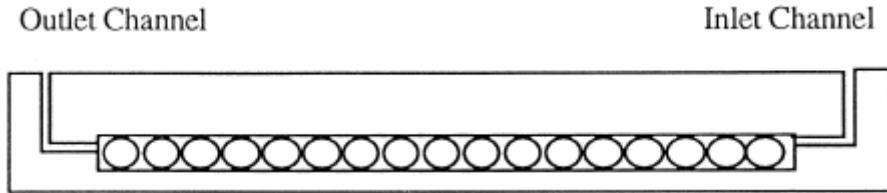


Figure 6. Side view of a glass-beads micro-model (Corapcioglu and Fedirchuk, 1999).

In principle, Hele–Shaw and glass-beads micro-models are easy to make. However, the use of optical microscopy poses a problem. The three-dimensional nature of the model makes it difficult, or sometimes impossible, to visualize the distribution of fluids under the level of the largest bead diameter. As such, much information cannot be recorded when optical means are employed.

2.3.2 Optical lithography

Developed during the last few decades, optical lithography (also called photolithography) is used when a specific flow network has already been designed with preferred parameters, like mean pore size, number of pores, geometry of pores, etc., and its features are very small in size. Such models cannot be created from the combination of materials, as done in Hele-Shaw or glass-beads models. They can be used to make models that carry any flow network and have a wide application for irregular or fractal patterns. Optical lithography models are also relatively inexpensive to produce.

The principles of optical lithography were introduced in the early 80's (Thompson et al., 1983, 1994). This method has been described in detail in the literature (see e.g., Cheng et al., 2004; Giordano and Cheng, 2001). First, the desired pattern for the micro-model is produced digitally, based on a statistical distribution, with or without a spatial correlation for the pores. The desired flow network is then printed on a transparent material. The transparent material with the network printed on it is called a mask. There are two ways of using the mask. For relatively small networks, the network printed on the mask is the magnified image of the desired network. For big or deep networks, the network printed on the mask has the exact dimensions as the desired network. Usually for deep networks, the negative of the network is printed on the mask. In this case, a copper covered glass plate is used as a mask. The network is printed by removing the copper layer from the mask. When the depth of the flow network is

relatively low, the mask is a normal transparency and the network is printed as it is on the mask.

Optical-lithography consists of the following general steps:

- Photoresist Application on a glass substrate
- Soft Bake
- Mask Aligner Set-Up
- Exposure
- Development
- Hard Bake

The network is commonly formed in a polymeric material called photo-resist. The glass substrate has to be made perfectly clean. After that, a thin layer of photo-resist, usually SU-8, is applied to it and the substrate is put to spin. The type of photo-resist and the duration of spinning determine the final thickness of the photo-resist layer, which is, in practice, the final depth of the network. Then the substrate is soft baked in order to harden the photo-resist.

The creation of the network on this layer of photo-resist is the second step of the procedure. The mask is projected on the photo-resist using ultraviolet light in a mask aligner. If the network has very small features, a transparency that carries a magnified image of the network can be used. This transparency is projected on the photoresist through an objective lens to bring the image back to the original size. In this way, the resolution of the projected image is improved. The area of the photo-resist that is exposed to UV light reacts with developing agents. Next, the exposed area of the photo-resist is washed away and what is left forms the flow network. When the network is deep, negative projection is used. In that case, the developed area is that which was not exposed to the UV light. The choice of development depends on the depth of the network and the type of photo-resist that has been used.

The inlet and outlet areas are developed in the same way. This time, there is no need for a magnified mask and projection because the dimensions of these areas are big enough and details do not matter. The mask has the actual dimensions of these areas. Inlet and outlet areas should be strengthened to endure the pressure imposed during the experiments. For this reason, pillars made of photo-resist are added within inlet and

outlet areas. Their dimensions are in the order of hundreds of micro-meters. An example of a micro-model constructed following optical lithography method is the one by Cheng and Giordano (2002), shown in Figure 7.

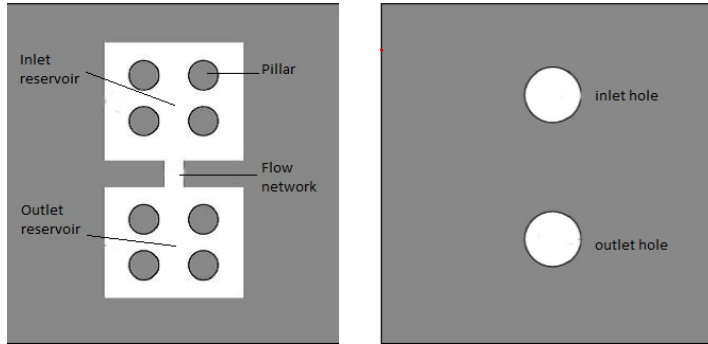


Figure 7. Bottom and upper plates (left and right drawings, respectively) of micro-models constructed by Cheng and Giordano (2002).

A second glass plate is used as a covering plate to complete the fabrication of the micro-model. Two holes are drilled on this glass plate for the inlet and outlet of the model. The micro-model is sealed with a thin layer of photo-resist on the upper glass plate. This layer acts like a glue and bonds the glass plate to the photo-resist with the application of mechanical pressure. This layer also ensures that micro-model pore walls are made of one material—namely the photo-resist only; avoiding mixed wettability in the model. The optical lithography method is relatively inexpensive and easy to implement. These two characteristics make them quite attractive. However, problems arise in making and using this kind of micro-model. Significant difficulty in sealing the model can occur when some features of the flow network are very small. This happens because there is not enough surface for the bonding between the thin layer of photo-resist that is used as glue and the photo-resist from the flow network that is in solid state.

Another major problem emerges from the photo-sensitive nature of photo-resist. Even after baking, exposure to light with a wavelength close to the violet or ultraviolet spectrum causes the photo-resist to produce nitrogen. The nitrogen bubbles, also called pockets, grow in size, breaking the solid photo-resist and gradually destroying the network. We reproduced this effect in the laboratory and the results are shown in figure 8. On the left, a photo-resist micro-model filled with water can be seen on the first day of its use and on the right, the same micro-model is shown after three days exposure to light. The model has been significantly damaged by the production of nitrogen. One solution to this problem is to replace all lights in the lab where a photo-

resist micro-model is being used with lights that have a spectral emission above 550 nm. This will ensure that there is no interaction between photo-resist and light. Also, the wavelength of observation lighting should be away from the violet region. Another solution is to use filters that cut off all wavelengths below 550 nm. In practice, both solutions are effective but both require extra expenses. In particular, the high-quality optical filters necessary to eliminate the undesired wavelengths can be very expensive.

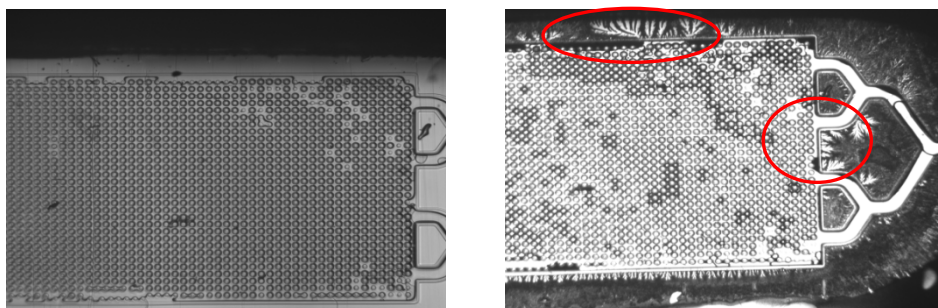


Figure 8. A photo-resist micro-model on the first day of its use (left) and the same micro-model after three days (right). The fractures in photo-resist can be seen clearly.

2.3.3 Etching method

The first etched micro-model was constructed by Mattax and Kyte in 1961 (Figure 9). The fabrication technique is based on chemical reactions and the interaction of laser and plasma radiation with glass, silicon or polymer (Zhang et al., 2010, 2011; Baouab et al., 2007; Gutierrez et al., 2008; Soudmand-asli et al., 2007; Weidman and Joshi, 1993; Jeong and Corapcioglou, 2005; Jeong and Corapcioglou, 2003; Baumann et al., 2002; Lanning and Ford, 2002). First, the desired pattern for the micro-model is produced with one of the methods mentioned in the previous section. The mask is prepared in one of the ways explained for optical lithography depending on the size and the depth of the desired network; the mask can be made to be the positive or the negative image of the network.

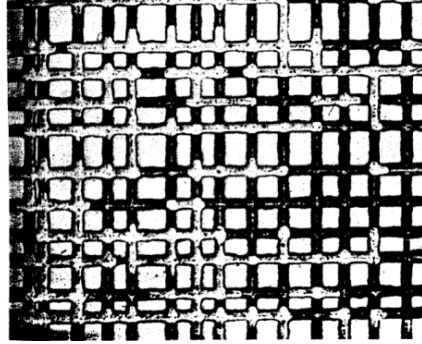


Figure 9. Capillary network in a portion of an etched micro-model (Mattax and Kyte, 1961)

The desired pattern is projected on a glass substrate that has already been covered with a layer of photo-resist, as in photo-lithography. But, in this case the network will be formed in the glass substrate and not in the photo-resist. The resolution of the mask strongly affects the outcome of the etching process. The thickness of the photo-resist will determine the depth of the desired flow network after the development of the network with the use of solvents. After the pattern is developed and exposed, the network is created using an etching method. Currently, there are two etching methods, which are explained below.

a) Chemical or wet etching

In chemical etching or wet etching, acids are used as etchants to etch the glass or silicon surface (Wegner and Christie, 1983; Johnston, 1962; Sagar and Castanier, 1998; Coskuner, 1997; Avraam et al., 1994; Sirivithayapakorn and Keller, 2003; Lago et al., 2002; McKellar and Wardlaw, 1982; Hornbrook et al., 1991; Upadhyaya, 2001; Jeong et al., 2000; Wan et al., 1996). The area covered by photo-resist remains unaffected by the acid. The depth of penetration depends on the etching rate of the acid (i.e., the penetration length over time) and the exposure time to the etchant. Alternatively, copper can be used, instead of the photo-resist, in lithography process. The copper then can be removed with the use of chemicals.

The wet etching process in an acidic bath, apart from the photo-lithographic step, may be broken down into three basic steps:

- diffusion of the etchant to the surface for removal;
- reaction between the etchant and the material being removed; and

- diffusion of the reaction byproducts from the reacted surface.

Wet etching is a very popular way of making micro-models. However, this method has some limitations. One shortcoming is that the pore walls are sloped rather than vertical. Also, there is a curvature at the bottom of pores. This happens because liquid acids are isotropic and thus erode glass in all directions. Figure 10 (from Iliescu et al., 2008) shows in black the micro-channels formed by wet etching technique on a glass substrate. The curvature at the bottom of the walls and the optical setup used to take the pictures create refraction, leaving no light to reach the camera's sensor. This effect hinders studying two-phase flow, especially if the optical visualization of fluids and their configuration in the network are important. One remedy would be to diffuse the illumination and increase the intensity of the light. Another effective solution is to use front-light illumination instead of back-light illumination. In this case, a strong contrast between the sample and the background is needed.

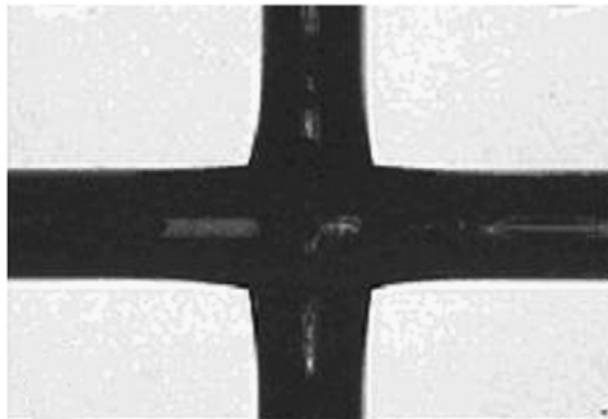


Figure 10. Optical images showing the intersection of two micro-channels (approximately $150\mu\text{m}$ in depth) etched in glass for 20 min in 49 per cent HF solution using amorphous silicon mask with a value of 100MPa (from Iliescu et al.,2008). The curved walls produce diffraction and the optical result is black.

b) Plasma or laser etching

Electromagnetic radiation provides another way to etch glass, or other transparent polymeric materials like PMMA or silicon. The radiation can be supplied from a laser source or from a beam of ions. The latter method is called ion milling, when using a noble-gas plasma (Durandet et al., 1990; Kolari et al., 2008). The most popular noble

gas for this purpose is Ar⁺. Using an ion gun, ions bombard the uncovered area, and by transfer of momentum, begin removing atoms from the glass surface.

The reactive ion etching process, apart from the photo-lithographic step, can be broken down in the following steps:

- generate etchant species (radicals or ions)
- reaction or momentum transfer with the Surface
- by-product desorption
- diffusion of by-product to bulk gas

Instead of ion milling, excimer (Basov et al., 1970) laser can be used to create the pattern on the glass substrate (Arnold et al., 1995). The technique is called LIGA (Lithographie, Galvanoformung, Abformung) and was introduced by Ehrfeld et al. (1987, 1994, 1996). The network pattern is directly formed on the substrate and the whole procedure is computer controlled.

Both procedures are very anisotropic, which means that the sloping effect at the walls is diminished. However, the control of the whole procedure is not easy. This procedure is usually reserved for very narrow and shallow channels. After the pattern has been created on the glass substrate, the inlet and outlet reservoirs are produced with wet-etching techniques. A second glass plate, on which two holes are drilled for the input and output, is used to cover the micro-model.

The sealing of the micro-model can be done in two ways, both of which are common for both wet and dry etched micro-models. One way is the use of a muffle furnace, or high temperature oven (Avraam et al., 1994). This method is used mostly for micro-models that are multi-layered. The other method involves placing a thin layer of polymer (a few nano-meters thick) between the two glass plates and baking in a UV oven (Tsakiroglou and Avraam, 2002). Heating the model and simultaneous application of a light pressure will have the desired effect for glass/glass bonding. Silicon and glass bonding can be achieved by gentle heating (~400 °C) while applying an electric field across the silicon/glass sandwich to ensure good contact via the associated electrostatic force. This method is known as field-assisted, or anodic, bonding (Giordano and Cheng, 2001). Anodic bonding will work only for moderate operating pressures of a few atmospheres within the micro-model. Other methods should be used if larger pressure must be applied (Holman and Little, 1981; Little, 1982).

Dry etching methods produce nearly vertical walls (82-90 degrees). The Deep Reactive-Ion Etching (DRIE) method, which is a plasma-etching method, also produces nearly vertical walls (88-90 degrees) with a very low surface roughness. The DRIE method can give good results for ratios between the depth and the width of an etched channel even higher than 20:1. However, there is still a maximum achievable aspect ratio between the depth and the width of the channel that depends on the material, the beam profile, etc. (Blauw et al., 2001, Yeom et al., 2003; Willingham et al., 2008).

Figure 11 (Ohara et al., 2010) shows that where the ratio between the depth and the width of the channels is from 6.6:1 to 1:2, the walls are vertical and the roughness of the bottom of the channels is low.

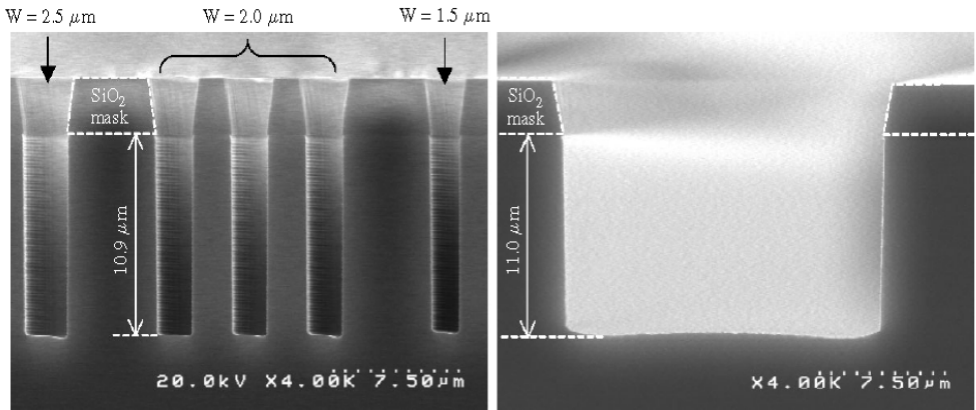


Figure 11. Mask openings and the channels produced with dry etching method; channel widths are 1.5–2.5 μm (left) and 20 μm (right) (Ohara et al.; 2010).

When the channels are deep and much narrow, it becomes difficult to get vertical walls and keep the roughness at the bottom of the channel low. Figure 12 (Yeom et al., 2005) shows that as the ratio of the depth to the width of the channels becomes larger, the quality of the channels becomes lower. The surface roughness increases and we don't get a rectangular shape at the bottom. Although such channels are not common to two-phase flow in porous media, they are presented here as an extreme example of reactive ion etching.

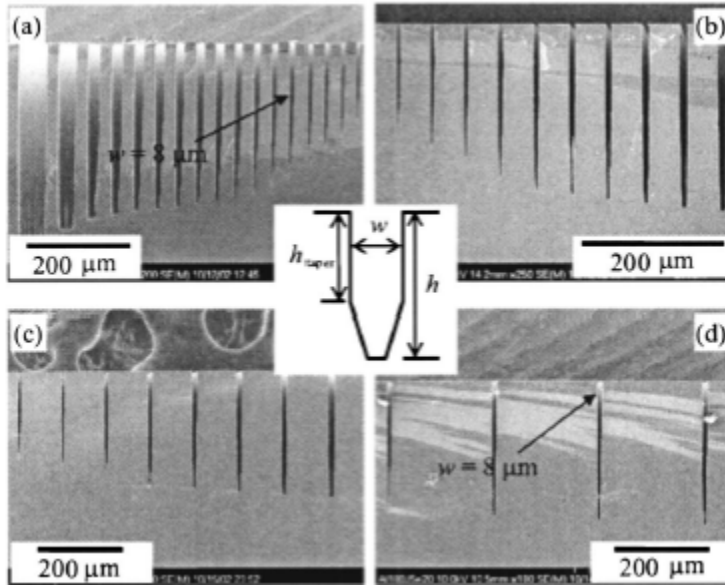


Figure 12. SEM images of silicon trenches, etched by ICP-DRIE process for three hours (Yeom et al., 2005). These are from four different initial pattern area densities: (a) 80 per cent microloading (explained in Hedlund et al., 1994) with 25 μm line spacing, (b) 50 per cent microloading with 50 μm line spacing, (c) 30 per cent microloading with 100 μm line spacing, and (d) 10 per cent microloading with 200 μm line spacing.

The Reactive Ion Etching method is a complicated and difficult procedure and many things can go wrong. Etching itself is a subject of on-going research. Given our current knowledge, however, etching remains one of the best ways to make good quality micro-models. Especially when optical microscopy with back light illumination is employed, etching is perhaps the best alternative. In particular, the stability of glass with respect to its chemical and physical properties is highly appreciated.

2.3.4 Stereo-lithography

Stereo-lithography (or SL) is a computer-based manufacturing process that was developed by Hull in 1986. As described by Melchels et al. (2010), it is a solid freeform fabrication technique. Stereo-lithography is an additive fabrication process that allows the fabrication of parts using a computer-aided design (CAD) file. The manufacturing of 3-D objects by stereo-lithography is based on the spatially controlled solidification of a liquid resin by photo-polymerization. The setup consists of a computer-controlled laser beam or digital light projector, a computer-driven building stage with a platform, and a resin reservoir. The platform is initially placed just below the resin surface, according

to the desired depth of the resin layer. The computer guides the laser beam to follow a path and illuminate a desired pattern on the resin surface. As a result of this, the resin in the pattern is solidified to a pre-specified depth, causing it to adhere to the support platform. After photo-polymerisation of the first layer, the platform is lowered incrementally, allowing the built layer to be recoated with liquid resin. Each time, the pattern is cured (i.e. solidified) to form another layer. As the depth of curing is slightly larger than the platform step height, good adherence to the first layer is ensured (i.e., unreacted functional groups on the solidified structure in the first layer polymerise with the illuminated resin in the second layer). These steps (i.e., the movement of the platform and the curing of a pattern in a layer of resin) are repeated until a solid, three-dimensional object of desired height is constructed. After draining and washing-off excess resin, the desired structure is obtained. In this structure, the conversion of reactive groups is usually incomplete, and post-curing with (stroboscopic) ultraviolet light is often employed to improve mechanical properties of the structures. In Figure 13, a schematic presentation of the process is presented.

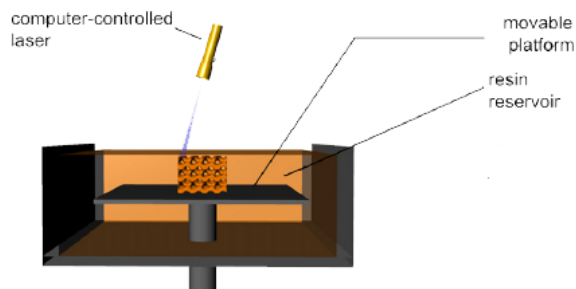


Figure 13. Schematic presentation of a bottom-up stereo-lithography system with scanning laser (Melchels et al., 2010)

To summarize, stereo-lithography fabrication method consists of the following steps:

- The laser beam forms the desired pattern on the resin surface
- Photo-polymerization
- The platform is incrementally lowered
- The previous steps are followed

- As soon as the construction is finished, the structure is cleaned from excess resin

Stereo-lithography is an effective way to make micro-models when the dimensions of the structure are not very small (larger than microns). Parts from a larger assembly (not micro-models but general structures) can be manufactured in one day and with great efficiency. The complexity of a flow network or a part of an assembly is not an issue. On the other hand, this procedure is quite expensive. Stereo-lithography micro-models have been used in studying flow (Crandall et al., 2008, 2009; Stoner et al., 2005; de Zélicourt et al., 2005). However, they are less popular when it comes to very small dimensions (micro-meter scale) because of the spatial resolution of the process.

2.3.5 Soft lithography

Soft lithography refers to methods for making structures using ‘soft’ materials like elastomeric stamps, moulds, and photo-masks (Quake et al., 2000; Rogers and Nusso, 2005; Wang et al. 2005, 2008; Shor et al., 2004). It is mostly reserved to create very small, simple geometric structures, on the micro- and nano-scale (Hug et al., 2003; Huh et al., 2007; Park et al., 2009). Variations of soft lithography method include micro contact printing (μ CP) (Xia and Whitesides, 1998), replica moulding (REM) (Senn et al., 2010), micro-transfer moulding (μ TM) (Xia and Whitesides, 1998), micro-moulding in capillaries (MIMIC) (Kim et al., 1996) and solvent-assisted micro-moulding (SAMIM) (Kim et al., 1997). These methods are particularly suitable for creating micro-scale structures, the scale of interest in two-phase flow, where soft lithography is most accurate.

One of the most widely used materials in soft lithography is PDMS, which is an elastomeric material. It is a liquid that is polymerized after mixing with a curing agent. The procedure for manufacturing a PDMS micro-model is explained in detail in Quake and Schere (2000), Auset and Keller (2004) and Markov et al. (2010). Usually, it consists of the following steps:

- The network of micro-model channels is created digitally. This network is printed on a transparency, which will be used as a mask in the next step.
- A silicon or glass wafer is spin-coated with photo-resist (positive or negative depending on the desired depth) to create a patterned silicon or glass wafer (called master) by using photo-lithography.

- The master wafer is put in a petri dish. Then, a mixture of liquid PDMS and curing agent is prepared. This mixture is then poured over the master wafer in the petri dish.
- The polymer is degassed under vacuum and then cured.
- After curing, the polymer is peeled from the master.
- The PDMS slab with the desired network is placed on a pre-cured thin slab of PDMS in order to close the network. Then it is exposed to ion plasma so that bonding can take place.

Soft lithography is widely used in two-phase flow studies. It is a method that produces detailed micro-models without severe production restrictions. However, one problem does arise. Because they are polymeric materials, their wetting properties may change with time. For instance, PDMS is initially hydrophobic, though not strongly. In the making of an all-PDMS micro-model, the two parts of the model are bonded with oxygen plasma. The treated PDMS becomes hydrophilic but the effect is not stable; it degrades with time and eventually recovers its hydrophobicity. This effect starts almost immediately after exposure, and it continues for hours, or even days, until the material reaches its initial condition (Murakami et al., 1998; Fritz and Owen, 1995). Thus, if hydrophilic behavior is needed, the micro-model must be used directly after its plasma treatment.

An alternative treatment is to force the PDMS surface to have specific wetting properties and become purely hydrophobic. This can be done with the application of a mixture of silane with ethanol (Zhou et al., 2010).

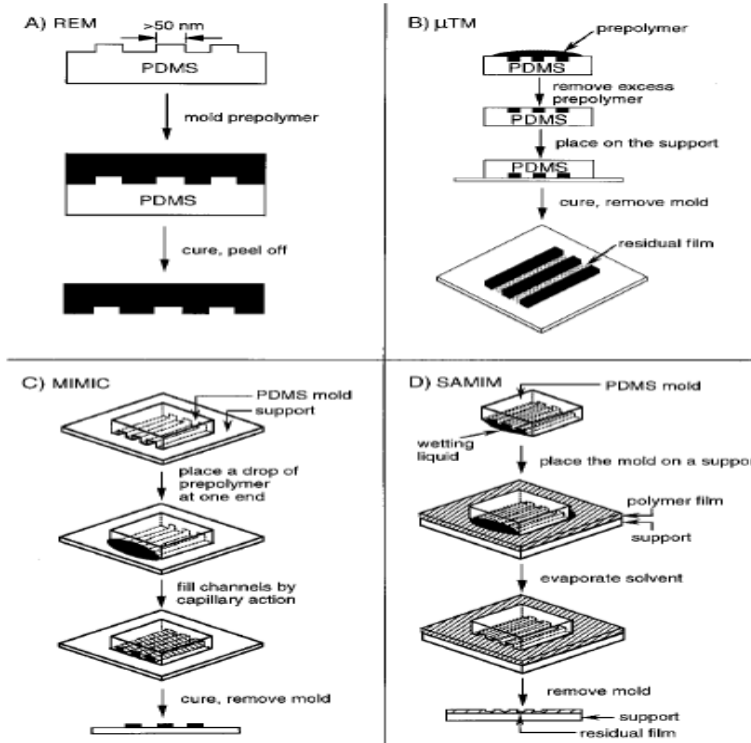


Figure 14. Schematic illustration of procedures for A) replica moulding, B) micro-transfer moulding, C) micro-moulding in capillaries, and D) solvent-assisted micro-moulding (Xia and Whitesides, 1998).

Another consideration is that the phases involved in the experiments will not make the material swollen or deformed. Gervais et al. (2006) studied the flow-induced deformation of PDMS models and provided a dimensionless number as a simple means of assessing whether deformation should be considered. This dimensionless number depends on the pressure drop along the network, the network's height and width, as well as the entry pressure of the features of the network. Depending on the value of this dimensionless number, deformation can be considered as important, or not. In table 1, the fabrication methods along with their main advantages and disadvantages and major references are presented.

Fabrication Method	Advantages	Disadvantages	Major references
Hele-Shaw and glass beads	Easy to make Choice of wetting properties Cheap to make No mask needed	Fixed or random network geometry Cannot be used under dynamic conditions as the lower half of the model cannot be visualized	Corapcioglu and Fedirchuk, 1997,1999; Chatenever and Calhoun, 1952.
Optical lithography	Accurate Can reproduce any network pattern Cheap to make	Not suitable for making for elongated models due to the manufacturing procedure Fixed wetting properties Cannot be exposed to regular light Requires a clean room to manufacture Mask needed	Thompson et al., 1983, 1994; Cheng et al., 2004
Wet etching	Relatively easy Choice of wetting properties depending on the chosen material Can reproduce any network pattern	The curvature on the walls makes back light illumination impossible Limited ratio between pore width and depth Mask needed	Wegner and Christie, 1983; Johnston, 1962; Sagar and Castanier, 1998
Deep Reactive Ion Etching - Laser etching- Ion etching	Highly accurate Can reproduce any network pattern	Limitation on the depth of the model Maximum ratio between width and depth Very expensive	Yeom et al., 2003; Ohara et al., 2010
Stereo lithography	3-D structures	Low resolution Very expensive	Hull, 1986; Melchels et al., 2010

Table 1. Fabrication methods along with their advantages and disadvantages

2.3.6 Micro-models materials

Glass or quartz, are materials that are widely used in micro-models, especially in Hele-Shaw and glass-bead micro-models. It is relatively easy to find well-polished glass or quartz plates or glass beads with a given diameter at a high accuracy. While the

construction of glass-bead micro-models is relatively easy, the creation of a flow network in glass or quartz plates is quite involved. However, if the flow network has to meet some stringent requirements (such as vertical walls, stable wettability properties, mechanical and chemical stability), then glass or quartz are the materials of choice. This creates some problems, given their physical properties.

Glass micro-models are relatively cheap to make using the chemical etching method. However, this cannot be done in a regular lab environment, because of the use of acids. This should be done in a well-controlled environment, like a clean room. When ion etching is employed, it is impossible to make them in a regular lab. The whole procedure requires specialized infrastructure, takes a lot of time and it is very expensive. Moreover, to date, there is an upper limit of about 20 to 30 microns on the maximum etched depth that can be reached with the channels still having a rectangular cross section. Additionally, there is a high probability that the whole procedure can fail in the last step of manufacturing, which is sealing the model. This is especially difficult if the features of the flow network are very small, providing not enough surface for bonding. Finally, given the cost in time and money, one has to be very careful with glass micro-models as they may break easily.

On the other hand, glass micro-models are stiff and rigid, and if the depth of the flow network is kept small (up to 20 μm) the whole manufacturing procedure can be well controlled. This provides very high quality micro-models that are practically insensitive to room temperature changes, have very well-defined wetting properties, can withstand pressures up to a few atmospheres, and hardly react with fluids that are commonly used in two-phase flow studies.

Soft materials, like PMMA and PDMS, are suitable for making inexpensive micro-models fast. PMMA, which is harder than PDMS, is an acrylic thermoplastic material, which is a good substitute for glass. It is not as rigid and stiff as glass, thus it is easier to treat. It can be etched either with laser radiation, with the use of ions, or chemically. PDMS micro-models are very cheap to produce, and can be made in a normal laboratory. However, one needs a master wafer, on which the flow network is formed; that has to be prepared in a clean room. Then, this wafer can be used to prepare from ten to fifteen micro-models in a normal lab.

While soft materials have the advantage of being very cheap and relatively easy to make, and do not require special laboratory (in the case of PDMS), there are some limiting issues. They react or absorb fluids and chemicals that are commonly used in two-phase flow studies. This results in a deformation (swelling) of the material that changes the properties of the flow network. For PDMS, there are some well-known

mixed wettability issues and change of properties with time. Special treatment may help but it is not always effective. These materials can deform under moderate pressures (less than an atmosphere) resulting in breaking the model in the case of PMMA, or destroying the bonding in the case of PDMS.

Silicon micro-models can be made in the same way as glass ones. Because of the different physical properties of the materials, tuning parameters should be properly adjusted, but the processes remain the same. But, they have severe limitations if they are to be used for two-phase flow studies. A major problem is that silicon is translucent and, therefore, one cannot use a wholly silicone-made micro-model for direct optical visualization. So, they are usually sealed with glass, or another transparent material. This means that the fluids involved will experience the presence of two different materials, with two different wetting properties. This is usually not desirable in two-phase flow studies. On the other hand, they provide the advantages that a glass-made micro-model has.

2.4 Micro-models visualization methods

2.4.1 Basic issues

Since their inception, a challenge in using micro-models has been the ability to monitor fluids configuration, fluid flow, and various features inside the micro-model. The choice of the visualisation method is essential to the outcome of any experiment. In a two-phase flow experiment, average saturation and specific interfacial area are some of the main variables of interest. The measurement of these variables is based on the study of pictures or videos. Given the dimensions of the pattern in a micro-model, the demands on resolution and color depth are quite strict. Moreover, in the case of dynamic experiments, where the fluids distributions need to be recorded as a function of time, a high image acquisition rate from the visualisation setup is also required.

Chatenever and Calhoun used cine-photo-micrography in their experiment in 1952. The apparatus consisted of a microscope and its accessories (lenses, mounts, etc.), a 16mm movie camera, a beam splitter, an arc illuminator, and an exposure meter. They obtained images of fluids distribution during an oil-flood experiment (Figure 15).

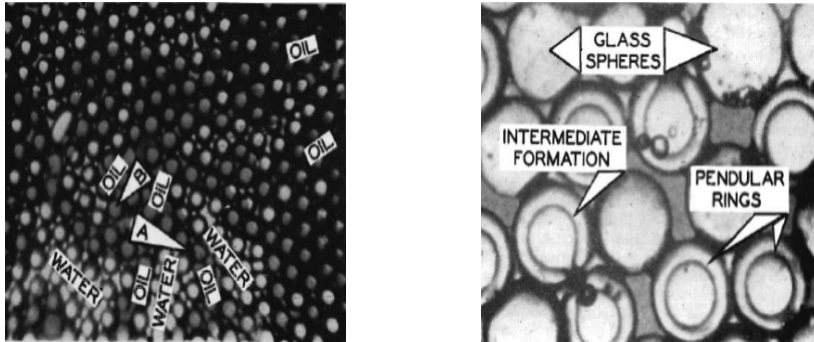


Figure 15. Images taken by Chatenever and Calhoun, 1952, during an oil-flood experiment. The right image is a magnified part of the left one. The spheres were uniform, with a size of 0.007 inches in radius. Left: A photomicrograph showing a portion of the channel flow structure established in an observation flow cell. Right: Close-up of fluids configuration and the final pendular rings formed during the oil flood.

The methods used to monitor two-phase flow, statically or dynamically, may be classified in four groups. These are methods making use of a microscope alone or along with a camera, photo-luminescent volumetric method, and fluorescent microscopy.

2.4.2 A microscope-camera visualization setup

This monitoring setup is quite simple. The micro-model is put under the objective lens of a microscope. The camera is mounted on the ocular of the microscope (Rangel-German and Kovscek, 2006; Keller et al., 1997, Corapcioglu et al., 2009; Vayenas et al., 2002; Paulsen et al., 1998). The camera is connected to a computer to allow for rapid data acquisition that can be stored in the computer. Images are processed and analyzed with appropriate software. From such analysis, one can determine average saturation and specific interfacial area (Cheng, 2002; Pyrak-Nolte et al.; 2008; Cheng et al., 2004; Chen et al., 2007). Figure 16 shows images obtained through visualization method.

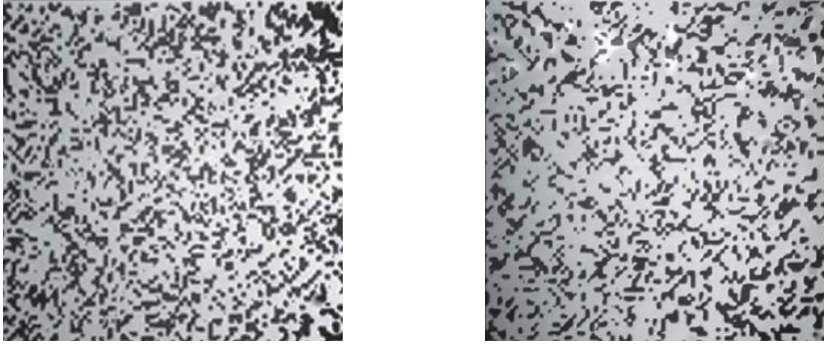


Figure 16. Images taken from a micro-model's flow network with a Qimaging Retiga EX camera through an Olympus microscope. The left picture is taken from a pattern with an aperture of 2 microns while the right picture is from a pattern with 1 micron aperture (Pyrak-Nolte et al., 2008). The size of the domain is $600\mu\text{m} \times 600\mu\text{m}$.

This technique is used when there is a need for a very high resolution—for example, when the smallest pore sizes are one to two microns or variables such as interfacial area need to be determined. This technique is not applicable when the micro-model is elongated and dynamic effects are being studied. The reason is that the optical window of a microscope is limited in size, meaning that while the microscope is focused on a specific area of the micro-model, there is no way to record what is going on in an area that is outside the optical window. A solution is to move the micro-model or the ocular of the microscope rapidly but this would introduce unknown inertial forces in the micro-model or poor image quality as the camera should be focused at all times, which would be difficult. For quasi-static conditions, this technique is quite appropriate.

2.4.3 Direct visualization with a camera

This method is somewhat similar to the setup described above. The difference is that no microscope is used and the camera captures images directly (Soll et al., 1993; Chang et al., 2009; Conrad et al., 1992; Hematpour et al., 2011). Thus the camera can be placed at different orientations with respect to the micro-model. The camera can be situated at a distance from the micro-model in order to exclude any vibrations affecting the system. The camera may also have an extra objective lens in order to increase the magnification of the system. High resolution digital cameras with sophisticated CCD and CMOS sensors allowed the elimination of the microscope.

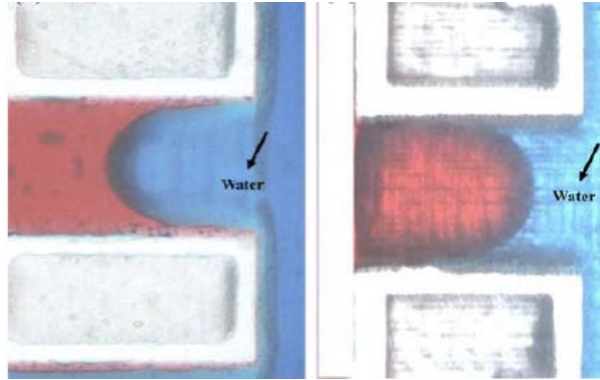


Figure 17. Photographs taken with a camera. (Chang et al., 2009). On the left, a channel from the micro-model is pictured. On the right, the same channel is pictured after treatment to become hydrophilic. In red is diesel fuel and in blue is water.

Figure 17 shows images of an acrylic micro-model taken with a camera at a resolution of 640x480 in a Red, Green, Blue (RGB) format (Chang et al., 2009). The micro-model shown in the right is treated to have a thin film of silicate coating on the acrylic surface. The effect of this treatment on micro-model wettability is quite visible. After heating in an oven at 110 °C, the silicate coating changed the wetting characteristics of the micro-model from hydrophobic (left) to hydrophilic (right).

Generally, cameras without a microscope are used to analyse and measure when magnification of the image is not necessary and the needs for resolution are not stringent. The use of a microscope provides better resolution but less flexibility. Currently, cameras built for monitoring micro-phenomena have a satisfying frame rate for photographs and video, as well as good resolution and color depth. Also, powerful software provides easy handling and analysis of the data acquired. Cameras have the advantage of moving without disturbing the micro-model. This offers the ability to monitor dynamic or static effects where the movement of the camera could be necessary. More than one camera can also be used to monitor different parts of a micro-model simultaneously. This cannot be done when using a microscope-camera setup.

2.4.4 Photo-luminescent Volumetric Imaging (PVI) – Confocal microscopy

Montemagno and Gray (1995) introduced the PVI method. In order to construct their porous medium, they used optical-quality quartz grains. They used two immiscible fluids, with their refractive indices matched to quartz (Budwig, 1994). The wetting phase was doped with property-selective fluorophores that preferentially partitioned onto the fluid-fluid interface. The system was surveyed with a planar laser source at

successive planes. The laser beam excited fluorophores and thereby illuminated fluid-fluid interfaces. A CCD camera was used to capture the fluorescent image (Figure 18). After processing of these images, a three-dimensional data set was generated showing the pore space as well as the location of the fluid-fluid interfaces.

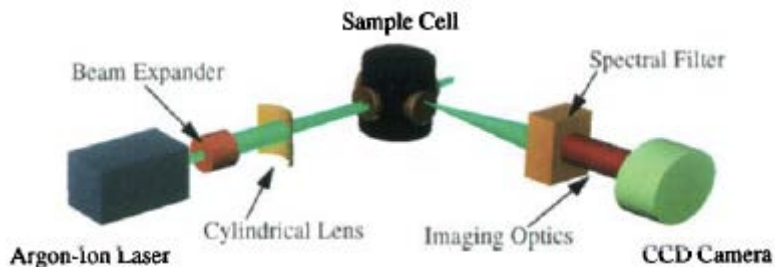


Figure 18. The experimental setup for PVI (Montemagno and Gray, 1995)

The experimental setup consisted of an Argon-ion laser source emitting at 514.5 nm, a beam expander, a cylindrical lens, the sample cell, a spectral filter, the imaging optics, and a CCD camera. The Argon-ion laser source emitted a laser beam with a diameter of 1.5 mm. The beam expander increased the beam's diameter to 25 mm and the cylindrical lens transformed the beam from cylindrical to planar. The beam's thickness was 125 μm and had a width of 15 mm in the sample cell. When the fluorophores in the sample cell were excited, they emitted a light with a different wavelength from that of the excitation source. This light passed through a spectral filter, which cut off any unwanted wavelengths and, with the proper optics, was directed to the CCD camera. After an exposure of approximately 100 ms the CCD system digitized the image and transferred it to a computer. The resolution gained was better than 1 μm over volumes even greater than 125 mm^3 . As a continuation of the work of Montemagno and Gray, Zang (1998) studied the application of photo-luminescent volumetric imaging in multiphase dynamics in porous media. Later, Stohr et al. (2003) used this method to perform 3-D measurements of single-phase flow and transport on the pore scale. This method was the first high-resolution index-matching- technique to visualize the flow of two immiscible liquids at the same time.

One application of fluorescent microscopy is Micro-Particle Imaging Velocimetry ($\mu\text{-PIV}$), a technique used to investigate micro-scale fluidic transport and mixing (Shinahara et al., 2004; Perrin et al., 2005; Fernandez-Rivas et al., 2007). Micro-PIV has been used to study pressure-driven flow (Meinhart et al., 1999; Tretheway and Meinhart, 2002; Devasenathipathy et al., 2003; Sato et al., 2003; Shinohara et al., 2004),

electro-osmotic flow (Devasenathipathy et al., 2002), and the fluid dynamics of blood capillaries in vivo (Sugii et al., 2002) and in vitro (Sugii and Okamoto, 2004; Okuda et al., 2003).

Micro-PIV is based on Particle Imaging Velocimetry method, where micron-size particles are used as markers in fluid flow to measure instantaneous velocity fields in experimental fluid mechanics (Keane and Andrian, 1992). These particles should match well the properties of the fluid under consideration; they should follow the movement of the fluid, should not affect its properties (such as viscosity), and should not sink. Lindken et al. (2009) presented a review of micro-PIV including recent developments, applications, and guidelines.

Wereley and Meinhart (2005) gave a detailed description of the technique in theory and practice. Figure 19 shows a schematic description of a typical micro-PIV hardware implementation.

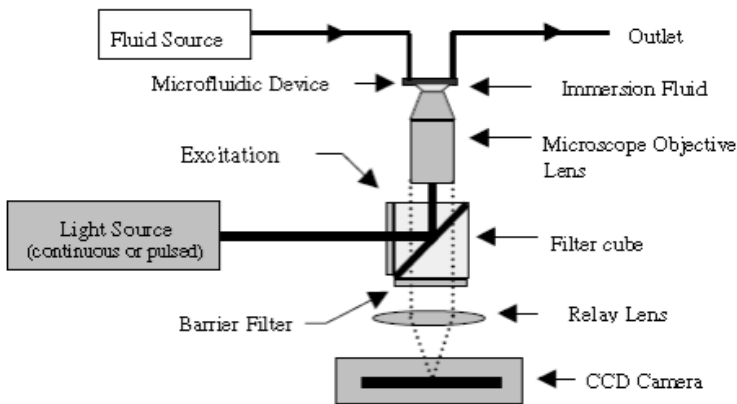


Figure 19. Schematic description of a typical micro-PIV hardware implementation (Wereley and Meinhart, 2005).

The imaging principle is fluorescent microscopy. The laser source, which can be pulsed or continuous wave, emits light that is guided to a lens that converts the light beam to a planar one. Light passing through the micro-model excites the fluorescent particles, and when they get de-excited, they emit light at a higher wavelength. The filter allows only light emitted from the fluorescent particles to reach the camera's sensor. In order to increase the efficiency of the technique, the objective of the microscope is put into immersion oil.

In this way, two-dimensional images can be obtained. Three-dimensional images can be constructed if fluorescent microscopy is combined with confocal microscopy. From

these images, the change in the position of an individual particle can be measured. Because the time interval between two sequential images is known, the whole velocity field can be computed. If the particles are property-selective, the flow velocity of individual phases can be measured using different particles for different phases.

Confocal microscopy is another technique based on the same effect (laser induced fluorescence) but is applied differently. It is a point-by-point imaging method. Confocal microscopy creates sharp images of specimens that would otherwise appear blurred when viewed with a conventional microscope. It also allows the construction of a three-dimensional image of the specimen by superposing two-dimensional images obtained at sequential layers. Marvin Minsky patented confocal microscopy in 1957 (Minsky, 1988). Semwogerere and Weeks (2005) presented the basic concepts of confocal microscopy.

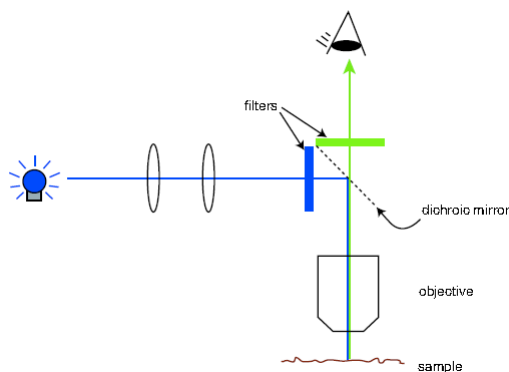


Figure 20. The basic setup for confocal microscopy (Semwogerere and Weeks, 2005).

Figure 20 provides a schematic of confocal microscopy (Semwogerere and Weeks, 2005). Light from a monochromatic light source (usually laser) is reflected from a dichroic mirror and projected on the specimen through an objective lens. The sample is either dyed with fluorescent dyes or contains fluorescent particles. These particles absorb the light from the light source and emit light when they get de-excited at a wavelength that is higher than the absorbed light. This emitted light passes through the dichroic mirror while the light from the light source is reflected back to the source. Two filters are used to ensure that only light that is along the optical axis will be used. Thus, the sample is visualized point-by-point in two-dimensions.

Confocal microscopy is ideal for effects that are relatively slow and where the smallest feature that needs to be visualized is less than the optical diffraction limit—precisely where conventional optical microscopy fails to give results (Lindek et al., 1996; Hell et

al., 1994, Baumann and Werth, 2004; Baumann and Werth, 2002; Baumann, 2007; Sirivithayapakorn and Keller, 2003; Keller and Auset, 2006; Baumann and Niessner, 2006, Wan and Wilson, 1994a, 1994b;). Grate et al. (2010) discussed the visualization of wetting film structures and a non-wetting immiscible fluid in a pore network micro-model using a solvatochromic dye.

In table 2, visualization methods along with their limitations and applicability are presented.

Visualization method	Suitable for	Limitations
Microscope and camera	Any transparent (partially), two dimensional micro-model High resolution optical images	Not suitable for three-dimensional models Limited in resolution (above 1 μ m)
Direct visualization with a camera	Relaxed needs in resolution High acquisition rate	Not suitable for three-dimensional models Very low resolution
Photo-luminescent Volumetric Imaging	Three-dimensional porous media. High resolution	Refractive index matching is necessary Relatively slow effects Relatively expensive
Confocal microscopy	Very high resolution (sub-micron) Quasi-static or very low speed effects	Effective for depths up to 250 μ m Relatively expensive Very low acquisition rate Not suitable for dynamic effects

Table 2. The visualizations methods along with their limitations and their applicability.

2.5 Applications of micro-models in studies of flow and transport in porous media

2.5.1 Studies of two-phase displacement processes

The majority of the applications of micro-models in studies of flow and transport in porous media are related to the immiscible displacement of two fluid phases (Avraam

et al., 1994; Baouab et al., 2007; Dawe et al., 2010, 2011; Budwig, 1994; Chatenever and Calhoun, 1952; Chen and Wilkinson, 1985; Chuoke et al., 1959; Corapcioglu et al., 2009; Coskuner, 1997; Cottin et al., 2011; Crandall et al., 2009; de Zelicourt et al., 2005; Toth et al., 2007; Tsakiroglou and Avraam, 2002; van der Marck and Glas, 1997; Wan et al., 1996; Chang et al., 2009; Theodoropoulou et al., 2005; Berejnov et al., 2008; Tsakiroglou et al., 2003, 2007). Processes of drainage and imbibition, as well as the mechanisms that dominate them, like viscous or capillary fingering, snap-off, etc., have been studied using micro-models (Zhang et al., 2011; Ferer et al., 2004; Grate et al., 2010; Gutiérrez et al., 2008; Hug et al., 2003; Huh et al., 2007; Jeong and Corapcioglu, 2003, 2005; Jeong et al., 2000; Kalaydjian, 1987; Lovoll et al., 2005; Mattax and Kyte, 1961; Montemagno and Gray, 1995; Pyrak-Nolte et al., 1988; Rangel-German and Kovsky, 2006; Stohr et al., 2003; Sugii and Okamoto, 2004; Tallakstad et al., 2009; Lenormand and Zarcone, 1985; Lenormand, 1989, Lenormand et al., 1988; Sharma et al. 2011; Romano et al., 2011; Frette et al., 1997).

One of the first studies of two-phase flow under quasi-static conditions and the relevant displacement mechanisms was presented in the work of Lenormand et al. (1983). They used a transparent polyester resin micro-model (Bonnet and Lenormand, 1977), with the channels in the form of a network of capillary ducts. They observed the displacement of the meniscus formed by the two phases under different conditions, like piston-type motion and snap-off. They determined that two types of imbibition can occur depending on the number and spacing of the ducts filled with the non-wetting phase. Later on, Chang et al. (2009) conducted displacement experiments following Lenormand's assumptions. They provided valuable experimental support and suggestions for Lenormand's displacement formulas, which are the basis for many related experimental and numerical studies. Lovoll et al. (2010) used a glass-beads micro-model to study the influence of viscous fingering on dynamic saturation-pressure curves. They obtained a scaling relation between pressure, saturation, system size, and the capillary number.

Dong and Chatzis (2010) studied the movement of a wetting film in a liquid-gas system. They used a consolidated glass-beads micro-model. They found that the capillary pressure controls the wetting film imbibition ahead of the main displacement front.

Cottin et al (2010) studied the transition from capillary to viscous flow during drainage, and its dependence on the capillary number. They employed two kinds of micro-models. One was manufactured using standard soft lithography techniques and the other was manufactured with wet etching techniques. Their experiments shed light on the role of viscous forces during the invasion process and their competition with the

capillary force. At very low applied capillary number, the invading liquid flowed through one single channel at the time and built a very open structure. At larger capillary number, the role of viscous forces increased.

2.5.2 Measurements of interfacial area and phase saturation

An important application of micro-models has been in the measurement of two-phase flow properties that cannot be determined with standard experiments. A major example is the quantification of the area of interfaces formed between phases, in particular the fluid-fluid interface. The significance of fluid-fluid interfaces in two-phase flow has been recognized as early as 1951. Rapoport and Leas (1951) elucidated the role of interfaces and interfacial energies in controlling the simultaneous flow of two fluids in a porous medium. Later on, theoretical studies proposed that a complete description of two-phase flow in a porous medium should take into account the evolution and dynamics of fluid-fluid interfaces (see e.g., Marle, 1981, 1982; Hassanizadeh and Gray, 1990, 1993a, 1993b). A major obstacle to making advances in this regard is our ability to measure specific interfacial area. Micro-models have made possible the experimental investigation of the role of interfaces (Crandall et al., 2010; Pyrak-Nolte et al., 2008).

Recently, two-phase flow studies were performed using photo-resist micro-models that had flow patterns based on stratified percolation (Cheng, 2002, Pyrak-Nolte et al., 2008; Cheng et al., 2004; Chen et al., 2007). In these studies, distributions of the two phases in the flow network during quasi-static drainage and imbibition were visualized. Phase saturation and interfacial area could be determined using image processing and relationships between phase saturation, capillary pressure, and interfacial area were investigated. They found that for each set of capillary pressure and saturation data point, a single value for specific interfacial area exists (see Figure 21). More importantly, the surfaces produced by the graphical representation of these triplets were nearly the same for drainage and imbibition, within the limits of experimental error (Chen et al., 2007; Cheng, 2002; Cheng et al., 2004; Liu et al., 2011). Later, dynamic drainage and imbibition displacement experiments were performed (Bottero, 2009; Crandall et al., 2010). Under these conditions, unlike qualitative experiments, capillary pressure within the network is not equal to the externally applied pressure anymore. Therefore, local capillary pressure was determined from the curvature of each individual interface.

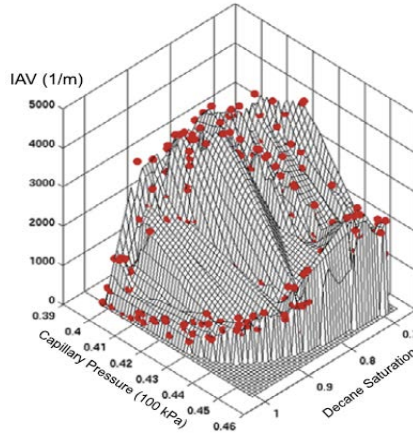


Figure 21. The graphical representation of the triplets during drainage experiments (Cheng et al., 2004).

In these visualizations, interfaces are seen as a line and there is no information on the third dimension. If one assumes the depth of the model to be constant, the area of interfaces can be calculated. However, the depth of a photo-resist model is not really constant. The photo-resist layer where the flow network lies is produced by spin-coating. Because centrifugal forces depend on the distance from the origin, the depth of the model is not the same everywhere. However, this discrepancy can be negligible in small micro-models.

The curvature of an interface in the third direction cannot be determined with optical means. If images are acquired in grayscale and a very high resolution, the curvature may be estimated by means of processing the change in the grey shade of the interface.. If only the quasi-static case is examined, fluorescent microscopy could present an alternative to the optical means to obtain three-dimensional images. In this case, the model should be very small in size (a few pores), given that the field of view is limited. Under dynamic conditions, conventional optical microscopy is the best way to deal with the situation. Any other method requires time for the image acquisition. During this time, the distribution of phases in the flow network changes in a way that makes the images acquired useless.

2.5.3 Measurements of relative permeability

The effective two-phase flow coefficients of porous media, such as the capillary pressure and relative permeability functions, bridge the gap between the microscopic flow dynamics and the macroscopic behavior of porous media flow (Kalaydjian, 1990;

Avraam and Payatakes, 1999; Chang et al., 2009; Rapoport and Leas, 1951; Karoutsos and Tsakiroglou, 2005; Tsakiroglou et al., 2003, 2007, Wang et al., 2006). Thus determining relative permeability of each phase as a function of saturation under a wide range of experimental conditions is important (Chang et al., 2009). Tsakiroglou et al. (2003) used micro-models to study the influence of the capillary number on non-equilibrium immiscible displacement in two-phase flow experiments. They showed that the relative permeabilities of the two phases are not only a function of saturation but also strongly depend on capillary numbers (Figure 22).

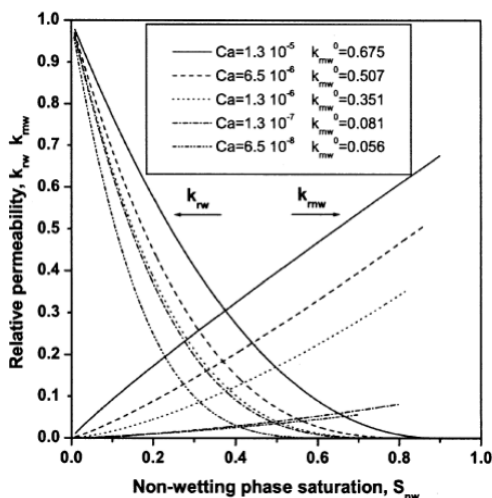


Figure 22. Estimated relative permeability—saturation curves for different capillary numbers (Tsakiroglou et al., 2003).

Tsakiroglou et al. performed their measurement with a glass-etched micro-model, initially totally filled with the wetting phase (distilled water with methylene blue). The non-wetting phase (paraffin oil) was then injected into the network, at a fixed flow rate with the use of a syringe pump. With the use of a CCD camera, successive shots of the displacement were captured from a central region of the network. The pressure drop along this central region of the network was measured with a differential pressure transducer, with respect to time. This procedure allowed the determination of saturation and relative permeability of each phase as a function of time.

Alternatively, Chang et al. (2009) calculated relative permeability by keeping a constant pressure head difference between the wetting and the non-wetting phase. For drainage, the non-wetting phase was introduced into a micro-model that was already fully saturated with the wetting phase, while the wetting phase flow rate was measured. This

was continued until steady state was reached. Images from the micro-model were taken with the use of a CCD camera.

The main issue that needs to be addressed in such measurements is the accuracy in determining phase pressures or in measuring phase saturation. Phase saturation measurement depends on the resolution of the visualization setup and can be usually quantified. Phase pressure, however, is very difficult to measure. Especially in complex flow networks with very small dimensions, it is practically impossible to measure local pressure within the micro-model. Post processing is necessary to retrieve and calculate the average value for a given spatial domain.

2.5.4 Enhanced oil recovery

Micro-models have also been used to study oil recovery from underground reservoirs in the presence of gas and water phases (Keller et al., 1997). Buckley (1990) reviewed the application of micro-models in multi-phase flow and enhanced oil recovery. Enhanced oil recovery relies on the displacement of oil by another liquid or gas towards a well where oil is collected (Liu, 2006). The most common techniques involve the injection of gases and chemicals, such as polymers and foams. The success of these techniques depends on the physical properties of each phase, the viscosity ratios, capillary number, temperature, reservoir conditions, and flow dynamics. These factors have been studied in a number of micro-models (Amani et al., 2010; Armstrong et al., 2010; Dong et al., 2007; Hematpour et al., 2011; Nguyen et al., 2002; Nourani et al., 2007; Sagar and Castanier, 1998; Soudmand-asli et al., 2007; Wyckoff and Botset, 1936; Zekri and El-Mehaideb, 2002; Mahers and Dawe, 1985; Wardlaw, 1980; Bora et al., 1997; Nguyen et al., 2002; Lago et al., 2002; Hornbrook et al., 1991; Romero et al., 2002; Sohrabi et al., 2001, 2004; Feng et al., 2004; van Dijke et al., 2002; Liu et al., 2002, 2006; Oren et al., 1992; Sayegh and Fisher, 2008; Doorwar and Mohanty; 2011; Wang et al., 2006, Naderi and Babadagli, 2011) .

Dong et al. (2007) used a micro-model to investigate the displacement mechanisms of alkaline flooding in enhanced heavy oil recovery (EOR). They observed that two mechanisms govern the EOR process. One was in-situ water-in-oil (W/O) emulsion and partial wettability alteration; the other was the formation of an oil-in-water (O/W) emulsion. Heavy oil was emulsified in brine by an alkaline plus a very dilute surfactant formula, entrained in the water phase, and produced out of the model. The upper left image in Figure 28 shows the micro-model containing heavy oil and irreducible water at the end of oil injection. The upper right section is an image of pore-level oil and water distribution. This image shows water films surrounding the solid boundaries and

the continuous oil phase staying in the central portion of pores and throats of the pore network. The image also shows that the micro-model is water-wet. The lower part of Figure 23 shows the picture of the micro-model network with an injection of a chemical slug. In alkaline injection, the injected water phase penetrated into the residual oil phase and created some discontinuous water ganglia inside the oil channels to form W/O emulsion. The viscosity of W/O emulsion is much higher than that of the crude oil. Therefore, the oil was displaced in the form of W/O emulsion with little fingering effect. Some oil also touched the pore walls, indicating that the pore wall became partially oil-wet. The wettability alteration also aided in blocking the water flow in those channels.

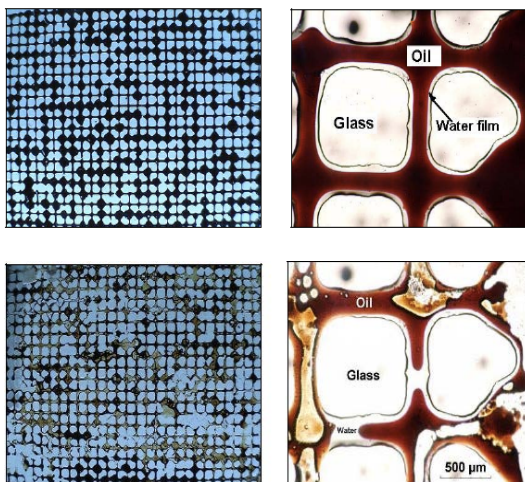


Figure 23. Above: Micro-model with heavy oil and irreducible water saturation. (Left) Portion of micro-model. (Right) pore-level image formation of W/O emulsion in alkaline injection. Below: (Left) Portion of micro-model. (Right) pore-level image (Dong et al., 2007).

Nourani et al. (2007) used a glass micro-model to simulate a fractured system and the microbial enhanced oil recovery (MEOR) technique (Stewart and Fogler, 2001, 2002; Soudmand-asli et al., 2007; Armstrong and Wildenschild, 2010; Amani et al., 2010; Zekri and El-Mehaideb, 2002, Terri et al., 2001). This method is based on the reduction of interfacial tension (IFT) and the change of the wettability of rock with the aid of bacteria to make the displacement of oil easier. In their work, five bacterial species were taken from MIS crude oil originating from one of the aging Persian fractured reservoirs. These micro-organisms are very strong in increasing oil recovery in the two ways mentioned above. Two series of visualization experiments were carried out to examine the behavior of microbial enhanced oil recovery in micro-models designed to

resemble the fractured system: static and dynamic. In the static experiments, a carbonate rock-glass micro-model was used to simulate the reservoir conditions. The dynamic experiments were performed in a glass micro-model that had a fracture with a 45 degrees inclination. The image processing methodology was used to determine the recovery achieved by MEOR in the micro-model made of glass.

2.6 Summary and Discussions

This review of micro-models presented the most important concepts behind choosing a flow network in a micro-model, the different manufacturing techniques of micro-models, the available visualization methods, and the various applications of micro-models.

The flow networks used in micro-models can be classified based on the model structure and the statistical distribution of sizes assigned to its features. The pattern chosen, the size distribution of its features, and the experimental purpose determine the choice of the micro-model's fabrication method. Wet etching techniques that are isotropic create a curvature on the walls of the micro-model. If optical microscopy with back-light illumination is used, this curvature on the walls may cause severe problems. It causes refraction and the images at the bottom of channels are shown in black. A possible, but not entirely effective, solution is to use a light diffuser. While dry etching techniques, like plasma etching, provide vertical walls, they are not that efficient when the depth of the micro-model becomes high. It is very difficult to reach depths equal to or higher than 50 μm without damaging the profile of the channel or the verticality of the walls.

An inexpensive and effective way of making micro-models is optical lithography. It is accurate and precise. However, optical lithography has a major drawback. If the photoresist, inside which micro-model channels are made, is exposed to ultraviolet or near-ultraviolet light, then it produces nitrogen that will eventually destroy the model on its way out of the closed system. A solution to this problem is to hard bake the model before using it, or use filters that partially block the harmful wavelengths. However, none of these solutions are permanent. The only effective solution is to totally eliminate wavelengths close to the harmful spectral region, which could be quite expensive.

Stereo-lithography is an effective way of making polymeric micro-models, provided they are not very small. This technique is effective in manufacturing integrated structures but it becomes problematic when the dimensions become very small (microns). Moreover, stereo-lithography is expensive because an integrated commercial system is needed in order to produce such models.

Soft lithography is an inexpensive and effective way of making polymeric micro-models. The major problem with these models, when it comes to flow studies, is that their wetting properties change with time. After some time, the wetting phase may become the non-wetting phase. Also, care must be taken to ensure that the phases involved in two-phase flow experiments will not cause the material to swell or become deformed. Hele-Shaw glass-bead models are easy to make without spending too much time and money. They are useful and simple. However, they have problems being visualized optically. The beads or spheres between the two glass plates limit visualization to only one side because they are three-dimensional objects. As such, measurements for saturation or interfacial area will not be accurate enough and some assumptions regarding the symmetry of menisci must be made.

All manufacturing methods requiring a mask are highly affected by the preciseness of the mask used to form the network on the material. If the mask is of low resolution, then the actual network will be of low resolution too.

Various ways of visualizing events occurring in a micro-model include using a camera, combination of a microscope and a camera, and laser-induced fluorescence. The use of a microscope, with or without a camera, is a purely optical way of visualizing flow through the micro-models. The accuracy of measurement is highly dependent on the resolution of the recording apparatus, which is always lower than the diffraction limit. Laser-induced fluorescence methods are more accurate. With their use, three-dimensional images can be reconstructed, which cannot be done with optical means. However, these methods are restricted in their acquisition time and their field of view. Thus, they can be used only under static, or nearly static, conditions. In the case of front light optical microscopy, the flow network can be formed in silicon and sealed with glass, or another transparent material. However, this would introduce wettability issues, as the phases involved will experience the presence of two different materials with different wetting properties, something that is not desired. Evidently, deciding on the appropriate micro-model for a specific application is complicated.

Micro-models have been and will continue to be a very powerful tool to study flow and transport phenomena on the micro-scale. However, further research is needed to improve their properties, the existing techniques of manufacturing and visualization, as well as the development of new materials and techniques. For instance, one of the limiting factors in the use of micro-models in two-phase flow is the optical visualization of flow and the distribution of fluids in three dimensional micro-models. This is important in the sense that single-layered micro-models are considered to be quasi-two-dimensional porous media. This raises some questions regarding their

correspondence to real porous media. The improvement of etching methods so as to create channels that have a rectangular cross section at depths higher than 40 μm is also a challenge. Another important issue is the development of micro-sensors for measuring local phase pressure, within the flow network of a micro-model; this will be a major advantage in two-phase flow studies. Also, the development of new materials, or the modification of the existing ones is needed to meet certain experimental requirements. For example, for reliable and accurate experimental results, it is important to have micro-models with stable wetting properties. Finally, the ultimate goal would be to have the ability to produce cheap, easy to make micro-models, that represent a real porous medium well, and to be able to take measurements that can be trusted, independently of the nature of the model, in terms of their dimensions.

Acknowledgements

This work was funded by The Netherlands Organization for Scientific Research (NWO), under grant no. 818.01.008. Authors are members of the International Research Training Group NUPUS, financed by the German Research Foundation (DFG) (grant no. GRK 1398) and NWO (grant no. DN 81-754). We appreciate critical comments by two anonymous referees, which helped to improve the manuscript.

2.7 References

Amani, H., Sarrafzadeh, M. H., Haghghi, M., Mehrnia, M. R. (2010), Comparative study of biosurfactant producing bacteria in MEOR applications, *Journal of Petroleum Science and Engineering*, Volume 75, Issues 1-2, pp. 209-214, ISSN 0920-4105, doi: 10.1016/j.petrol.2010.11.008.

Armstrong, R. T., Wildenschild, D. (2010), Designer-Wet Micro-models for Studying Potential Changes in Wettability during Microbial Enhanced Oil Recovery, American Geophysical Union, Fall Meeting 2010.

Arnold, J., Dasbach U., Ehrfeld W., Hesch K., Loewe H. (1995), Combination of excimer laser micromachining and replication processes suited for large scale production ('Laser-LIGA'), *Applied Surface Science*, Vol 86, pp. 251-258.

Auset, M., and A. A. Keller (2004), Pore-scale processes that control dispersion of colloids in saturated porous media, *Water Resour. Res.*, 40, W03503, doi:10.1029/2003WR002800.

Avraam, D.G., and A.C. Payatakes (1999), Flow mechanisms, relative permeabilities, and coupling effects in steady-state two-phase flow through porous media. The case of strong wettability, *Ind Eng Chem Res*, **38** (3), pp. 778–786.

Avraam, D. G., Kolonis, G. B., Roumeliotis, T. C., Constantinides, G. N. and Payatakes, A. C. (1994), Steady-state two-phase flow through planar and nonplanar model porous media, *Transport in Porous Media*, **16**, 1, 0169-3913, pp. 75-101, Doi: 10.1007/BF01059777.

Baouab, Z., M. Najjari , H. Ouerfelli, S. Ben Nasrallah (2007), Experimental study of the effects of hydraulic gradient and injected-gas flow rate on fragmentation in porous media, *Journal of Petroleum Science and Engineering*, **59**, 250–256.

Basov, N. G., Danilychev, V.A., Popov, Y. M., and Khodkevich, D. D., (1970), *JETP Lett.* **12**, 329.

Baumann, T. (2007), Colloid transport processes: Experimental evidence from the pore scale to the field scale, In F. H. Frimmel, F. von der Kammer & H.-C. Flemming, *Colloidal transport in porous media*, 55-86, Springer, Berlin.

Baumann, T., and C. J. Werth (2004), Visualisation and modelling of polystyrol colloid transport in a silicon micro-model, *Vadose Zone J.*, **3**, pp. 434-443.

Baumann, T., and R. Niessner (2006), Micro-model study on repartitioning phenomena of a strongly hydrophobic fluorophore at a colloid/1-octanol interface, *Water Resour. Res.*, **42**, W12S04.

Baumann, T., C. J. Werth and R. Niessner (2002), Visualisation of colloid transport processes with magnetic resonance imaging and in etched silicon micro-models, *DIAS Report Plant Prod*, **80**, 25-30.

Berejnov, V.; Djilali, N.; Sinton, D.(2008), Lab-on-chip methodologies for the study of transport in porous media: Energy applications, *Lab on a Chip*, **8** (5), pp. 689–693.

Blauw, M. A., T. Zijilstr, and E. van der Drift (2001), Balancing the etching and passivation in time-multiplexed deep dry etching of silicon, *J. Vac. Sci. Technol. B*, **19**, pp. 2930-2934.

Blunt, M. and King P. (1991), Relative permeabilities from two- and three-dimensional pore-scale network modeling, *Transport in Porous Media*, Vol. **6**, 4, 0169-3913, pp. 407 – 433, Doi: 10.1007/BF00136349.

Bonnet, J., Lenormand, R. (1977), Realisation de micro-modeles pour l'etude des ecoluments polyphasiques en milieu poreux, *Revue de l' Insitut francais du petrole*, **42**, pp. 477-480.

Bora, R., Maini, B. B., and Chakma, A. (1997), "Flow visualization studies of solution gas drive process in heavy oil reservoirs using a glass micro-model," presented at the *SPE International Thermal Operations and Heavy Oil Symposium*, Bakersfield, California, USA, SPE 37519.

Bottero, S. "Advances in the theory of capillarity in porous media", Ph.D. thesis, November 2009, Utrecht University.

Buckley, J.S. (1990), Multiphase Displacements in Micro-models, *Interfacial Phenomena in Oil Recovery*, N.R. Morrow, ed., Marcel Dekker, Inc., New York City, pp. 157-189.

Budwig, R. (1994), Refractive index matching methods for liquid flow investigations, *Exp Fluids*, **17**, pp 350-355.

Chang, L.-C., Z. H.-H. Chen, H.-Y. Shan, (2009), Effect of connectivity and wettability on the relative permeability of NAPLs, *Environ Geol.*, **56**:1437-1447, doi: 10.1007/s00254-008-1238-8.

Chang, L.-C., J.-P. Tsai, H.-Y. Shan, H.-H. Chen (2009), Experimental study on imbibition displacement mechanisms of two-phase fluid using micro model, *Environ Earth Sci*, **59**:901-911, doi: 10.1007/s12665-009-0085-6.

Chatenever, A. and Calhoun Jr., J.C. (1952), Visual examinations of fluid behavior in porous media: Part 1, *Petroleum Transactions, AIME* **195**, pp. 149-156.

Chen, J.-D., and Wilkinson D (1985), Pore-scale viscous fingering in porous media, *Phys. Rev. Lett.*, **55**, pp. 1892-1895.

Chen, D., L. J. Pyrak-Nolte, J. Griffin, and N. J. Giordano (2007), Measurement of interfacial area per volume for drainage and imbibition, *Water Resour. Res.*, **43**, W12504, doi:10.1029/2007WR006021.

Cheng, J.-T. (2002), Fluid flow in ultra-small capillaries, Ph.D. Thesis, Purdue University.

Cheng, J.-T., L. J. Pyrak-Nolte, D. D. Nolte, and N. J. Giordano (2004), Linking pressure and saturation through interfacial areas in porous media, *Geophys. Res. Lett.*, **31**, L08502, doi:10.1029/2003GL019282.

Cheng, J.-T., and N. J. Giordano (2002), Fluid flow through nanometer-scale channels, *Phys. Rev. E*, **65**, 031206.

Chuoque, R. L., P. van Meurs, and C. van der Poel (1959), The instability of slow, immiscible, viscous liquid-liquid displacements in permeable media, *Trans. Am. Inst. Min. Metall. Pet. Eng.*, **216**, 188- 194.

Corapcioglu, M.Y., and P. Fedirchuk (1999), Glass bead micro-model study of solute transport, *J. Contam. Hydrol.*, **36**, pp. 209–230.

Corapcioglu, M.Y., Chowdhury, S. and Roosevelt, S.E. (1997), Micro-model visualization and quantification of solute transport in porous media, *Water Resources Research*, **33**, 11, pp. 2547–2558.

Corapcioglu, M. Y., Yoon, S., and Chowdhury, S. (2009), Pore-Scale Analysis of NAPL Blob Dissolution and Mobilization in Porous Media, *Transport in Porous Media*, **79**(3), pp. 419-442, doi: 10.1007/s11242-008-9331-8.

Coskuner, G. (1997), Microvisual Study of Multiphase Gas Condensate Flow in Porous Media, *Transport in Porous Media*, **28**, pp. 1-18.

Cottin, C., Bodiguel, H., and Colin, A. (2010), Drainage in two-dimensional porous media: From capillary to viscous flow, *Phys. Rev. E.*, **82**:4.

Cottin, C., Bodiguel, H., and Colin, A. (2011), Influence of wetting conditions on drainage in porous media: A microfluidic study, *Phys. Rev. E.*, **84**:2.

Crandall, D., G. Ahmadi, D. Leonard, M. Ferer, and D. H. Smith (2008), A new stereolithography experimental porous flow device, *Rev. Sci. Instrum.*, **79**, 044501, doi:10.1063/1.2903740

Crandall, D., G. Ahmadi, M. Ferer, D. H. Smith (2009), Distribution and Occurrence of Localized-Bursts in Two-Phase Flow through Porous Media, *Physica A*, Vol. **388**, pp. 574-584.

Crandall, D., Ahmadi, G., Smith, D. H., Bromhal, G. (2010), Direct, dynamic measurement of interfacial area within porous media, 7th International Conference on Multiphase Flow, ICMF 2010, Tampa, FL, USA, May 30-June 4, 2010.

Dawe, R.A., Caruana, A., Grattoni, C.A., (2010), Microscale visual study of end effects at permeability discontinuities, *Transp. Porous Media.*, doi:10.1007/s11242-010-9642-4.

Dawe, R.A., Caruana, A., Grattoni, C.A., (2011), Immiscible Displacement in Cross-Bedded Heterogeneous Porous Media, *Transp. Porous Media*, doi: 10.1007/s11242-010-9687-4.

de Zélicourt, D., K. Pekkan, H. Kitajima, D. Frakes, and A. P. Yoganathan (2005), Single-step stereolithography of complex anatomical models for optical flow measurements, *J Biomech Eng*, **127**: 204-207.

Devasenathipathy, S., Santiago J. G. and Takehara K. (2002), Particle tracking techniques for electrokinetic microchannel flows, *Anal. Chem.*, **74**, pp. 3704–13.

Devasenathipathy, S., Santiago J. G., Wereley S. T., Meinhart C. D. and Takehara K. (2003), Particle imaging techniques for microfabricated fluidic systems, *Exp. Fluids*, **34**, pp. 504–14.

Doorwar, S., and Mohanty, K. K., (2011), Viscous fingering during non-thermal heavy oil recovery, SPE Annual Technical Conference and Exhibition, Denver, Colorado, USA.

Dong, M., Liu, Q. and Li, A. (2007), Micro-model Study of the Displacement Mechanisms of Enhanced Oil Recovery By Alkaline Flooding, SCA 2007-47, International Symposium of the Society of Core Analysts, Calgary, AB Canada, Sept 10 – 12.

Dong, M., and Chatzis, I. (2010), Effect of Capillary Pressure on Wetting Film Imbibition Ahead of Main Liquid–Gas Displacement Front in Porous Media, *Petroleum Science and Technology*, **28**:9, pp.955-968.

Durandet, A., O. Joubert, J. Pelletier, M. Pichot (1990), Effects of ion bombardment chemical reaction on wafer temperature during plasma etching, *Journal of Applied Physics*, Volume **67**, Issue 8, pp.3862-3866, doi: 10.1063/1.345009.

Ehrfeld W., Abraham M., Ehrfeld U., Lacher M., Lehr H. (1994), Materials for LIGA products, Proc. *7th IEEE Int Workshop on Micro Electro Mechanical Systems*, Kanagawa, Japan.

Ehrfeld W., Lehr H., Michel F. Wolf A. (1996), Micro electro discharge machining as a technology on micromachining, in *SPIE Proceedings Series*, **2879**, pp 332-337.

Ehrfeld, W., Bley P., Goetz F., Hagmann P., Maner A., Mohr J., Moser H.O., Muenchmeyer D., Schelb W., Schmidt D., Becker E.W. (1987), Fabrication of microstructures using the LIGA process, Proc. *IEEE Micro Robots and Teleoperators Workshop*, Hyannis (Eds Gabriel KJ; Trimmer WSN) p. 1, IEEE Katalog No: **87** TH 0204-8.

Feng, Q. X., Di, L. C., Tang, G. Q., Chen, Z. Y., Wang, X. l., and Zou, J. X. (2004), A visual micro-model study: the mechanism of Water Alternative Gas displacement in porous media, presented at the *SPE/DOE 14 th symposium on Improved Oil Recovery*, Tulsa, Oklahoma, USA, SPE 89362.

Ferer, M., Ji, C., Bromhal, G. S., Cook, J., Ahmadi, G., Smith, D. H., (2004), Crossover from capillary fingering to viscous fingering for immiscible unstable flow: Experiment and modelling, *Phys. Rev. E*, **70** (1).

Fernández Rivas, D., M. N. Kashid, D. W. Agar and S. Turek (2005), Slug Flow Capillary Microreactor: Hydrodynamic Study, *African Physical Review*, **1**, Special Issue (Microfluidics):0005.

Frette, O. I., Maloy, K. J., Schmittbuhl, J. (1997), Immiscible displacement of viscosity matched fluids in two dimensional porous media, *Phys. Rev. E.*, **55**, pp. 2969-2975.

Fritz, J. L., and Owen, M. J., (1995), Hydrophobic recovery of plasma-treated polydimethylsiloxane, *Journal of Adhesion*, **54**, pp. 33-45.

Gervais, T., El-Ali, J., Günther, A., and Jensen, K. F. (2006), Flow-induced deformation of shallow microfluidic channels, *Lab on a Chip*, **6**(4), 500-507.

Giordano, N., and J.-T. Cheng (2001), Microfluid mechanics: progress and opportunities, *J. Phys.: Condens. Matter*, **13**, R271, doi: 10.1088/0953-8984/13/15/201.

Grate JW, C Zhang, TW Wietsma, MG Warner, NC Anheier, Jr, BE Bernacki, G Orr, and M Oostrom. 2010. "A note on the visualization of wetting film structures and a nonwetting immiscible fluid in a pore network micro-model using a solvatochromic dye". *Water Resources Research*, **46**:W11602. doi:10.1029/2010WR009419

Grate, J. W., Zhang, C., Wietsma, T. W., Warner, M. G., Anheier Jr., N. C., Bernacki, B. E., Orr, G., and Oostrom, M. (2010), A note on the visualization of wetting film structures and a nonwetting immiscible fluid in a pore network micro-model using a solvatochromic dye, *Water Resour. Res.*, **46**, W11602, doi:10.1029/2010WR009419.

Gutiérrez, B., F. Juárez, L. Ornelas, S. Zeppieri, A. López de Ramos (2008), Experimental Study of Gas–Liquid Two-Phase Flow in Glass Micro-models, *Int. J. Thermophys.*, **29**:2126–2135, DOI 10.1007/s10765-007-0305-9.

Hassanizadeh, S.M and W.G. Gray (1990), Mechanics and thermodynamics of multiphase flow in porous media including interphase boundaries, *Adv. Water Resour.*, **13**, 169-186.

Hassanizadeh, S.M and W.G. Gray (1993), Thermodynamic basis of capillary pressure in porous media, *Water Resour. Res.*, **29**, pp. 3389-3405.

Hassanizadeh, S.M and W.G. Gray (1993), Toward an improved description of the physics of two-phase flow, *Adv. Water Resour.*, **16**, pp. 53-67.

Hassanizadeh, S.M., and , W.G. Gray (1979), General Conservation Equations for Multi-phase Systems 1. Averaging Procedure, *Advances in Water Resources*, **2**, pp. 131-144.

Hassanizadeh, S.M., and W.G. Gray (1979), General Conservation Equations for Multi-phase Systems 2. Mass, Momenta, Energy, and Entropy Equations, *Advances in Water Resources*, **2**, pp. 191-208.

Hassanizadeh, S.M., and W.G. Gray (1980), General Conservation Equations for Multi-phase Systems 3. Constitutive Theory for Porous Media Flow, *Advances in Water Resources*, **3**, pp. 25-40.

Hassanizadeh, S.M., M.A. Celia, and H.K. Dahle (2002), Dynamic effects in the capillary pressure-saturation relationship and their impacts on unsaturated flow, *Vadose Zone Journal*, **1**, pp. 38-57.

Hedlund, C., Blom, H. O., Berg, S. (1994), Microloading effect in reactive ion etching, *Journal of Vacuum Science Technology A: Vacuum Surfaces and Films*, **12**, 4, pp. 1962-1965.

Heiba, A.A., Sahimi, M., Scriven, L.E. and Davis, H.T. (1982), Percolation theory of two-phase relative permeability. SPE 11015, presented at the 57th Annual Fall Meeting of the Society of Petroleum Engineers, New Orleans, LA.

Hell, S. H., Stelzer, E. H. K., Lindek, S., and Cremer, C., (1994), Confocal microscopy with an increased detection aperture: type-B 4Pi confocal microscopy, *Optics Letters*, **19**, 3, pp. 222-224.

Hematpour, H., Mardi, M., Edalatkhah, S., Arabjamaloei, R. (2011), Experimental Study of Polymer Flooding in Low-Viscosity Oil Using One-Quarter Five-Spot Glass Micro-model, *Petroleum Science and Technology*, Vol. **29**, 11, pp. 1163-1175.

Holman, R., and Little, W. A., (1981), Refrigeration for Cryogenic Sensors and Electronic Systems, *NBS Special Publication*, **607**, ed J. E. Zimmerman, D. B. Sullivan, and S. E. McCarthy (Washington, DC: US Government Printing Office), p. 160.

Hornbrook, J. W., Castanier, L. M., and Pettit, P. A. (1991), Observation of foam/oil interactions in a new, high-resolution micro-model, presented at the 66th Annual Technical Conference and Exhibition of SPE, Dallas, Texas, USA, SPE 22631.

Hug, T. S., Parrat, D., Kunzi, P.-A., Staufer, U., Verpoorte, E., de Rooij, N. F., (2003), Fabrication of nanochannels with PDMS, silicon and glass walls and spontaneous filling by capillary forces, 7th International Conference on Miniaturized Chemical and Biochemical Analytical Systems, California, USA.

Huh, D., Mills, K. L., Zhu, X., Burns, M. A., Thouless, M. A., and Takayama, S., (2007), Tuneable elastomeric nanochannels for nanofluidic manipulation, *Nature Materials*, **6**, pp. 424-428, doi:10.1038/nmat1907.

Iliescu, C., B. Chen, J. Miao (2008), On the wet etching of Pyrex glass, *Sensors and Actuators A: Physical*, Volume **143**, Issue 1, Micromechanics Section of Sensors and Actuators (SAMM), based on contributions revised from the Technical Digest of the IEEE 20th International Conference on Micro Electro Mechanical Systems (MEMS 2007) - MEMS 2007, IEEE 20th International Conference on Micro Electro Mechanical Systems, Pages 154-161, ISSN 0924-4247, DOI: 10.1016/j.sna.2007.11.022.

Jeong S.W. and M.Y. Corapcioglu (2003), A micro-model analysis of factors influencing NAPL removal by surfactant foam flooding, *J. Contam. Hydrol.*, **60**, pp. 77-96.

Jeong S.W. and M.Y. Corapcioglu (2005), Force analysis and visualization of NAPL removal during surfactant-related floods in a porous medium, *Journal of Hazardous materials*, Vol. **46**, Issues 1-3, pp. 8-13, doi: 10.1016/j.jhazmat.2005.06.015.

Jeong, S.W., M.Y. Corapcioglu, and S.E. Roosevelt (2000), Micro-model study of surfactant foam remediation of residual trichloroethylene, *Environ. Sci. Technol.*, **34**, pp. 3456–3461.

Johnston, W.G. (1962), Dislocation etch pits in non-metallic crystals with bibliography, *Progress in ceramic science*, vol **2**, Burke JE (ed), pp 1-75. Pergamon Press, New York.

Kalaydjian, F. (1990), Origin and quantification of coupling between relative permeabilities for two-phase flows in porous media, *Transp. Porous Media*, **5**, pp. 215–229.

Keane, R. D., R. J. Andrian (1992), Theory of cross-correlation analysis of PIV images, *Applied Scientific Research*, **49**, 3, 0003-6994, pp. 191-215, Doi: 10.1007/BF00384623.

Keller, A. A., Auset, M. (2006), A review of visualization techniques of biocolloid transport processes at the pore scale under saturated and unsaturated conditions, *Advances in Water Resources*, **30**, pp. 1392–1407.

Keller, A.A., M.J. Blunt and P.V. Roberts (1997), Micro-model observation of the role of oil layers in three-phase flow, *Transp. Porous Media*, **26**, pp. 277–297.

Kim, E., Y. Xia, X.-M. Zhao and G.M. Whitesides (1997), Solvent-assisted microcontact molding: A convenient method for fabricating three-dimensional structures on surfaces of polymers, *Adv. Mater.*, **9**:651–54.

Kim, E., Y. Xia, and G. M. Whitesides (1996), Micromolding in Capillaries: Applications in Materials Science, *J. Am. Chem. Soc.*, **118** (24), pp 5722–5731, DOI:10.1021/ja960151v.

Kolari, K., V. Saarela and S. Franssila (2008) , Deep plasma etching of glass for fluidic devices with different mask materials, *J. Micromech. Microeng.*, **18**, 064010 (6pp), doi: 10.1088/0960-1317/18/6/064010.

Lago, M., Huerta, M., and Gomes, R. (2002), Visualization Study During Depletion Experiments of Venezuelan Heavy Oils Using Glass Micro-models, *Journal of Canadian Petroleum Technology*, **41** (1), doi: 10.2118/02-01-03.

Lanning, L.M., Ford R.M. (2002), Glass micro-model study of bacterial dispersion in spatially periodic porous networks, *Biotechnol. Bioeng.*, **78**: 556–566.

Lenormand, R., (1989), Flow Through Porous Media: Limits of Fractal Patterns, *Proc. R. Soc. London, Ser. A*, **423**, pp. 159-168..

Lenormand, R.; Zarccone, C.; Sarr, A., (1983), Mechanisms of the displacement of one fluid by another in a network of capillary ducts, *J. Fluid Mech.*, 135, pp. 337–353.

Lenormand, R. (1989), Application of fractal concepts in petroleum engineering, *Physica*, D 38, 230.

Lenormand, R., and C. Zarccone (1985), Invasion percolation in an etched network: Measurement of a fractal dimension, *Phys. Rev. Lett.*, 54, 2226.

Lenormand, R.; Zarccone, C., (1985), Two-Phase flow experiments in a twodimensional permeable medium, *Physicochem. Hydrodyn*, 6 (5_6), pp. 497–506.

Lenormand, R., E. Touboul and C. Zarccone (1988), Numerical models and experiments on immiscible displacements in porous media, *J. Fluid Mech.*, **189**, pp. 165–187

Lindek, S., Cremer, C., and Stelzer, E. H. K., (1996), Confocal theta fluorescence microscopy with annular apertures, *Applied Optics*, **35**, 1, pp. 126-130.

Lindken, R., M Rossi, S. Grosse, and J. Westerweel (2009), Micro-Particle image velocimetry (microPIV): recent developments, applications, and guidelines, *Lab on a chip*, **9** (17):2551–2567.

Little, W.A., (1982), Microminiature refrigeration — small is better, *Physica B+C*, Volumes **109-110**, Part 3, pp. 2001-2009, ISSN 0378-4363, 10.1016/0378-4363(82)90564-2.

Liu, Q. (2006), Interfacial phenomena in enhanced heavy oil recovery by alkaline flood, Ph.D.Thesis, University of Regina, Regina, Saskatchewan, Canada.

Liu, Z., Yue, X., Hou, J., and Zhang, L. (2002), Comparison of displacement oil mechanism of polymer, ASP and foam of ASP in micro pores and dead ends of pores, SPE Asia Pacific Oil and Gas Conference and Exhibition, SPE 77876.

Liu, Y., Nolte, D. D., Pyrak-Nolte, L. J., (2011), Hysteresis and Interfacial Energies in Smooth-walled Microfluidic Channels, *Water Resour. Res.*, **47**, W01504, doi:10.1029/2010WR009541.

Lovoll, G., Meheust, Y., Maløy, K. J., Aker, E., Schmittbuhl, J., (2005), Competition of gravity, capillary and viscous forces during drainage in a two-dimensional porous medium, a pore scale study, *Energy*, **30** (6), pp. 861-872.

Lovoll, G., Jankov, M., Maloy, K. J., Toussaint, R., Schmittbuhl, J., Schafer, G., Meheust, Y., (2010), Influence of viscous fingering on dynamic saturation-pressure curves in porous media, *Transp. Porous Media*, **86** (1), pp. 335–354.

Mahers E.G., Dawe R.A., (1985), Visualisation of Microscopic Displacement Processes Within Porous Media in EOR Capillary Pressure Effects, "3rd European Meeting on Improved Oil Recovery", Rome, **1**, pp. 40-58, 16- 18 April .

Markov, D.A., Samson P.C., Schaffer D.K., Dhummakupt A., Wikswo J.P., Shor L.M. (2010). Window on a Microworld: Simple Microfluidic Systems for Studying Microbial Transport in Porous Media, *JoVE*, **39**, <http://www.jove.com/index/Details.stp?ID=1741>, doi: 10.3791/1741.

Marle, C.-M. (1981), From the pore scale to the macroscopic scale: Equations governing multiphase fluid flow through porous media, *Proceedings of Euromech 143*, Delft, Verruijt, A. and Barends, F. B.J. (eds.), pp. 57-61.

Marle, C. M. (1982), On macroscopic equations governing multiphase flow with diffusion and chemical reactions in porous media, *Intl. J. Engng Sci.*, **20**, pp. 643-662

Mattax, C.C. and Kyte, J.R. (1961), Ever see a water flood?, *Oil and Gas Journal*, **59**, pp. 115-128.

McKellar, M. and Wardlaw, N. C., 1982, A method of making two-dimensional glass micro-models of pore system, *J. Can. Petrol. Technol.* **21**(4), pp. 1-3.

Meinhart, C. D., Wereley S. T., and Santiago J. G. (1999), PIV measurements of a microchannel flow, *Exp. Fluids*, **27**, pp. 414-9.

Melchels, F. P.W., Feijen, J., Grijpma, D. W. (2010), A review on stereolithography and its applications in biomedical engineering, *Biomaterials*, Volume **31**, Issue 24, Pages 6121-6130, ISSN 0142-9612,

Minsky, M. (1988), Memoir on inventing the confocal microscope, *Scanning*, **10**, pp. 128-138.

Montemagno, C. D., and W. G. Gray (1995), Photoluminescent volumetric imaging: A technique for the exploration of multiphase flow and transport in porous media, *Geophys. Res. Lett.*, **22**(4), 425-428, doi:10.1029/94GL02697.

Murakami, S.-I., Kuroda, T., and Osawa, Z., (1998), Dynamics of polymeric solid surfaces treated with oxygen plasma: Effect of aging media after plasma treatment, *Journal of Colloid and Interface Science*, **202**, pp. 37-44.

Naderi, K., and Babadagli, T., (2011), Visual analysis of immiscible displacement processes in porous media under ultrasound effect, *Phys. Rev. E*, **83**, 5.

Nguyen, Q. P., Thissen, M. H. G., and Zitha, P. L. J. (2002), Effect of trapped foam on gas tracer diffusion in a visual microflow model, presented at the SPE Improved Oil Recovery Symposium, Tulsa, OK, USA, SPE 75208.

Nolte, D.D., and L. J. Pyrak-Nolte (1991), Stratified continuum percolation—scaling geometry of hierarchical cascades, *Phys Rev A*, **44** 10, pp. 6320–6333.

Nolte, D.D., L. J. Pyrak-Nolte and N. G. W. Cook (1989), The Fractal Geometry of Flow Paths in Natural Fractures in Rock and the Approach to Percolation, *PAGEOPH*, Vol. **131**.

Nourani, M., H. Panahi, D. Biria, R. Roosta Azad, M. Haghighi, A. Mohebbi (2007), Laboratory Studies of MEOR in Micro-model as a Fractured System, 10.2118/110988-MS, Eastern Regional Meeting, 17-19 October 2007, Lexington, Kentucky USA.

Nuss, W. F., and R. L. Whiting (1947), Technique for reproducing rock pore space [in oil sands], *AAPG Bulletin*, **31**: 2044-2049.

Ohara, J., Asami, K., Takeuchi, Y. and Sato, K. (2010), Development of RIE-lag Reduction Technique for Si Deep Etching Using Double Protection Layer Method, *IEEJ Transactions on Electrical and Electronic Engineering*, **5**: 125–130. doi: 10.1002/tee.20506.

Okuda, R., Sugii Y. and Okamoto K. (2003), Velocity measurement of blood flow in a microtube using micro PIV system, Proc. *PSFVIP-4*, June 3-5, 2003, Chamonix, France.

Oren, P.E., Billiotte, J., Pinczewski, W.V. (1992), Mobilization of Waterflood Residual Oil by Gas Injection for Water-Wet Conditions, *SPE Formation Evaluation*, **7**, 10.2118/20185-PA.

O'Melia, C.R. (1989), Particle--particle interactions in aquatic systems, *Colloids Surfaces*, **39**, pp. 255-271, doi: 10.1016/0166-6622(89)80191-X.

Park, S.-m., Huh, Y. S., Craighead, H. G., Erickson, D., (2009), A method for nanofluidic device prototyping using elastomeric collapse, *Proceeding of the National Academy of Sciences of the United States of America*, vol. **106**, no. 37, 15549-15554, doi: 10.1073/pnas.0904004106.

Paulsen, J. E., Oppen, E. and Bakke, R. (1998), Biofilm morphology in porous media, a study with microscopic and image techniques, *Water Science and Technology*, Volume **36**, Issue 1, 0273-1223, doi: 10.1016/S0273-1223(97)00317-X.

Pereira, G.G., W.V. Pinczewski, D.Y.C. Chan, L. Paterson and P.E. Øren (1996), Pore-scale network model for drainage-dominated three-phase flow in porous media, *Transp. Porous Media*, **24**, pp. 167–201.

Perrin, C.L., K. S. Sorbie, P. M. J. Tardy (2005), Micro-PIV: A New Technology for Pore Scale Flow Characterization in Micro-models, Society of Petroleum Engineers, 10.2118/94078-MS.

Pyrak-Nolte, L. J., D. D. Nolte, D. Chen, and N. J. Giordano (2008), Relating capillary pressure to interfacial areas, *Water Resour. Res.*, **44**, W06408, doi:10.1029/2007WR006434.

Pyrak-Nolte, L.J., Cook, N.G.W., and D.D. Nolte (1988), Fluid Percolation through Single Fractures, *Geophysical Research Letters*, Vol. **15**, no. 11, pp. 1247-1250.

Quake, S. R., and A. Scherer (2000), From micro- to nanofabrication with soft materials, *Science*, **290**, 1536–1540.

Rangel-German, E. R., and A. R. Kovscek (2006), A micro-model investigation of two-phase matrix-fracture transfer mechanisms, *Water Resour. Res.*, **42**, W03401, doi:10.1029/2004WR003918.

Rapoport.L.A. and W.J.Leas (1951),Relative permeability to liquid in liquid-gas systems, *Pet.Trans.*,**192**, pp. 83-98.

Rogers, J. A. and Nuzzo, R. G. (2005), Recent progress in soft lithography, *Materials today*, **8**, pp. 50–56.

Romano, M., Chabert, M., Cuenca, A., and Bodiguel (2011, H., Strong influence of geometrical heterogeneity on drainage in porous media, *Phys. Rev. E*, **84**.

Romero, C., Alvarez, J. M., and Muller, A. J. (2002), Micro-model studies of polymer-enhanced foam flow through porous media, presented at the SPE/DOE Improved Oil Recovery Symposium, Tulsa, Oklahoma, USA, SPE 75179.

Sagar, N. S., and L. M. Castanier (1998), Pore-level visualization of oil-foam interactions in a silicon micro-model, in *Proceedings of the SPE/DOE Improved Oil Recovery Symposium*, paper SPE 39512, Soc. of Pet. Eng., Richardson, Tex.

Sandnes, B., H. A. Knudsen, K. J. Måløy, and E. G. Flekkøy (2007), Labyrinth Patterns in Confined Granular-Fluid Systems, *Phys. Rev. Lett.*, **99**, 3, pp. 038001.

Sato, Y., Irisawa G., Ishizuka M., Hishida K. and Maeda M. (2003),Visualization of convective mixing in microchannel by fluorescence imaging, *Meas. Sci. Technol.*, **14**, pp. 114–121.

Sayegh, S. G., Fisher, D. B. (2008), Enhanced Oil Recovery by CO₂ Flooding in Homogeneous and Heterogeneous 2D Micro-models, Canadian International Petroleum Conference, doi:10.2118/2008-005.

Sbragaglia, M., R. Benzi, L. Biferale, S. Succi, K. Sugiyama and F. Toschi (2007), Generalized lattice Boltzmann method with multirange pseudopotential, *Phys. Rev. E*, **75**, p. 026702.

Semwogerere, D., and E.R. Weeks (2005),Confocal microscopy, *Encyclopedia of Biomaterials and Biomedical Engineering*, eds. G. Wnek and G. Bowlin (Taylor & Francis, 2005).

Senn, T., J. P. Esquivel, M. Lörger, N. Sabaté and B. Löchel (2010), Replica molding for multilevel micro-/nanosstructure replication, *J. Micromech. Microeng.*, **20** , pp. 115012, doi: 10.1088/0960-1317/20/11/115012.

Sharma, J., Inwood, S. B., and Kovscek, A. R., (2011), Experiments and Analysis of Multiscale Viscous Fingering during Forced Imbibition, Society of Petroleum Engineers, 143946-MS.

Shinohara, K., Sugii Y., Okamoto K., Madarame H., Hibara A., Tokeshi M. and Kitamori T. (2004), Measurement of pH field of chemically reacting flow in microfluidic devices by laser-induced fluorescence, *Meas. Sci. Technol.*, **15**, pp. 955–960.

Shinohara, K., Y. Sugii, A. Aota, A. Hibara, M. Tokeshi, T. Kitamori and K. Okamoto (2004), High-speed micro-PIV measurements of transient flow in microfluidic devices, *Meas. Sci. Technol.*, **15**, 1965, doi: 10.1088/0957-0233/15/10/003.

Shor, Leslie M., Karl J. Rockne, L. Y. Young, Gary L. Taghon, and David S. Kosson (2004), Combined effects of contaminant desorption and toxicity on risk from PAH contaminated sediments, *Risk Analysis: An International Journal*, **24**(5) 1109-1120.

Sirivithayapakorn, S., and Keller, A. (2003), Transport of colloids in saturated porous media: A pore-scale observation of the size exclusion effect and colloid acceleration, *Water Resources Research*, Vol. **39**, No. 4, 1109, doi:10.1029/2002WR001583.

Sohrabi M., Henderson G.D., Tehrani D.H., Danesh A., (2001), Visualization of Oil Recovery by Water Alternating Gas (WAG) Injection Using High Pressure Micro-models - Oil-Wet & Mixed-Wet Systems, SPE 71494, Louisiana, 30 September-3 October .

Sohrabi, M., Tehrani, D., Danesh, A., and Henderson, G. D. (2004), Visualization of oil recovery by Water-Alternating-Gas injection using High-Pressure micro-models, *SPE Journal*, **9**(3), pp. 290-301.

Soll, W.E., Celia, M.A., and Wilson, J.L. (1993), Micro-model studies of three-fluid porous media systems: Pore-scale processes relating to capillary pressure-saturation relationships, *Water Resour. Res.*, **29**, pp. 2963-2974, doi:10.1029/93WR00524.

Soudmand-asli, A., Sh. Ayatollahi, H. Mohabatkar, M. Zareie and S.F. Shariatpanahi (2007), The in situ microbial enhanced oil recovery in fractured porous media, *J. Pet. Sci. Eng.*, **58**, pp. 161–172.

Stewart, T. L., Fogler, H. S. (2001), Biomass plug development and propagation in porous media, *Biotechnology and Bioengineering*, **72**(3), pp. 353-363.

Stewart, T. L., Fogler, H. S. (2002), Pore-scale investigation of biomass plug development and propagation in porous media, *Biotechnology and Bioengineering*, Vol. **77**(5), pp. 577-588, doi: 10.1002/bit.10044.

Stöhr, M., Roth, K., Jähne, B. (2003), Measurement of 3D pore-scale flow in index-matched porous media, *Experiments in Fluids*, **35**, 2, 0723-4864, pp. 159-166, 10.1007/s00348-003-0641-x.

Stoner, D. L., S. M. Watson, R. D. Stedtfeld, P. Meakin, L. K. Griffel, T. L. Tyler, L. M. Pegram, J. M. Barnes, and V. A. Deason (2005), Application of Stereolithographic Custom Models for Studying the Impact of Biofilms and Mineral Precipitation on Fluid Flow, *Appl. Environ. Microbiol.*, **71**, pp. 8721-8728, doi:10.1128/AEM.71.12.8721-8728.2005.

Sugii, Y., and Okamoto K. (2004), Quantitative visualization of micro-tube flow using micro-PIV, *J. Vis.*, **7**, pp. 9-16.

Sugii, Y., Nishio S. and Okamoto K. (2002), In vivo PIV measurement of red blood cell velocity field in microvessels considering mesentery motion, *Physiol. Meas.*, **23**, pp. 403-16.

Tallakstad, K. T., Lovoll, G., Knudsen, H. A., Ramstad, T., Flekkoy, E. G., Maloy, K. J. (2009), Steady-state, simultaneous two-phase flow in porous media: An experimental study, *Phys. Rev. E*, **80**, 3.

Theodoropoulou, M. A.; Sygouni, V.; Karoutsos, V.; Tsakiroglou, C. D. (2005), Relative permeability and capillary pressure functions of porous media as related to the displacement growth pattern, *Int. J. Multiphase Flow*, **31** (10_11), pp. 1155-1180.

Thompson, L. F., C. G. Willson, and M. J. Bowden (1994), Introduction to Microlithography, 2nd ed., *Am. Chem. Soc.*, Washington, D. C., doi: 10.1002/pi.1995.210370312.

Thompson, L.F., C.G. Wilson and M.J. Bowden (1983), Introduction to Microlithography, *ACS Symp. Ser.*, **219**.

Tóth, T., D. Horváth, and Á. Tóth (2007), Density fingering in spatially modulated Hele-Shaw cells, *J. Chem. Phys.* **127**, 234506.

Tretheway, D. C., and Meinhart C. D. (2002), Apparent fluid slip at hydrophobic microchannel walls, *Phys. Fluids*, **14**, L9-12.

Tsakiroglou, C. D., Theodoropoulou, M. A., Karoutsos, V. (2003), Nonequilibrium capillary pressure and relative permeability curves of porous media, *AIChE Journal*, Vol. 49., pp. 2472-2486.

Tsakiroglou, C. D., Theodoropoulou, A., Karoutsos, V., Papanicolaou, D., Sygouni, V., (2003), Experimental study of the immiscible displacement of shear-thinning fluids in pore networks, *J. Colloid Interface Sci.*, 267 (1), pp. 217-232.

Tsakiroglou, C.D., and Avraam, D.G. (2002), Fabrication of a New Class of Porous Media Models for Visualization Studies of Multiphase Flow Process, *J. of Material Sci.*, **37**, 353.

Tsakiroglou, C.D., Avraam, D.G., and Payatakes, A.C. (2007), Transient and steady-state relative permeabilities from two-phase flow experiments in planar pore networks, *Adv. Water Resources*, **30**, pp. 1981-1992.

Upadhyaya, A. (2001), Visualization of Four-Phase Flow Using Micro-models, M.S. report, Stanford Univ., Stanford, Calif. (Available at <http://ekofisk.stanford.edu/pereports/web/default.htm>).

van der Marck, S. C., Glas, J. (1997), Pressure measurements during forced imbibition experiments in micro-models, *European journal of mechanics. B, Fluids*, vol. **16**, 5, pp. 681-692.

van Dijke, M. I. J., Sorbie, K. S., Sohrabi, M., Tehrani, D., and Danesh, A. (2002), Three-phase flow in WAG processes in mixed-wet porous media: pore-scale network simulations and comparison with micro-model experiments, presented at the SPE/DOE Improved Oil Recovery Symposium, Tulsa, Oklahoma, USA, SPE 75192.

Vayenas, D. V., E. Michalopoulou, G. N. Constantinides, S. Pavlou, A. C. Payatakes (2002), Visualization experiments of biodegradation in porous media and calculation of the biodegradation rate, *Advances in Water Resources*, Volume **25**, Issue 2, Pages 203-219, ISSN 0309-1708, DOI: 10.1016/S0309-1708(01)00023-9.

Wan, J., and J. L. Wilson (1994a), Visualization of the role of the gas-water interface on the fate of transport of colloids in porous media, *Water Resour. Res.*, **30**(1), pp. 11-23.

Wan, J., and J. L. Wilson (1994b), Colloid transport in unsaturated porous media, *Water Resour. Res.*, **30**(4), pp. 857-864.

Wan, J., Togunaga, T.K., Tsang, C.F. and Bodvarsson, G.S. (1996), Improved glass micro-model methods for studies of flow and transport in fractured porous media, *Water Resources Research*, **32**, pp. 1964-1995

Wang, Wei, Leslie M. Shor, Eugene J. LeBoeuf, John P. Wikswo, and David S. Kosson (2005), Mobility of protozoa through narrow channels, *Applied and Environmental Microbiology*, **71**(8), pp. 4628-4637.

Wang, J., Dong, M., Asghari, K., (2006), Effect of Oil Viscosity on Heavy-Oil/Water Relative Permeability Curves, "SPE/DOE Symposium on Improved Oil Recovery", Tulsa, Oklahoma, 22-26 April.

Wang, Wei, Leslie M. Shor, Eugene J. LeBoeuf, John P. Wikswo, Gary L. Taghon, and David S. Kosson (2008), Protozoa migration in bent microfluidic channels, *Applied and Environmental Microbiology*, **74**(6), pp. 1945-1949.

Wardlaw, N. C. (1980), The effects of pore structure on displacement efficiency in reservoir rocks and in glass micro-models, SPE/DOE Enhanced Oil Recovery Symposium, 20-23 April 1980, Tulsa, Oklahoma, doi: 10.2118/8843-MS.

Wegner, M.W., Christie, J.M. (1983), Chemical etching of deformation substructures in quartz, *Phys Chem Minerals*, **9**:67–78.

Weidman, T.W., and A.M. Joshi (1993), New photodefinable glass etch masks for entirely dry photolithography: Plasma deposited organosilicon hydride polymers, *Appl. Phys. Lett.*, **62**, pp. 372-374.

Wereley, S.T., and C.D. Meinhart (2005), Micron-Resolution Particle Image Velocimetry, Micro- and Nano-Scale Diagnostic Techniques, ed. Kenny Breuer, Springer-Verlag, New York, (2005).

Willingham, T. W., Werth, C. J., and Valocchi, A. J. (2008), Evaluation of the Effects of Porous Media Structure on Mixing-Controlled Reactions Using Pore-Scale Modeling and Micro-model Experiments, *Environmental Science & Technology*, **42** (9), pp. 3185-3193.

Wyckoff, R. D., and Botset, H. G. (1936), The Flow of Gas-Liquid Mixtures Through Unconsolidated Sands, *J. of App. Physics*, **7**, pp. 325-345, doi:10.1063/1.1745402.

Xia, Y. and Whitesides, G. M. (1998), Soft Lithography. *Angewandte Chemie International Edition*, **37**: 550–575.

Yeom, J., Y. Wu, J. C. Selby, and M. A. Shannona,(2005), Maximum achievable aspect ratio in deep reactive ion etching of silicon due to aspect ratio dependent transport and the microloading effect, *Journal of Vacuum Science & Technology B: Microelectronics and Nanometer Structures*, **23**: 6, pp. 2319 – 2329,1071-1023.doi:10.1116/1.2101678.

Yeom, J., Y. Wu, and M. A. Shannon (2003), Proceedings of Transducers '03-The 12th International Conference on Solid State Sensors, Actuators and Microsystems, IEEE, Boston, MA, p. 1631.

Zang, W. (1998), Application of photo-luminescent volumetric imaging in multiphase dynamics in porous media, Ph.D. thesis, Cornell University.

Zekri, A.Y., El-Mehaideb, R.A. (2002), Microbial and water flooding of fractured carbonate rocks: an experimental approach, Paper SPE 75217 presented at the SPE/DOE improved oil recovery symposium held in Tulsa, Oklahoma.

Zhang, C., Dehoff, K., Hess, N., Oostrom, M., Wietsma, T. W., Valocchi, A. J., Fouke, B. W., and Werth, C. J. (2010), Pore-Scale Study of Transverse Mixing Induced CaCO₃ Precipitation and Permeability Reduction in a Model Subsurface Sedimentary System, *Environ. Sci. Technol.*, **44**, pp. 7833–7838.

Zhang, C., Oostrom, M., Grate, J. W., Wietsma, T.W., and Warner, M.G., (2011), Liquid CO₂ Displacement of Water in a Dual-Permeability Pore Network Micro-model, *Environmental Science & Technology*, **45**(17):7581-7588. doi:10.1021/es201858r.

Zhang, C., Oostrom, M., Wietsma, T. W., Grate, J. G., and Warner, M.G., (2011), Influence of Viscous and Capillary Forces on Immiscible Fluid Displacement: Pore-Scale Experimental Study in a Water-Wet Micro-model Demonstrating Viscous and Capillary Fingering, *Energy and Fuels*, **25**(8):3493-3505. doi:10.1021/ef101732k

Zhou, J., Ellis, A. V., and Voelcker, N. H., (2010), Recent developments in PDMS surface modification for microfluidic devices, *ELECTROPHORESIS*, **31**, 1, 10.1002/elps.200900475.

Chapter 3

Quasi-static, two-phase flow pore network model

3.1 Introduction

The conventional theory of two-phase flow is based on a macro-scale equation derived empirically by Henry Darcy (1856). Darcy's equation for the case of slow flow of two immiscible fluids can be written in the following form:

$$\vec{q}_\alpha = -\frac{k_{r\alpha} \cdot \vec{K}}{\mu_\alpha} \cdot (\vec{\nabla} P_\alpha - \rho_\alpha \vec{g}) \quad (1),$$

where \mathbf{q} is the Darcy velocity vector, $k_{r\alpha}$ is the relative permeability of α -phase, \mathbf{K} is the intrinsic permeability tensor, μ_α is the fluid viscosity of α -phase, P_α is the α -phase pressure, ρ_α is the α -fluid density and \mathbf{g} is the gravitational acceleration vector. In two-phase flow, the pressures of the two fluid phases are different because of the capillary pressure induced by the interfaces. In current theories, this is modeled by introducing capillary pressure, and assuming that it is a function only of saturation (Bear et al., 1968):

$$P_n - P_w = P_c(S_w) \quad (2)$$

where P_c is the capillary pressure, P_n is the pressure of the non-wetting phase, P_w is the pressure of the wetting phase and S_w is the saturation of the wetting phase. Thus, while the traditional theory does take into account the capillary pressure, which is the result of the presence of fluid-fluid interfaces, it does not explicitly include these interfaces as an independent variable. This has resulted in the fact that P_c is not a unique function of S_w but it is hysteretic. Computational and experimental works (Chen and Kibbey, 2006; Cheng et al., 2004; Held and Celia, 2001; Joekar-Niasar et al., 2007; Reeves and Celia, 1996) have shown that in fact P_c is not only a function of S_w but also depends on the specific interfacial area, a_{wn} (area of the fluid-fluid interface per unit volume of porous medium).

A rigorous derivation of governing equations for two-phase flow in porous media, based on principles of mass, momentum and energy conservation and the second law of thermodynamics, has resulted in the following extension of Darcy's law for two-phase flow (Hassanizadeh and Gray, 1993a; Hassanizadeh and Gray, 1993b):

$$\vec{q}_\alpha = -\frac{k_{r\alpha} \cdot \vec{K}}{\mu_\alpha} \cdot (\vec{\nabla} P_\alpha - \rho_\alpha \vec{g} - \lambda_\alpha^1 \nabla S_\alpha - \lambda_\alpha^2 \nabla a^{wn}) \quad (3)$$

where λ_α^1 and λ_α^2 are new material coefficients that are related to the rate of change of free energy of α -phase due to a change in saturation and interfacial area, respectively. Thermodynamic theories have also led to the following generalized equation for capillary pressure (Hassanizadeh and Gray, 1993a):

$$P_n - P_w = P_c(S_w, a^{wn}) \quad (4)$$

which indicates that the capillary pressure is not only a function of saturation, but also of the specific interfacial area, a^{wn} . This is in line with results of computational and experimental results [Chen and Kibbey, 2006; Cheng et al., 2004; Held and Celia, 2001; Pyrak-Nolte et al. 2008; Chen et al., 2006; Niessner and Hassanizadeh, 2008; Joekar et al., 2008]. Introduction of specific interfacial area into the theory for two-phase flow makes it possible to model hysteresis in $P_c - S_w$ relationship and to account for driving forces specific to two-phase flow. Equations (3) and (4) must be supplemented by equations of conservation of mass and interfacial area.

In order to study two-phase flow in a porous medium, an artificial porous medium with known properties had to be manufactured. This artificial porous medium is called a micro-model. Even though there is no definition of a micro-model, one may state that a micro-model must satisfy two major requirements. It should be a representation of a porous medium. Thus, it should allow flow through it and this flow should be in the micro-scale. This means that the dimensions of the features of the flow network, like pore bodies and throats should be on the micro scale. It should also provide the ability to visually observe the flow. Taking these requirements into consideration, we could say that a micro-model is a construct with the following general characteristics. It is made of a transparent material, usually glass, but it could also be polymeric. In this way, visual observation is possible. The flow pattern is a network of pores and throats with their dimensions up to the millimeter scale. This requirement is essential for two-phase flow studies as capillary effects are inversely proportional to the pore size. The overall size of a micro-model is on the centimeter scale. There must be also an inlet and an outlet area for the introduction and removal of the wetting and non-wetting phase. The flow network lies in a channel between the inlet and outlet area. Given the fact that there is no way to visualize optically the effects on the third dimension of the micro-model, it is considered to be a two-dimensional porous medium.

In this work, an elongated, glass-etched micro-model with dimensions $5 \times 35 \text{ mm}^2$ was manufactured and used as a representation of a real porous medium. The fluids

involved were inked water as the wetting phase, and fluorinert as the non-wetting phase. With the use of an innovative setup designed for optical microscopy for elongated samples, the distribution of fluids in the flow network during drainage, and its evolution in time, could be visualized and recorded. The experimental results obtained for drainage under quasi-static conditions were compared to the results obtained from a pore network model. The flow network of the micro-model was designed based on the pore network generated from the pore network model. In this way, the comparison between experiment and model referred to the same geometry and topology for the flow network.

In the pore network model, drainage and imbibition were modeled under quasi-static conditions. A number of realizations were chosen based on the number of pore bodies and pore throats of the flow network. With the use of the computational results for the flow rates versus the externally applied pressure, relative permeability of each phase could be calculated. Graphs between capillary pressure, saturation and interfacial area were constructed for drainage and imbibition. The comparison between these graphs showed that the inclusion of interfacial area as a separate state variable provides with an alternative way and more effective way of modeling the hysteretic behavior of the system.

3.2 Model description

3.2.1 Structure

The elongated pore network topology was generated by using Delaunay triangulation, as it is considered to be a good representation of a real porous medium (Heiba et al., 1992).

The pore network was represented as a collection of pore bodies and throats. In Delaunay triangulation, points are connected to their neighbors by non-intersecting bonds. Connected points form triangles that are as equilateral as possible. The coordinates of the triangulation points were generated in MatLab. These points were considered to be the centers of the pore bodies. The connections between the centers of two neighboring pore bodies were considered as the pore throats of the network.

The pore bodies were considered to be circular (planar view) while pore throats were rectangular. Both pore bodies and throats were considered to have a rectangular cross-section. The co-ordination factor of the network is not fixed, varying from 4 to 6 for the 2000-points network and from 6 to 9 for the 6000-points network.

The planar radius of the pore bodies was assigned by using a random number generator. For the number generator, log-normal distribution has been employed. The mean pore size was selected to be equal to 40 μm , 50 μm and 70 μm , with a variance of 12 μm , 15 μm and 21 μm respectively, independently of the pore bodies' number. The length of the pore throats was defined as the distance between the centers of the neighboring pore bodies minus the summation of their radii. The width of a pore throat was assigned by using the following set of equations (Joekar-Niasar et al., 2010):

$$r_{ij} = \rho_i \rho_j (\rho_i^{1/n} + \rho_j^{1/n})^{-n}, n > 0, \quad \tilde{R}_{i,j} = R_{i,j} / d, \quad \rho_{i,j} = \frac{\tilde{R}_{i,j} \sin(\pi/4)}{(1 - \tilde{R}_{i,j} \cos(\pi/4))^n} \quad (5)$$

where r_{ij} is the dimensionless radius of the pore throat ij and d is the distance between the two centers. In this way, there is an extra tuning parameter for the network, n . Pore throats become broader or thinner when n becomes smaller or bigger respectively. In case the width of the pore throat becomes larger than the diameter of the smallest connected pore, then the width of the throat is automatically assigned to be 90% of the diameter of the smallest connected pore.

Special attention was paid to the fact that the distribution of sizes for pore bodies and pore throats should overlap to an extent. It has been reported in many papers that if there is some overlapping, then imbibition is facilitated. In figure 1 the distribution of sizes between pore bodies and pore throats for log-normal distribution can be seen. The depth of the network was assumed to be constant and equal to the mean pore size. This assumption had to be made for two reasons. The first reason was that if the depth of the model was close to the mean pore size, then it would be safer to assume that the interface in the third dimension, that is not observable, is approximately the same as the one seen in the other two. The second reason is that the smallest dimension in a pore throat determines the entry capillary pressure, as it will be shown later. If the depth is much smaller than the width of a throat, then this will be the dominant dimension with respect to the value of the entry capillary pressure.

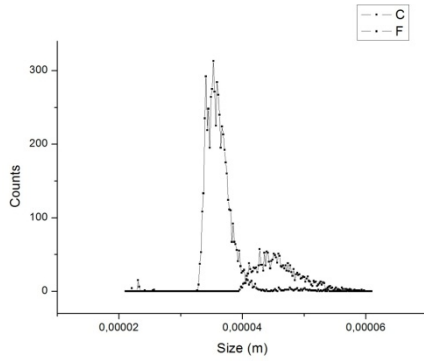
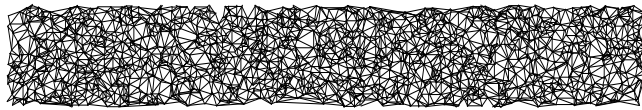
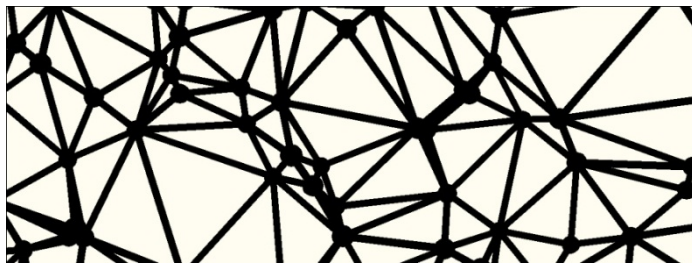


Figure 1. The distribution of sizes for pore bodies and pore throats for log-normal size distribution.

In figure 2, the image of the whole network, as well as a magnified part of it, can be seen.



(1)



(2)

Figure 2. (1) Image of the pore-network with 2000 pore bodies and 6000 pore throats and a mean pore size of 40 μm . The void space is represented in black. (2) Image of a part of the pore-network with 2000 pore bodies and 6000 pore throats. The geometry of the pore bodies and the pore throats can easily be seen.

The porosity of the network has been defined as the summation of the volumes of the pore throats and the pore bodies, divided by the total volume of the domain. The pores at the edges are assumed to be directly connected to the reservoirs, one (reservoir) per phase.

3.2.2 Numerical experiments

Our intention was to simulate under quasi-static conditions drainage and imbibition for two-phase flow. In a few words one can say that drainage is the process where a porous medium that is fully saturated with the wetting phase starts to get filled with the non-wetting phase, with the aid of an externally applied pressure. In this way, the wetting phase is pushed out of the porous medium. Imbibition is the inversed process where the wetting phase invades back into the network spontaneously by lowering the externally applied pressure on the non-wetting phase. In this work, the fluids used were water as the wetting phase and fluorinert as the non-wetting phase. The entry capillary pressure of a pore throat is defined from equation 6 (Joekar-Niasar et al,2009).

$$P_c^{entry} = \sigma^{nw} \left(\frac{-(a+b) \cos \theta + \sqrt{(a+b)^2 \cos^2 \theta + 4ab \left(\frac{\pi}{4} - \theta - \sqrt{2} \cos \theta \left(\frac{\pi}{4} + \theta \right) \cos \theta \right)}}{4 \left(\frac{\pi}{4} - \theta - \sqrt{2} \cos \theta \left(\frac{\pi}{4} + \theta \right) \cos \theta \right)} \right)^{-1} \quad (6)$$

Where σ^{nw} is the interfacial tension between phases, a and b are the width and the depth of the throat respectively and θ is the contact angle between the fluid-fluid interface and the solid surface.

Modified Young-Laplace equation had to be employed in order to calculate the entry capillary pressure, given the rectangular cross-section of the pore throats. It is a straightforward assumption that the entry capillary pressure of the pore bodies is always lower than the one of the pore throats as they always have a bigger cross-sectional area.

In the case of overlapping, the same equation has been employed but the dimensions of the pore throat are assumed to be 1nm in length and its width is given by the following formula based on figure 3.

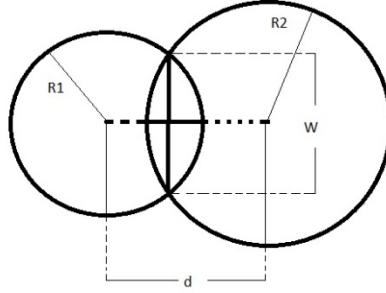


Figure 3. Schematic of two overlapping pore bodies forming a two-dimensional pore throat.

$$W = 2\sqrt{R_1^2 - (R_1 + R_2 - d)^2} \quad (7)$$

The width of the pore throat is taken from equation 3, while the depth of the throat is still the depth of the network.

Some trapping assumptions have been made. For drainage, two different concepts have been employed. One concept is that the wetting phase can be trapped inside the network, if two neighboring pore bodies can be filled with the non-wetting phase, or if a wetting phase cluster gets disconnected from the wetting phase reservoir. The other concept is that the wetting phase cannot be trapped under any circumstances.

For imbibition, again two different concepts for trapping have been employed. The first is that the system can imbibe only through the pores that are directly connected to the wetting phase. If two pores that are connected with a throat can imbibe while the throat does not, the non-wetting phase can be trapped inside this throat. The other case is that if there is corner flow, any pore can imbibe at any time and it is not required that this pore is in direct contact with the wetting phase. Snap off has been taken into account. Our network is a spatially correlated network so it was expected that snap-off mechanism would be significant given the small contact angle.

3.2.3 Drainage-Imbibition

In order to study drainage in two-phase flow, the whole network is assumed to be initially totally filled with the wetting phase. In our case the wetting phase is water. The pressure of the wetting phase reservoir is assumed to be zero at all times. All the pores that are filled with the wetting phase and are connected to the wetting phase reservoir have pressure equal to zero. Drainage was assumed to be over as soon as the non-

wetting phase broke through the network or when the whole wetting phase was pushed out of the system. The later can happen experimentally with the use of a membrane at the end of the network. During imbibition both concepts for the non-wetting phase trapping were employed.

3.2.4 Relative permeability

Relative permeability is assumed to be a function of saturation. During drainage and for given saturation of the wetting phase, relative permeabilities for the two-phases are determined. By repeating the procedure for a sequence of saturations, the curve that describes the relation between saturation and relative permeability can be constructed. This can be done by solving the pressure field in the flow network. By calculating the flow rate with respect to each phase in every pore throat, relative permeability can be calculated. In order to calculate the flow rate in every pore throat, Poiseuille's law had to be employed. For a circular cross section, Poiseuille's law is shown in equation 5.

$$q_{ij} = \frac{\pi}{8\mu} r_{ij}^4 \frac{P_i - P_j}{l_{ij}} \quad (8)$$

Where q_{ij} is the discharge along the pore throat ij , P_i and P_j are the pressures at the i, j pore bodies respectively, and l_{ij} is the throat's length.

Given the fact that in our case the cross sectional area was not circular but rectangular, Poiseuille's laws for the wetting phase can be written as in equation 9 (Patzek and Kristensen, 2001).

$$q_{ij} = \frac{A^2}{\mu} \frac{0.5623}{16} \left[0.3214(16G)^3 + 0.0630(16G)^2 + 0.6109(16G) \right] \frac{P_i - P_j}{l_{ij}} \quad (9)$$

G , that is called shape factor, is defined in equation 10.

$$G = \frac{Area}{Perimeter^2} \quad (10)$$

and is dimensionless.

For the non-wetting phase many approximations for Poiseuille's law have been employed but they do not differ much from the following. From the rectangular cross-sectional area, the equivalent circular one can be assigned to any pore throat. This means that for a cross-sectional area equal to $a \cdot b$, with a and b being the width and the height of a pore throat respectively, the equivalent circular cross-section will have a radius equal to:

$$r = \sqrt{\frac{ab}{\pi}}$$

After this assumption for the non-wetting phase, Poiseuille's law has been used in its original form for a circular cross sectional area with a radius as mentioned earlier. The volume balance for each pore body demands that

$$\sum_{j=1}^{N_i} q_{ij} = 0 \quad (11)$$

Relative permeability can be obtained by solving the linear system of equations for every pore. This system of equations has the form $A \cdot B = X$. B is known as it carries the pressure of every pore body that is connected to the reservoirs for both phases. A is also known as its elements can be calculated through the conductance of the pore bodies that are inter-connected and are filled with the phase studied. In this way total flow rate and intrinsic permeability can be calculated. The non-wetting phase is free to move as soon as there is connectivity of the phase in the network something that does not happen until breakthrough. After breakthrough, there is no reason for saturation to change as there is a flow path formed and preferred. For this reason, it has been assumed that as soon as the non-wetting phase breaks through the first REV, then calculations for this REV start. Since for the whole domain there is no breakthrough yet, saturation in this REV can change. This is in a way equivalent to the assumption that the whole domain is a part of a bigger conceptual domain. In this way, even after breakthrough our domain is considered to be an REV in a bigger domain.

3.2.5 REV determination

One of the things of great importance that had to be determined was the smallest size of the network that the network becomes insensitive to its size. This volume of the network that has this property is called Representative Elementary Volume. The REV size of the network has been determined based on changes in the (P_c, S) curve and the

relative permeability of the network for each phase. The determination of REV is of great importance as the purpose of the relevant to this work experiment is based on the statistical results from the whole domain divided in REV. For the 2000-pores network we have 11.42 pore bodies per square millimeter on average. Tests have been run for networks of approximately 100, 150, 200, 250, 350 and 400 pore bodies with sizes 5x2, 5x3, 5x4, 5x5, 5x7 and 5x7 square millimeters respectively and the same boundary conditions were imposed as the ones imposed to the whole domain. The graphs acquired from the simulations for various numbers of pore bodies and various sizes for the domain were compared to the graph taken from the whole network. For the networks with approximately 400 pore bodies and the whole domain, relative permeability curves for the wetting phase have been obtained in order to be compared. These curves are presented in Figure 4.

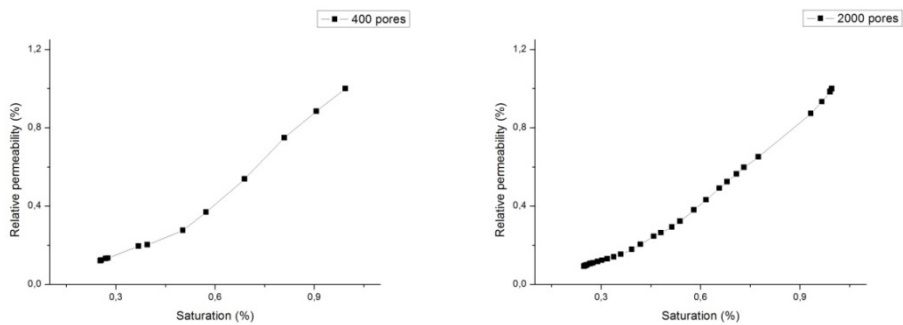


Figure 4. Relative permeability vs saturation curves for 400 pore bodies (left) and the whole network (right).

Based on the results for (P_c, S) curves and relative permeability versus saturation curves for various numbers of pore bodies and various domain sizes, it was safe to assume that the size of an REV covers an area of 5x7 square millimeters, for the 2000-pore bodies network. This means that in the whole domain of 5x35 square millimeters we have five REV. Similar results were obtained for all the networks.

3.3 Numerical results

3.3.1 Pc-S curves

In figure 5, Pc-S curves during drainage and imbibition for a 2000-pore network can be seen. This network had approximately 6000 pore throats and a mean pore size equal to 40 μm . On the left side of figure 5, Pc-S curves are obtained assuming that there is no corner flow and no residual saturation for the wetting phase so that the system is eventually totally drained. In addition to this, the only pores that can imbibe are the ones that are directly connected to the wetting phase reservoir. On the right side of figure 5 is the same network again assuming corner flow for the wetting phase but this time calculations stop as soon as the non-wetting phase breaks through the flow network. Snap-off was assumed for imbibition and that is the reason that the wetting phase saturation did not become equal to unity again. Because of snap-off, big clusters of isolated non-wetting phase were formed in the network, putting a limit in the saturation of the wetting phase.

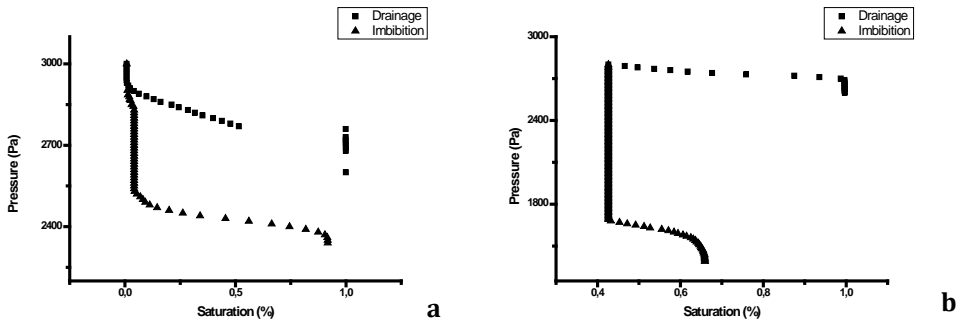


Figure 5. Pc-S curve for a 2000-pores network. a) it is assumed that a membrane is present at the output of the network. b) calculations stop right after breakthrough.

The situation that the image on the left hand describes can be obtained experimentally by applying a membrane at the end of the network. This membrane should have pores that are smaller than the smallest pore in the flow network.

3.3.2 $a^{wn} - S$ curves

Specific interfacial area has been calculated during drainage and imbibition. It has been calculated for both cases, with or without corner flow, for the wetting phase.

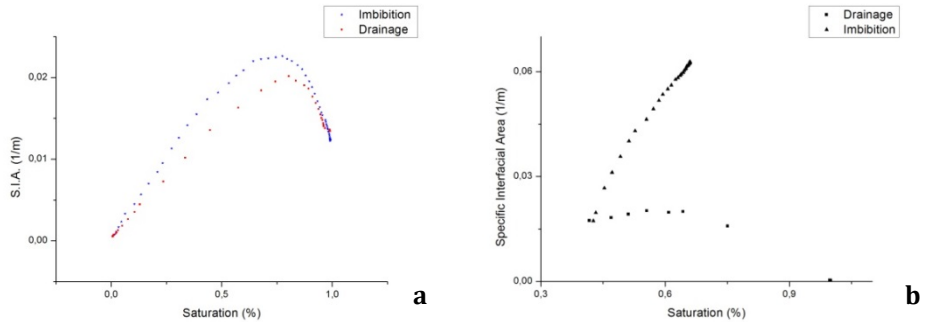


Figure 6. a) Specific Interfacial Area versus Saturation curve for drainage and imbibition. b) It is assumed that there is corner flow for the wetting phase.

In figure 6, specific interfacial area versus saturation curve can be seen. In this case it has been assumed that drainage stops at breakthrough and snap-off takes place. This means that any pore in the network that is directly connected to the wetting phase reservoir can imbibe at any time. For drainage, specific interfacial area presents a maximum value at wetting phase saturation close to 60%. During imbibition snap-off takes place. Interfacial area increases as some isolated or connected pores gradually get isolated from the non-wetting phase and they form new interfaces with the surrounding wetting phase. Specific interfacial area reaches to a plateau at saturation close to 64%. This happens because some clusters full of non-wetting phase are formed and they are cut-off from the non-wetting phase reservoir. These clusters are isolated thus saturation cannot get lower and specific interfacial area remains the same at all times.

3.3.3 Relative permeability

Relative permeability for each phase has been calculated for different saturations of the wetting phase during drainage. In figure 10 the graphs for relative permeability of both phases during drainage are presented.

As it can be seen in the graph, wetting phase relative permeability starts from a value equal to one and as the wetting phase saturation decreases, relative permeability also decreases. It does not become zero though as there is some residual saturation providing some mobility to the wetting phase. On the other hand, the non-wetting phase is not moving until it breaks through the first REV. This happens at a saturation of close to 77% for the wetting phase. As saturation decreases, relative permeability

increases. This happens because the mobility of the non-wetting phase increases. The intrinsic permeability of the network with 6000 pore bodies has been found to be equal to $K_{in}=1,04.10^{-10} \text{ m}^2$.

In figure 7, relative permeability for both phases versus saturation during drainage can be seen.

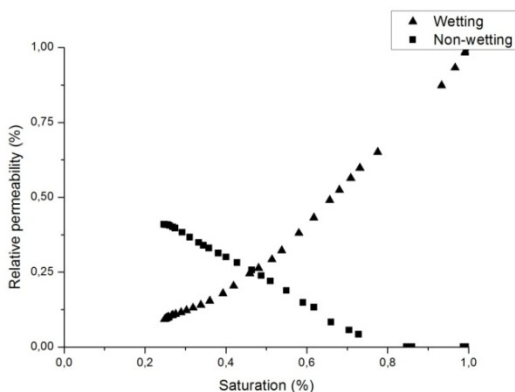


Figure 7. Relative permeability of both phases with respect to saturation.

3.3.4 P_c - S^w - a^{wn} surfaces

Using the data points that have been acquired from the simulation runs for drainage and imbibition we were able to plot the surfaces relating capillary pressure, saturation and interfacial area. The data presented were acquired from the 2000-pores network.

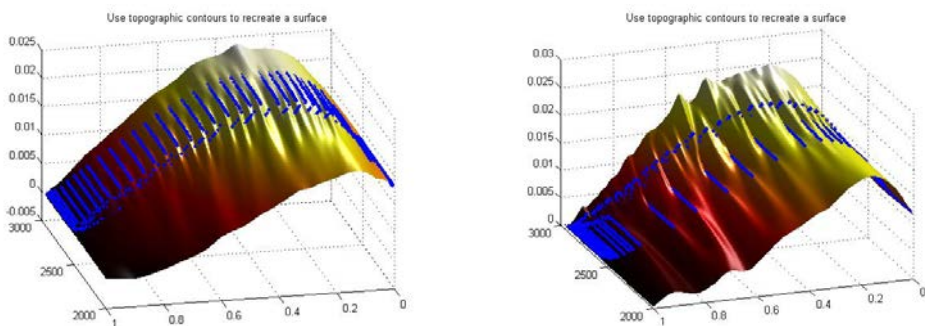


Figure 8. P_c - S^w - a^{wn} surfaces for imbibition (left) and drainage (right).

In figure 8, the surfaces for imbibition and drainage are presented, after performing second order fitting to the obtained data. In order to be able to compare the two surfaces acquired, it was important that fitting would take place by using only the data acquired. First, the average value between the surfaces had to be determined. Then, the relative difference between each surface and the average has been calculated. In this way the absolute relative difference between the two surfaces was found to be close to 10%. As it can be seen in Figure 1, the size distribution between pore bodies and pore throats overlap to some extent but not extensively. In the case when the size distribution employed is beta and the overlapping between the size distribution is more extensive (not presented here), then the difference between drainage and imbibition is 1%. As it has been shown in the work of Al-Raoush and Willson (2005a, 2005b), when there is large overlap between the distribution of sizes for pores and throats, it is very hard to distinguish between them in a real porous medium. Thus, the difference between drainage and imbibition surfaces should be less.

3.4 References

Al-Raoush, R. I., Willson, C. S. (2005a), Extraction of physically realistic pore network properties from three-dimensional synchrotron X-ray microtomography images of unconsolidated porous media systems, *Journal of Hydrology*, Vol. 300, Issues 1-4, pp. 44-64, ISSN 0022-1694, DOI: 10.1016/j.jhydrol.2004.05.005.

Al-Raoush, R. I., Willson, C. S. (2005b), A pore-scale investigation of a multiphase porous media system, *Journal of Contaminant Hydrology*, Vol. 77, Issues 1-2, pp. 67-89, ISSN 0169-7722, DOI: 10.1016/j.jconhyd.2004.12.001.

Bear, J., Zaslavsky, D., and Imray, S. (1968), Physical principles of water percolation and seepage : and (Ed.): Arid zone research XXIX, Unesco, 1968, Paris, 465 p, *Journal of Hydrology*, Volume 12, Issue 1, December 1970, Page 63, ISSN 0022-1694, DOI: 10.1016/0022-1694(70)90033-8.

Chen, D., L. Pyrak-Nolte, J. Griffin, and N. Giordano (2006), Measurement of interfacial area per volume for drainage and imbibition, *Water Resour. Res.*, 43, W12504, doi:10.1029/2007WR006021.

Chen, L., and Kibbey, T. C. G. (2006), Measurement of Air-Water Interfacial Area for Multiple Hysteretic Drainage Curves in an Unsaturated Fine Sand, *Langmuir*, 22 (16), pp. 6874-6880, doi: 10.1021/la053521e.

Cheng, J.-T., L. J. Pyrak-Nolte, D. D. Nolte, and N. J. Giordano (2004), Linking pressure and saturation through interfacial areas in porous media, *Geophys. Res. Lett.*, 31, L08502, doi:10.1029/2003GL019282.

Hassanizadeh, S.M., and Gray, W.G. (1993a), Thermodynamic basis of capillary pressure in porous media, *Water Resour. Res.*, 29, pp. 3389-3405.

Hassanizadeh, S.M., and Gray, W.G. (1993b), Toward an improved description of the physics of two-phase flow, *Adv. Water Resour.*, 16, pp. 53-67.

Heiba, A., Sahimi, M., Scriven, L., and Davis, H. (1992), Percolation theory of two-phase relative permeability, *SPE Reserv. Eng.*, 7, pp. 123-132.

Held, R. J., and Celia, M. A. (2001), Modeling support of functional relationship between capillary pressure, saturation, interfacial area and common lines, *Advances in Water Resources*, 24, pp. 325-343.

Joekar-Niasar, V., Hassanizadeh, S. M., Dahle, H. K. (2010), Non-equilibrium effects in capillarity and interfacial area in two-phase flow: Dynamic pore-network modeling", *Journal of Fluid Mechanics*, doi:10.1017/S0022112010000704.

Joekar-Niasar, V., Hassanizadeh, S. M., Pyrak-Nolte, L., Berentsen, C. (2009), Simulating drainage and imbibition experiments in a high porosity micro-model using an unstructured pore network model, *Water Resources Research*, vol. 45, pp. W02430, doi:10.1029/2007WR006641.

Joekar-Niasar, V., S. M. Hassanizadeh, and A. Leijnse (2008), Insights into the relationships among capillary pressure, saturation, interfacial area and relative permeability using pore-scale network modeling, *Transp. Porous Media*, doi:10.1007/S11242-007-9191-7.

Niessner, J., and S. M. Hassanizadeh (2008), A model for two-phase flow in porous media including fluid-fluid interfacial area, *Water Resour. Res.*, 44, W08439, doi:10.1029/2007WR006721.

Patzek, T. W., and Kristensen, J. G. (2001), Shape Factor Correlations of Hydraulic Conductance in Noncircular Capillaries: II. Two-Phase Creeping Flow, *Journal of Colloid and Interface Science*, Vol. 236, Issue 2, pp. 305-317, ISSN 0021-9797, doi: 10.1006/jcis.2000.7414.

Pyrak-Nolte, L. J., D. D. Nolte, D. Chen, and N. J. Giordano (2008), Relating capillary pressure to interfacial areas, *Water Resour. Res.*, 44, W06408, doi:10.1029/2007WR006434.

Reeves, P.C., Celia, M.A., (1996), A functional relationship between capillary pressure, saturation, and interfacial area as revealed by a pore-scale network model, *Water Resour. Res.*, 32, pp. 2345-2358.

Chapter 4

Part 1: Reservoir-on-a-Chip (ROC): A new paradigm in reservoir engineering

Abstract

In this study, we design a microfluidic chip, which represents the pore structure of a naturally occurring oil-bearing reservoir rock. The pore-network has been etched in a silicon substrate and bonded with a glass covering layer to make a complete microfluidic chip, which is termed as 'Reservoir-on-a-chip' (ROC). Here we report, for the first time, the ability to perform traditional water-flooding experiments in a ROC. Oil is kept as the resident phase in the ROC, and water-flooding is performed to displace the oil phase from the network. The flow visualization provides specific information about the presence of the trapped oil phase and the movement of the oil/water interface/meniscus in the network. The recovery curve is extracted based on the measured volume of oil at the outlet of the ROC. We also provide the first indication that this oil-recovery trend realized at chip-level can be correlated to the flooding experiments related to actual reservoir cores. Hence, we have successfully demonstrated that the conceptualized 'Reservoir-on-a-Chip' has the features of a realistic pore-network and in principle is able to perform the necessary flooding experiments that are routinely done in reservoir engineering.

4.1.1 Introduction

A typical oil field (or reservoir) extends a few hundred meters below the earth's surface and is porous in nature, containing oil and water phases in an interconnected three-dimensional (3D) network of pores. When extracting oil by normal pressurization is no longer possible from these reservoirs, secondary and tertiary extraction methods involving injection of a second phase are generally followed. Water-flooding is one such principal method (secondary extraction), where water is the injected fluid phase in order to displace the resident oil phase in the reservoir rock.¹ Traditional lab-scale

flooding experiments use a core from a sample reservoir-rock for experimentation and collection of recovery data,² known as core-flooding experiments. However, the fluid transport processes in a reservoir occur at a pore-scale, the smallest structural feature in such reservoirs (in order of nanometer to millimeter). In order to develop efficient recovery methods, one needs to understand the underlying physical processes that occur at the pore-scale.

A large body of literature exists regarding the investigation of multi-phase fluid flow in pore-scale. The extensively employed technique in such investigations is pore network modeling (network simulators)³⁻⁵. Pore network models need a complete description of geometrical and topological information of pore space and a complete understanding of physical processes occurring at pore-scale^{3,4}. The geometrical and topological information of pore space of rock is represented with a network of pores (large void spaces) connected to throats (small constrictions)^{3,4,6}. This type of representation of porous media with a network of pores was first developed by Fatt in the 1950's⁷. Heiba et al.⁸ used percolation theory to explain the multi-phase transport properties. Lenormand et al.^{9,10} studied the pore scale displacement mechanisms for both drainage and imbibition directly using etched ordered networks in glass. These etched networks are known as micro-models. The results obtained in experiments are correlated and included in the pore-network models to compute multiphase transport properties.³ However, these estimated properties are limited to a simplified network of pores and do not represent the actual pore space⁴. With the improvement of high-resolution digital imaging and computerized image analysis, researchers have been able to quantify rock microstructure^{5,6,11,12}. It is now possible to reconstruct the 3D pore space using micro-computed tomography (micro- CT),^{5,6,11-14} focused ion beam-scanning electron microscope (FIB-SEM),¹³ nuclear magnetic resonance (NMR) imaging^{15,16} or ultrasonic scanning¹⁷. Multiphase flow properties are calculated with direct numerical simulations on 3D reconstructed pore space using the finite element method (FEM),^{18,19} finite volume method (FVM),^{20,21} finite difference method (FDM)²² or lattice Boltzmann method (LBM)²³⁻²⁷. However, these types of simulations are computationally expensive, limited to small sample sizes and not possible to scale-up to actual field scale^{3,4}. Hence, physically realistic pore-network structures representing the actual pore space is extracted to simplify the simulations and improve the conventional pore network models^{12,28,29}. This physically realistic representation provides a direct mapping of pore bodies and throats. Various multiphase transport properties are computed using these physically realistic network models. It is possible to scale up the sample sizes using stochastic random network generators to estimate the multiphase properties^{30,31}.

However, in numerical modeling, the properties are predicted with arbitrary wetting characteristics³⁻⁵. Experimental investigations at pore-scale are required to validate or improve the numerical studies. Direct visualization of the multiphase transport process is difficult because of the non-transparent nature of the porous media³². Oren and Pinczewski³³ have performed three-phase flow experiments in oil-wet micro-models and Van Dijke et al.^{34,35} have extended such experiments for water-alternating gas injection in oil-wet glass micro-models. Sohrabi et al.³⁶ have also studied water alternating gas injection using high pressure micro-models in both oil-wet and mixed-wet systems. Polymer flooding in glass micro-models^{37,38} has been studied as well, and Meybodi et al.,³⁹ Jamaloei and Kharrat⁴⁰⁻⁴² have performed detailed investigations of displacement behaviors in this context. Perrin et al.⁴³ have even investigated the quantitative information of the velocity field inside such pore network micro-models using micro-PIV (particle image velocimetry). The studies mentioned here do not use actual realistic pore spaces of rock samples and are limited to two-dimensional (2D) representations. However, Bowden et al.^{44,45} and others^{33,34} have represented the porous medium in the form of packed beds to study the multiphase flows. They even demonstrated flooding experiments to determine recovery efficiency in such packed beads⁴⁴. Recently, Sen et al.⁴⁶ computed the velocity components in a packed bed mimicking porous media using micro-PIV. These experiments are limited to engineered porous media which often include random or orderly packed granular systems without having a realistic representation of pore connectivity. In a more recent effort, Berejnov et al.⁴⁷ has represented the porous medium as a structured microfluidic network with prescribed geometries. In their experiments, they have performed investigations of fluid flow parameters and wettability in such networks, by tuning surface properties. Aktas et al.⁴⁸ and Buchgraber et al.^{49,50} have conducted displacement experiments in etched glass micro-models represented by a repeated pattern of a SEM image of sandstone. A single SEM image of sandstone still lacks the connectivity of actual pore space.

In this study, we demonstrate a novel method for the design and fabrication of a porous medium, where a pore network representation of the porous medium has been replicated in a microfluidic chip. Conceptually, the entire porous reservoir pertaining to oil/gas recovery has been miniaturized, without losing the pore-scale characteristic of its complex features. To the best of the authors' knowledge, for the first time water-flooding experiments are attempted on such a microfluidic chip to obtain the desired oil recovery curves. Hence, we coin a new term 'Reservoir-on-a-Chip' (ROC) to refer to this unique microfluidic chip, which is believed to be the first of its kind. It is to be kept in

mind that the word “reservoir” traditionally refers to the inlet and outlet fluid storage spaces in a typical LOC. Here the intent is to extend the traditional concept of LOC to reservoir engineering and hence the term “reservoir” refers to the natural occurring porous media (geological formation) in which oil/ water/gas phases co-exist.

4.1.2 Reservoir-on-a-chip: ROC

4.1.2.1 Introduction

Here, we describe the conceptual map for fabricating a Reservoir- on-a-Chip. The advent of modern imaging techniques has made it possible to describe the pore architecture of the porous medium directly⁵¹⁻⁵⁴. Bera et al.¹³ have demonstrated the characterization of reservoir-rock cores using methods such as microcomputed tomography (micro-CT) and focused ion beam-scanning electron microscopy (FIB-SEM). They quantified the pore space in terms of porosity, pore connectivity between pores of various shape and size, as well as pore-volume distribution. These well-defined methods are followed for investigating the pore space in a sandstone/carbonate dolomitic core¹³, some of the principal oil-bearing rock specimens. FIB-SEM can be used to characterize the internal micro-structure, and then the obtained pore-structure data can be reconstructed by using image analysis software (for e.g., Avizo, Tomography, Fiji, Simpleware Scan IP etc.). The obtained 3D reconstructed pore space is a result of extensive image-processing steps, which capture the most realistic representation of a reservoir. Using maximal ball algorithm,^{28,29} medial axis algorithm¹² or triangulation,⁵⁵ this pore-space is converted to a network containing pores and throats. Proper care has been taken to extract the information without losing any microstructural details. Such network representation of the porous reservoir is more realistic than adhoc attribution of pores and throats to a pore network model or representing the porous medium as packed bed of spheres or sand grains^{33,34}. The microstructural information is extracted from the 3D reconstructed images by direct mapping of pores and throats. The extracted microstructural information is used to represent the 2D pore-network using stochastic random network generators^{30,31} or Delaunay triangulation⁵⁶. In this way, percolation of phases was ensured. This stochastic method can also be used to produce bigger sample sizes with realistic pore space information. Then taking this network image, one can etch the features in silicon or glass using photolithography processes. Appropriate microfluidic connections can be made on the microfabricated chip for subsequent experiments related to water flooding. Thus, keeping intact the essence of a real reservoir-rock, the pore-network is fabricated on a silicon substrate based on the

state-of-art microfabrication techniques. A covering glass layer with inlet-outlet ports is bonded with the network layer, making it a complete microfluidic device. We call this novel chip ‘Reservoir-on-a-chip’ (ROC). Fig. 1 illustrates the conceptual mechanisms of converting a reservoir-rock specimen to an ROC, which facilitates the investigation of the pore-scale transport pertaining to oil recovery processes in reservoir engineering.

4.1.3 Experimental section

4.1.3.1 Pore network design

A key step in the microfabrication process is to fabricate a mask which has the appropriate features replicating a porous medium.

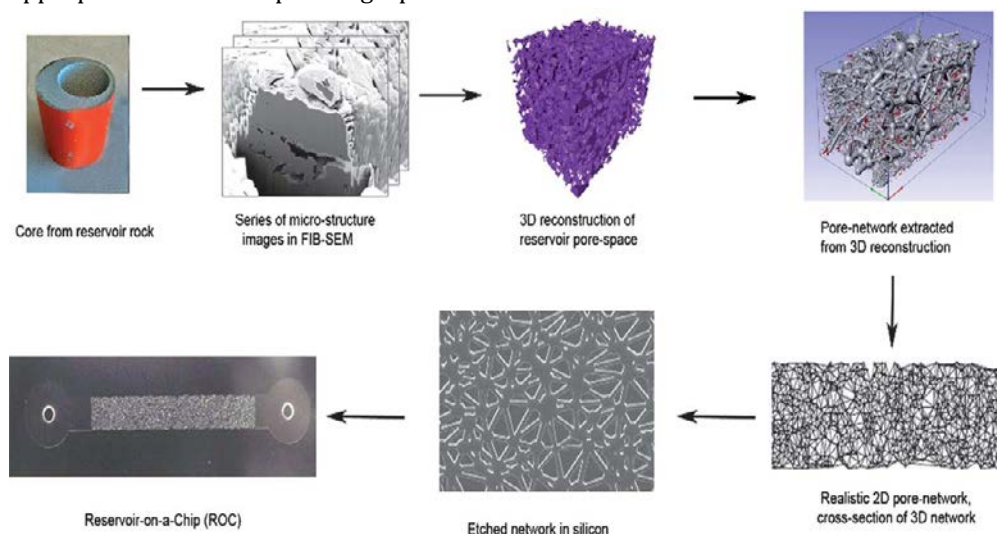


Figure 1. The conceptual flow-map for “Reservoir on a Chip”.

To this effort, a 2D pore-throat network has to be designed based on the realistic reconstructed pore space of reservoir-cores, as explained in the previous section. Details of the network design are described by Karadimitriou et al.⁵⁶. It is observed that Delaunay triangulation is a suitable way to represent a typical porous medium in terms of the number of pores, throats and their connectivity⁵⁵. In the present study, the 2D network was designed with 2000 pores and 6000 throats using Delaunay triangulation. In this type of triangulation, the length of a throat is defined as the difference between the distance separating the pore-centers and the summation of the individual pore radius. The width of a throat is assigned such that it is always less than (not more than

90%) the smallest pore it is connected to. The mean pore size of the network is 40 μm and a log-normal distribution is adopted for pores and throats. The smallest pore in the present network is 25 μm . A Delaunay triangulation routine in Matlab (Mathworks Inc., Natick, MA, USA) is used for generating the network. Based on the triangulation steps, the co-ordinates of the pore centers are chosen, and the network is created. The output from the Matlab routine, in the form of a pore-throat network, was then imported into AutoCAD (Version 2010, Autodesk Inc., San Rafael, CA), using LISP (list processing language). Furthermore, the AutoCAD file containing the imprint of the network is modified to accommodate the inlet and outlet ports and suitable entrance and exit regions located at either side of the original pore network.

As shown in Fig. 2(a), the final design of the pore network, which is transferred to a glass substrate (acting as a mask in the microfabrication step), consists of the pore-throat structure (35 μm in length and 5 μm in width), rectangular entrance and exit regions (5 μm length and 5 μm width) and circular inlet-outlet regions (10 μm diameter). Fig. 2(b) illustrates the nature of the distribution of pores and throats in the network.

4.1.3.2 Fabrication and characterization of ROC

In this section, we provide some key steps involved in fabricating the ROC on a silicon substrate. The microfluidic chip is fabricated on a 4" diameter circular silicon substrate (0.5 mm thick, Silicon Valley Microelectronics Inc., Santa Clara, CA). After cleaning the substrates in a standard piranha solution (H_2SO_4 and H_2O_2 in 3 : 1 ratio; 30 min) and drying, a standard photolithography technique is used for transferring the designed pore network from the patterned mask to the substrate. We used a positive photo mask on a glass wafer (125 mm by 125 mm square plate and 2 mm thick) with a chrome coating. The detailed patterned structure of the mask is shown in Fig. 2(a). A 2.5 mm thick layer of UV sensitive photo-resist HPR 506 (Fujifilm Electronic Materials Inc., Mesa, Arizona) on the silicon substrate is used during this process. Inductively coupled plasma reactive ion etching (ICPRIE) is used for dry-etching the substrate with the desired pattern on silicon (STS, Newport, UK). An etch-rate of 4.95 $\mu\text{m min}^{-1}$ is selected in this step. The covering layer with inlet-outlet ports is fabricated on glass (Borofloat, 100 mm by 100 mm square, 1 mm thick). Abrasive water-jetting (2652 JetMachining Center, OMAX, Kent, WA) is used for drilling these holes on a covering glass layer, and bonded with the silicon layer using SUSS bonder (CB6L, SUSS Microtec, Garching). The average depth, roughness and pore-throat sizes of the fabricated ROC is measured

using scanning electron microscopy (ZEISS, Germany) along with a surface profilometer (Ambios XP 300, Ambios Technology Inc, Santa Cruz, CA). The average depth of the etched silicon network is 40.93 μm . The roughness of the ROC is in the order of 4–6 nm, which is negligible, compared to the depth of the fabricated channel. SEM characterization shows that almost vertical wall-profile (Fig. 2(c)) in the ROC has been achieved, which ensures the proper replication of the pore network in the fabricated ROC. Fig. 2(e) shows the complete ROC (containing 2000 pores and 6000 throats), in which subsequent experiments are performed. The fabricated ROC is water-wet due to the following reasons: (1) Piranha cleaning of silicon and glass layers before bonding, results in the formation of a very thin layer of oxide film on the surface of the silicon. This can contribute to a minor modification of the silicon surface wettability towards water wet⁵⁷. During anodic bonding of silicon to glass, silicon is oxidized at 315 °C, which forms a solid film of silicon dioxide. This caused the ROC to exhibit a permanent water-wet behavior.

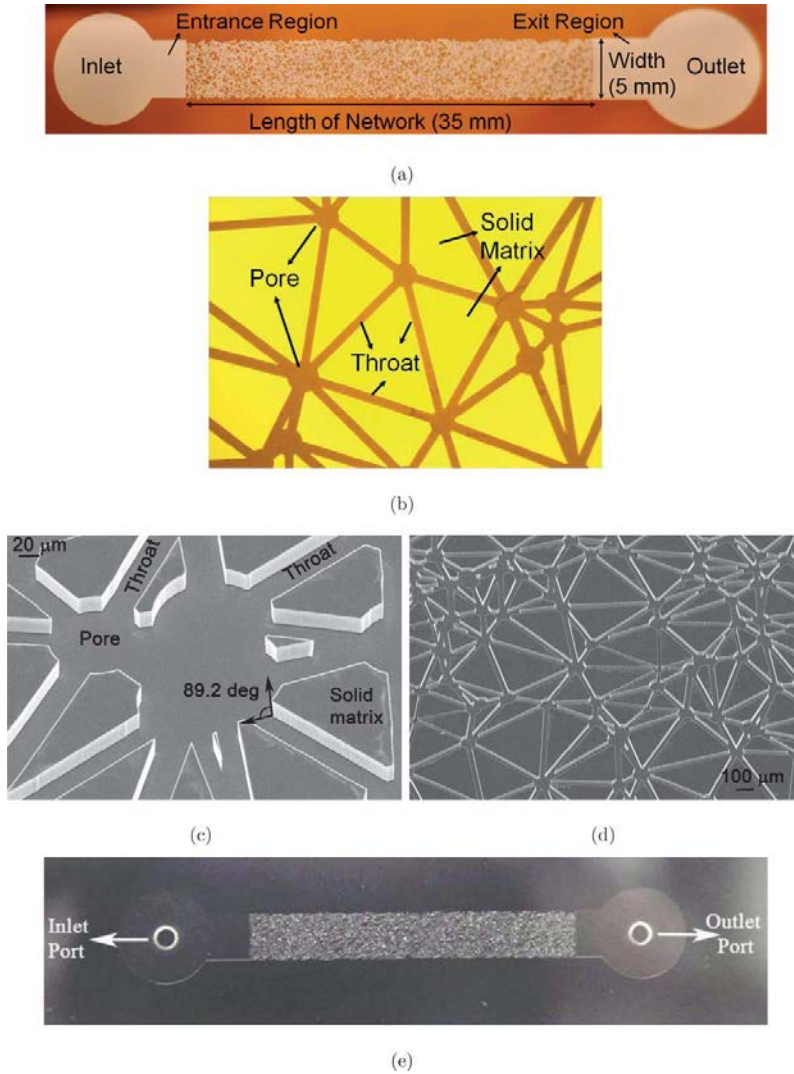


Fig. 2 Reservoir-on-a-Chip (ROC) (a) pore network patterned on glass mask, along with inlet-outlet and entrance-exit regions; (b) the pore and throat distribution of the network in the mask; (c) near-vertical wall-profile obtained in the network, fabricated on silicon; (d) pore-throat distribution of network in etched silicon; (e) complete ROC obtained in etched silicon after covering with glass layer.

4.1.3.3. Water-flooding experiments

A complete realization of the 'Reservoir-on-a-Chip' can be achieved once the fabricated ROC is used to perform recovery experiments, analogous to those done in traditional core-flooding and reported micro-model experiments. In this section, we describe the

water-flooding experiments with a ROC, and discuss the subsequent recovery data. The experimental set-up for water-flooding with ROC (Fig. 3) includes a microscope (180_ magnification, 1.3 Mpixel CMOS image sensor, ViewSolutions GE-5, Howard Electronic Instruments Inc., El Dorado, KS) for the visualization of oil/water phases in the 'Reservoir-on-a-Chip'. The ROC is placed inside a custom-made casing, with microfluidic connectors attached, for controlling fluid flow and efficient visualization. We illuminated the ROC using a light source from the top to capture high-resolution videos and images of fluid transport within the network. M1 lubricant oil (L.S. Starrett Company, Athol, MA; specific gravity 0.788 at 15.5 °C, viscosity _2.2 cSt) has been used as the oil phase to be displaced by water. This lubricant oil is representative of light oils, which can be obtained from crude oils after refining. Hadia et al.² used paraffin oils (light and heavy) for their study of core flooding experiments. The oil used in the present work has similar properties to that of the light paraffin oils used by Hadia et al.² This clean M1 lubricant oil is employed in the present work to demonstrate water-flooding.

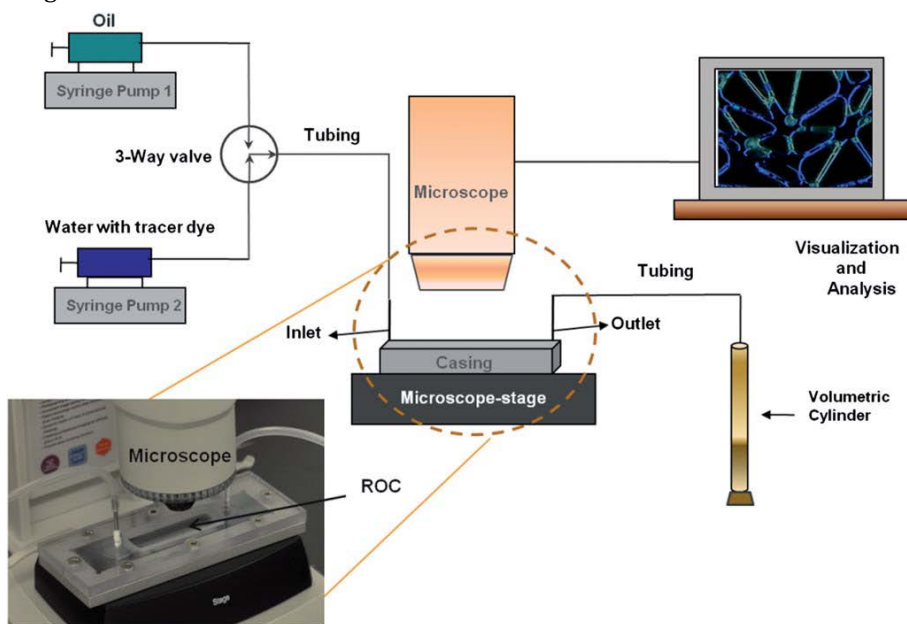


Fig. 3 Schematic of the experimental set-up used in performing water-flooding experiments with ROC; inset illustrates the magnified image of ROC housed in a casing, placed under the microscope for flow visualization experiments.

For properly distinguishing the oil/water interface during the fluid transport, a blue tracer dye (Bright Dyes, Promag Enviro systems Inc., Burnaby, BC) is mixed with deionized water. Two syringe pumps (Harvard Apparatus, MA) have been used for

controlling oil/water flow rates in this experiment. A 3-way valve is used to connect the syringe pumps to the inlet port of ROC, for selective injection of oil/water phases. For collecting the volume of displaced oil, a precision volumetric glass cylinder (Corning Inc., NY) is connected to the outlet of ROC for measuring the displaced oil from the ROC during water-flooding. Using the syringe pump, oil is introduced in the ROC at a constant injection rate of 50 ml min^{-1} and continued until the chip is completely filled with oil. Various 'dead volumes' in relation to the microfluidic connections and tubing are calculated.

Dead volume was calculated by summing up the volumes in the inlet and outlet tubes, inlet and outlet ports, entrance and exit reasons and 3-way valve. Proper care has been taken while measuring the dead volume. Errors are estimated based on the least count of the instruments used for measurements. From the error analysis, it is found that the major source of error is from the precision volumetric glass cylinder. The total dead volume for the chip is calculated to be $816 \text{ ml} \pm 54 \text{ ml}$. The total quantity of resident oil in the ROC is calculated by subtracting the dead volumes from the total injected oil volume. In the next step, DI water containing the tracer dye is injected at a rate of 100 ml min^{-1} into the ROC. In this process, water displaces the resident oil from the ROC. The volume of displaced oil is measured in the collecting cylinder and compared to the original volume of resident oil present in the ROC. The choice of the flow rate is based on the current experimental constraints. In actual reservoir water-flooding case, a typical injection rate of 60 ml h^{-1} translates to an average pore velocity of 1 ft per day in typical oil fields. Such a high flow rate (1000 ml min^{-1}) can cause leakage and the flow transients will be too fast to be captured with the current optical set-up.

4.1.4 Results and discussion

The displacement of non-wetting fluid (oil) by wetting fluid (water) is investigated in the fabricated ROC. Wetting fluid (water) fills pores or throats with the highest threshold capillary pressure. The images of the water-flooding experiment have been taken at various places in the network and at different magnifications, in order to understand the average trend of fluid transport at these locations. Fig. 4 shows a series of images at one such specific network location taken before and during water-flooding. Fig. 4(a) shows the network completely filled with the oil phase (denoted by the green color). Once water-flooding is initiated, oil slowly gets displaced due to the injection pressure and the water phase enters the network. Fig. 4(b) is the image at the same location of the network at a later instance of time (5 min from the start of water-flooding), with the oil/water interfaces visible due to the optical contrast between the

oil and blue tracer dye. The green color in the image represents the oil phase, while the blue color represents water. Oil seems to be present in some pore-throats although the invading water phase had already passed these locations. Hence, water is not able to displace oil from each pore and throat uniformly, which mimics the natural water-flooding process one observes in the reservoir scale. The oil/water interfaces at the same network location but at a later instance of time (13 min from the start of water-flooding) is shown in Fig. 4(c). In this image, we notice the presence of similar characteristics of the oil/water phases as in the previous figure. The detailed displacement process captured in a video shows that the velocity of oil displacement from throats has reduced with time. There are certain throats under observation, where the movement of the fluids is no longer occurring and stagnant phases of oil/water are noticed. Interested readers can refer to the video.† The stagnant phases imply that those pockets of resident oil phases will not be displaced by water flooding alone and they require other tertiary or enhanced recovery schemes, as observed in a practical oil reservoir. The first drop of water at the ROC outlet is observed at the time instance, which corresponds to Fig. 4(c). This process is often referred to as 'breakthrough' in reservoir engineering. From that time onward, both water and oil phases are found at the outlet of ROC. Fig. 4(d) represents the oil/water phases present at another location in the network during the experiment, at a time instance of 10 min from the start of water-flooding. Similar characteristics of displacement as those of the previous location can be observed, such as, stagnant phases in throats, etc.

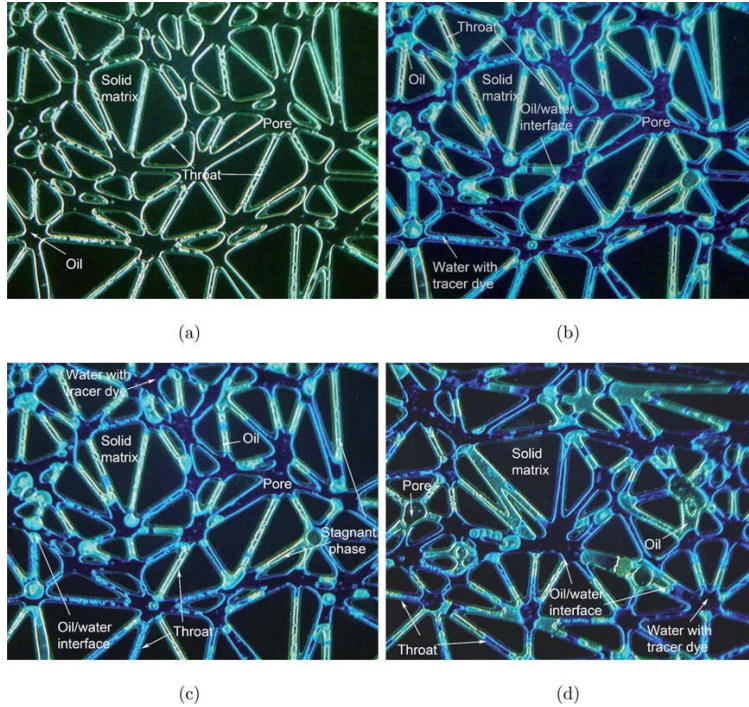


Fig. 4 Distribution of the oil phase (green color) and water phase (blue color) in the pore network during water-flooding experiments. (a) The presence of the oil phase at the start of the water-flooding process ($t = 0$); (b) Relative positions of the oil and water phases at $t = 5$ min; (c) Relative positions of the oil and water phases at $t = 13$ min. The presence of trapped oil is observed at the later part of the water-flooding process; (d) A different section of the pore network capturing the same dynamics of the oil and water phases at $t = 10$ min.

It is observed that (from Fig. 4) the non-wetting phase (oil) was trapped primarily in the largest pore spaces, the pores with the highest aspect ratios (ratio of pore size to throat size), and the pores with the highest coordination numbers (number of throats connected to pores). Capillary forces are responsible for oil trapping. The capillary number (relative effect of viscous forces versus surface tension acting across an interface between oil and water) is very low (6.10^{-7}) based on the present experimental conditions. This low capillary number causes the discontinuous water phase flow in the network within 10 to 15 min of injection. The reduction in the capillary force results in reduced trapped oil in pore spaces. Based on the volume data of total displaced oil, the fraction of recovered oil is calculated. A characteristic curve comparing the fraction of oil recovered with the injected water volume is presented in Fig. 5. This plot is similar to a recovery curve in traditional core-flooding experiments. In this case, original oil in

place (OOIP) denotes the volume of oil inside the ROC, before water-flooding starts. We observe a linear pattern at the beginning of water-flooding (up to about 500 ml of water injection), implying that the invading water phase displaces the resident oil at the same rate as its injection. However, as more water is injected with time, the fraction of oil recovered is comparatively less, which has been explained in terms of the trapped volume of oil. The maximum fraction of oil recovered by this stimulated water-flooding process is about 65%, which corresponds to values obtained in typical core flooding experiments.²

Proper care must be taken to extrapolate the results obtained from this ROC to the core-scale flooding and eventually to field scale. Still, the ROC has numerous advantages over existing micro-models, since it uses the microstructural information of actual 3D reconstructed pore-spaces, which provides a better representation of the pore-structure of rock with pore connectivity. In addition, the ROC provides a better visualization of complex fluid flows and displacement mechanisms at the pore scale.

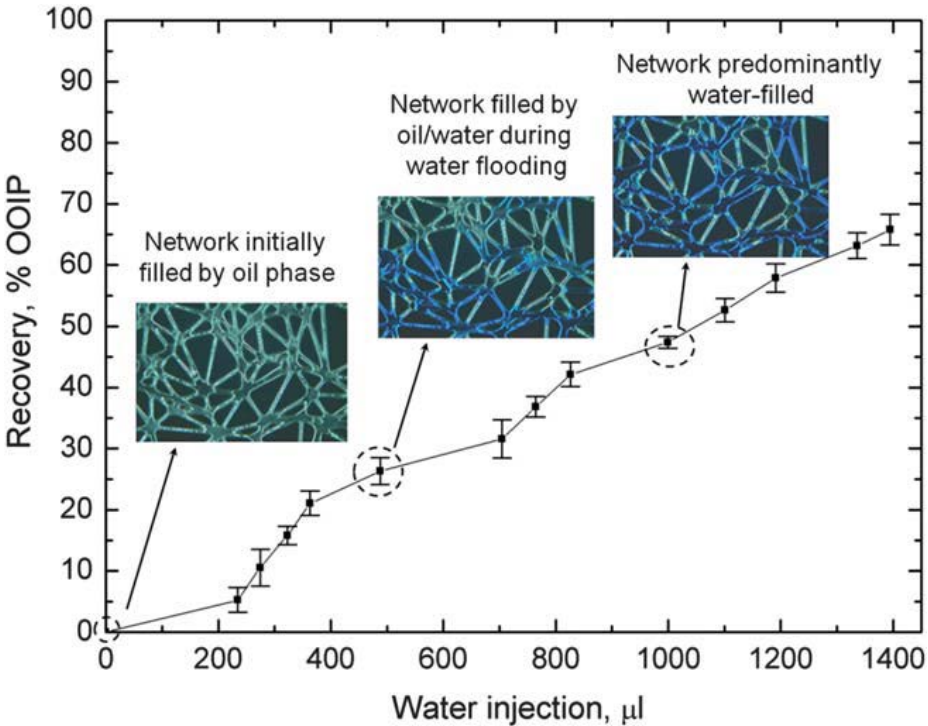


Fig. 5 Fraction of oil recovered in terms of original oil in place (OOIP) by injecting water at a constant flow rate of 100 ml min⁻¹, which is analogous to the recovery curve used in reservoir engineering by Hadia et al.² Insets show images of oil (green color)/water (blue color) phases corresponding to different time instances during the water-flooding process.

4.1.5 Conclusion

A novel concept for the miniaturization approach towards reservoir engineering and the study of water-flooding techniques on a chip related to oil recovery has been presented in this work. Instead of the usual approach of core-flooding or experimentation in micro-models containing random pore network representing porous medium, a methodology has been described where reservoir-rock is converted to a microfluidic chip for the pore-scale study of oil displacement experiments.

The sample core of such rock-specimens is characterized and reconstructed using advanced microscopy such as FIB-SEM, micro-CT, etc. Based on the reconstructed pore-space, a realistic pore network is designed and fabricated on silicon. Various parameters such as mean pore size and depth of the network have been designed in a manner such that this network is the most precise representation of an oil reservoir, and we coin the term 'Reservoir-on-a-Chip' (ROC) for this fabricated microfluidic device. Water-flooding experiments have been performed in this ROC. It is observed that, the invading water phase cannot displace oil from all the pore-throats in the chip and oil remains as a stagnant phase at different locations due to capillary trapping. The analysis of the recovery curve based on the fraction of oil recovered reveals a similar type of oil displacement pattern as obtained in a core-scale flooding experiment, which underlines the realization of the concept addressed in this study.

4.1.6 References

1. G. Pope, Society of Petroleum Engineers Journal, 1996, 20, 191–205.
2. N. Hadia, L. Chaudhari, S. K. Mitra, M. Vinjamur and R. Singh, Exp. Therm. Fluid Sci., 2007, 32, 355–361.
3. S. Bakke and P. E. Oren, SPE Journal, 1997, 2, 136–149.
4. M. J. Blunt, Curr. Opin. Colloid Interface Sci., 2001, 6, 197–207.
5. M. J. Blunt, M. D. Jackson, M. Piri and P. H. Valvatne, Adv. Water Resour., 2002, 25, 1069–1089.
6. P. Valvatne and M. Blunt, Water Resour. Res., 2004, 40, W074061–W0740621.
7. I. Fatt, Trans AIME, 1956, 207, 144–159.
8. A. A. Heiba, M. Sahimi, L. E. Scriven and H. T. Davis, Society of Petroleum Engineers of AIME, (Paper) SPE, 1992.
9. R. Lenormand, C. Zarcone and A. Sarr, J. Fluid Mech., 1983, 135, 337–353.

- 10 R. Lenormand, E. Touboul and C. Zarcone, *J. Fluid Mech.*, 1988, 189, 165–187.
11. M. Blunt, *Curr. Opin. Colloid Interface Sci.*, 2001, 6, 197–207.
12. R. I. Al-Raoush and C. S. Willson, *J. Contam. Hydrol.*, 2005, 77, 67–89.
13. B. Bera, S. K. Mitra and D. Vick, *Micron*, 2011, 42, 412–418.
14. C. S. Willson, R. W. Stacey, K. Ham and K. E. Thompson, *Proceedings of SPIE - The International Society for Optical Engineering*, 2004, 101–111.
15. J. D. Seymour and P. T. Callaghan, *AIChE J.*, 1997, 43, 2096–2111.
16. W. E. Kenyon, *Nuclear Geophysics*, 1992, 6, 153–171.
17. J. T. Geller and L. R. Myer, *J. Contam. Hydrol.*, 1995, 19, 85–104.
18. G. Bohrer, H. Mourad, T. A. Laursen, D. Drewry, R. Avissar, D. Poggi, R. Oren and G. G. Katul, *Water Resour. Res.*, 2005, 41, 1–17.
19. A. C. Gunde, B. Bera and S. K. Mitra, *Energy*, 2010, 35, 5209–5216.
20. R. C. Acharya, S. E. A. T. M. V. der Zee and A. Leijnse, *Adv. Water Resour.*, 2007, 30, 261–272.
21. Y. Zaretskiy, S. Geiger, K. Sorbie and M. Frster, *Adv. Water Resour.*, 2010, 33, 1508–1516.
22. X. Zhan, L. M. Schwartz, M. N. Toksz, W. C. Smith and F. D. Morgan, *Geophysics*, 2010, 75, F135–F142.
23. B. Manz, L. F. Gladden and P. B. Warren, *AIChE J.*, 1999, 45, 1845– 1854.
24. J. F. Chau, *Phys. Rev. E: Stat., Nonlinear, Soft Matter Phys.*, 2006, 74, 056304.
25. R. D. Hazlett, S. Y. Chen and W. E. Soll, *J. Pet. Sci. Eng.*, 1998, 20, 167–175.
26. T. Ramstad, P. E. Oren and S. Bakke, *SPE Journal*, 2010, 15, 923– 933.
27. T. Ramstad, P. E. Oren and S. Bakke, *Proceedings - SPE Annual Technical Conference and Exhibition*, 2009, 2561–2576.
28. A. S. Al-Kharusi and M. J. Blunt, *J. Pet. Sci. Eng.*, 2007, 56, 219–231.
29. H. Dong and M. J. Blunt, *Phys. Rev. E: Stat., Nonlinear, Soft Matter Phys.*, 2009, 80, 036307.
30. N. A. Idowu and M. J. Blunt, *International Petroleum Technology Conference, IPTC 2008*, 2008, 1183–1198.
31. N. A. Idowu and M. J. Blunt, *Transp. Porous Media*, 2010, 83, 151– 169.
32. S. Litster, D. Sinton and N. Djilali, *J. Power Sources*, 2006, 154, 95–105.

33. P. E. Oren and W. V. Pinczewski, *Transp. Porous Media*, 1995, 20, 105–133.
34. M. I. J. Van-Dijke, K. Sorbie, M. Sohrabi and A. Danesh, *J. Pet. Sci. Eng.*, 2006, 52, 71–86.
35. M. I. J. Van-Dijke, K. S. Sorbie, M. Sohrabi and A. Danesh, *SPE Journal*, 2004, 9, 57–66.
36. M. Sohrabi, A. Danesh and M. Jamiolahmady, *Transp. Porous Media*, 2008, 74, 239–257.
37. D. Broseta, F. Medjahed, J. Lecourtier and M. Robin, *SPE Advanced Technology Series*, 1995, 3, 103–112.
38. D. Broseta and F. Medjahed, *J. Colloid Interface Sci.*, 1995, 170, 457–465.
39. H. E. Meybodi, R. Kharrat and X. Wang, *Transp. Porous Media*, 2011, 89, 97–120.
40. B. Y. Jamaloei and R. Kharrat, *Transp. Porous Media*, 2009, 76, 199–218.
41. B. Y. Jamaloei and R. Kharrat, *Transp. Porous Media*, 2010, 81, 1–19.
42. B. Y. Jamaloei, K. Asghari, R. Kharrat and F. Ahmadloo, *J. Pet. Sci. Eng.*, 2010, 72, 251–269.
43. C. L. Perrin, K. S. Sorbie, P. M. J. Tardy and J. P. Crawshaw, 67th European Association of Geoscientists and Engineers, EAGE Conference and Exhibition, incorporating SPE EUROPE2005- Extended Abstracts, 2005, 933–940.
44. S. A. Bowden, J.M. Cooper, F. Greub, D. Tambo and A. Hurst, *Lab Chip*, 2010, 10, 819–823.
45. S. A. Bowden, R. Wilson, J. Parnell and J. M. Cooper, *Lab Chip*, 2009, 9, 828–832.
46. D. Sen, D. Nobes and S. K. Mitra, *Microfluid. Nanofluid.*, 2011, DOI: 10.1007/s10404-011-0862-x.
47. V. Berejnov, N. Djilali and D. Sinton, *Lab Chip*, 2008, 8, 689–693.
48. F. Aktas, T. Clemens, L. M. Castanier and A. R. Kavscek, *Proceedings - SPE Symposium on Improved Oil Recovery*, 2008, 384–394.
49. M. Buchgraber, T. Clemens, L. M. Castanier and A. R. Kavscek, *SPE Reservoir Eval. Eng.*, 2011, 14, 269–280.
50. M. Buchgraber, T. Clemens, L. M. Castanier and A. R. Kavscek, *Proceedings - SPE Annual Technical Conference and Exhibition*, 2009, 78–96.
51. R. Hazlett, *Transp. Porous Media*, 1995, 20, 21–35.
52. R. wirth, *Chem. Geol.*, 2009, 261, 217–229.

53. J. Wilson, W. Kobsiriphat, R. Mendoza, H. Chen, J. Hiller, D. Miller, K. Thornton, P. Voorhees, S. Adler and S. Barnett, *Nat. Mater.*, 2006, 5, 541–544.
54. N. S. K. Gunda, H. Choi, A. Berson, B. Kenney, K. Karan, J. Pharoah and S. K. Mitra, *J. Power Sources*, 2011, 196, 3592–3603.
55. M. Sahimi, A. A. Heiba, H. T. Davis and L. E. Scriven, *Chem. Eng. Sci.*, 1986, 41, 2123–2136.
56. N. Karadimitriou, S. Hassanizadeh and P. Kleingeld, *First International Conference on Frontiers in Shallow Subsurface Technology*, 2010.
57. K. J. Seu, A. P. Pandey, F. Haque, E. A. Proctor, A. E. Ribbe and J. S. Hovis, *Biophys. J.*, 2007, 92, 2445–2450

Part 2: A novel Deep Reactive Ion Etched (DRIE) glass micro-model for two-phase flow experiments

Abstract

In the last few decades, micro-models have become popular experimental tools for two-phase flow studies. In this work, the design and fabrication of an innovative, elongated, glass-etched micro-model with dimensions of 5 x 35 mm² and constant depth of 43 micron is described. This is the first time that a micro-model with such depth and dimensions has been etched in glass by using a dry etching technique. The micro-model was visualized by a novel setup that allowed us to monitor and record the distribution of fluids throughout the length of the micro-model continuously.

Quasi-static drainage experiments were conducted in order to obtain equilibrium data points that relate capillary pressure to phase saturation. By measuring the flow rate of water through the flow network for known pressure gradients, the intrinsic permeability of the micro-model's flow network was also calculated. The experimental results were used to calibrate a pore-network model and test its validity.

Finally, we show that glass-etched micro-models can be valuable tools in single and/or multi-phase flow studies and their applications.

4.2.1 Introduction

An efficient way to study two-phase flow in a porous medium is through the development of an artificial transparent porous medium with known properties, commonly referred to as "micro-model". An extensive review of micro-models use in two-phase flow studies (including fabrication methods and materials and visualization techniques) can be found in Karadimitriou and Hassanizadeh¹.

Up to now, most micro-models that have been used to study flow and transport in porous media are small domains of square, or nearly square, dimensions²⁻⁷. Therefore, one may interpret them as being one Representative Elementary Volume (REV). An REV is the volume of a homogeneous porous medium above which the system

properties are insensitive to the averaging domain's size. In this work, an elongated, glass-etched micro-model with dimensions $5 \times 35 \text{ mm}^2$ was manufactured. The pore network was designed such that the REV size was around $5 \times 7 \text{ mm}^2$. So, our micro-model was considered to be five times the REV size. The REV size was determined through pore-network modeling. Simulations were run for the whole extent of the micro-model. Then, capillary pressure-saturation curves were obtained for a sequence of gradually increasing sub-domain sizes and compared to each other. The subdomain size beyond which the capillary pressure-saturation curve remained unchanged was considered to be the REV.

In the work of Naga Siva et al.⁸, the micro-fluidic device was also elongated, but it was made of two different materials. The flow network was created in a silicon substrate, and the whole model was sealed with a glass slide. This was needed because silicon is translucent and the model had to have a transparent side so that it could be visualized. However, that created a mixed-wettability system with undesirable and uncontrolled effects in two-phase flow processes.

In this work, we describe the design and fabrication of an elongated all-glass Deep Reactive Ion Etched (DRIE) micro-model. We have replicated a flow network that on average has the properties of an oil rock reservoir in a microfluidic chip. Comparative studies between pore-network modeling and micro-model experiments of the same flow network were made in order to investigate the efficiency of the use of such micro-models in two-phase flow studies. Properties of the flow network, such as intrinsic permeability, the relationship between phase saturation and capillary pressure, as well as phase flow rates, were measured and modeled.

The advantages of this micro-model were the following. First, the micro-model had a uniform wettability given that it is made of one material, namely glass. Second, the micro-model was totally transparent. In this way, direct optical visualization was made possible with the use of an innovative optical setup that will be described later.

To the best of our knowledge, this is the first time that two-phase flow studies are performed with such a uniformly wetting and elongated microfluidic glass chip with realistic pore sizes. The optical setup is also a breakthrough in real-time visualization methods for elongated samples.

4.2.2 Pore-network model description

The pore network was represented by an assembly of pore bodies (large pores) connected to each other by smaller pores, called pore throats. The pore network

topology was generated using Delaunay triangulation, as it is considered to provide a good representation of a real porous medium⁹. In Delaunay triangulation, points are connected to their neighbors by non-intersecting bonds. Connected points form triangles that are as equilateral as possible. The coordinates of the triangulation points were generated in MatLab. These points were considered to be the centers of the pore bodies. The overall dimensions of the network were 5 x 35 mm². In figure 1, the image of the whole network, as well as a magnified part of it, are shown.

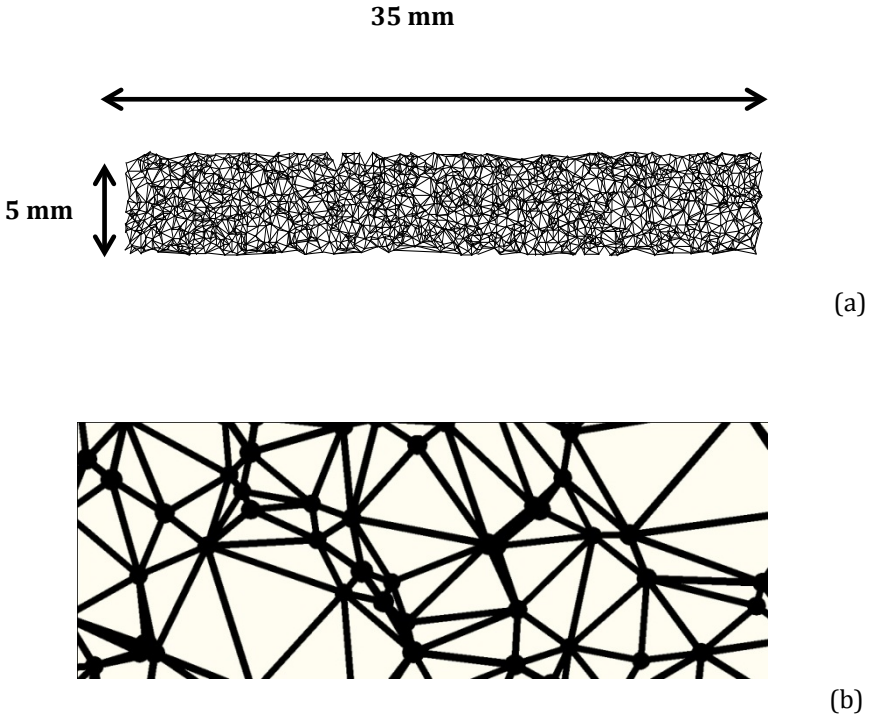


Figure 1. (a) Image of a pore-network with 2000 pore bodies and 6000 pore throats and a mean pore size of 70 μm . The void space is shown in black. (b) Zoom-in image of the network.

The pore network had a quasi-three-dimensional nature. It comprised a two-dimensional network of pores, but each pore was a three-dimensional element as it had a depth. The pore bodies had a cylindrical shape (they were circular in planar view; see Figure 1b) while pore throats had a parallelepiped shape (i.e, rectangular in planar view). Both pore bodies and pore throats had a rectangular cross-section. The SEM image of a typical cross section is shown in Figure 7. The coordination number, which is

the number of connections of a pore body, varied from 4 to 6, depending on the total number of pore bodies.

The sizes of pore bodies were assigned from a truncated log-normal distribution. The mean pore size was selected to be equal to 70 μm . This value was selected in order for the visualization setup to be effective, as it will be explained later.

The length of a pore throat was defined as the distance between the centers of the neighboring pore bodies, d , minus the sum of their radii. The width of a pore throat was assigned such that it would always be smaller than the diameters of two neighboring pore bodies. This was given by a number of formulas used by Joekar-Niasar et al.¹⁰.

Special attention was paid to the fact that the statistical distribution of sizes for pore bodies and pore throats should overlap to some extent, as this is the case in real porous media¹¹⁻¹³. The depth of the network was chosen to be constant and close to the mean pore size.

4.2.3 Experimental setup and procedure

Micro-model

In the introduction of this manuscript, a general description of the micro-model was given. In the following sections, some more details are given regarding the construction of the micro-model.

Flow network

As mentioned earlier, the micro-model's flow network was exactly the same as the one that was used for numerical simulations. With the use of LISP¹⁴ the network was converted to an Autocad sketch. Two reservoirs were added the same sketch and connected to the ends of the flow network. The Autocad sketch was then used for the production of a mask that was needed for the etching process.

Construction of the micro-model

In order to construct a glass-etched micro-model with DRIE, a chromium mask had to be prepared first (Compugraphics Intl. Ltd, Scotland). The mask was made of a glass plate coated with a thin layer of chromium. The flow network and the two reservoirs were created in the chromium layer. Areas of the mask that corresponded to the void space were transparent, while the rest was covered by chromium. In order to increase

the efficiency of the procedure and the maximum achievable depth, a layer of photoresist was applied on the glass slide in which the micro-model was to be created. First, the flow network was etched in the photoresist layer, over its full thickness, with the use of photo-lithography as an intermediate step^{15,16}. Then, the glass slide was etched and flow network and the two reservoirs were created in it.

The pore network was printed on the by a laser-printing equipment at a resolution of 0.7 micron/pixel, which is quite high. It was essential for the resolution of the mask to be much higher than the resolution of our visualization setup. In this way, the rasterization of the mask would not be visible within the features of the flow network.

The etching was done using the Deep Reactive Ion Etching (DRIE) method¹⁷⁻¹⁹. This method was chosen as it is very accurate. Also, because it is highly anisotropic, it provides almost vertical walls. This was essential for the needs of the visualization setup, as explained shortly. However, there are some known issues (fabrication limits, accuracy of the process, etc.) with the maximum achievable depth^{20,21}. In our case, we achieved a depth of 43 μm ; this is the first reported microfluidic device made of glass with such a large depth.

Inflow and outflow reservoirs were also etched in the glass plate containing the flow network. They were etched with the use of wet-etching techniques and not with DRIE method, as the needs for detail were relaxed. A second glass plate was used to cover and seal the model with the help of chemicals and a large mechanical pressure. At the center of each reservoir, a hole was drilled in the cover glass plate for the introduction and removal of fluids.

The micro-model shown in Figure 2 has 3000 pore bodies and 9000 pore throats with a mean pore size of 70 μm . This micro-model was used to perform the experiments.

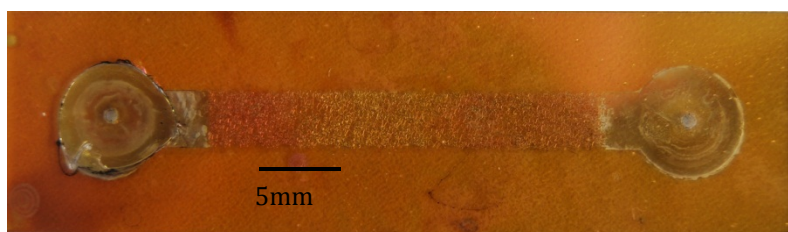


Figure 2. Picture of a micro-model with 3000 pore bodies and 9000 pore throats with a mean pore size of 70 μm . The two round reservoirs and the holes for introduction and removal of the two fluids are visible too.

Flow Visualization.

In most micro-model studies, a microscope has been used for visualization and a camera for recording images. As explained before, the main objective of this work was to design and fabricate an elongated micro-model for the study of two-phase flow under dynamic as well as quasi-static conditions. So, it was important for the visualization setup to allow simultaneous monitoring of flow throughout the whole micro-model as a function of time. For this reason, the use of a microscope was not applicable. The observation frame of a microscope is usually square. The smallest dimension of the object under observation and the required resolution always determine the size of this frame. In our case, the smallest dimension of the micro-model was the 5 mm. For the results of image processing to be reliable, the resolution had to be such that the smallest feature in the flow network could be visualized with at least 10 pixels. . Given that the narrowest throat had a width of 28 μm , the resolution of the visualization setup had to be at least 2.8 $\mu\text{m}/\text{pixel}$. This meant that only a frame of 5 x 5 mm^2 could be visualized, without being able to monitor the rest of the micro-model. One option would be to move the camera or the microscope. However, this procedure would take time, so the images obtained would not refer to the same time frame. Also, it would take too much time to process these images in order to eliminate any overlapping. Moreover, the movement of the model could introduce new, unknown forces that would affect the fluids distribution. For this reason, an alternative visualization method had to be developed.

Visualization setup

To visualize the whole micro-model, an innovative optical setup had to be designed and materialized. This setup involved an optical table, a collimated light source, a prism, an objective lens with a long focal length, three beam splitters, four cameras, and a computer for data acquisition. A schematic representation of the visualization setup can be seen in figure 3, with a photo shown in figure 4.

A beam splitter splits a light beam into two identical perpendicular ones. In theory, the intensity of the two beams would be half the intensity of the initial one. In practice, the intensity of the two beams was close to 47% of the initial value, due to energy losses in the beam splitter.

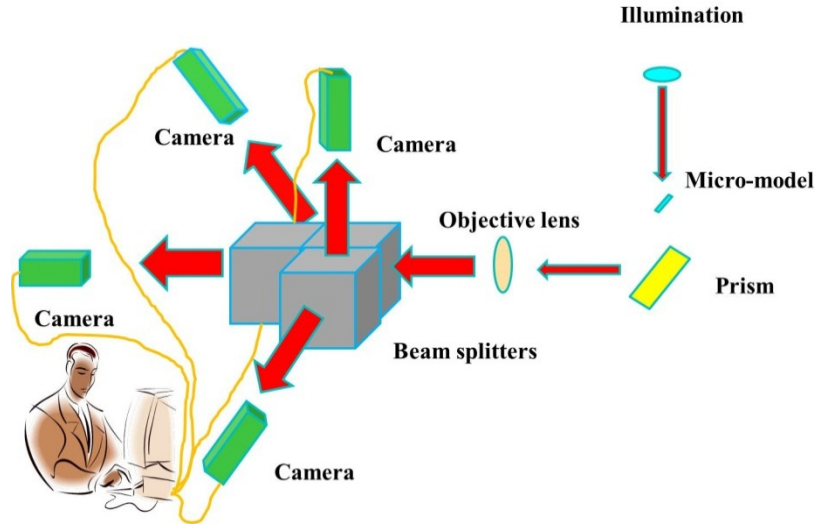


Figure 3. Schematic representation of the visualization principle of the experimental setup.

As shown in figure 3, a LED light source with tunable intensity emitting at 570 nm (Jenoptik) was used as the illumination source. The light source was put exactly at the focal point of a lens that had a focal length of 135 mm with respect to infinity. This arrangement provided a highly collimated light beam, at least for our working distance, with a diameter of 50 mm. This light beam, after passing through the glass micro-model, passed through a prism, so that its orientation would become parallel to the optical table. A Zeiss Sonnar T135mm f/1.8 ZA objective lens with a focal length of 135 mm was used to magnify the image. Right after the objective lens, three beam splitters (Edmund Optics) were combined in a way that they gave four identical reproductions of the initial light beam. The beam splitters were cubic with a side length of 35 mm. They were put inside a black box and their sides were covered with black paper in order to prevent internal reflections that would produce “ghost” images. These four images were captured by four GC-2450 Prosilica Ethernet cameras at a resolution of 5 Mpixels. The cameras were connected to a computer through Ethernet cables for data acquisition. They could record sequential pictures at a rate of 15 frames per second at the maximum resolution. By eliminating some lines from the sensor with the use of the appropriate software, the frame rate could reach 18 frames per second. The cameras were positioned such that they were focusing on four sequential parts of the initial image, visualizing most of the micro-model’s length.

The design of this setup and the magnification was based on the micro-model size, the size of the camera sensor, and the requirement that the width of the smallest pore throat should be at least 10 pixels long. This meant that a minimum resolution of 2.8 $\mu\text{m}/\text{pixel}$ was needed. Given the fact that the actual pixel size of the sensor of a GC-2450 camera is 3.45 μm , the magnification factor of the optical setup had to be 1.25. Thus, the initial size of the micro-model of 5 x 35 mm² would become 6.25 x 43.75 mm² after magnification. Given that the actual size of the sensor of each camera was 7.072 x 8.445 mm², a total area of 7.072 x 33.78 mm² could be monitored simultaneously at a resolution of 2.8 $\mu\text{m}/\text{pixel}$ by the four cameras. That was 80% of the whole length of the micro-model. With a small compromise of reducing the resolution to 3.0 $\mu\text{m}/\text{pixel}$, an even bigger area could be covered, close to 85% of the total area.

The fact that the objective lens had an external filter diameter of 77 mm and a maximum aperture of f/1.8 provided the ability to produce images with minimal aberration and uniform light intensity. Its focal length of 135 mm provided the needed space for position the cameras within the boundaries of the optical table.

Pressure measurement and control

The micro-model was placed on a stage and it was directly connected to two external reservoirs, one for each phase. At exactly the same level as the level of the micro-model, two pressure transducers were installed to measure the pressure in the reservoirs. These transducers were connected to the controlling unit of a Bronkhorst differential pressure controller. The differential pressure controller had an RS-232 interface that was connected to a computer. In this way, it was possible to set, measure, and control the differential pressure between the two reservoirs at any instant. The controller was calibrated in a way that at its maximum span, the measured pressure would be 35 kPa with an accuracy of 35 Pa. The pressure controller was used to adjust the pressure in the non-wetting phase reservoir by increasing or decreasing the flow delivered to the non-wetting phase reservoir. . By increasing the pressure of the non-wetting phase reservoir, drainage could be initiated. The pressure in the wetting phase reservoir was always atmospheric.

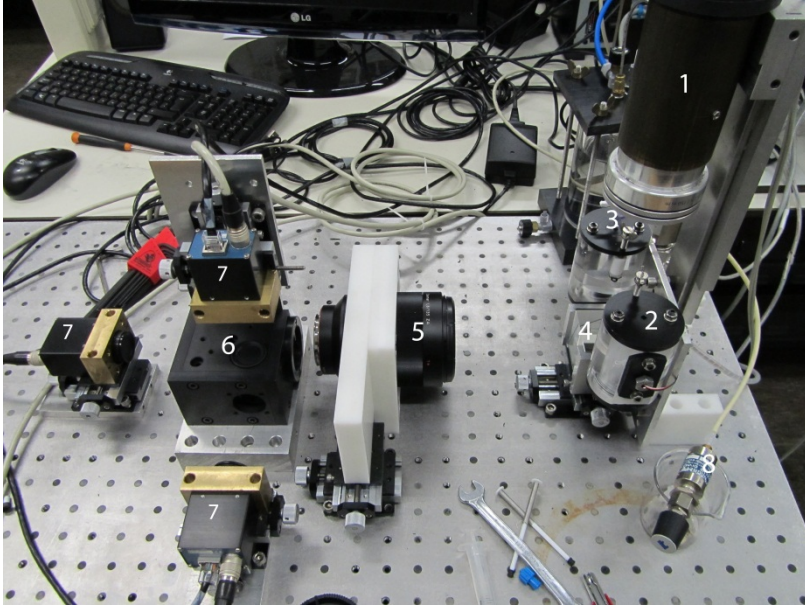


Figure 4. The experimental setup: 1) illumination, 2) wetting phase reservoir, 3) non-wetting phase reservoir, 4) prism, 5) lens, 6) box with beam-splitters, 7) cameras, 8) leak valve. There is another camera behind the box with the beam splitters that cannot be seen from this angle.

4.2.4 Two-phase displacement experiments

For our displacement experiments, dyed water was used as the wetting phase, and Fluorinert FC-43 as the non-wetting phase. The interfacial properties of dyed water and fluorinert, such as interfacial tension and contact angle, were measured. The interfacial tension between dyed water and fluorinert was found to be 55 mN/m, and the contact angle was 26 degrees. The dye was added to the water for increasing the optical contrast between the two phases and their easy identification in the images. In our preliminary experiments, the model was initially filled with the wetting phase. Drainage was initiated by gradually increasing the non-wetting phase pressure incrementally until it entered the micro-model. After each pressure step, the system was left for 20 minutes to reach equilibrium. Incremental pressure increase and the invasion of the non-wetting phase were continued until it reached the end of the model.

4.2.5 Results

During displacement experiments, images of the micro-model were acquired at various times and stored. In this part of the study, only equilibrium results were analyzed. In figure 5, sequential images taken from part of the network are shown.

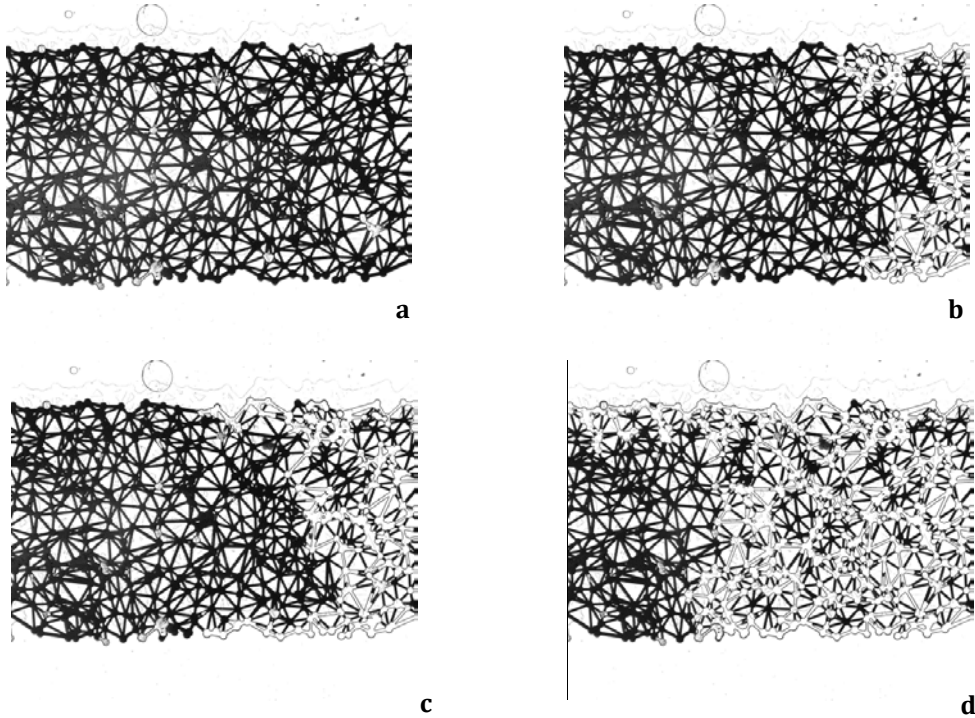


Figure 5. Images obtained from the micro-model during drainage. Initially the model is filled with the wetting phase (shown in dark color). Drained model at three sequential equilibrium states (b), (c), and (d). The non-wetting phase is shown in light color.

After image processing and calculation of average saturation, and with the use of the recorded values of the applied pressure, the Pc-S curve for drainage could be constructed. In figure 6, the measured data are shown along with the results obtained from the pore-network model for the same flow network. Results showed satisfactory agreement.

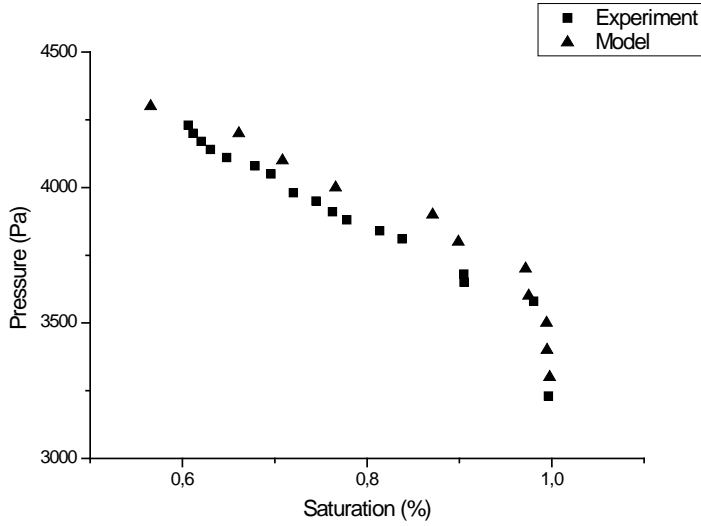


Figure 6. Pc-S data obtained from the experiment and the numerical model.

In order to measure the intrinsic permeability of the network, water was introduced into the micro-model at an imposed pressure. With the use of a Bronkhorst flow meter, the corresponding flow rate was measured at the outlet of the micro-model. Then with the use of Darcy’s law²² for single-phase flow, equation 1, K_{in} could be calculated

$$\vec{q} = -\frac{K_{in}}{\mu} \cdot (\vec{\nabla}P - \rho \vec{g}) \quad (1)$$

By repeating this measurement for different applied pressures and the corresponding flow rates, a mean value for the intrinsic permeability of the network was calculated, and found to be equal to $K_{in}=6.10 \cdot 10^{-12} \text{ m}^2$.

4.2.6 Discussion and Conclusions

In this work, a novel Deep Reactive Ion Etched, micro-fluidic device made of glass, with a depth of 43 μm , pre-defined properties, and suitable for single and/or multi-phase flow studies, was presented.

The data that were obtained experimentally for the Pc-S curve for the micro-model with 3000 pore bodies and 9000 pore throats, and a mean pore size of 70 μm , were compared to those obtained from the simulation for the same flow network. Intrinsic permeability was also calculated as an extra means of validating the correspondence between the experiment and the numerical model.

The comparison between the experimental results and the results obtained by the numerical model showed that there was a very good agreement between them. Pc-S curves collapsed onto each other, and the value obtained for intrinsic permeability was accurately estimated by the numerical model.

We observed that at a wetting-phase saturation of around 60%, all measured data points fell on top of each other. This happened because drainage was fully developed as soon as the non-wetting phase broke through the network. Additional drainage was not possible because the remaining wetting phase existed in isolated domains. However, in the numerical model the system was allowed to be fully drained.

Despite the fact that DRIE is highly anisotropic and can produce vertical walls, when the depth becomes large, for instance more than 20 μm , the walls become slightly sloped. This is visible in SEM images shown in figure 7.

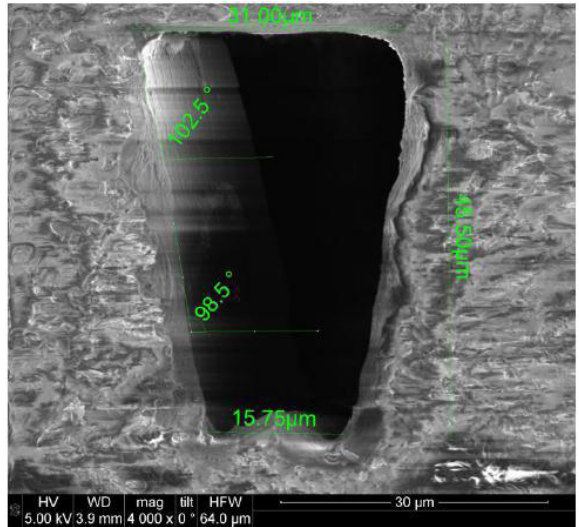


Figure 7. A SEM image showing the cross section of a pore throat formed in the micro-model.

In addition to the wall slope, the bottom surfaces of the channels were not smooth. In order to account for this slope and the roughness of the bottom and top surface in the numerical model, the parameters that affected the size distribution have been accordingly tuned. The slope on the walls of the network channels introduced some problems in the visualization efficiency. When there is a slope on the walls, light that comes from the illumination source gets refracted and never reaches the camera's

sensor. As a result, the two-dimensional projection of the slope appeared in black. Given that the slope was not high, its effect was not significant in the visualization setup.

The displacement of two fluid phases in the model could be directly visualized and recorded as a function of time. The agreement between the results obtained from micro-model experiments and pore-network model simulations were satisfactory. This agreement verified that a glass micro-model with uniform properties is a useful tool for studying and understanding two-phase flow processes.

4.2.7 References

1. Karadimitriou, N. K., and Hassanizadeh, S. M. (2012), A review of micro-models and their use in two-phase flow studies, *Vadose Zone Journal*, accepted for publication.
2. Pyrak-Nolte, L. J., D. D. Nolte, D. Chen, and N. J. Giordano (2008), Relating capillary pressure to interfacial areas, *Water Resour. Res.*, 44, W06408, doi:10.1029/2007WR006434.
3. Berejnov, V., Djilali, N., and Sinton, D., (2008), Lab-on-chip methodologies for the study of transport in porous media: energy applications, *Lab Chip*, 8, pp. 689–693.
4. Tsakiroglou, C.D., and Avraam, D.G. (2002), Fabrication of a New Class of Porous Media Models for Visualization Studies of Multiphase Flow Process, *J. of Material Sci.*, 37, 353.
5. Chen, D., L. Pyrak-Nolte, J. Griffin, and N. Giordano (2007), Measurement of interfacial area per volume for drainage and imbibition, *Water Resour. Res.*, 43, W12504, doi:10.1029/2007WR006021.
6. Chen, L., and Kibbey, T. C. G. (2006), Measurement of Air–Water Interfacial Area for Multiple Hysteretic Drainage Curves in an Unsaturated Fine Sand, *Langmuir*, 22 (16), pp. 6874–6880, doi: 10.1021/la053521e.
7. Cheng, J.-T., L. J. Pyrak-Nolte, D. D. Nolte, and N. J. Giordano (2004), Linking pressure and saturation through interfacial areas in porous media, *Geophys. Res. Lett.*, 31, L08502, doi:10.1029/2003GL019282.
8. Naga Siva, G., Bera, B., Karadimitriou, N. K., Mitra, S. K., and Majid Hassanizadeh, S. M., (2011), Reservoir-on-a-Chip (ROC): A new paradigm in Reservoir Engineering, *Lab Chip*, DOI:10.1039/C1LC20556K, 2011
9. Heiba, A., Sahimi, M., Scriven, L., and Davis, H. (1992), Percolation theory of two-phase relative permeability, *SPE Reserv. Eng.*, 7, pp. 123–132.

10. Joekar-Niasar, V., Hassanizadeh, S. M., Dahle, H. K. (2010), Non-equilibrium effects in capillarity and interfacial area in two-phase flow: Dynamic pore-network modeling", *Journal of Fluid Mechanics*, doi:10.1017/S0022112010000704.
11. Al-Raoush, R. I., Willson, C. S. (2005a), Extraction of physically realistic pore network properties from three-dimensional synchrotron X-ray microtomography images of unconsolidated porous media systems, *Journal of Hydrology*, Vol. 300, Issues 1-4, pp. 44-64, ISSN 0022-1694, DOI: 10.1016/j.jhydrol.2004.05.005.
12. Al-Raoush, R. I., Willson, C. S. (2005b), A pore-scale investigation of a multiphase porous media system, *Journal of Contaminant Hydrology*, Vol. 77, Issues 1-2, pp. 67-89, ISSN 0169-7722, DOI: 10.1016/j.jconhyd.2004.12.001.
13. Joekar-Niasar, V., S. M. Hassanizadeh, and A. Leijnse (2008), Insights into the relationships among capillary pressure, saturation, interfacial area and relative permeability using pore-scale network modeling, *Transp. Porous Media*, doi:10.1007/S11242-007-9191-7.
14. McCarthy, J., Brayton, R.; Edwards, D., Fox, P., Hodes, L., Park, D. (1960), *LISP I Programmers Manual*. Boston, Massachusetts: Artificial Intelligence Group, M.I.T. Computation Center and Research Laboratory, Accessed May 11, 2010.
15. Thompson, L.F., C.G. Wilson and M.J. Bowden (1983), *Introduction to Microlithography*, ACS Symp. Ser., 219.
16. Thompson, L. F., C. G. Willson, and M. J. Bowden (1994), *Introduction to Microlithography*, 2nd ed., Am. Chem. Soc., Washington, D. C., doi: 10.1002/pi.1995.210370312.
17. Blauw, M. A., T. Zijlstr, and E. van der Drift (2001), Balancing the etching and passivation in time-multiplexed deep dry etching of silicon, *J. Vac. Sci. Technol. B*, 19, pp. 2930-2934.
18. Willingham, T. W., Werth, C. J., and Valocchi, A. J. (2008), Evaluation of the Effects of Porous Media Structure on Mixing-Controlled Reactions Using Pore-Scale Modeling and Micro-model Experiments, *Environmental Science & Technolog*, 42 (9), pp. 3185-3193.
19. Yeom, J., Y. Wu, and M. A. Shannon (2003), *Proceedings of Transducers '03-The 12th International Conference on Solid State Sensors, Actuators and Microsystems*, IEEE, Boston, MA, p. 1631.
20. Yeom, J., Y. Wu, J. C. Selby, and M. A. Shannona,(2005), Maximum achievable aspect ratio in deep reactive ion etching of silicon due to aspect ratio dependent transport and the microloading effect, *Journal of Vacuum Science & Technology B: Microelectronics and Nanometer Structures*, 23: 6, pp. 2319 - 2329,1071-1023.doi:10.1116/1.2101678.

21. Ohara, J., Asami, K., Takeuchi, Y. and Sato, K. (2010), Development of RIE-lag Reduction Technique for Si Deep Etching Using Double Protection Layer Method, IEEJ Transactions on Electrical and Electronic Engineering, 5: 125–130. doi: 10.1002/tee.20506.
22. Darcy, H. (1856), Les Fontaines Publiques de la Ville de Dijon, Dalmont, Paris.

Karadimitriou, N. K., Xiarchos, I., and Hassanizadeh, S. M., 2013, In situ surface treatment of PDMS to enhance natural hydrophobicity, submitted to Surface and Coatings Technology

Chapter 5

In situ surface treatment of PDMS to enhance natural hydrophobicity

Abstract

Micro-models have been increasingly employed in various ways in porous media research, to study the pore-scale behavior of fluids. Micro-models have proven to be a valuable tool by allowing the observation of flow and transport at the micron scale in chemical, biological, and physical applications. They have helped to improve our insight of flow and transport phenomena at both micro- and macro-scales.

Up to now, PDMS has not been a favorable material to make micro-models from, for two-phase flow studies, due to its wettability issues. For two-phase flow studies, it is very important that the micro-model has stable and well controlled wetting properties. In this work, we present an easy and inexpensive way of making PDMS strongly and uniformly hydrophobic, so as to be reliably used in two-phase flow studies.

5.1 Introduction

In porous media research, micro-models have been increasingly applied in various ways to study the behavior of fluids inside micro structures. Studies have included chemical, biological, and physical applications. Micro-models have proven to be a valuable tool for the observation of flow and transport on the micron scale. They have helped to increase our ability to describe flow and transport phenomena on pore and larger scales.

An overview of various issues related to micro-models (such as network generation, fabrication materials and methods, visualization methods, and various applications) was given in Karadimitriou and Hassanizadeh [1]. They define a micro-model as “an artificial representation of a porous medium, made of a transparent material. This

fluidic device bears a flow network, with features on the micro-scale, and an overall size of up to a few centimeters”.

One of the materials widely used in making micro-models is Poly-dimethyl-siloxane (PDMS). It is a viscoelastic, silicon-based organic polymer. It is optically transparent, inert, non-toxic, and nonflammable. Given its mechanical and chemical properties, PDMS could be suitable for manufacturing micro-models for the study of two-phase flow. PDMS is hydrophobic in its natural state. However, its intrinsic hydrophobicity is not strong and not uniform. This can be changed by exposing the surface of the material to air or oxygen plasma radiation, or to ultra-violet light. This process makes the material highly hydrophilic, but only for limited time. The material will return to its initial and natural hydrophobic state after some hours. This gradual change in the hydrophobicity of the material makes it unsuitable for experiments that take many hours to complete.

For instance, in two-phase flow studies under quasi-static conditions, experiments can last for more than 12 hours. During this period, the material hydrophobicity changes, and it becomes variably hydrophobic (also called mixed wettability). This is undesirable as it makes the experimental results difficult to interpret, if not impossible. An extensive review on the recent developments in PDMS surface modification for micro-fluidic devices can be found in the work of Zhou et al. [2]. They state that there is an abundance of literature on the topic of silanization of plasma-based oxidation, but comparatively little on in situ wet-chemical oxidation, which is our point of interest in this work.

For two-phase flow studies, we usually need stable and (and well-controlled) hydrophobicity (or hydrophilicity). We have developed a novel procedure for making PDMS uniformly and permanently hydrophobic. In this process, Trichloro(1H,1H,2H,2Hperfluorooctyl) silane (Sigma-Aldrich), from now on called TCP-silane, is dissolved in ethanol. The solution is usually called silane. We introduce the solution into the flow network of a micro-model in order to change its surface properties and make it strongly and uniformly hydrophobic. This process is called silanization. Silanization has been mostly employed for the surface treatment of silicon wafers before performing soft lithography, so as to prevent PDMS from bonding with the wafer. In this process, vapors of TCP-silane interact in vacuum with the surface of the silicon wafer.

In our two-phase flow studies, we used a PDMS micro-model. The flow network had dimensions of 5 x 30 mm². It consisted of 3000 pore bodies and 9000 pore throats, with a mean pore size of 40 microns, and a depth equal to the mean pore size. For the two

immiscible liquids, we used Fluorinert FC-43 (from 3M) as the wetting phase (colorless), and water dyed with ink as the non-wetting phase. Fluorinert is a colorless (refraction index, $n=1.291$), fluorine based, and inert liquid. It is 4.7 times more viscous ($\mu=4.7 \cdot 10^{-3} \text{ Pa}\cdot\text{s}$) and 1.86 times heavier than water ($\rho=1860 \text{ Kgr/m}^3$). The interfacial tension between water and Fluorinert is 58 mN/m. Further details on the flow network of the micro-model, like geometry, pore size distribution, etc., can be found in Karadimitriou et al. [3].

5.2 Silanization process

For the silanization process, a solution of TCP-silane in 96% pure ethanol was prepared in a 2-ml beaker. The beaker was air-proof, and the components of the solution were introduced in the beaker using a syringe with a needle. The solution was thoroughly mixed with an electrical stirrer. In order to determine the most suitable concentration of TCP-silane in ethanol, flat PDMS slabs were treated with different concentrations. They were coated with the solution and then put into the oven to dry out. Then, a glass beaker was completely filled with fluorinert and a droplet of dyed water was carefully placed on the surface of fluorinert. As water is lighter, the droplet remained at the surface of fluorinert. Then, the beaker was covered with a dry slab of treated PDMS (as shown in Figure 1), making contact with both water and fluorinert. The contact angle shown in figure 1 was then measured using the ImageJ software.

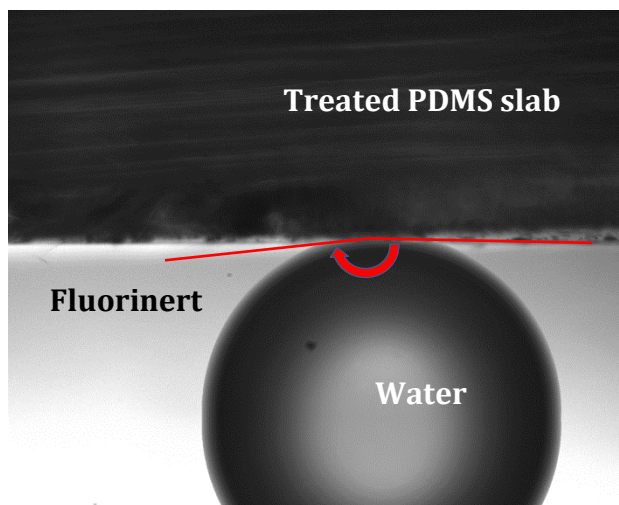


Figure 1. A droplet of dyed water in fluorinert, in contact with a treated PDMS slab. The indicated angle was measured with ImageJ software.

Then, the measured contact angle was plotted against the volumetric concentration of TCP-silane in ethanol (ratio of TCP-silane volume to ethanol volume, v_s/v_e), as depicted in figure 2. This plot was used to determine the optimal concentration of TCP-silane in ethanol for the silanization process. The most suitable concentration was considered to be the one for which the contact angle was the largest.

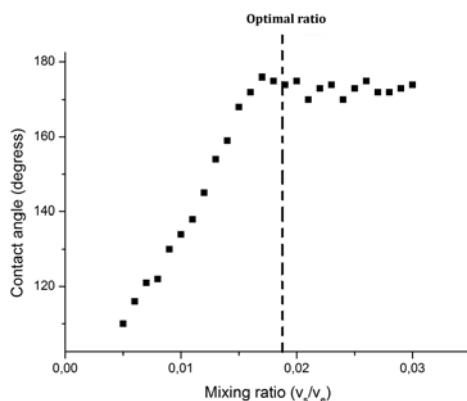


Figure 2. Dyed water contact angle on a PDMS surface silanized with different concentrations of TCP-silane in ethanol.

The concentration that was used in every silanization process was $0.018 v_s/v_e$, which made the PDMS surface more hydrophobic in the presence of fluorinert. From now on, the solution of TCP-silane in ethanol is referred to as “silane”.

We tried two different ways of introducing silane into the micro-model: i) direct injection of silane liquid and ii) injection of silane vapors and subsequent condensation. For the direct injection of silane, one milliliter of the solution was taken out of the beaker with the use of a Terumo 1-ml syringe with a needle. Then, the needle was removed and a filter was placed at the tip of the syringe. The filter was a Millex filter, with a pore size of 0.45 microns. It was used in order to hold back any micro particles in the solution. The syringe was then put in a syringe pump, and the solution was pumped through the filter into the initially empty flow network, at a rate of $3\mu\text{l}/\text{minute}$. The injection and flow of silane through the micro-model was continued for half an hour. Then, the model was put in an oven to dry and be ready for two-phase flow experiments.

For the injection of silane vapors, a needle was punched into the rubber cap of the beaker containing silane. We made sure that the needle tip would stop in the beaker headspace and would not contact the solution. The other end of the needle was connected by a very short tube to the inlet of the micro-model. The beaker was then placed on a hot plate at 1150 Celsius; silane vapor started to flow into the pore network. After some time, it was observed that a mixture of gas and liquid formed in the network and then flew through it. This process was continued for half an hour, and then the micro-model was detached from the tubing and put into an oven to dry out. Results of these two silanization methods are discussed in the next section.

5.3 Post-treatment observations

The injection of silane liquid caused the hydrophobicity of the material, in the presence of fluorinert, to increase significantly. This can be seen in figure 3, where two pictures of the network before and after silanization are shown. In dark shade is water dyed with ink, while the colorless wetting phase is fluorinert FC-43. Before silanization, the material was only weakly hydrophobic, and not uniformly. The contact angle for water was measured with the ImageJ software, with an accuracy of around 4°. It was found to vary from 90° to 120°; so, it was weakly hydrophobic. After treatment, the material became strongly hydrophobic. Most contact angles were found to vary between 172° and 180°; in some areas, even as low as 165°. So, although the micro-model had become strongly hydrophobic, the effect was not uniform.

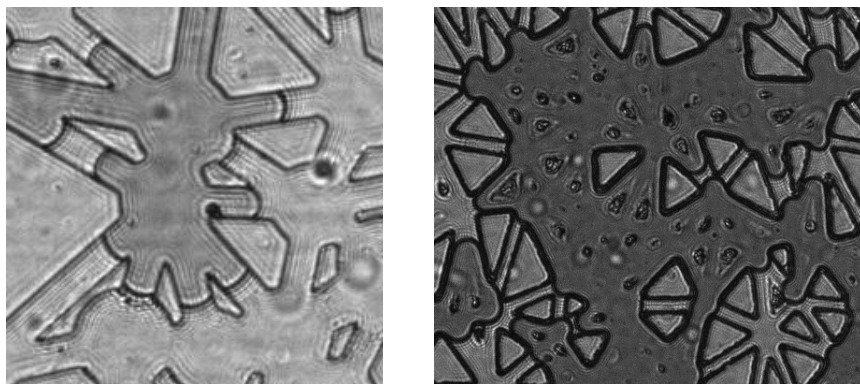


Figure 3. Results of treatment of micro-model with silane liquid: before treatment (left), and after treatment (right). Pores are filled with the non-wetting phase (darker regions) and the wetting phase (lighter regions).

So, this method of treatment of PDMS was not considered to be successful in making it as hydrophobic as needed. Moreover, the interaction of the solution with (tiny amounts) of moisture present either in ethanol, or in the flow network, produced some “flakes” within the micro-model. These flakes, which had varied in size from 2 to 15 microns, could block the channels of the flow network, rendering the micro-model useless. Another problem was that we noted that the surface of the flow network in some areas seemed to be corroded. The reason for this corrosion is discussed shortly. The corrosion would roughen the PDMS surface and locally change the properties of the flow network, and introduce unknown effects in the experiments. The presence of flakes and some corroded areas can be seen in figure 4.

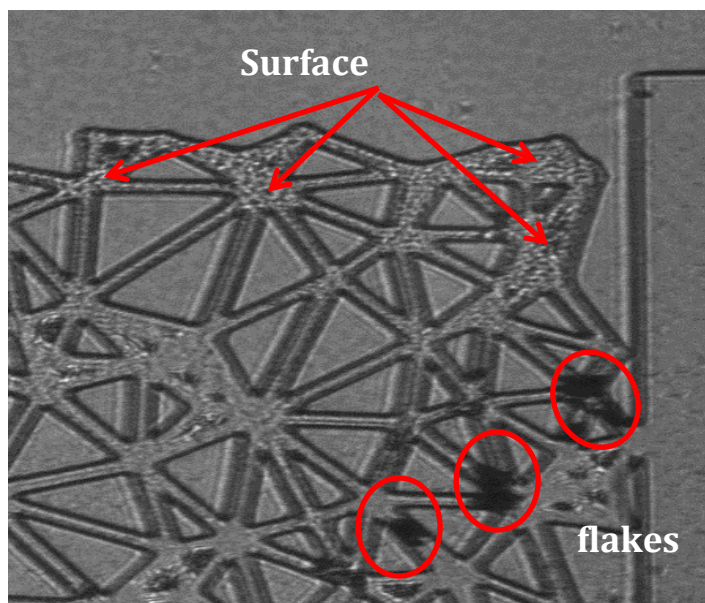


Figure 4. Part of the flow network with flakes blocking the flow path. The flakes are marked with a red circle. The corroded areas of the material are indicated with arrows.

Our second silanization method, namely the injection of silane vapors, gave excellent results. This process resulted in a strongly and uniformly hydrophobic PDMS surface, with contact angle varying between 1760 and 1800. This hydrophobic behavior was uniform throughout the whole network, and remained unchanged with time even after months of use. We still found a few flakes in the network, but their sizes were much

smaller than in the first method, and we did not observe any blocking of the network. Also, there was no corrosion on the surface of the flow network.

5.4 Discussion

As mentioned before, the volumetric ratio of TCP-silane in ethanol was chosen to be 0.018 v_s/v_e . We found that higher concentrations would create more flakes in the flow network, in the case of direct injection of liquid silane into the micro-model.

A question that came up was why the silanization with silane vapor created much fewer flakes, if any, and there was no corrosion of the surface, as was the case when we silanized with silane liquid. In order to give an answer to this question, we explain the reactions occurring in the two silanization processes.

In the case of silanization of PDMS with silane liquids, four consecutive reactions occur [4],[5], which are explained below.

First, TCP-silane reacts with the alcohol producing alcoxysilane and HCl:



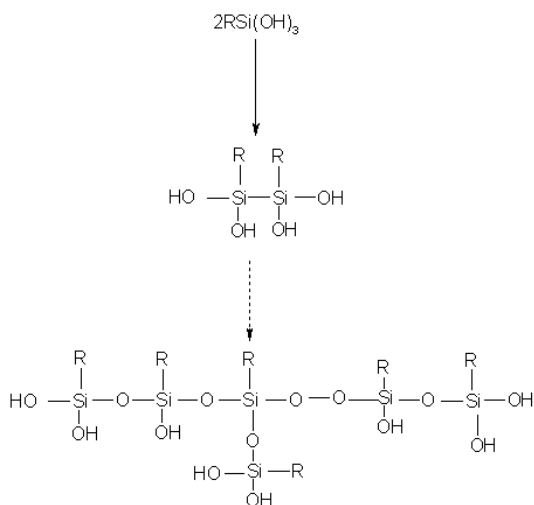
Hydrogen chloride, which is in gaseous state when produced, forms hydrochloric acid when it comes in contact with traces of water in ethanol, water absorbed by the PDMS surface, or the air humidity inside the micro-model. Hydrochloric acid is highly corrosive. This explains the corrosion on the PDMS surface when silane liquid is injected into the micro-model.

a) A second reaction takes place between the alcoxysilane and the water present in ethanol or in the micro-model. This reaction is called hydrolysis and creates silanol groups and ethanol:



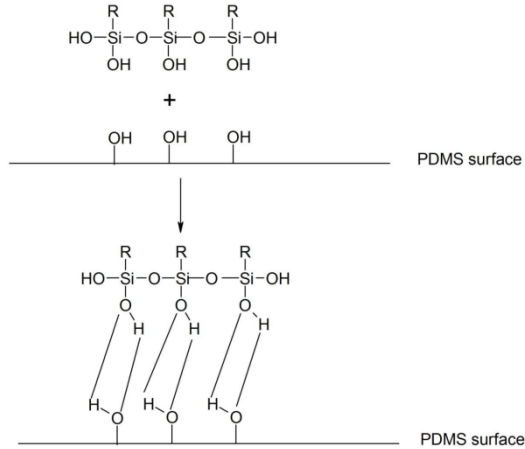
The silanol group is also shown as $\text{RSi}(\text{OH})_3$, where the tail group R denotes $\text{CF}_3(\text{CF}_2)\text{CH}_2\text{CH}_2$.

b) The produced silanol groups bond with each other to form siloxane polymers (poly-silanol, involving Si-O-Si); this is called alcoholic condensation. An example of simplified forms of these groups is the pentamer shown below:



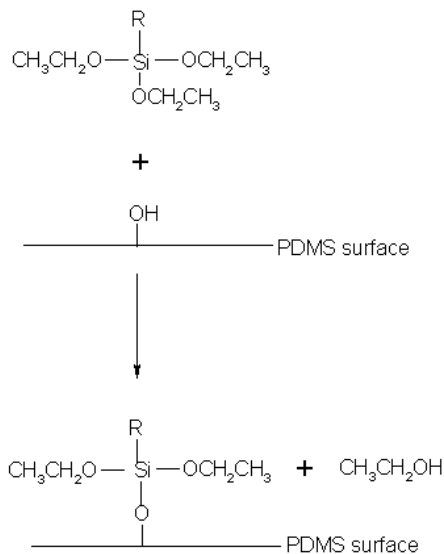
The actual structures of molecules may be far more complex since the tri-functionality of silane (three functional groups of -OH) can lead to many possible structures. The molecular size increases as a result of this alcoholic condensation of silano-triols (three -OH molecules) and oligomeric silanes. Also, the solubility decreases with increase in the molecular weight. Oligomers heavier than a trimer do not remain dissolved but form precipitates in the solution [10]. They are responsible for the flakes (of about 2-15 microns) that are formed in the flow network.

c) Finally, hydrogen bonding occurs between silano-triols produced in step (b) and hydroxyls on the PDMS surface:



The result of these reactions is the formation of a monolayer of silane. However, the quality of this monolayer is very sensitive to the amount of water in the system. If there is not enough water, only the monolayer is not formed everywhere; some parts of PDMS surface remain uncovered. If there is too much water, the organosilanes may polymerize (to form precipitates) and the monolayer is not formed at all. This can result in heterogeneous surface properties (see [4]-[8]), which explains the variation of the contact angle in the flow network.

In our second treatment method, namely the injection of silane vapors, the PDMS surface modification occurs under anhydrous conditions (as there is no water present). The condensed silane vapor reacts with the PDMS surface and forms a monolayer of silane due to chemisorption with the following mechanism:



Extended reaction time (4 – 12 hours) and elevated temperatures (50 – 120 °C) [9] are typically involved. The heat treatment of treated PDMS is necessary to prevent formation of flakes. This is because the reactivity of the above reaction is lower than the alcoholic condensation of silanol groups (explained as reaction (b) and (c) above). Heating accelerates the chemisorption instead of reactions (b) and (c), and thus polymerization does not occur. In our initial attempts, a small number of flakes was produced because the heating was not done long enough. Corrosion of the PDMS did not occur because reaction (a) took place under anhydrous conditions, so there was no HCl in the vapors that were injected into the flow network.

The hydrophobicity of the tail group ($\text{R}=\text{CF}_3(\text{CF}_2)_5\text{CH}_2\text{CH}_2$) along with the length of the molecule and tightness of the layer packing have a significant role in the overall hydrophobicity of the self-assembled monolayer. Increased contact of the fluids flowing in the flow network with the tail group and reduced contact with the hydroxylated PDMS surface result in a more hydrophobic surface. Indeed, hydrophobicity is not only dependent on the length of the molecule, but also on the density of the monolayer packing. Of great importance is also the tilt of the angles on the hydrocarbon chain [10]. With the use of heat, a closely packed monolayer is achieved, as well as a better surface coverage, which leads to a more hydrophobic surface.

5.5 Summary and conclusion

PDMS is a popular material for constructing hydrophilic micro-models used in two-phase flow studies. However, its wettability is not stable in time. We have developed a novel silanization procedure for making the flow network of a PDMS micro-model uniformly, stably, and strongly hydrophobic. This is done through delivering the silane into the micro-model in vapor form instead of liquid. Silane vapors injected into the micro-model condense on the PDMS surface of the flow network and form a monolayer of organosilane. This process causes PDMS to become stably and uniformly hydrophobic. Contact angles were found to vary between 176 and 180 degrees. Moreover, contrary to the use of the liquid silane, no flakes were produced in the process. Also, the surface of PDMS remained unharmed from corrosion, since no HCl was produced in the vapor treatment method.

Acknowledgements

The authors are members of the International Research Training Group NUPUS, financed by the German Research Foundation (DFG) and Netherlands Organization for Scientific Research (NWO).

5.6 References

- [1] Karadimitriou, N.K., and Hassanizadeh, S. M., 2012, A Review of Micro-models and their Use in Two-Phase Flow Studies, *Vadose Zone Journal*, doi:10.2136/vzj2011.0072.
- [2] Zhou, J., Ellis, A. V., Voeckler, N. H., (2010), Recent developments in PDMS surface modification for microfluidic devices, *Electrophoresis*, **31**, pp. 2-16.
- [3] Karadimitriou, N. K., Joekar-Niasar, V., Hassanizadeh, S. M., Kleingeld, P. J., Pyrak-Nolte, L. J., 2012, A novel deep reactive ion etched (DRIE) glass micro-model for two-phase flow experiments, *Lab on a Chip*, DOI:10.1039/C2LC40530J
- [4] Arkles, B., 2006, Hydrophobicity, hydrophilicity and silanes: water, water everywhere is the refrain from the rhyme of the ancient mariner and a concern of every modern coatings technologist, *Paints and Coatings Industry*, October 2006 issue.
- [5] <http://www.gelest.com/goods/pdf/faq/question%207.pdf>

[6] Glass, N. R., Tjeung, R., Chan, P., Yeo, L. Y., and Friend, J. R., 2011, Organosilane deposition for microfluidic applications, *BIOMICROFLUIDICS*, **5**, 036501.

[7] Ulman, A., 1996, Formation and Structure of Self – Assembled Monolayers, *Chem. Rev.*, **96**, pp. 1533 – 1554.

[8] Peroz, C., Reboud, V., and Sotomayor Torres, C. M., 2012, Nanoimprint technologies, in Nanofabrication, Techniques and Principles, Maria Stepanova, Steven Dew (Eds.), Wien, Springer – Verlag, pp. 123.

[9] Arkles, B., 1977, Tailoring surfaces with Silanes, *CHEMTECH*, **7**, pp. 766 – 778.

[10] Hatsuo Ishida, Controlled Interphases in Glass Fiber and Particulate Reinforced Polymer: Structure of Silane Cupling Agents in Solutions and on Substrates and on Substrates in G. Akovali (ed.), *The Interfacial Interactions in Polymeric Composites*, 169-199, 1993 Kluwer Academic Publishers. Printed in the Netherlands.

Karadimitriou, N. K., Musterd, M., Kleingeld, P. J., Kreutzer, M. T., Hassanizadeh, S. M., Joekar-Niasar, V., 2013, "On the fabrication of PDMS micro-models by rapid prototyping and their use in two-phase flow studies", *Water Resources Research*, DOI: 10.1002/wrcr.20196 .

Chapter 6

On the fabrication of PDMS micro-models by rapid prototyping, and their use in two-phase flow studies

Abstract

Micro-models have been increasingly employed in various ways in porous media research, to study the pore-scale behavior of fluids. Micro-models have proven to be a valuable tool by allowing the observation of flow and transport at the micron scale in chemical, biological, and physical applications. They have helped to improve our insight of flow and transport phenomena at both micro- and macro-scales.

Up to now, most micro-models that have been used to study flow and transport in porous media were small square or nearly square domains. In this work, an elongated PDMS micro-model, bearing a flow network with dimensions $5 \times 30 \text{ mm}^2$ was manufactured. The pore network was designed such that the REV size was around $5 \times 7 \text{ mm}^2$. So, our flow network was considered to be nearly four times the REV size. Using such micro-models, we established that the inclusion of interfacial area between the wetting and the non-wetting fluids models the hysteretic relationship between capillary pressure and saturation in porous media.

In this paper, we first present the procedure for manufacturing PDMS micro-models with the use of soft lithography. Then, we describe an innovative and novel optical setup that allows the real-time visualization of elongated samples. Finally, we present the results obtained by quasi-static, two-phase flow experiments.

6.1 Introduction

In porous media research, micro-models have been increasingly employed in various ways, to study the pore-scale behavior of fluids. Micro-models have proven to be a valuable tool by allowing the observation of flow and transport at the micron scale in

chemical, biological, and physical applications. They have helped to improve our insight of flow and transport phenomena at both micro- and macro-scales.

An overview of various issues related to micro-models, such as network generation, fabrication materials and methods, visualization methods, and different applications, was given in Karadimitriou and Hassanizadeh (2012). They defined a micro-model as “an artificial representation of a porous medium, made of a transparent material. This fluidic device bears a flow-network, with features on the micro-scale, and an overall size of up to a few centimeters.”

Micro-models have been mostly used in studying displacements of two immiscible fluid phases in porous media (Chang et al., 2009; Corapcioglu et al., 2009; Avraam et al., 1994; Baouab et al., 2007, NagaSiva et al., 2011). Processes of drainage and imbibition, as well as the mechanisms that dominate them, like viscous or capillary fingering, snap-off, etc., have been studied using micro-models (Zhang et al. 2011; Ferer et al., 2004; Grate et al., 2010; Gutiérrez et al., 2008; Hug et al., 2003; Huh et al., 2007).

Recently, two-phase flow studies were performed using photo-resist micro-models that had flow patterns based on stratified percolation (Cheng, 2002; Pyrak-Nolte et al., 2008; Cheng et al., 2004; Chen et al., 2007; Liu et al., 2011). In these studies, distributions of the two phases in the flow network during quasi-static drainage and imbibition were visualized. Phase saturation and interfacial area could be determined using image processing and relationship between phase saturation, capillary pressure, and specific interfacial area was investigated.

Micro-models have been made of different materials with their advantages and disadvantages. A detailed account of these issues can be found in Karadimitriou and Hassanizadeh (2012). One important property of micro-models is wettability. Glass or quartz micro-models are uniformly and stably hydrophilic, which is a major advantage. Also, vertical pore walls can be created (which is usually desired) using deep reactive-ion etching method. But, then the pores cannot be made more than 30 micron deep (Ohara et al., Yeom et al., 2005 2010; Karadimitriou et al., 2012). Deeper pores can be created in glass using chemical etching (Johnston, 1962; Wegner and Christie, 1983; McKellar and Wardlaw, 1982; Er et al., 2010), but then pore walls will be curved at the bottom, as the erosion process is highly isotropic. Silicon micro-models have the disadvantage that the pore walls are made of two materials. The pore network is created in silicon but, because silicon is not transparent, the micro-model is usually covered by a glass plate (NagaSiva et al., 2011; Baumann and Werth, 2004; Willingham et al., 2008). This results in a mixed wettability. Photo-resist micro-models have the advantage that they are relatively easy to make, but only in a special clean room

environment. Also, they are sensitive to ultra violet light; so that nitrogen is produced under regular light, which eventually destroys the network. Moreover, photo-resist micro-models gradually degenerate after a number of uses.

A transparent material often used for micro-fluidic devices is Poly-Di-Methyl-Siloxane (PDMS). PDMS is a viscoelastic, silicon-based organic polymer. It is optically transparent, inert, non-toxic, and non-flammable. PDMS is hydrophobic in its natural state. But, this hydrophobicity is variable in time and space (Murakami et al., 1998; Fritz and Owen, 1995). This is a major disadvantage. However, we have developed a treatment process in order to make PDMS surface wettability uniform and stable. A solution of Trichloro-perfluoro-octyl-silane (silane in short) in 96%-pure ethanol was injected through a filter into the micro-model, so as to change its surface chemistry and make it uniformly and strongly hydrophobic.

PDMS is a material which is easy and safe to use in a normal laboratory environment. PDMS micro-models are relatively cheap to make and are reusable almost without limit. Finally, the geometrical characteristics of the features of the micro-model can easily be very well controlled, as it will be shown later in this paper.

Up to now, most micro-models that have been used to study flow and transport in porous media were small, (nearly) square domains, so that they could be visualized under a microscope. Therefore, one may interpret them as being one Representative Elementary Volume (REV). An REV is the volume of a homogeneous porous medium above which the system properties are insensitive to the averaging domain size. Often, only one average value for porosity, saturation, or capillary pressure is given for the whole micro-model. In the present work, an elongated micro-model with dimensions $5 \times 30 \text{ mm}^2$ was manufactured. The pore network was designed such that the REV size was around $5 \times 7 \text{ mm}^2$ (the determination of REV size is explained in Sec. 2.2 below). So, our micro-model was considered to be nearly four times the REV size. A long micro-model is similar to a column experiment; one can determine gradients in saturation, capillary pressure, and interfacial area. But, then a microscope is not suitable for real-time visualization of a long micro-model under transient flow conditions. Therefore, we have designed and constructed an innovative and novel optical setup using digital cameras, for observing and imaging fluids distribution along the whole model at any given time.

Through performing experiments in such micro-models, we investigated the role of fluid-fluid interfaces in the hysteretic relationship between capillary pressure and saturation in porous media. With this work, we provide experimental evidence to support the theories which propose that for a complete description of two- or multi-

phase flow, interfacial area should be included as one of the state variables, in addition to pressure and saturation (Hassanizadeh and Gray, 1990, 1993a, 1993b).

In this paper, we first present the procedure for manufacturing PDMS micro-models with the use of soft lithography (Xia and Whitesides, 1998; Duffy et al., 1998). Then, we describe our visualization setup that allowed the real-time visualization of elongated samples. Finally, we present the results obtained from quasi-static, two-phase flow experiments.

6.2 Construction of the Micro-model

6.2.1 Main steps

A micro-model is commonly composed of two slabs. One slab contains the pore network and the other slab, which is featureless, is used as a cover. This creates a closed network of pores. The manufacturing process of our PDMS micro-model consisted of a number of steps, which are briefly mentioned here and explained in detail in the following subsections. First, the flow network was designed, as well as the inlet and the outlet areas. This design was transferred to a mask. The mask was a plastic transparency sheet with the flow network and reservoirs being transparent and in their actual dimensions, and the solid phase being black. It was used in the process of creating a patterned silicon wafer that would serve as a mold. This wafer, usually called the “master”, was used for the preparation of a PDMS slab with the network and the two reservoirs formed in it. Another PDMS slab without any features was then used to cover the micro-model. Finally, the micro-model was treated in order to acquire a uniform wettability. These manufacturing steps will be explained in detail shortly.

6.2.2 Design of the flow network and the reservoirs.

An elongated pore network with an overall size of 5 x 30 mm² was designed. The pore network was represented by an assembly of pore bodies and pore throats with a wide distribution of sizes. The network topology was generated using Delaunay triangulation, which is considered to provide a good representation of real porous media (Heiba et al., 1992). In the Delaunay triangulation, points are connected to their neighbors by non-intersecting bonds. Connected points form triangles that are as equilateral as possible. The co-ordinates of the triangulation points were generated by the use of a fixed routine in MatLab. These points were considered to be the centers of pore bodies. The number of pore bodies directly connected to a pore body, which is

usually called the co-ordination number, was not constant throughout the whole network; it varied from 4 to 6 for the 2000-points network, from 5 to 8 for the 3000-points network, and from 6 to 9 for the 6000-points network.

Pore bodies were cylinders and the pore throats were parallelepipeds. In planar view, pore bodies were circular while pore throats were rectangular. They had the same depth and had a rectangular cross section.

Pore body sizes were assigned from a truncated log-normal distribution. The length of a pore throat was defined as the distance between two connected pore bodies, minus the sum of their radii. The width of a pore throat was assigned by using the following set of equations (Joekar-Niasar et al., 2010a):

$$r_{ij} = \rho_i \rho_j (\rho_i^{1/n} + \rho_j^{1/n})^{-n}, n > 0, r_{ij} = w_{ij} / d, \tilde{R}_i = R_i / d, \rho_i = \frac{\tilde{R}_i \sin(\pi / 4)}{(1 - \tilde{R}_i \cos(\pi / 4))^n} \quad (1)$$

where R_i is the radius of pore body i , w_{ij} is the width of the pore throat ij , and d is the distance between the two centers. In this formula, n is an extra tuning parameter for specifying the pore throat size. It also makes sure that the width of the pore throat would always be smaller than the diameter of the smallest pore body that it is connected to.

In figure 1, the whole network as well as a magnified image of part of it can be seen. . The pore network was designed such that the REV size was around $5 \times 7 \text{ mm}^2$. So, our micro-model was considered to be nearly four times the REV size. The REV size was determined through pore-network modeling as follows. Simulations were run for the whole extent of the micro-model. Then, capillary pressure-saturation curves under quasi-static conditions were obtained for a sequence of gradually increasing sub-domain sizes and compared to each other. The subdomain size beyond which the capillary pressure-saturation curve remained unchanged was considered to be the REV size.

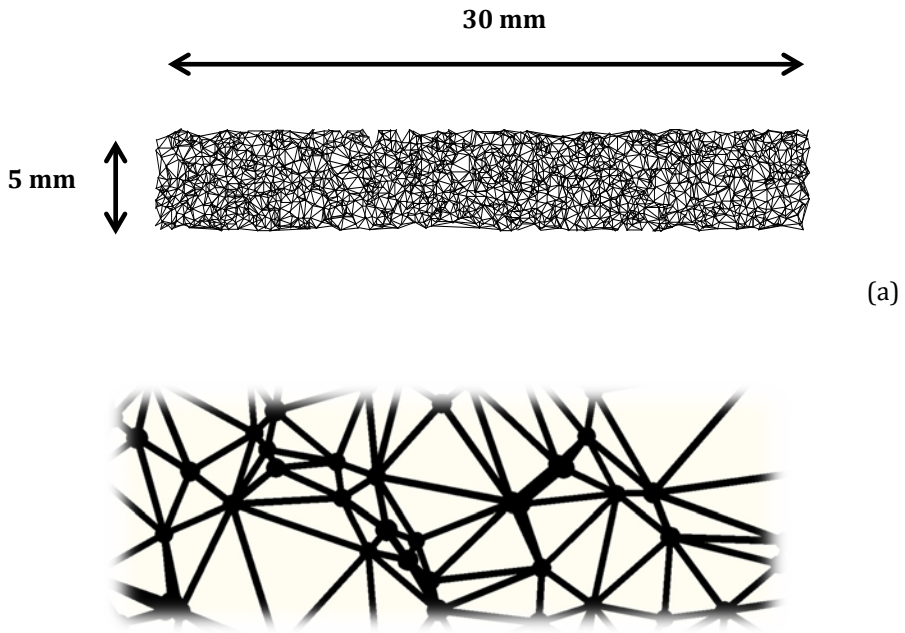


Figure 1. (a) Image of the pore-network with 2000 pore bodies and 6000 pore (b) coats and a mean pore size of $40\ \mu\text{m}$. The void space is shown in black. (b) Zoomed-in image of a part of the network.

For the introduction of each phase into the flow network, two reservoirs, one for each phase, were designed at the beginning and the end of the flow network. Special attention was paid to the design of the reservoirs. They were much bigger than the size of a single pore body, whereas their height was the same as the rest of the model. This created a very high ratio between the width and the height of the reservoir. This consequently led to the collapse of the top surface and blocking of the flow in an earlier design of the micro-model. In fact, Bietsch and Michel (2000) have shown that there is a maximum ratio between the distance separating two sequential features in PDMS, and their height, as well as between the void space between these features and their own volume. So, pillars were added to support the reservoir's top surface and prevent it from collapsing. In figure 2, the reservoir can be seen, where the void space is shown in black and the PDMS pillars are in white. The large difference in the size of pores of the micro-model and the reservoir are also evident in this figure.

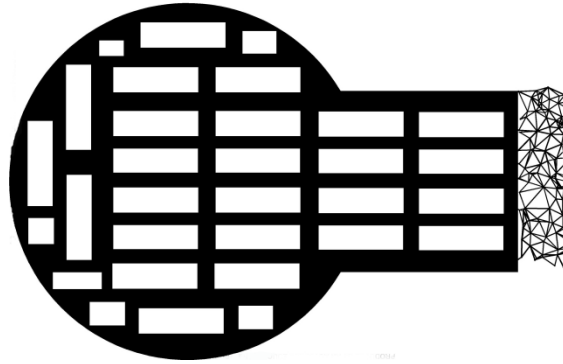


Figure 2. The schematic of the reservoir with the supporting pillars. The void space is shown in black and pillars in white.

The Autocad drawing of the flow network with the two reservoirs, was then sent to the CAD/Art Company (Oregon, U.S.A.), in order to create a mask at a resolution of 20,000 dots per inch.

6.2.3 Preparation of a patterned silicon wafer with photo-lithography.

A necessary step in the manufacturing process of PDMS micro-models was the preparation of a silicon wafer that bore the features of the micro-model (flow network and reservoirs) and would be used as a mold. This wafer is usually called the “master”. For this purpose, first, the silicon wafer was put in an oven for 15 minutes, at 120 degrees Celsius. This was done in order to remove any moisture from the surface of the wafer that might harm the adhesion process later on in the process. The wafer was then spin coated with SU8 2025 photo-resist. It was put on a spin-coater and a small portion of photo-resist was poured on it. The choice of rotation speed and time depends on the desired depth of the photo-resist layer, which had to be the same as the depth of the flow network.. Calibration curves were provided by the supplier of the photo-resist. For example, to achieve a thickness of 40 μm , the wafer was put to spin for 90 seconds at a rotation rate of 2000 rounds per minute. Then, the wafer was put on a hotplate and was soft-baked at 65 degrees Celsius for 3 minutes, and immediately after that at 95 degrees Celsius for 6 minutes. In this way, the photo-resist became harder and degassed, photo-sensitive, but not yet solid. Right after this step, the wafer and the mask (which contained the flow network and the two reservoirs), were put under an aligner, where they were illuminated by ultra-violet light. Parts of the photo-resist-

coated surface of the wafer that were visible through the mask open areas were exposed to the light. Depending on the height of the photo-resist layer, the energy level of the light beam had to be tuned to penetrate the thickness of the photo-resist layer, according to the specifications of the photo-resist supplier. As soon as this step was finished, the wafer was hard baked on a hot plate at 65 degrees Celsius for 1 minute and immediately after that at 95 degrees Celsius for 6 minutes to allow cross-linking of the exposed photo-resist. The wafer was then put in a glass petri dish and was covered with Mr-dev 600 developer liquid (micro resist technology GmbH). By gently moving the petri dish with the wafer in it for approximately ten minutes, the photo-resist areas that were not exposed to the ultra-violet light were dissolved. This led to the features of the network and the reservoir to be formed on the wafer.

In this way, a wafer was made that could be used as a mold to make replicates of the same network (as explained in the next section). This part of the process of the manufacturing of PDMS requires a clean room environment. The whole operation was performed in the class-10000 clean room facility of the Kavli Institute of Nanoscience Delft. The rest of the process was carried out in our regular laboratory.

In our regular laboratory, the master was then put in a vacuum chamber and was silanized. A droplet of silane was put in the vacuum chamber; it evaporated and formed a monolayer on the surface of the master that prevented the PDMS from adhering to the master's surface. In this way, PDMS could be easily peeled off the wafer, without leaving any residues. If an unsilanized master is used, then the photo-resist features on the master would be peeled off together with the PDMS slab.

6.2.4 Fabrication of a PDMS micro-model

The raw materials that were needed to make a PDMS micro-model were a silicon elastomer base (Dow Corning Sylgard 184), and the corresponding elastomer curing agent. The silicon elastomer base, which was in liquid state, was mixed with the elastomer curing agent at a mass ratio of 10:1. The two components were mixed thoroughly by stirring them in a cup for a few minutes. The quantity of PDMS that was used, determined the thickness of the slabs created. In our work, typical values for the weights of the two components were 50 gr and 5gr, respectively. The resulting amount of PDMS would make sure that the PDMS slabs were thick enough to create a relatively rigid micro-model. Also, it was thin enough for the inlet and outlet holes to be punched without creating cracks in the material.

After mixing, the mixture was full of trapped air bubbles. So, the cups with the mixture were put into a vacuum chamber to remove the trapped air. It was important not to use the same vacuum chamber that was used for the silanization of the master, as it was already contaminated with silane. We released the vacuum suction periodically for two reasons. First, the degassing of the material was faster in the first five minutes of the process, and then it became slow. Second, the rising trapped air would raise the level of the liquid in the cup. If the vacuum was not released, it would have spilled over the cup. After degassing, the content of one cup was poured over the master silicon wafer in a petri dish, with the design of the micro-model pointing upward. The material had to be poured as slowly as possible in order to avoid having too much trapped air. It was also important not to pour PDMS directly on top of the features of the master wafer, but on the blank surface of the wafer, allowing the liquid PDMS to flow slowly into and over the flow network. Otherwise, there was a chance that dust particles become trapped in the main structure of the flow network, resulting in a defective micro-model.

Next, a layer of PDMS was poured in another petri dish to form a plain slab without any features. This PDMS slab was used as the sealing layer of the micro-model. Then, the two petri dishes were put in the vacuum chamber to remove any trapped air.

After degassing, the two petri dishes were put in an oven at 68 degrees for at least two hours in order to cure and solidify liquid PDMS. In general, various combinations of temperature and curing time can be employed. The limit combinations are: more than 48 hours in ambient temperature and 10 minutes at 200 degrees. For the latter case, a glass petri dish should be used, as a plastic one will deform because of the heat. However, longer curing times and less curing temperature is favorable to avoid creating stresses in the material. Ambient temperature is not a very good option as it takes too much time, and the material may be exposed to dust particles that may stick on its surface before it solidifies.

After curing, the PDMS slabs were allowed to reach ambient temperature before bonding them. In this way permanent distortions because of excessive stress on the material could be avoided.

The PDMS slab had to be separated from the silicon wafer in a way that it would not destroy the wafer's features. First, with the use of a scalpel or sharp pointy knife, PDMS was cut around the wafer's edges and was gently removed from the petri-dish. The wafer was gently separated from PDMS. It was essential that this procedure was as slow as possible, so that the features on the wafer would not be detached from the wafer. The petri dish that had only plain PDMS slab was much easier to handle. One just had to cut the edges and remove the PDMS slice from the petri dish.

Microscope glass slides (Menzel-Glaser) with dimensions of 76 mm x 26 mm were used as guides to cut the parts of PDMS slab containing the flow network and the two reservoirs. Pieces of the same size were also cut from the plain PDMS slab, which was to be used for sealing the micro-models. Inlet and outlet holes were punched into the middle of the reservoir areas of the slab with features using a leather hole punching tool.

The two PDMS slabs had to be put together and bonded. The plain PDMS slab was placed in such a way that its surface that was in contact with the petri dish would form the inner side of the micro-model. This ensured that the surface would be smooth and free of dust particles.

There are various bonding techniques (Eddings et al., 2008). These techniques involve oxygen plasma (Duffy et al., 1998, 1999), corona discharge (Haubert et al., 2006), partial curing of PDMS in an oven (Go and Shoji, 2004; Eddings and Gale, 2006), use of a curing agent (Samel et al., 2007), and stamp/stick (Satyanarayana et al., 2005). We tried two techniques: oxygen plasma and corona discharge. A discussion of these bonding methods and related issues is given below.

For the oxygen plasma bonding, an Expanded Tabletop Plasma Cleaner (Sigma-Aldrich) was used. Typical values for control parameters of the oxygen cleaner were a vacuum pressure of 0.3-0.4 mbar, output power of 30 W, and exposure time of up to three minutes.

There is no known recipe for an effective use of the corona treater. For this reason, a number of measurements were carried out to determine the optimal exposure time and distance between the specimen and the treater. In this case, optimal meant that after bonding, the micro-model would withstand the highest possible applied pressure without any leakage. It was observed that the tolerance to applied pressures was related to the contact angle of a droplet of water on top of PDMS after treatment, in air. The lowest contact angle seemed to create a bonding with the maximum tolerance to the applied pressure (see figure 3). A typical value of 15 kV of voltage was used. It was found that if the distance between the specimen and the treater was less than 4 cm, the bonding effect was more or less insensitive to the distance. For a distance of 1.5 cm, different exposure times were tested and the contact angle was measured. Results of the measured contact angle for different exposure times are shown in figure 4.

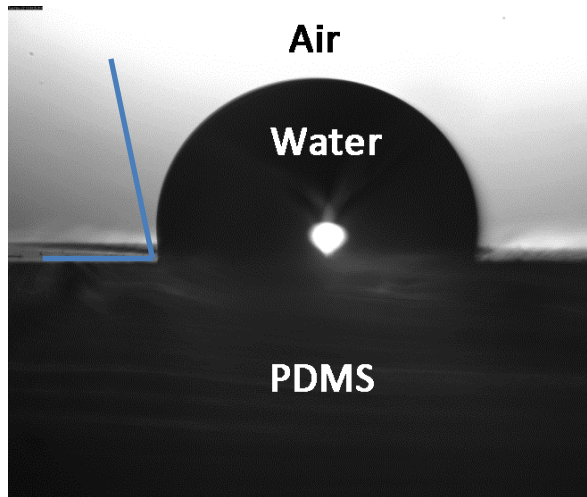


Figure 3. A water droplet in contact with PDMS and surrounded by air. Contact angle between air and PDMS is shown.

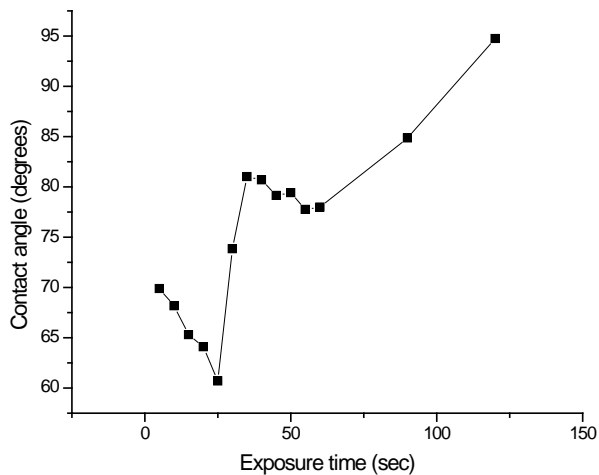


Figure 4. The air contact angle versus time of exposure to corona discharge. Note that because the contact angle is measured in the air, a contact angle of zero means that the surface is completely hydrophobic.

These results show that the smallest contact angle is achieved at an exposure time of 25 second. So, this was the exposure time used in our treatments of micro-models.

In both cases of oxygen plasma or corona discharge treatment, after exposure, the two parts of the micro-model were put together and a gentle mechanical pressure was applied to them until chemical bonding was achieved. Special attention was paid to removing the air trapped between the contacting surfaces of the two slides. This was achieved simply by applying some extra pressure on the relevant areas and expelling the air.

In order to make the micro-model more rigid, using the same bonding procedure, a microscope glass slide (Menzel-Glaser) was bonded to the side of the micro-model that did not have inlet and outlet holes.

For the bonding to mature, the model was left to rest for a few hours or, even better, put in the oven overnight at a moderate temperature (± 68 degrees). This step was particularly important for the corona discharge bonding. Otherwise, bonding could be reversed.

6.3 Issues with PDMS models

In this section we will explain how to solve a number of known issues related to the use of PDMS material in two-phase flow experiments.

6.3.1 Wettability issues

One of the most important properties of a micro-model is the wettability of its material. In two-phase flow studies, it is very important to have a uniform and stable wettability throughout its flow network. In our experiments, it did not matter whether the micro-model was hydrophobic or hydrophilic, as long as it remained uniformly and permanently in the same state. Hereunder, we describe the wettability problems of PDMS micro-models and explain how we achieved stable and uniform wettability properties.

PDMS is hydrophobic in its natural state. But its wettability properties change during, and as a result of, the bonding process. For example, the oxygen plasma technique, introduced by Duffy et al. (1998), causes PDMS to become hydrophilic. Duffy et al. tried to enhance the bonding strength by activating layers of cross-linked PDMS, through surface oxidation. It is believed that surface oxidation exposes silanol groups (Si-OH) at the surface of the PDMS layers and, when brought together, they form covalent siloxane bonds (Si-O-Si). This process makes PDMS even more hydrophilic. However, the material returns to its original state when exposed to the atmosphere for some time (a few minutes to a few hours) (Bodas and Khan-Malek, 2007). The corona discharge

technique has an opposite effect, compared to oxygen plasma treatment. It makes the material more hydrophobic than its natural state. But also in this case, PDMS returns to its original hydrophobicity level. Our PDMS micro-models, which were bonded by the oxygen plasma treatment technique, originally had a hydrophilic behavior, as expected. However, within a relatively short time (around 12 hours after bonding), their wettability started to change gradually. After roughly three days, the material was hydrophobic with non-uniform wettability. In figure 5, a magnified part of the network filled by two immiscible fluids can be seen. The snapshot was taken at equilibrium, so there is no further movement of the fluid-fluid interfaces. It is evident that there is mixed wettability even within a very small area. The contact angle between the phases was measured under static conditions with ImageJ software, and was found to vary from 80 to 60 degrees. Even days after bonding, in some parts of the network, a mixed wettable condition was visible. This showed that the wettability of PDMS is a function of time, and is dependent on the initial wettability condition.

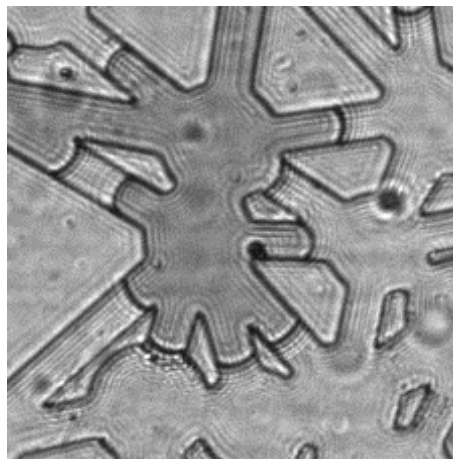


Figure 5. Snapshot taken from a part of the flow network filled with two immiscible liquids. In dark color is the non-wetting phase. The wetting phase is colorless. The contact angles varied from 80 to 60 degrees.

Similar observations were made after treating the micro-model with corona discharge bonding, where the material was more hydrophobic than in its natural state. The wettability problem was solved by employing and improving a silanization technique. In this technique, a solution of silane in 96%-pure ethanol was injected through a filter. The pores of the filter were 0.45 microns wide. In this way, silicon,

which a by-product of the reaction of TCP with water in ethanol and in the air, was kept out of the flow network, preventing blockage.

A total volume of 1 ml of a 0.018 v/v solution was introduced into the micro-model at a pumping rate of 3 $\mu\text{l}/\text{min}$. Then, the model was put in an oven at 68 degrees Celsius overnight to dry out. After that, the micro-model was ready for use.

After this silanization procedure, the micro-model network was uniformly hydrophobic everywhere. The phases used in this study were fluorinert as the wetting phase, and water dyed with ink as the non-wetting one. Fluorinert is a colorless (refraction index, $n=1.291$), fluorine based, and inert liquid. It is 4.7 times more viscous ($\mu=4.7 \cdot 10^{-3} \text{ Pa}\cdot\text{s}$) and 1.86 times heavier than water ($\rho=1860 \text{ Kgr}/\text{m}^3$). The interfacial tension between water and Fluorinert is 58 mN/m .

In figure 6, a magnified part of the network can be seen during drainage. It is a snapshot taken under quasi-static conditions. Fluorinert is seen in light color and water in dark color. It is obvious that the water is the non-wetting phase, and fluorinert is the wetting one. The contact angles are clearly small everywhere. That was also cross-checked with the use of ImageJ software to measure the contact angle from the image. Values between zero and 4° were found.

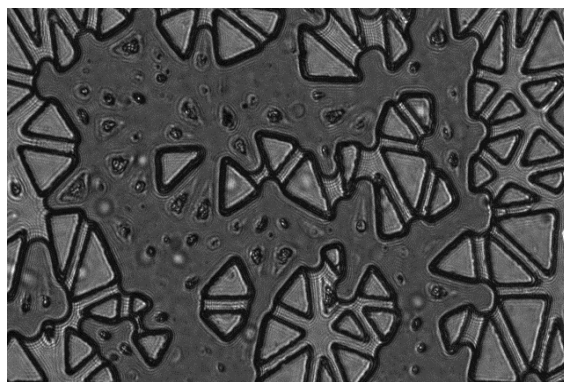


Figure 6. A magnified image of the network during drainage. The curvatures of the interfaces show a strong wettability of the medium to fluorinert (seen in light color).

The contact angle was also measured under pressure-free conditions as follows. A droplet of water was dropped in a beaker filled with fluorinert. As water is much lighter, it stayed on the surface. Then, a silanized PDMS slab was put on top of them. The contact angle between water, fluorinert, and PDMS was measured. We found it to be equal to 4° .

6.3.2 Deformation of micro-model

An issue that needs attention is the possibility of swelling of PDMS due to contact with organic liquids and its deformation under the pressures of liquids. PDMS swells when it comes in contact with non-polar organic solvents, like hydrocarbons, toluene, and dichloromethane. Lee et al. (2003) examined the compatibility of organic liquid with PDMS. They stated that the problem of liquid compatibility has three aspects: 1) the absorption of the liquid in PDMS, and potential swelling of PDMS, 2) the diffusion of liquid components in PDMS, and 3) the dissolution of oligomers (swelling oils) in PDMS. In the work of Dangla et al. (2010), the dynamics of penetration of solvents in PDMS and its relation to volume dilation were studied in a model experiment, allowing a precise measurement of the diffusion coefficients of oils in PDMS. The two liquids that we used, water and fluorinert, do not cause swelling of PDMS. In general, alcohols, polar solvents, and fluorine-based fluids do not have a swelling effect on PDMS.

In the work of Gervais et al. (2006), the effect of liquids pressure on the deformation of shallow micro-fluidic channels was examined. Such deformation can, in turn, affect the laminar flow profile and pressure distribution within the channels. They came up with a dimensionless number for assessing the significance of this deformation, depending on the pressure drop along a channel, its width and height, and the Young modulus of PDMS. Based on this dimensionless number, we determined that the deformation of PDMS in our experiments can be neglected.

6.4 Experimental setup

6.4.1 Visualization setup

In most micro-model studies, conventional microscopy is employed for visualization of pore-scale processes. But, this method would be inadequate for the visualization of our elongated flow network. The reasons are that with a conventional microscope, only a square part of the flow network can be visualized at a high resolution, at any given time. The rest of the model would be outside the field of view of the microscope. For this reason, we designed an innovative optical setup which allowed us to visualize and record images of the whole micro-model at any given time.

A picture of the experimental setup is shown in figure 7. Major components of the optical setup were: (1) a collimated LED light source mounted with an objective lens F 3.2/105 mm, (2) a prism (Edmund Optics) with dimensions of 50 mm x 50 mm, (3) a

SONY Sonnar F1.8/135 mm magnifying lens, (4) a box containing three beam splitters (Edmund Optics) with dimensions of 35 mm x 35 mm, and (5) four 5-Megapixel Prosilica GC-2450 cameras. The micro-model (A) was placed horizontally on a stage between the light source and the prism. The input and output holes of the micro-model were aligned with the holes of an inflow reservoir (B) and an outflow reservoir (C), respectively. The whole setup was placed on a vibration-free optical table (Standa Opto-Mechanics). In figure 8, a schematic representation of the visualization setup is shown.

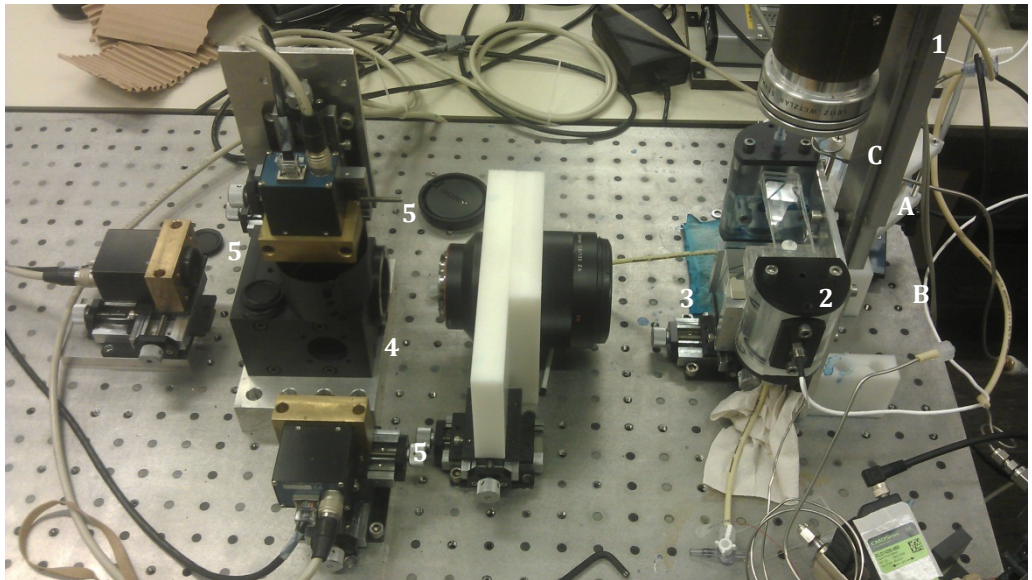


Figure 7. The experimental setup for the visualization of the elongated micro-model: 1) LED light source mounted with an objective lens. 2) Prism. 3) Magnifying lens. 4) Box with three beam splitters. 5) High resolution CMOS cameras. The micro-model is labeled A and the inflow/outflow reservoirs are designated by B and C, respectively.

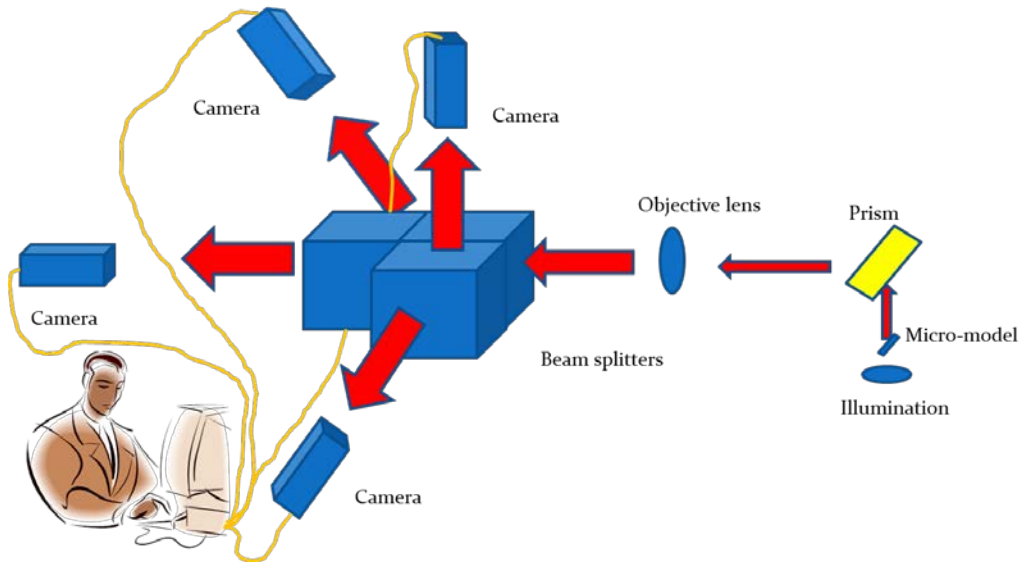


Figure 8. A schematic representation of the visualization setup

The working of the visualization setup was as follows. The collimated light passed through the micro-model, and it was bent by the prism to become parallel to the optical table. The beam splitters reproduced four identical images in four perpendicular directions. In each direction, there was a camera placed such that each camera received a different part of the image. By adding the images of all four cameras, the whole extent of the flow network could be visualized. The distance between the optical parts of the setup, as well as their optical properties (like focal length, numerical aperture of the lens, etc.) were carefully chosen, so that the final image that every camera would receive, could fit exactly in the camera's sensor. The part of the micro-model recorded by each camera was about $5 \times 7 \text{ mm}^2$. This corresponded to one REV.

We confirmed this by determining the porosity over domains of 5 mm in width and increasingly larger length, starting with a domain length of 56 microns (equivalent of 20 pixels). We obtained a porosity value of 50% for domain sizes of $5 \times 7 \text{ mm}^2$ (figure 10).

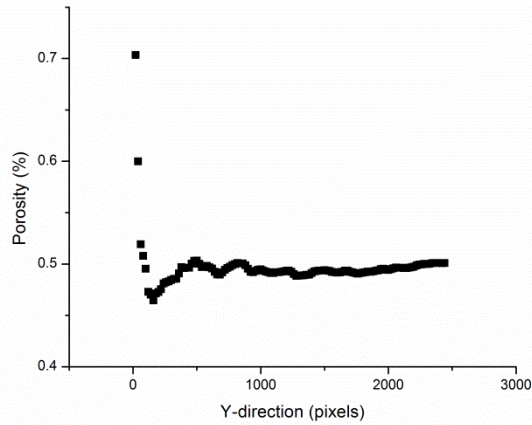


Figure 9. Porosity of an increasingly growing in one direction domain in the micro-model. The other direction was equal to 5 mm, which was the width of the model. Porosity reaches a constant value of 50% when the domain size is $5 \times 7 \text{ mm}^2$.

A detailed explanation of the visualization setup can be found in Karadimitriou et al. (2012). In figure 10, images from the four cameras of a network with dimensions of 5 mm x 30 mm are shown.

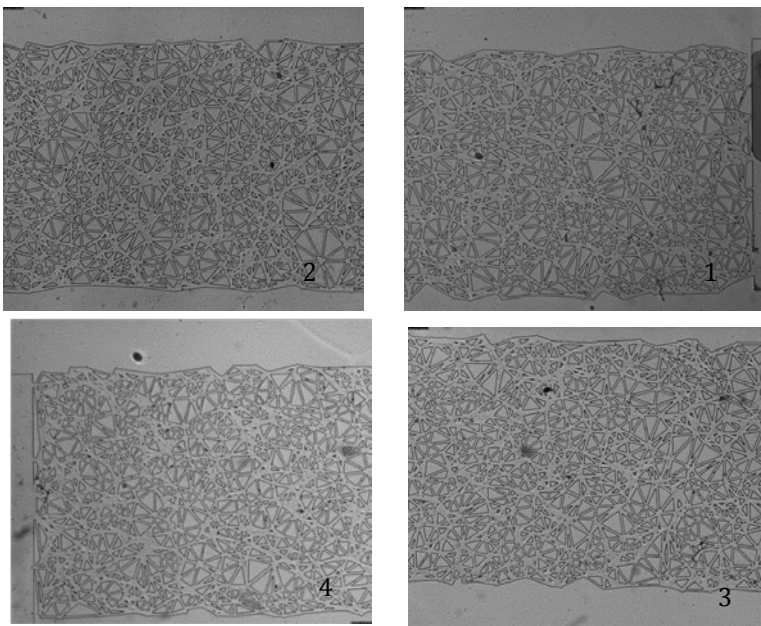


Figure 10. The four images of the flow network numbered according to their sequence in the micro-model. In total, the pictures cover an area of 5 x 30 mm, visualized at a resolution of 2.8 $\mu\text{m}/\text{pixel}$.

6.4.2 Pressure measurement and control

The inflow and outflow of fluids were controlled through the two external reservoirs B and C. At exactly the same level as the level of the micro-model, two pressure transducers (Kulite XTL-190M-0,7B-D) were installed, one in each reservoir, to measure the fluid pressures. These transducers were connected to a differential pressure controller (Bronkhorst). The differential pressure controller had an RS-232 interface that was connected to a computer. In this way, it was possible to set, measure, and control the differential pressure between the two reservoirs at any instant. The controller was calibrated in a way that the maximum pressure difference would be 27 kPa with an accuracy of 25 Pa. The pressure controller could adjust the pressure in the non-wetting phase reservoir by increasing or decreasing the through-flow rate. The pressure in the wetting phase reservoir was always atmospheric. By increasing the pressure of the non-wetting phase reservoir, drainage could be initiated. At the end of, or during, a drainage event, imbibition could be brought about by reducing the pressure of the non-wetting phase reservoir.

6.5 Quasi-static experiments

The micro-models used in this set of experiments had 3000 pore bodies, nearly 9000 pore throats, and the mean pore size was 40 μm . Their depth was equal to 40 μm . The micro-model was initially saturated with the wetting phase, which was Fluorinert FC-43. The non-wetting phase was water dyed with ink. The pressure of the non-wetting phase was increased, until it was just high enough for the non-wetting phase to enter the flow network. The spatial configuration of the fluids in the micro-model was continuously monitored and when there was no change (usually after 20 minutes), we assumed that equilibrium was reached. By stepwise increase of the non-wetting phase pressure with 50 Pa, subsequent stages of drainage were achieved. At every equilibrium step, a snapshot of the fluids configuration in the network was acquired. The drainage experiment was over once the non-wetting phase reached the end of the micro-model and entered the outflow reservoir (i.e. breakthrough). Then, quasi-static imbibition experiment was carried out by stepwise decrease of the non-wetting phase pressure. All experiments were conducted in a constant-temperature room at 21 ± 1 $^{\circ}\text{C}$.

6.6 Results

The acquired images were analyzed with IDL software package (IT&T Visual Information Solutions) to calculate saturation and the specific interfacial area between Fluorinert and dyed water at an imposed capillary pressure. Results were used to plot capillary pressure-saturation curves as well as capillary pressure-saturation-interfacial area surfaces.

In figure 11, data points for capillary pressure and saturation for a series of drainage-imbibition cycles are shown. It is obvious that the capillary pressure-saturation relationship is highly hysteretic. These results clearly show that the knowledge of pressure and saturation is not enough to fully specify the state of the system.

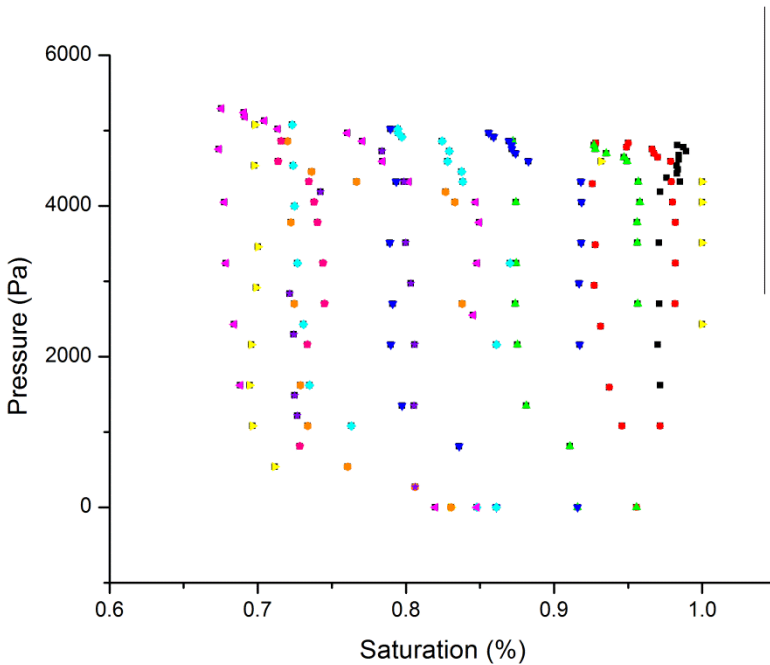


Figure 11. Capillary pressure as a function of Fluorinert saturation for primary drainage, main imbibition, and scanning curves.

The hysteretic behavior of the system can also be seen in figure 12, where two images from the same part of the network. Left image is from imbibition and the right one is from drainage. The phase saturation is nearly the same in both images, but the capillary

pressure is significantly different. In the left picture, the capillary pressure is 4833 Pa, while in the right picture the applied pressure is 2160 Pa. But, also the interfacial areas of the two images are significantly different ($2.8 \cdot 10^{-7} \text{ m}^2$ and $7.4 \cdot 10^{-7} \text{ m}^2$ respectively).

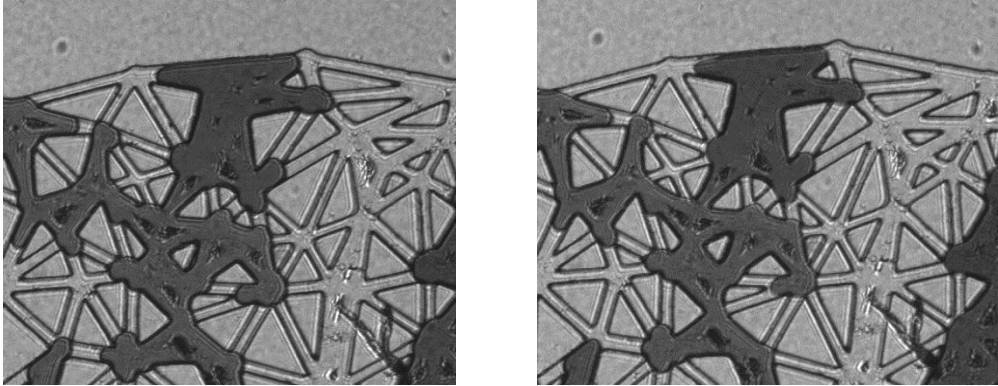


Figure 12. Images from a small part of the network at drainage (left) and imbibition (right). In both images, the wetting phase saturation is 72%. In the left picture, the capillary pressure is 4833 Pa, while in the right picture the applied pressure is 2160 Pa.

In quasi-two-dimensional micro-models, like the one that we used in our experiments, there is very limited corner flow of the wetting phase. The only parts of the network where the wetting phase stays connected with the wetting phase reservoirs are the corners along the upper and lower side boundaries of the network. The wetting phase in all other corners remains isolated due to the two-dimensional nature of the micro-model. The flow through these side boundary corners was quite limited, because of their limited volume, and the system exhibited a highly hysteretic behavior. As soon as the pressure was low enough for the non-wetting phase to free the upper and lower boundaries of the network, then imbibition was very fast.

As it was mentioned above, theoretical, numerical, and experimental results have shown that it is crucially important to include interfacial area for a complete description of two-phase flow in porous media (see e.g., Hassanizadeh and Gray, 1990, 1993b; Held and Celia, 2001; Cheng et al., 2004; Joekar-Niasar et al. , 2010b;; Joekar-Niasar and Hassanizadeh, 2011, 2012).

In figure 13a, all equilibrium data of saturation, capillary pressure, and specific interfacial area from imbibition and drainage experiments are plotted. In figure 13b, a surface fitted to these data points is shown. The fitted surface can be described by the following function (after Joekar-Niasar and Hassanizadeh, 2012):

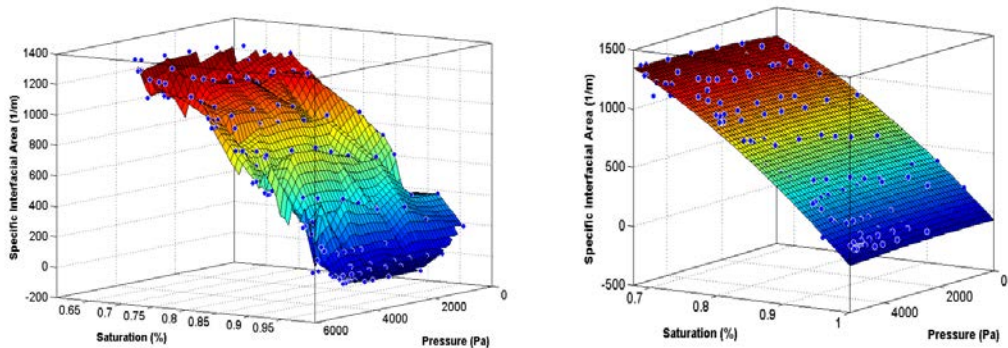


Figure 13. From left to right, the surfaces that were formed by data points obtained during drainage and imbibition, both interpolated and fitted, are presented.

$$a^{wn} = \alpha \cdot S \cdot (1 - S)^{\beta} \cdot P_c^{\gamma}$$

The choice of such a fitting function was made so that at a wetting phase saturation of zero, there will be zero interfacial area. Specific interfacial area and capillary pressure are measured in S. I. units. In the table that follows, the values for the fitting parameters, their confidence levels, as well as R2 values are given.

Parameter	Value	Confidence levels
α	2538,59	2315,79 – 2759,65
β	1,185	1,165 – 1,205
γ	0,004594	-0,005873 – 0,01506
R ²	0.991548	

As it can be seen in the table, there was a very good match for the fitting of all data points by a single surface.

We also fitted individual surfaces to drainage and imbibition data points separately. The maximum difference between the two surfaces was found to be about 8%, while on average, the mean difference was around 4%. The reason for the difference between the two individual surfaces, one for drainage and one for imbibition was the creation of

disconnected non-wetting phase after primary drainage. The disconnection of the non-wetting phase created interfaces that in future steps, a part of it would get reconnected, and a part of it would remain disconnected.

It can be seen in figure 14, where snapshots of the same part of the micro-model during primary drainage (left image) and main imbibition (right image) are shown, that the disconnection of the non-wetting phase created many interfaces. A big part of the disconnected phase would get reconnected, but not all of it. The wetting phase saturation was almost the same in the two situations (83.4 % and 84.0%, respectively). But, the values of capillary pressure and interfacial area were significantly different. For the left image, the pressure was 4833 Pa and the interfacial area was roughly $2.8 \cdot 10^{-7} \text{ m}^2$. For the right side, the pressure was 1080 Pa (thus lower) whereas the interfacial area was around $2.1 \cdot 10^{-6} \text{ m}^2$ (i.e., much higher).

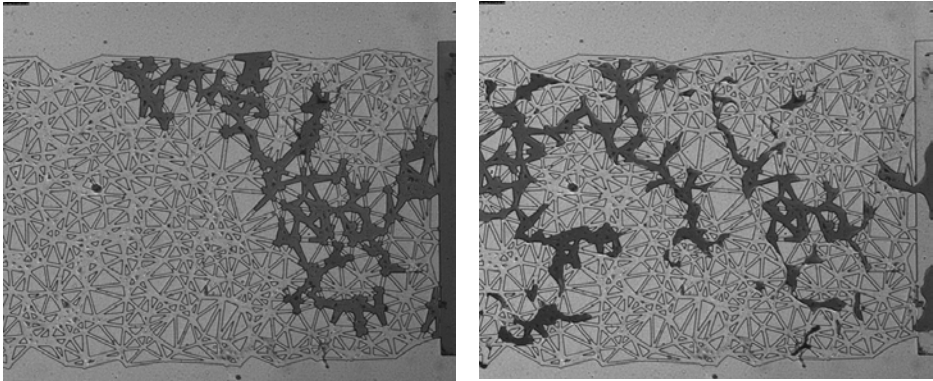


Figure 14. The configuration of fluids in drainage (left) and imbibition (right) in the same part of the flow network.

6.7 Discussion

The experimental results showed that the relation between capillary pressure and saturation for drainage and imbibition is hysteretic; we have many possible equilibrium curves. However, the inclusion of interfacial area as a new state variable can eliminate hysteresis. Instead of many curves, we get one unique surface, which is the locus of all drainage and imbibition data points. This also means that we can estimate a unique value of interfacial area for every capillary pressure-saturation pair. This surface is unique for a given set of fluids and solid phases and a given percolation pattern. In fact, after repeating the experiment many times, for the same pressure steps, the same percolation patterns were obtained. When the pressure steps were slightly increased,

then the distribution of fluids in the network were different. But, we still obtained the same Pc-S-awn surface. When the experiment was repeated with different pairs of liquids (we used perfluorodecalin and water), the pattern was different than the one with fluorinert and water, but still reproducible under the same conditions. Of course, we got a different Pc-S-awn surface than for water and fluorinert.

Finally, we verified our initial claim that our flow domain comprised four REV's. We divided the flow domain into four sub-domains and compared the capillary pressure-saturation-specific interfacial area surfaces of subdomains with each other as well as with the surface for the whole domain. The results showed that the fitted surfaces matched well, with the highest mismatch being less than 4%.

6.8 Conclusions

We have developed a relatively simple and highly effective method for constructing PDMS micro-models. Through a series of steps, which in total take less than a week, we can construct a fully functional micro-model. The most time-consuming part is the production of the master wafer, which takes almost six days, including the preparation of the mask and shipping. After that, the micro-model can be ready in four to five hours. Up to now, PDMS micro-models were not considered to be suitable for well-controlled two-phase flow experiments because of their mixed wettability, and the fact that it changes with time. We have developed a reliable procedure for making PDMS micro-models that are uniformly and stably hydrophobic. This is a major improvement in addressing wettability problems of PDMS and makes it a very attractive alternative to other materials, like photoresist, silicon, glass or quartz. In comparison to previous experimental work on the significance of the inclusion of interfacial area as a separate variable, we may make the following observations. It is the first time that an elongated micro-model is being used. This offered the ability to study the concept of REV, and to verify its average properties related to interfacial area experimentally. It was observed and verified that corner flow is not present in a two-dimensional micro-model, except from the upper and lower boundaries of the flow network. This made the capillary pressure-saturation curve to be highly hysteretic. The network configuration allowed for the existence of residual saturation for, wetting and non-wetting phases. Because we did not have corner flow, the lowest wetting phase saturation we could reach was around 60%. Therefore, we could not reach maximum values of the specific interfacial area. So, in comparison to other two-dimensional micro-models, the interfacial area that we measured was smaller than

We have shown that the visualization setup, using four cameras, can provide dynamic images of the distribution of two immiscible liquids over the whole length of the micro-model. By performing quasi-static experiments, we have shown the validity of the hypothesis that capillary pressure- saturation-interfacial area data points form a unique surface for all drainage and imbibition processes.

6.9 References

Avraam, D. G., Kolonis, G. B., Roumeliotis, T. C., Constantinides, G. N. and Payatakes, A. C. (1994), Steady-state two-phase flow through planar and nonplanar model porous media, *Transport in Porous Media*, **16**, 1, 0169-3913, pp. 75-101, Doi: 10.1007/BF01059777.

Baouab, Z., M. Najjari , H. Ouerfelli, S. Ben Nasrallah (2007), Experimental study of the effects of hydraulic gradient and injected-gas flow rate on fragmentation in porous media, *Journal of Petroleum Science and Engineering*, **59**, pp. 250-256.

Baumann, T., and C. J. Werth (2004), Visualisation and modelling of polystyrol colloid transport in a silicon micro-model, *Vadose Zone J.*, **3**, pp. 434-443.

Bietsch, A. and Michel, B., (2000), Conformal contact and pattern stability of stamps used for soft lithography, *J. Appl. Phys.*, **88**, 4310.

Bodas, D. and Khan-Malek, C., 2007, Hydrophilization and hydrophobic recovery of PDMS by oxygen plasma and chemical treatment—An SEM investigation, *Sensors and Actuators B: Chemical* **123**, pp. 368-373.

Chang, L.-C., J.-P. Tsai, H.-Y. Shan, H.-H. Chen (2009), Experimental study on imbibition displacement mechanisms of two-phase fluid using micro model, *Environ Earth Sci*, **59**:901-911, doi: 10.1007/s12665-009-0085-6.

Chen, D., L. J. Pyrak-Nolte, J. Griffin, and N. J. Giordano (2007), Measurement of interfacial area per volume for drainage and imbibition, *Water Resour. Res.*, **43**, W12504, doi:10.1029/2007WR006021.

Cheng, J.-T. (2002), Fluid flow in ultra-small capillaries, Ph.D. Thesis, Purdue University.

Cheng, J.-T., L. J. Pyrak-Nolte, D. D. Nolte, and N. J. Giordano (2004), Linking pressure and saturation through interfacial areas in porous media, *Geophys. Res. Lett.*, **31**, L08502, doi:10.1029/2003GL019282.

Corapcioglu, M. Y., Yoon, S., and Chowdhury, S. (2009), Pore-Scale Analysis of NAPL Blob Dissolution and Mobilization in Porous Media, *Transport in Porous Media*, **79**(3), pp. 419-442, doi: 10.1007/s11242-008-9331-8.

Dangla, R., Gallaireb, F., and Baroud, C. N., (2010), Microchannel deformations due to solvent-induced PDMS swelling, *Lab Chip*, **10**(21), DOI: 10.1039/c003504a

Duffy, D. C., Olivier, J. C. M., Schueller, J. A., and Whitesides. G. M., (1998), Rapid prototyping of microfluidic systems in poly(dimethylsiloxane), *Anal. Chem.*, **70**, pp. 4974-84.

Duffy, D. C., Schueller, O. J. A., Brittain, S. T., and Whitesides, G. M., (1999), Rapid prototyping of microfluidic switches in poly(dimethyl siloxane) and their actuation by electro-osmotic flow, *J. Micromech. Microeng.*, **9**, 211-7.

Eddings, M. A., and Gale, B. K., (2006), A PDMS-based gas permeation pump for on-chip fluid handling in microfluidic devices, *J. Micromech. Microeng.*, **16**, pp. 2396-402.

Eddings, M.A., Johnson, M.A., Gale, B.K., (2008), Determining the optimal PDMS-PDMS bonding technique for microfluidic devices, *J. Micromech. Microeng.*, **18**(6).

Er, V., Babadagli, T., and Xu, Z., (2010), Pore-Scale Investigation of the Matrix-Fracture Interaction During CO₂ Injection in Naturally Fractured Oil Reservoirs, *Energy & Fuels*, **24** (2), pp. 1421-1430.

Ferer, M., Ji, C., Bromhal, G. S., Cook, J., Ahmadi, G., Smith, D. H., (2004), Crossover from capillary fingering to viscous fingering for immiscible unstable flow: Experiment and modelling, *Phys. Rev. E*, **70** (1).

Fritz, J. L., and Owen, M. J., (1995), Hydrophobic recovery of plasma-treated polydimethylsiloxane, *Journal of Adhesion*, **54**, pp. 33-45.

Gervais, T., El-Ali, J., Gunther, A., and Jensen, K. F., (2006), Flow-induced deformation of shallow microfluidic channels, *Lab Chip*, **6**, pp. 500-507.

Go, J. S., and Shoji, S., (2004), A disposable, dead volume-free and leak-free in-plane PDMS microvalve, *Sensors Actuators A*, **114**, pp. 434-44.

Grate, J. W., Zhang, C., Wietsma, T. W., Warner, M. G., Anheier Jr., N. C., Bernacki, B. E., Orr, G., and Oostrom, M. (2010), A note on the visualization of wetting film structures and a nonwetting immiscible fluid in a pore network micro-model using a solvatochromic dye, *Water Resour. Res.*, **46**, W11602, doi:10.1029/2010WR009419.

Gutiérrez, B., F. Juárez, L. Ornelas, S. Zeppieri, A. López de Ramos (2008), Experimental Study of Gas-Liquid Two-Phase Flow in Glass Micro-models, *Int. J. Thermophys.*, **29**:2126-2135, DOI 10.1007/s10765-007-0305-9.

Hassanizadeh, S. M., and W. G. Gray, 1993a, Toward an improved description of the physics of 2-phase flow, *Adv. Water Resour.*, **16**(1), 53–67.

Hassanizadeh, S. M., and W. G. Gray, 1993b, Thermodynamic basis of capillary pressure in porous media, *Water Resour. Res.*, **29**(10), 3389 – 3405.

Hassanizadeh, S.M and Gray, W.G., (1990), Mechanics and thermodynamics of multiphase flow in porous media including interphase boundaries, *Adv. Water Resour.*, **13**, 169-186.

Haubert, K., Drier, T., Beebe, D., (2006), PDMS bonding my means of a portable, low-cost corona system, *Lab Chip*, **6**, pp. 1548–1549.

Heiba, A.A., Sahimi, M., Scriven, L.E. and Davis, H.T. (1992), Percolation theory of two-phase relative permeability. SPE 11015, presented at the 57th Annual Fall Meeting of the Society of Petroleum Engineers, New Orleans, LA.

Held, R. J., and M. A. Celia (2001), Modeling support of functional relationships between capillary pressure, saturation, interfacial area and common lines, *Adv. Water Resour.*, **24**, 325– 343.

Hug, T. S., Parrat, D., Kunzi, P.-A., Stauffer, U., Verpoorte, E., de Rooij, N. F., (2003), Fabrication of nanochannels with PDMS, silicon and glass walls and spontaneous filling by capillary forces, 7th International Conference on Miniaturized Chemical and Biochemical Analytical Systems, California, USA.

Huh, D., Mills, K. L., Zhu, X., Burns, M. A., Thouless, M. A., and Takayama, S., (2007), Tuneable elastomeric nanochannels for nanofluidic manipulation, *Nature Materials*, **6**, pp. 424-428, doi:10.1038/nmat1907.

Joekar-Niasar, V., Hassanizadeh, S. M., Pyrak-Nolte, L. J., Berentsen, (2010a), C., Simulating drainage and imbibition experiments in a high-porosity micro-model using an unstructured pore-network model, *Water Resources Research*, **45**: W02430, doi:10.1029/2007WR006641

Joekar-Niasar, V., M. Prodanovic, Dorthe Wildenschild, and S.M. Hassanizadeh, (2010b), Network Model Investigation of Interfacial Area, Capillary Pressure and Saturation Relationships in Granular Porous Media, *Water Resources Research*, vol. **46**: W06526, doi:10.1029/2009WR008585.

Joekar-Niasar, Vahid; S. Majid Hassanizadeh, (2011), Specific Interfacial Area; the Missing State Variable in Two-Phase Flow Equations, *Water Resources Research*, Vol. **47**, W05513, doi:10.1029/2010WR009291, 2011

Joekar-Niasar, V., and Hassanizadeh, S. M., (2012), Uniqueness of Specific Interfacial Area–Capillary Pressure–Saturation Relationship Under Non-Equilibrium Conditions in

Two-Phase Porous Media Flow, *Transport in Porous Media*, Doi: 10.1007/s11242-012-9958-3.

Johnston, W.G. (1962), Dislocation etch pits in non-metallic crystals with bibliography, *Progress in ceramic science*, vol 2, Burke JE (ed), pp 1-75. Pergamon Press, New York.

Karadimitriou, N. K., and Hassanizadeh, S. M., 2012, A Review of Micro-models and their Use in Two-Phase Flow Studies, *Vadose Zone Journal*, doi:10.2136/vzj2011.0072.

Karadimitriou, N.K., Joekar-Niasar, V., Hassanizadeh, S. M., Kleingeld, P. J., and Pyrak-Nolte, L. J., (2012), A novel deep reactive ion etched (DRIE) glass micro-model for two-phase flow experiments, *Lab on a Chip*, DOI: 10.1039/C2LC40530J.

Lee, J., Park, C., and Whitesides, G. M., (2003), Solvent Compatibility of Poly(dimethylsiloxane)-Based Microfluidic Devices, *Anal. Chem.*, **75**, pp. 6544–6554.

Liu, Y., Nolte, D. D., Pyrak-Nolte, L. J., (2011), Hysteresis and Interfacial Energies in Smooth-walled Microfluidic Channels, *Water Resour. Res.*, **47**, W01504, doi:10.1029/2010WR009541.

McKellar, M. and Wardlaw, N. C., 1982, A method of making two-dimensional glass micro-models of pore system, *J. Can. Petrol. Technol.* **21**(4), pp. 1-3.

Murakami, S.-I., Kuroda, T., and Osawa, Z., (1998), Dynamics of polymeric solid surfaces treated with oxygen plasma: Effect of aging media after plasma treatment, *Journal of Colloid and Interface Science*, **202**, pp. 37-44.

NagaSiva, G., Bera, B., Karadimitriou, N. K., Mitra S. K., and Hassanizadeh, S. M., (2011), Reservoir-on-a-Chip (ROC): A new paradigm in Reservoir Engineering, *Lab on Chip*, Vol. **11**, pp. 3785 - 3792, (Featured Article), DOI:10.1039/C1LC20556K.

Ohara, J., Asami, K., Takeuchi, Y. and Sato, K. (2010), Development of RIE-lag Reduction Technique for Si Deep Etching Using Double Protection Layer Method, *IEEJ Transactions on Electrical and Electronic Engineering*, **5**: 125–130, doi: 10.1002/tee.20506.

Pyrak-Nolte, L. J., D. D. Nolte, D. Chen, and N. J. Giordano (2008), Relating capillary pressure to interfacial areas, *Water Resour. Res.*, **44**, W06408, doi:10.1029/2007WR006434.

Samel, B., Chowdhury, M. K., and Stemme, G., (2007), The fabrication of microfluidic structures by means of full-wafer adhesive bonding using a poly(dimethylsiloxane) catalyst, *J. Micromech. Microeng.*, **17**, pp. 1710-4.

Satyanarayana, S., Karnik, R. N., and Majumdar, A., (2005), Stamp-and-stick room-temperature bonding technique for microdevices, *J. Microelectromech Syst.*, **14**, pp. 392-9.

Wegner, M.W., Christie, J.M. (1983), Chemical etching of deformation substructures in quartz, *Phys Chem Minerals*, **9**:67–78.

Willingham, T. W., Werth, C. J., and Valocchi, A. J., (2008), Evaluation of the Effects of Porous Media Structure on Mixing-Controlled Reactions Using Pore-Scale Modeling and Micro-model Experiments, *Environmental Science & Technology*, **42** (9), pp. 3185-3193

Xia, Y. and Whitesides, G. M. (1998), Soft Lithography. *Angewandte Chemie International Edition*, **37**: 550–575.

Yeom, J., Y. Wu, J. C. Selby, and M. A. Shannona,(2005), Maximum achievable aspect ratio in deep reactive ion etching of silicon due to aspect ratio dependent transport and the microloading effect, *Journal of Vacuum Science & Technology B: Microelectronics and Nanometer Structures*, **23**: 6, pp. 2319 – 2329,1071-1023.doi:10.1116/1.2101678.

Zhang, C., Oostrom, M., Wietsma, T. W., Grate, J. G., and Warner, M.G., (2011), Influence of Viscous and Capillary Forces on Immiscible Fluid Displacement: Pore-Scale Experimental Study in a Water-Wet Micro-model Demonstrating Viscous and Capillary Fingering, *Energy and Fuels*, **25**(8):3493-3505. doi:10.1021/ef101732k

Karadimitriou, N. K., Hassanizadeh, S. M., Joekar-Niasar, V., and Kleingeld, P. J., Micro-model study of specific interfacial area-capillary pressure-saturation relationship under transient conditions in two-phase flow, article under preparation.

Chapter 7

Micro-model study of Specific interfacial area - Capillary pressure - Saturation relationship under transient conditions in two-phase flow

Abstract

One of the main relationships used in two-phase flow modeling is the capillary pressure – saturation relationship. It is well known that this relationship is process dependent. One will obtain different capillary pressure – saturation curves for drainage and imbibition. This effect is called hysteresis. A theory derived through rational thermodynamics (Hassanizadeh and Gray, 1993a) suggests that the introduction of a new state variable, called specific interfacial area, can result in a unique relation between capillary pressure, saturation, and specific interfacial area. Specific interfacial area is defined as the ratio of the total area of interfaces between two phases to the total volume of the porous medium.

This study investigates whether the relationship between capillary pressure-saturation and specific interfacial area is different when obtained under steady-state and transient two-phase flow in an elongated PDMS micro-model. Experimental results show that the relationship between capillary pressure and saturation depends on the displacement process (drainage or imbibition). It is also different under quasi-static and dynamic conditions. In addition to this, we provide experimental evidence to support the extended theories of two-phase flow, where specific interfacial area should be included as a separate state variable.

7.1 Introduction

7.1.1 Specific interfacial area and two-phase flow

A corner stone of theories of two-phase flow in porous media is the capillary pressure-saturation relationship. It actually relates the difference in macro-scale pressures of

two immiscible fluids to the saturation of one of the fluids. Almost always, it is measured under static conditions, and then it is used to model transient conditions. It is well known that this relationship is hysteretic, and does not explicitly include any information on the dynamics of the interfaces formed between the two phases. One may get many capillary pressure – saturation curves, for the same porous medium, for the same set of phases, but for different initial conditions and for different displacement processes. Following an approach based on volume averaging and rational thermodynamics, Hassanizadeh and Gray (1990, 1993b) developed a macroscale theory of two-phase flow. They postulated that the hysteretic behavior of P^c - S^w relationship can be modeled by introducing fluid-fluid specific interfacial area as an additional state variable. Based on this theory capillary pressure-saturation-specific interfacial area data points from drainage and imbibition processes under equilibrium or/and non-equilibrium conditions would fall on a unique surface. This can be formulated as follows:

$$F(P^c, S^w, a^{wn}) = 0 \quad (1)$$

A growing number of numerical and experimental works show that under quasi-static conditions, drainage and imbibition P^c - S^w - a^{wn} surfaces (formed by data points from drainage and imbibition experiments, respectively) coincide with each other, within the margin of experimental error. The earliest studies were done by Reeves and Celia (1996), and Held and Celia (2001), who performed quasi-static pore-network modeling. The first experimental evidence for the uniqueness of P^c - S^w - a^{wn} surface was provided by Cheng et al (2004) and later by Chen et al (2007) and Pyrak-Nolte et al. (2008). They performed two-phase flow experiments in a micro-model. However, all these studies have one thing in common; they considered equilibrium conditions only. Under equilibrium (quasi-static) conditions, the interfaces were not moving in the porous medium. A combination of pore-network modeling and micro-model experimental results was performed by Joekar-Niasar et al. (2009), Porter et al (2009) and Karadimitriou et al (2013).

The question one may ask is whether the relationship obtained under equilibrium conditions for P^c - S^w - a^{wn} would be applicable under dynamic conditions too. This question was addressed by Joekar-Niasar and Hassanizadeh (2012) using a dynamic pore-network model. They determined the macroscale capillary pressure, saturation, and interfacial area for an elongated averaging domain during transient flow. The capillary pressure was calculated as the average of local-scale capillary pressure

(within the pores) at any given time. Such a study cannot be done experimentally. One needs to obtain macroscale capillary pressure under dynamic conditions. One can measure macroscale fluid pressures (by using selective pressure transducers, as e.g. in Bottero et al., 2011). But, under dynamic conditions, capillary pressure is different from fluid phase pressures. This was clearly shown by Joekar-Niasar et al., 2010. So, an important question is how to measure macroscale capillary pressure in an experiment. In our micro-model experiments, we are using images from dynamic displacement experiments in order to determine macroscale capillary pressure. This allows us to examine how capillary pressure – saturation – interfacial surfaces changes under dynamic conditions.

In the extended theories of two-phase flow proposed by Hassanizadeh and Gray (1990), there are also terms related to the average velocity of interfaces and their rate of production. Pop et al. (2009), and Niessner and Hassanizadeh (2008), proposed that the interfacial area production term (E^{wn}) should depend on saturation and its rate of change. Joekar-Niasar et al., (2010a) studied the dependence of interfacial area production term on dynamic parameters, like viscosity ratio and different global pressure difference, using a dynamic pore network model. However, the size of their network was nearly one REV. Joekar-Niasar and Hassanizadeh (2011) used an elongated flow network in their dynamic pore network model. In this work, we use experimental data to investigate the dependence of the production term, as well as the interfacial velocity (\mathbf{w}^{wn}), on saturation and its rate of change.

7.1.2 Micro-models and two phase flow

An overview of various issues related to micro-models and their use in two-phase flow studies, such as network generation, fabrication materials and methods, visualization methods, and different applications, was given in Karadimitriou and Hassanizadeh (2012b). They defined a micro-model as “an artificial representation of a porous medium, made of a transparent material. This fluidic device bears a flow network, with features on the micro-scale, and an overall size of up to a few centimeters.”

Micro-models have been mostly used in studying displacements of two immiscible fluid phases in porous media (Avraam et al., 1994; Baouab et al., 2007; Chang et al., 2009; Corapcioglu et al., 2009; NagaSiva et al., 2011). Processes of drainage and imbibition, as well as the mechanisms that dominate them, like viscous or capillary fingering, snap-off, etc., have been studied using micro-models (Zhang et al. 2011; Ferer et al., 2004; Grate et al., 2010; Gutiérrez et al., 2008; Hug et al., 2003; Huh et al., 2007).

Recently, two-phase flow studies were performed using photo-resist micro-models that had flow patterns based on stratified percolation (Cheng, 2002; Pyrak-Nolte et al., 2008; Cheng et al., 2004; Chen et al., 2007; Liu et al., 2011). In these studies,

distributions of the two phases in the flow network during quasi-static drainage and imbibition were visualized. Phase saturation and interfacial area could be determined using image processing and the relationship between phase saturation, capillary pressure, and specific interfacial area under equilibrium conditions was investigated. Under static conditions, the pore pressure of each phase can be assumed to be constant everywhere and equal to the pressure of its corresponding boundary reservoir. This means that the local capillary pressures at all fluid-fluid interfaces – and thus the average capillary pressure – are all equal to the difference in boundary reservoirs pressures. But, this cannot be assumed under transient flow conditions. There is pressure gradient within the pores that is a function of time and space. Capillary pressures at interfaces will be different from each other and will not be any more equal to the difference in boundary reservoirs pressures. Currently, there is no easy way of measuring local pressure within the pores. But, we can determine the local capillary pressure at each interface from its curvatures using Young-Laplace equation. This requires knowing the radii of principal curvatures of the interface. But, our visualization method provides planar images only. So, only the planar curvature can be determined from image processing. There is no optical way of visualizing the micro-model in depth. So, the in-depth curvature cannot be determined. Commonly, researchers have assumed the in-depth radius of curvature to be equal to half the depth of the micro-model (Cheng et al., 2004; Chen et al., 2007; Pyrak-Nolte et al., 2008). This contribution to the local capillary pressure was assumed to be the same for all interfaces. But, this is an approximation that can be too gross for wider pores. In this work, we determine the hidden curvature differently, with the only assumption being that the contact angle is the same in both directions, as explained shortly.

7.2 Experimental setup

The details on the materials used and the manufacturing process of the micro-model, as well as the topology of the flow network, the fluids used as the wetting and the non-wetting phase, the visualization setup used to monitor flow in the micro-model, and finally how pressure was measured and controlled, can be found in Chapter 6, in sections 6.2 and 6.4.

7.3 Dynamic experiments

7.3.1 Experimental process

The micro-model was initially saturated with the wetting phase, namely Fluorinert. As mentioned before, the non-wetting phase was water dyed with ink. The pressure of the non-wetting phase reservoir was increased to a specific value, namely 6300 Pa. The flow induced by this pressure corresponded to a maximum capillary number equal to $2 \cdot 10^{-5}$. The non-wetting phase started to enter the flow network, displacing the wetting phase. As soon as breakthrough of the non-wetting phase took place, its pressure at the outlet dropped to zero. As a result, the wetting phase then started to go back into the network, displacing the non-wetting phase. The spatial configuration of the fluids in the micro-model was continuously monitored, and it was recorded at a frame rate of 1 picture per second. After primary drainage and main imbibition, a number of scanning measurements was performed for intermediate steps. All experiments were conducted in a constant-temperature room at 21 ± 1 °C.

7.3.2 Data processing

7.3.2.1 P_c - S_w - A^{wn}

The acquired images were analyzed with IDL software package (IT&T Visual Information Solutions) to calculate local capillary pressure, saturation, and the specific interfacial area between fluorinert and dyed water. All interfaces were identified as two-dimensional arcs. For each fluid-fluid interface, the position of the apex, and the two points where it touched the walls of the flow network, were identified. Then, a circle was fitted to these three points. The radius of the fitted circle was considered to give the radius of planar curvature of the interface. The width of the flow channel was calculated as the chord of the fitted circle. The length of the interfaces was calculated in two ways; either as the arc-length of the circle with respect to the opening angle, or as a line element with a sequence of pixels, identified directly in the image. These two lengths were compared so as to have an extra way of testing the accuracy of fitting. The contact angle between the meniscus and the wall was also determined. In figure 6, the identified interfaces are shown.

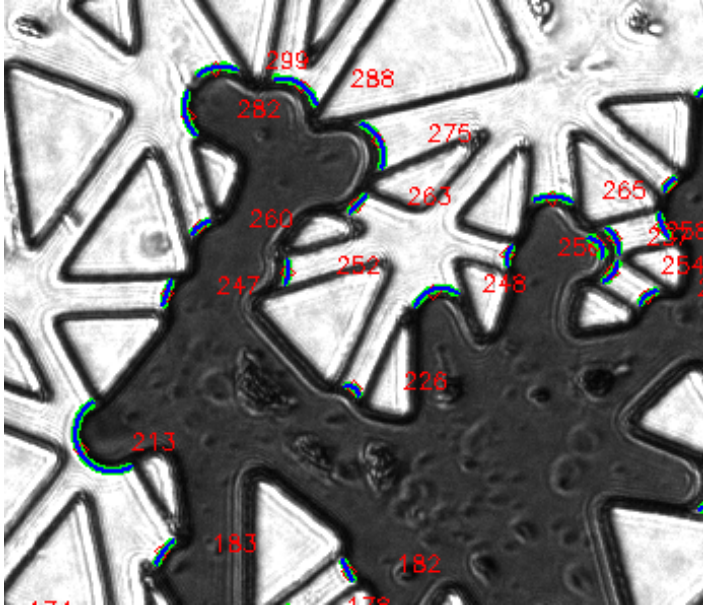


Figure 6. Image from a part of the flow network where the interfaces are identified and identified with a number.

According to Young-Laplace equation, capillary pressure p^c is equal to:

$$p^c = \sigma \cdot \left(\frac{1}{r_1} + \frac{1}{r_2} \right) \quad (2),$$

where r_1 and r_2 are the principal curvature radii and σ is the interfacial tension. In our case, we identified the r_1 and r_2 as the planar and in-depth curvature radii. For the planar curvature we have:

$$r_1 = \frac{w}{2 \cdot \cos \theta} \quad (3),$$

where w is the pore and θ is the contact angle.

Similarly, the radius of in-depth curvature is:

$$r_2 = \frac{d}{2 \cdot \cos \theta} \quad (4),$$

where d was the depth of the flow network.

Equations (2), (3) and (4) can be combined to obtain the following expression for local capillary pressure in terms of known parameters:

$$p^c = \sigma \cdot \left(\frac{1}{w} + \frac{1}{d} \right) \cdot \frac{w}{r_1} \quad (5)$$

The area of an interface is calculated from the following equation:

$$A = 4 \cdot r_1 \cdot r_2 \cdot \theta^2 = \frac{w \cdot d}{\cos^2 \theta} \cdot \theta^2 \quad (6)$$

where θ can be obtained by inverting equation (3):

$$\theta = \cos^{-1} \frac{w}{2 \cdot r_1} \quad (7)$$

Then, the average capillary pressure of a collection of interfaces was calculated as follows:

$$\bar{P}^c = \frac{\sum_{i=1}^N p_i^c \cdot A_i}{\sum_{i=1}^N A_i} \quad (8)$$

7.3.2.2 Interfacial area production term and velocity

The net rate of production of interfaces is given by equation (9).

$$\frac{\partial a^{wn}}{\partial t} + \nabla \cdot (a^{wn} \vec{w}^{wn}) = E^{wn} \quad (9)$$

where α^{wn} is interfacial area, \mathbf{w}^{wn} is the interfacial velocity, and E^{wn} is the net production term of interfaces.

The rate of change of interfacial area was calculated within an averaging moving domain, with dimensions of 5 x 7 mm². At any given time, the averaging domain was

moved along the flow network by 300 pixels, equal to 840 microns. In this way, average values for interfacial area and saturation, as well as their rate of change, were obtained. The formulation used in the calculation of average quantities was the one followed by Joekar-Niasar and Hassanizadeh (2011). The macroscopic velocity of the interfaces was determined based on the time rate of change of the apexes (as the center of mass) of the interfaces, within the averaging domain.

7.4 Results

7.4.1 P^c - S - A^{wn} surface

The results obtained by image processing were used to plot average capillary pressure-saturation curves as well as average capillary pressure-saturation- specific interfacial area surfaces. In figure 7, data points for average capillary pressure and saturation for a series of drainage-imbibition cycles are shown. It is obvious that the capillary pressure-saturation relationship is highly hysteretic. These results clearly show that the knowledge of pressure and saturation is not enough to fully specify the state of the system.

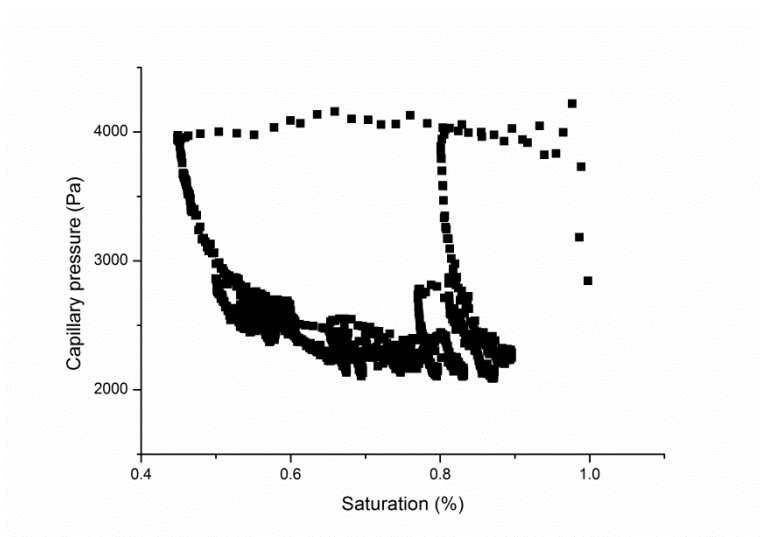


Figure 7. Average capillary pressure as a function of wetting phase saturation for primary drainage, main imbibition, and scanning curves.

As it was mentioned above, theoretical, numerical, and experimental results have shown that it is crucially important to include interfacial area for a complete description of two-phase flow in porous media (see e.g., Hassanizadeh and Gray, 1990, 1993b; Held and Celia, 2001; Cheng et al., 2004; Joekar-Niasar et al. , 2010; Joekar-Niasar and Hassanizadeh, 2011, 2012). In particular, if capillary pressure, saturation, and specific interfacial area data points are plotted, they will form a surface which would be the locus of both imbibition and drainage data points.

In figure 8, all data for saturation, average capillary pressure, and specific interfacial area from imbibition and drainage experiments under dynamic conditions are plotted. The surface is rough because we simply connect the data points to each other.

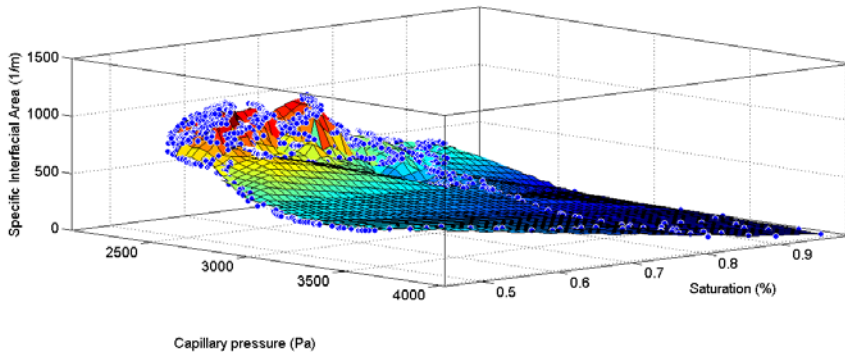


Figure 8. The interpolated surface that was formed by data points obtained during drainage and imbibition are presented.

7.4.2 Production term and interfacial velocity

The application of equation 9 within a moving domain, in combination with the experimental data, lead to the calculation of the net production of interfacial area, as well as the interfacial velocity. For the same averaging domain, average saturation and its rate of change was calculated. By using these measurements, surfaces for the production term and interfacial velocity as a function of saturation and its rate of change were plotted.

In figure 9, the interpolated surfaces for the production term (9a) and interfacial velocity (9b), versus saturation and its rate of change for a maximum capillary number of $2 \cdot 10^{-5}$ are plotted.

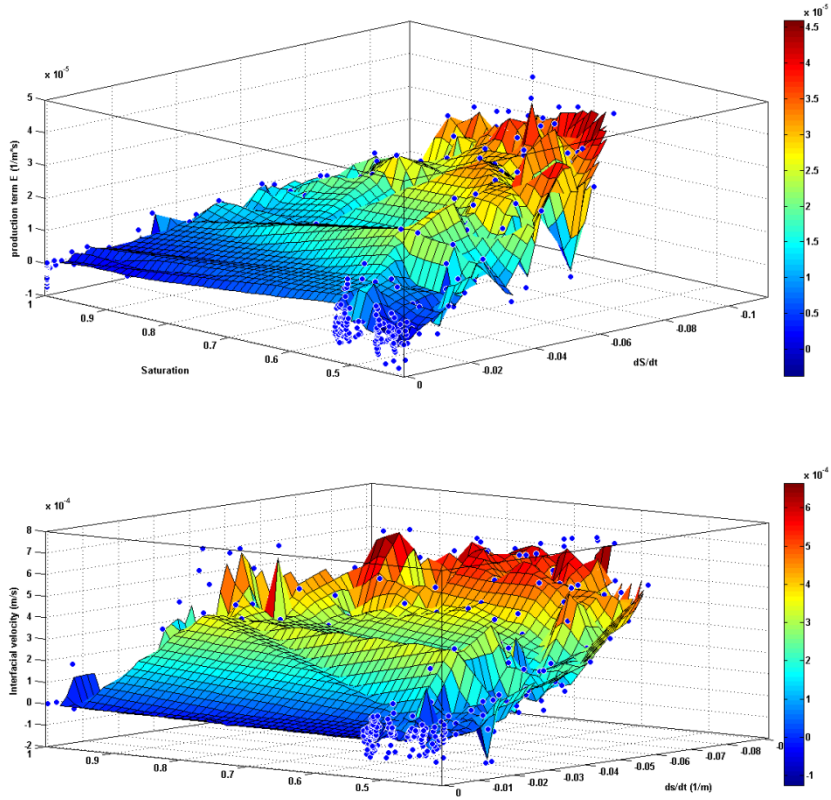


Figure 9. Production term (9a) and interfacial velocity (9b) plotted versus saturation and its rate of change.

The experimental data for the production term were fitted to a first order polynomial equation.

$$E^{wn} \left(S^w, \frac{\partial S^w}{\partial t} \right) = p00 + p10 \cdot S^w + p01 \cdot \frac{\partial S^w}{\partial t} \quad (11)$$

In table 1, which follows, the values for the fitting parameters for the production term, their confidence levels, as well as R^2 value are given.

Parameter	Value	Confidence levels
p00	3.885e-006	3.606e-006, 4.164e-006
p10	-5.07e-006	-5.456e-006, -4.684e-006
p01	-0.0003185	-0.0003211, -0.0003158
R ²	0.9948	

Table 1. The fitting parameters for the production term, along with R² fitting factor for a maximum capillary number of 2.10⁻⁵ are shown.

The experimental data for the interfacial velocity were also fitted to a first order polynomial equation.

$$\bar{v}^{wn}(S^w, \frac{\partial S^w}{\partial t}) = p00 + p10 \cdot S^w + p01 \cdot \frac{\partial S^w}{\partial t} \quad (12)$$

In table 2, which follows, the values for the fitting parameters for interfacial velocity, their confidence levels, as well as R2 value are given.

Parameter	Value	Confidence levels
p00	1.766e-005	1.342e-005, 2.19e-005
p10	-0.005692	-0.005735, -0.005648
p01	-1.766e-005	-2.407e-005, -1.126e-005
R ²	0.9953	

Table 2. The fitting parameters for interfacial velocity, along with R² fitting factor for an externally applied pressure of 6300 Pa are shown.

7.5 Discussion

The experimental results showed that the relation between capillary pressure and saturation for drainage and imbibition under dynamic conditions is hysteretic, as expected. However, the inclusion of interfacial area as a new state variable can

significantly eliminate hysteresis. Instead of many curves, we get one unique surface, which is the locus of all drainage and imbibition data points. This also means that we can estimate a unique value of interfacial area for every capillary pressure-saturation pair, given the initial conditions. This surface is unique for a given set of fluids and solid phases, a given percolation pattern, and given boundary conditions. In comparison to the quasi static case studied in Karadimitriou et al. (2013), where the same micro-model was used, we can make the following observations. The average capillary pressure under dynamic conditions is lower than the one under quasi-static, while the average capillary pressure under dynamic conditions during imbibition is higher than the one in the quasi-static case. The lowest saturation for the wetting phase under dynamic conditions is lower than this in the quasi-static case. Finally, the highest value of specific interfacial area under dynamic conditions is lower than this in the quasi-static case, and it goes to even lower values for higher capillary numbers. In figure 10, the surface constructed from data obtained under quasi static conditions, and the experimental data obtained for two maximum capillary numbers are shown. The green dots correspond to a maximum capillary number of 2.10^{-5} , while the dark ones correspond to a capillary number of 6.10^{-5} .

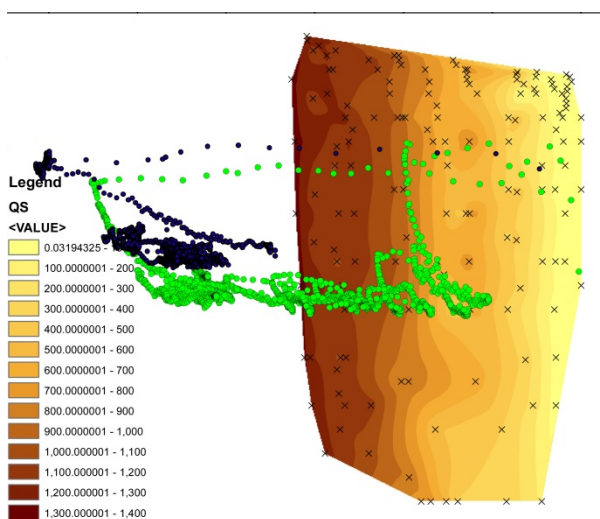


Figure 10. The surface constructed from quasi-static data cross-shown with the experimental data obtained under dynamic conditions

As it can be see the spread of the dynamic data and the quasi-static ones are very different. The two major reasons for this difference are the following. Capillary

pressure measured under quasi-static conditions was the one applied at the boundaries of the flow network, while under dynamic conditions it was locally (within a single pore) measured. The second reason was that the in the quasi static experiment there was more disconnected phase than in the dynamic ones. This lead to higher values for interfacial area, since the more the disconnected phase is, the higher the interfacial area is.

The comparison between two dynamic experiments, for two maximum capillary numbers, led to the following observations. The maximum interfacial with respect to wetting phase saturation was decreasing, by increasing pressure. The highest capillary number led to remobilization of the non-wetting phase, causing the lowest wetting phase saturation to decrease. Finally, even though the external pressure was significantly increased, the average capillary pressure was only increased by nearly 300 Pa.

In figure 11 the dynamic surfaces for two capillary numbers are plotted together. They show a relatively good match, but very different from the quasi-static case.

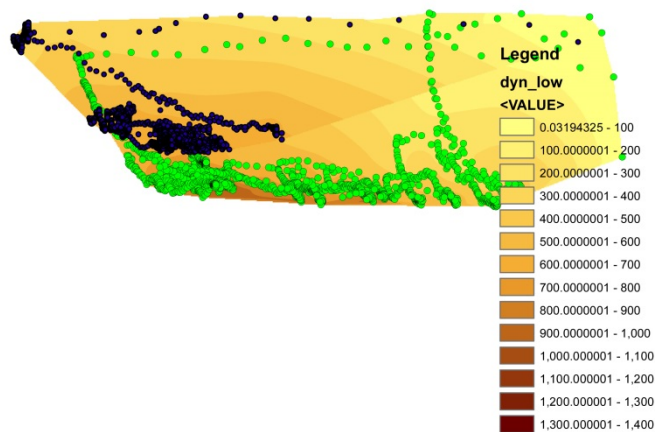


Figure 11. Dynamic surfaces for two capillary numbers ($2 \cdot 10^{-5}$ and $6 \cdot 10^{-5}$)

The relative difference between the two surfaces obtained from the two dynamic cases is nearly 30%. However, if only the data obtained from the experiments are used, and

not the interpolated points, then the average difference are reduced to nearly 15%. This difference happens because of the empty space between interpolated data points. One would expect that the average capillary pressure under primary drainage would be at least equal, if not higher, to the average entry capillary pressure of the pores and throats of the flow network. Instead, the average capillary pressure measured for primary drainage is lower than the one under quasi-static conditions. The actual case is that the interfaces which are at the front of the non-wetting phase have curvatures which correspond to higher pressures than the entry pressure of the throats. However, a front cannot easily be defined in this case, as the viscosity ratio of the two phases is 0.21, which makes it unfavorable for drainage. We mostly observe a fingerous behavior during drainage. So, the interfaces that belong to the front are the ones where the wetting phase is directly connected to its reservoir. In figure 12, the average capillary pressure of the interfaces which are located at the front during primary drainage is plotted versus saturation, for a capillary number of 2.10⁻⁵.

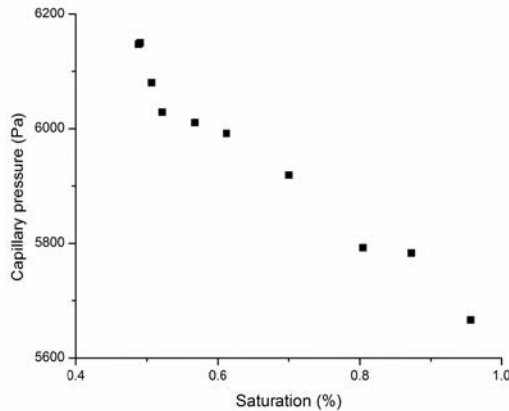


Figure 12. Capillary pressure at the front of the non-wetting phase plotted versus wetting phase saturation.

As the non-wetting phase is propagating inside the flow network, interfaces are formed that do not belong to the front. All these interfaces that are behind the front have lower curvatures which correspond to lower capillary pressures.

During main imbibition, the interfaces that are located at the invading front can relax, while the interfaces which are located away from the front do not yet feel this change since the high viscous forces will not let the reach relax. Eventually, parts of the non-

wetting phase become disconnected, and form interfaces which are under pressure. This leads to an average capillary pressure under main imbibition which is higher than the one under equilibrium conditions.

During drainage steps after main imbibition, the disconnected non-wetting phase reconnects quite fast. As soon as the non-wetting phase reconnects, the wetting phase saturation decreases, but the average capillary pressure does not increase drastically. Because of reconnection, the non-wetting phase propagates into the flow network while it is growing in volume, but the reconnection is faster than the volume growing. So, the non-wetting phase is present and connected in the pores and throats without having to overcome the entry pressures. In a short time it reaches the wetting phase reservoir, and then there is no reason for further increase of the average capillary pressure, since there is a connecting path to an area many times bigger than the size of the throats.

In reference to the interfacial area production term, we make the following observations. The production term depends linearly both with saturation and its rate of change. However, the coefficient for dS/dt is at least one order of magnitude higher than this for saturation. Furthermore, it reaches the maximum value in the range of intermediate saturations. This is due to the increased possibility for the creation of invasion sites at intermediate saturations. When saturation is close to one, or to the residual wetting phase saturation, there are not many pores available to be invaded, thus the production term goes to zero. As saturation starts to become lower than one, more pores become available to be filled with the non-wetting phase. This causes the production term to increase. At intermediate saturation, it reaches its maximum value. As saturation continues to decrease, fewer pores become available to be invaded. This causes the production term to decrease, eventually reaching zero. When the applied pressure is increased, the net rate of interfacial area production increases, since the process is faster. The rate of change of wetting phase saturation increases too. The overall behavior though, stays qualitatively the same.

In reference to average interfacial velocity, we can make the following observations. It shows a similar behavior to this of the production term. It shows a linear dependency on saturation and its rate of change. But, as in the case of the production term, it is mostly a linear function of dS/dt , and less of saturation. Average interfacial velocity is zero for wetting phase saturation equal to one. As the saturation decreases, average velocity increases, reaching its maximum value at intermediate saturations. As saturation continues decreasing, interfacial velocity decreases too, eventually reaching zero. The experimental results obtained for interfacial velocity and interfacial

production term, are qualitatively in accordance with the findings from Joekar-Niasar and Hassanizadeh (2011). With the use of a dynamic pore network model for an elongated flow network, Joekar-Niasar and Hassanizadeh showed similar results.

7.6 Conclusion

This work is the first experimental work on the significance of the inclusion of interfacial area as a separate variable in two-phase flow under transient flow conditions. With the use of an elongated, PDMS micro-model, we have shown the validity of the hypothesis that capillary pressure- saturation-specific interfacial area data points form a unique surface for drainage and imbibition under transient flow conditions, and for given initial conditions. We have also shown that this surface is representative, within experimental error, not only for all four REV's, but also for any area within the flow network with dimensions equal to $5 \times 7 \text{ mm}^2$.

However, when this surface is compared to the surface obtained under equilibrium conditions, there is a mismatch. This means that one surface cannot describe well enough two-phase flow under dynamic and quasi-static. This cannot be accounted as a result questioning the validity of the initially proposed theory by Hassanizadeh and Gray, since in this theory it is assumed that both phases are connected, something that is not valid in the experiments.

7.7 Suggested future work

A series of dynamic two-phase flow experiments for different capillary numbers, as well as different viscosity ratios between phases, will provide great insight into the factors that affect P_c-S^w curve and $P_c-S^w-A^{wn}$ surface. The results from these experiments can be used to fill the right-hand side of equation 1, so that this equation will describe two-phase flow under any flow conditions, even when the phases get disconnected.

7.8 References

Avraam, D. G., Kolonis, G. B., Roumeliotis, T. C., Constantinides, G. N. and Payatakes, A. C. (1994), Steady-state two-phase flow through planar and nonplanar model porous media, *Transport in Porous Media*, **16**, 1, 0169-3913, pp. 75-101, Doi: 10.1007/BF01059777.

Baouab, Z., M. Najjari, H. Ouerfelli, S. Ben Nasrallah (2007), Experimental study of the effects of hydraulic gradient and injected-gas flow rate on fragmentation in porous media, *Journal of Petroleum Science and Engineering*, **59**, pp. 250–256.

Bottero, S., Hassanizadeh, S. M., Kleingeld, P. J., Heimovaara, T. J., 2011, Nonequilibrium capillarity effects in two-phase flow through porous media at different scales, *Water Resources Research*, **47**, 10, DOI: 10.1029/2011WR010887.

Chang, L.-C., J.-P. Tsai, H.-Y. Shan, H.-H. Chen (2009), Experimental study on imbibition displacement mechanisms of two-phase fluid using micro model, *Environ Earth Sci*, **59**:901-911, doi: 10.1007/s12665-009-0085-6.

Chen, D., L. J. Pyrak-Nolte, J. Griffin, and N. J. Giordano (2007), Measurement of interfacial area per volume for drainage and imbibition, *Water Resour. Res.*, **43**, W12504, doi:10.1029/2007WR006021.

Cheng, J.-T. (2002), Fluid flow in ultra-small capillaries, Ph.D. Thesis, Purdue University.

Cheng, J.-T., L. J. Pyrak-Nolte, D. D. Nolte, and N. J. Giordano (2004), Linking pressure and saturation through interfacial areas in porous media, *Geophys. Res. Lett.*, **31**, L08502, doi:10.1029/2003GL019282.

Corapcioglu, M. Y., Yoon, S., and Chowdhury, S. (2009), Pore-Scale Analysis of NAPL Blob Dissolution and Mobilization in Porous Media, *Transport in Porous Media*, **79**(3), pp. 419-442, doi: 10.1007/s11242-008-9331-8.

Ferer, M., Ji, C., Bromhal, G. S., Cook, J., Ahmadi, G., Smith, D. H., (2004), Crossover from capillary fingering to viscous fingering for immiscible unstable flow: Experiment and modelling, *Phys. Rev. E*, **70** (1).

Fritz, J. L., and Owen, M. J., (1995), Hydrophobic recovery of plasma-treated polydimethylsiloxane, *Journal of Adhesion*, **54**, pp. 33-45.

Grate, J. W., Zhang, C., Wietsma, T. W., Warner, M. G., Anheier Jr., N. C., Bernacki, B. E., Orr, G., and Oostrom, M. (2010), A note on the visualization of wetting film structures and a nonwetting immiscible fluid in a pore network micro-model using a solvatochromic dye, *Water Resour. Res.*, **46**, W11602, doi:10.1029/2010WR009419.

Gutiérrez, B., F. Juárez, L. Ornelas, S. Zeppieri, A. López de Ramos (2008), Experimental Study of Gas–Liquid Two-Phase Flow in Glass Micro-models, *Int. J. Thermophys.*, **29**:2126–2135, DOI 10.1007/s10765-007-0305-9.

Hassanizadeh, S.M., Gray, W.G., (1990), Mechanics and thermodynamics of multiphase flow in porous media including interphase boundaries, *Adv. Water Resour.*, **13**, pp. 169–186.

Hassanizadeh, S.M., Gray, W.G., (1993a), Thermodynamic basis of capillary pressure in porous media. *Water Resour. Res.*, **29**, pp. 3389–3405.

Hassanizadeh, S.M., Gray, W.G., (1993b), Toward an improved description of the physics of two-phase flow, *Adv. Water Resour.*, **16**, pp. 53–67.

Heiba, A.A., Sahimi, M., Scriven, L.E. and Davis, H.T. (1992), Percolation theory of two-phase relative permeability. SPE 11015, presented at the 57th Annual Fall Meeting of the Society of Petroleum Engineers, New Orleans, LA.

Held, R.J., Celia, M.A., (2001), Modeling support of functional relationships between capillary pressure, saturation, interfacial area and common lines, *Adv. Water Resour.*, **24**, pp. 325–343.

Hug, T. S., Parrat, D., Kunzi, P.-A., Stauffer, U., Verpoorte, E., de Rooij, N. F., (2003), Fabrication of nanochannels with PDMS, silicon and glass walls and spontaneous filling by capillary forces, 7th International Conference on Miniaturized Chemical and Biochemical Analysts Systems, California, USA.

Huh, D., Mills, K. L., Zhu, X., Burns, M. A., Thouless, M. A., and Takayama, S., (2007), Tuneable elastomeric nanochannels for nanofluidic manipulation, *Nature Materials*, **6**, pp. 424–428, doi:10.1038/nmat1907.

Joekar-Niasar, V., Hassanizadeh, S.M., Leijnse, A., (2008), Insights into the relationships among capillary pressure, saturation, interfacial area and relative permeability using pore-network modeling, *Transp. Porous Media*, **74**(2), pp. 201–219, doi:10.1029/2010WR009291.

Joekar-Niasar, V., Hassanizadeh, S.M., Pyrak-Nolte, L.J., Berentsen, C., (2009), Simulating drainage and imbibition experiments in a high-porosity micro-model using an unstructured pore network model, *Water Resour. Res.*, 45, W02430, doi:10.1029/2007WR006641.

Joekar-Niasar, V., Prodanovic, M., Wildenschild, D., Hassanizadeh, S.M., (2010), Network model investigation of interfacial area, capillary pressure and saturation relationships in granular porous media, *Water Resour. Res.*, 46, W06526, doi:10.1029/2009WR008585.

Joekar-Niasar, V., Hassanizadeh, S.M., (2011), Specific interfacial area; the missing state variable in two-phase flow?, *Water Resour. Res.*, 47, W05513, doi:10.1029/2010WR009291.

Joekar-Niasar, V., and Hassanizadeh, S. M., (2012), Uniqueness of Specific Interfacial Area–Capillary Pressure–Saturation Relationship Under Non-Equilibrium Conditions in Two-Phase Porous Media Flow, *Transport in Porous Media*, 94, pp. 465-486, DOI 10.1007/s11242-012-9958-3.

Karadimitriou, N.K., Joekar-Niasar, V., Hassanizadeh, S. M., Kleingeld, P. J., and Pyrak-Nolte, L. J., (2012a), A novel deep reactive ion etched (DRIE) glass micro-model for two-phase flow experiments, *Lab on a Chip*, DOI: 10.1039/C2LC40530J.

Karadimitriou, N. K., and Hassanizadeh, S. M., (2012b), A Review of Micro-models and their Use in Two-Phase Flow Studies, *Vadose Zone Journal*, doi:10.2136/vzj2011.0072.

Karadimitriou, N. K., Musterd, M., Kleingeld, P. J., Kreutzer, M. T., Hassanizadeh, S. M., and Joekar-Niasar, V., (2012c), On the fabrication of PDMS micro-models by rapid prototyping, and their use in two-phase flow studies, submitted to *Water Resources Research*.

Liu, Y., Nolte, D. D., Pyrak-Nolte, L. J., (2011), Hysteresis and Interfacial Energies in Smooth-walled Microfluidic Channels, *Water Resour. Res.*, 47, W01504, doi:10.1029/2010WR009541.

Murakami, S.-I., Kuroda, T., and Osawa, Z., (1998), Dynamics of polymeric solid surfaces treated with oxygen plasma: Effect of aging media after plasma treatment, *Journal of Colloid and Interface Science*, 202, pp. 37-44.

NagaSiva, G., Bera, B., Karadimitriou, N. K., Mitra S. K., and Hassanizadeh, S. M., (2011), Reservoir-on-a-Chip (ROC): A new paradigm in Reservoir Engineering, *Lab on Chip*, Vol. **11**, pp. 3785 - 3792, (Featured Article), DOI:10.1039/C1LC20556K.

Porter, M.L., Schaap, M.G., Wildenschild, D., (2009), Lattice-boltzmann simulations of the capillary pressure–saturation–interfacial area relationship for porous media, *Adv. Water Resour.*, 32(11), pp. 1632–1640, doi:10.1016/j.advwatres.2009.08.009.

Pyrak-Nolte, L. J., D. D. Nolte, D. Chen, and N. J. Giordano (2008), Relating capillary pressure to interfacial areas, *Water Resour. Res.*, **44**, W06408, doi:10.1029/2007WR006434.

Reeves, P.C., Celia, M.A., (1996), A functional relationship between capillary pressure, saturation, and interfacial area as revealed by a pore-scale network model, *Water Resour. Res.*, 32, pp. 2345–2358.

Zhang, C., Oostrom, M., Wietsma, T. W., Grate, J. G., and Warner, M.G., (2011), Influence of Viscous and Capillary Forces on Immiscible Fluid Displacement: Pore-Scale Experimental Study in a Water-Wet Micro-model Demonstrating Viscous and Capillary Fingering, *Energy and Fuels*, **25**(8):3493-3505. doi:10.1021/ef101732k

Chapter 8

Visualization of pore-scale two-phase displacement mechanisms

8.1 Introduction

In the last 25 to 30 years, micro-models, as artificial representations of natural porous media, have been increasingly used to study the behavior of fluids at the pore scale. They have been proven to be valuable tools by enabling us to observe the flow of fluids and the relevant mechanisms that take place during flow. Micro-models are of great value in improving our understanding of (multiphase) flow and transport in porous media. In the work of Karadimitriou et al. (2012), an extensive review of micro-models and their use in two-phase flow studies is presented. In this article, methods for generating networks of pores are described, as well as the means for manufacturing a micro-model. Various visualization setups are presented along with their advantages and limitations. The major applications of micro-models in two-phase flow, along with the necessary experimental parameters are also presented. In the work of Karadimitriou et al. (2013) the procedure for manufacturing PDMS micro-models with the use of soft lithography is presented. Then, an innovative and novel optical setup that allows the real-time visualization of elongated samples is described. Finally, they present the results obtained by quasi-static, two-phase flow experiments.

In this work, we discuss a number of pore-scale mechanisms based on visualizations of two-phase flow in the same PDMS micro-models. Knowledge of these pore-scale mechanisms helps us to gain tangible insights into the dynamics of two-phase flow.

There are two main pore filling mechanisms in two-phase flow: drainage and imbibition. Drainage refers to the situation where the non-wetting phase displaces the wetting; this can only occur under the application of an external force. The opposite sequence, where the wetting phase displaces the non-wetting phase, is referred to as imbibition. It can occur spontaneously due to capillary forces. These two mechanisms are affected by pore sizes and morphology, fluids and solid properties (such as surface tension and viscosity), and boundary conditions. While at the macroscale, we see only

either drainage or imbibition occurring, a host of complex phenomena occur at the pore scale.

In a quasi-two dimensional micro-model, like ours, the corner flow of the wetting phase is very limited. It was only present in the cases where the wetting phase was connected through the corners of the closed boundaries of the flow network. All the other islands of the solid phase in the flow network have wetting phase trapped in their corners, but these corners are not connected, since these islands are isolated. Thus, it is possible in a quasi-two dimensional micro-model to have trapped wetting phase. As soon as the wetting phase gets trapped, any further increase of the pressure does not have any effect on the local saturation of the system. This can be seen in Figure 1.

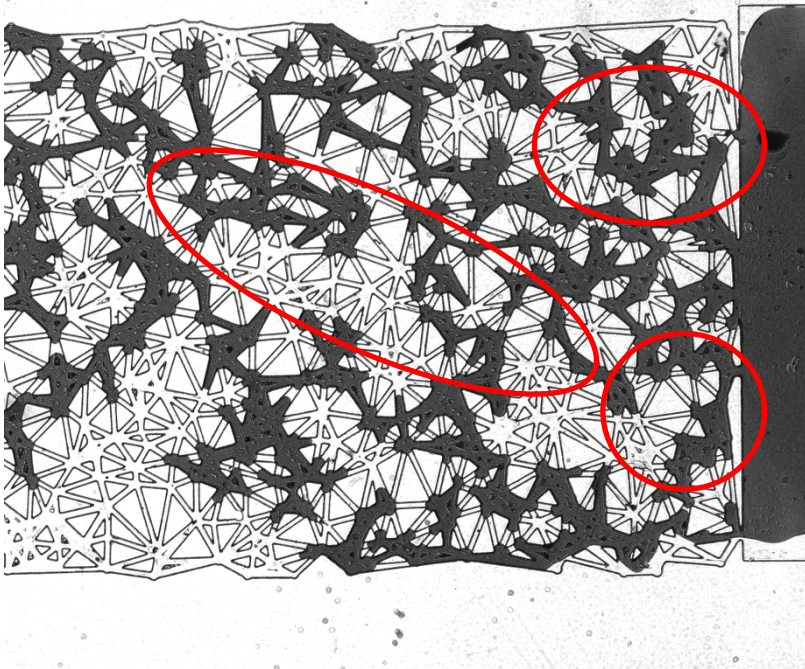


Figure 1. Part of the network with the inlet of the non-wetting phase. During drainage, in some parts of the network, the wetting phase gets disconnected from the reservoir, due to the absence of corner flow. These areas are marked in red.

The fact that corner flow was limited only to the closed boundaries of the flow network also led to a very slow response of the system to the pressure drops while imbibing. As soon as the upper and lower boundaries of the network were free from the non-wetting phase, a piston-like movement of the wetting phase was observed.

8.2 Experimental setup

The mechanisms reported here were observed during two-phase flow experiments. These experiments were carried out in a hydrophobic PDMS micro-model. The dimensions of the flow network were $5 \times 30 \text{ mm}^2$. The fluids used were Fluorinert FC-43 as the wetting, and water dyed with ink as the non-wetting phase. Flow in the micro-model was visualized with the use of an innovative setup, which allowed the visualization of elongated samples. Pressure was applied and measured at the reservoirs of the two-phases. The details on the materials used and the manufacturing process of the micro-model, as well as the topology of the flow network, the fluids used as the wetting and the non-wetting phase, the visualization setup used to monitor flow in the micro-model, and finally how pressure was measured and controlled, can be found in Chapter 6, in sections 6.2 and 6.4.

8.3 Mechanisms during drainage

8.3.1 Haines jump

One of the most well-known, pore-scale phenomena is the Haines jump, which was first described by Haines (1930). It occurs when a meniscus passes through a pore constriction during drainage. After filling one pore, usually the non-wetting phase has to go through a constriction in order to invade the next pore. So, the non-wetting phase pressure, and thus the capillary pressure, has to build up as the meniscus moves into the constriction, in order to overcome the entry capillary pressure. Typically, this is a slow process. The capillary pressure reaches a maximum value at the narrowest section of the constriction, where the meniscus curvature also reaches its maximum value. Immediately after that point, the pore opens up into the next pore. The meniscus is then unstable, the non-wetting phase pressure is relatively high, and there is little resistance to its movement. So, the non-wetting phase fills the next pore and new menisci are formed at its exit openings. This process occurs very fast. So, it appears that the meniscus jumps from one constriction to the other constriction. In fact, it may break into more menisci during this jump. In our experiments, as we were monitoring the real-time movement of menisci, we could clearly see Haines jumps during drainage. Some are shown in figure 2. With the red arrow, flow direction of the non-wetting phase is designated.

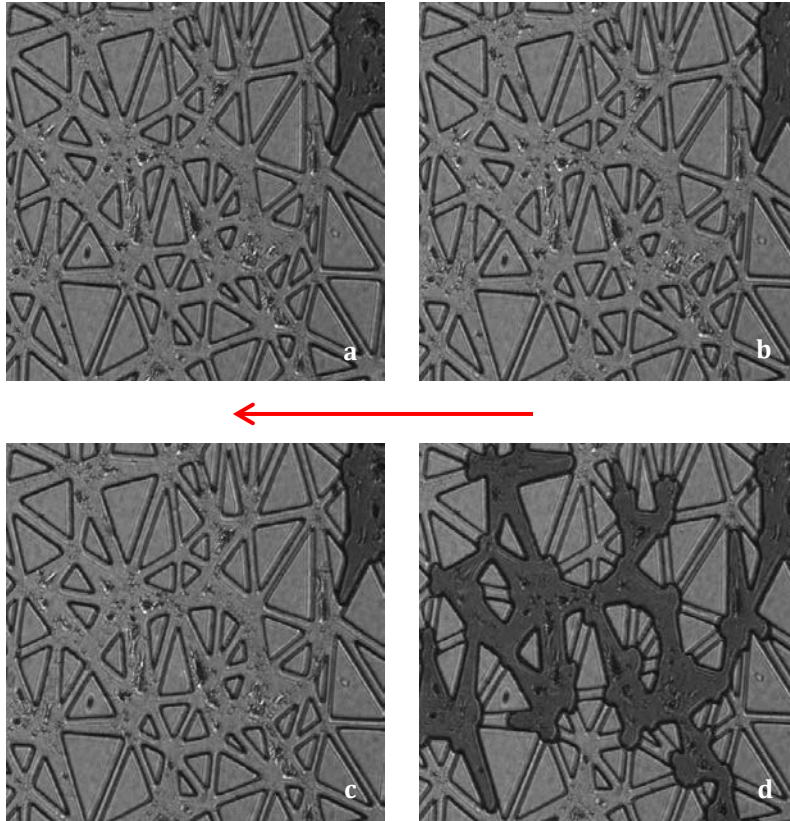


Figure 2. Parts of pictures taken during drainage. The four images were taken in a sequence of 0.5 seconds. Pressure is building up at the constriction, and eventually floods a number of pores.

Figure 2 shows parts of sequential pictures taken from the flow network during drainage. The time step between the pictures was 0.5 seconds. In images a-c, pressure is building up at the constriction. From picture (a) to picture (c) the interface between the two-phases had moved only for a few microns. In picture (d) the interface has overcome the constriction, and it flooded a number of pores in 0.5 seconds.

8.3.2 Capillary end effects.

A laboratory experiment is almost always carried out in a relatively small domain. This may cause the inflow and out flow boundaries to have a significant effect on what happens within the domain. Especially during two-phase drainage experiments, the

outflow boundary can affect processes taking place in the domain, once the non-wetting phase reaches it. During drainage, for the non-wetting phase to continue invading the domain, its pressure (and thus the capillary pressure) has to increase progressively. As the non-wetting phase reaches the outflow boundary, which is filled with the wetting phase, the capillary pressure reaches its highest value. This means that fluid-fluid interfaces have a large curvature. As soon as these interfaces pass the outflow boundary and enter the larger space of the outflow reservoir, they can relax and attain a much smaller capillary pressure. This means that the non-wetting phase drops as soon as it reaches the wetting phase reservoir. As the non-wetting phase is continuous (and thus the capillary pressure) its pressure drops everywhere in the vicinity of the outflow reservoir. This means that the interfaces within the domain become relaxed, and local imbibition takes place, with the wetting phase re-entering from the outflow reservoir. These processes could be much more pronounced in micro-models, as they are usually small. Even though our micro-model was relatively long, end effects could be clearly observed. In Figure 3, images (a) and (b) are taken just before and right after the non-wetting phase enters the outflow reservoir. We clearly see that the non-wetting phase recedes in regions which are shown in red circles. Our computations showed that both saturation and macroscale capillary pressure, averaged over the end section of the micro-model, decreased right after the breakthrough.

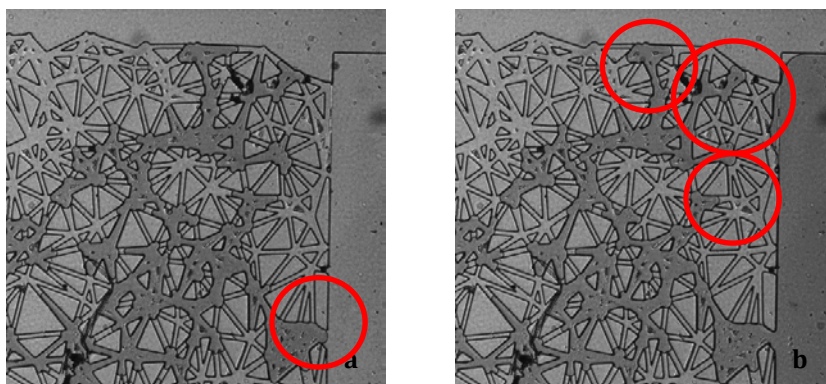


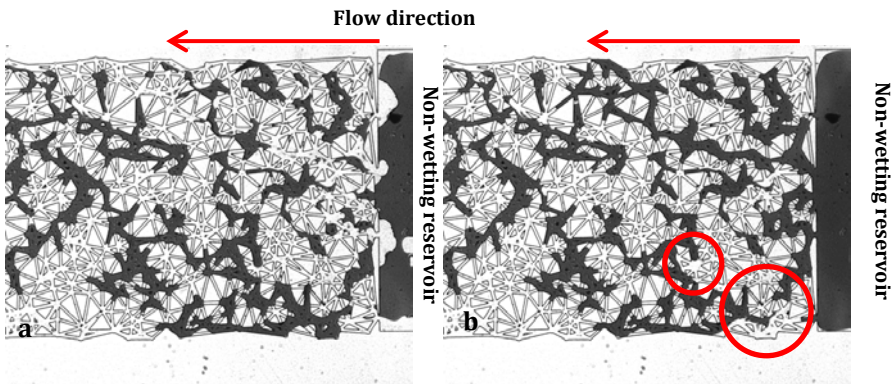
Figure 3. Image taken from a micro-model just before breakthrough (a), and right after (after 1 second) (b). In the right image, the relaxed and retreated interfaces are marked with red circles.

8.3.3 Local imbibition – mobilization of the non-wetting phase

It was often observed that during drainage, in some parts of the network, imbibition was taking place. During drainage, there were many interfaces competing. As soon as

one of them could pass through a throat and the leading interface was found in a bigger void area, the remaining interfaces receded. Local imbibition was then observed. This was the case mostly when there was a Haines jump in the vicinity of the competing interfaces.

Another case where local imbibition could be observed is during main or secondary drainage, right after an imbibition event. In this situation, there are many areas of disconnected non-wetting phase. The front of the invading non-wetting phase would push the wetting phase forward. This causes local rise of the wetting phase pressure in pores filled by a disconnected cluster of the non-wetting phase. This causes local imbibition in those pores. The downstream end of the cluster of disconnected non-wetting phase would move forward causing local drainage. These events are shown in Figure 4. Images (a) and (b) are taken by the first camera and (c) and (d) are taken by the second camera. Images (c) and (d) are from the same instances as (a) and (b) respectively. In picture (a), the flow network is visualized immediately after the completion of imbibition step. In picture (b), drainage has started. In the areas within the red circles, local imbibition has taken place. In the same time, picture (c) is taken from the second part of the flow network when imbibition was complete. In picture (d), and within the red ellipse, local drainage has taken place. This is an immediate consequence of the lack of corner flow in the micro-model. As the non-wetting phase is introduced back into the network, displacing the wetting phase, some disconnected parts of the non-wetting phase may get mobilized, so as for the wetting phase to move. With the red arrow, flow direction of the non-wetting phase is designated.



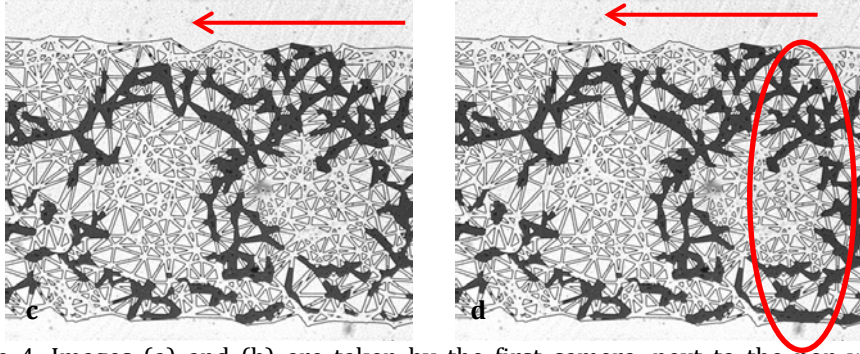


Figure 4. Images (a) and (b) are taken by the first camera, next to the non-wetting phase reservoir. Images (c) and (d) are from an adjacent part of the network, taken by the second camera. In image (a), the flow network is shown immediately after the completion of imbibition. In image (b), drainage has started again. The areas within the red circle indicate local imbibition during drainage. The same observed in images (c) and (d).

The latter kind of local imbibition during drainage usually takes place close to the non-wetting phase reservoir.

8.4 Mechanisms during imbibition

8.4.1 Snap-off

Snap-off is an imbibition mechanism during which, the non-wetting phase gets disconnected within a pore, due to the wetting phase invading it locally. This is a direct outcome of the drop in capillary pressure (due to a drop in the non-wetting phase pressure, or rise of the wetting phase pressure). The fluid-fluid interface curvature decreases (i.e. the interface becomes flatter), the non-wetting phase local thickness or diameter becomes smaller, and eventually it snaps off and retreats into neighboring pores. This is clearly shown in Figure 5, where the non-wetting phase at three places becomes thinner and thinner and then breaks off. This may also result in the non-wetting phase forming disconnected clusters.

Snap-off may also occur if there is corner flow of the wetting phase. In that case, the wetting phase enters a pore that is still filled by the non-wetting phase, via its corners. Due to wall roughness, or variation in pore width, it can accumulate somewhere within the pore and eventually fill up the whole width of the pore and cause the snap-off of the non-wetting phase. This mechanism was not often observed in our micro-model, because we have very limited corner flow, as explained in the introduction.

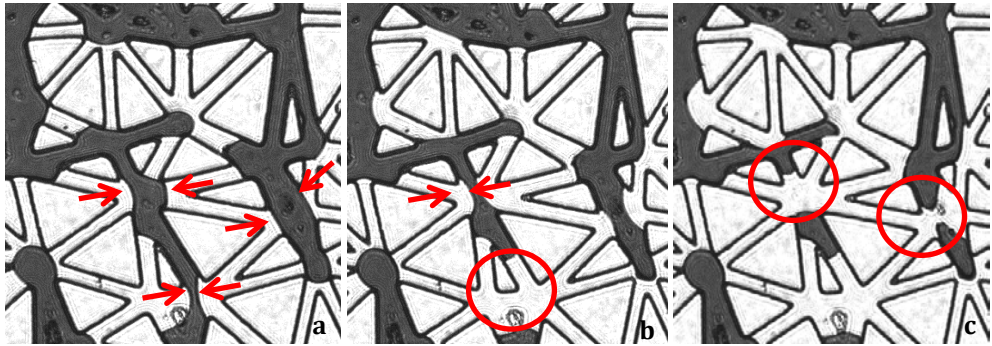


Figure 5. Consecutive images from a part of the flow network during imbibition. With the red arrows the local flow direction of the wetting phase is shown. The areas where snap-off occurred are designated with a red circle. It can also be seen that the non-wetting phase gets locally disconnected.

8.4.2 Cooperative filling

According to Wardlaw and Yu (1988) and Ioannidis et al. (1991), cooperative filling occurs when there is small variability of pore size, and small pore body to pore throat aspect ratio. Such local geometrical features result in a mechanism called cooperative filling. Cooperative filling is an imbibition mechanism that occurs in “higher porosity” regions of the porous medium. Commonly, a fluid-fluid interface spans the width of a single pore body or pore throat. This is certainly the case during drainage, where the radius of curvature of interfaces is small. But, during imbibition, at places where the capillary pressure drops (locally), the curvature becomes small (i.e. flat interface), it does not fit within one pore but it spans a number of pores. It may even happen that an interface spans the length of a pore. This case can be seen in Figure 6.

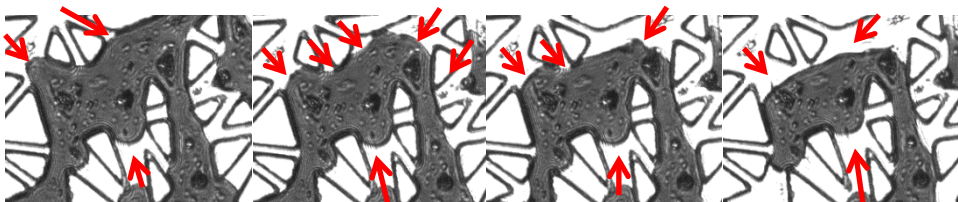


Figure 6. Consecutive (0.5 seconds interval) images from a part of the network, where cooperative filling can be observed. With red arrows the local flow direction is designated.

When the ratio of pore body to pore throat size is small, like in figure 6, imbibition phenomena are controlled by the fluid topology, and the efficiency of wetting invasion increases significantly (Joekar-Niasar et al., 2009; Vidales et al., 1998; Mahmud and Nguyen, 2006) and the effect of snap-off decreases.

8.4.3 Capillary end effects

At the end of drainage event, we drop the non-wetting phase reservoir pressure to zero, in order to initiate imbibition. One would expect that the pores filled with the non-wetting phase, and connected to the reservoir, will start draining into it. But the following can occur in the area close to the reservoir. The curvature of the interfaces starts to relax, and a limited local imbibition occurs. This is illustrated in figure 7. Picture 7a was taken right after the non-wetting phase reservoir pressure was set to zero. The non-wetting phase started to drain into the reservoir via the connected pathways. Moreover, local imbibition occurs through snap-off. This is seen in Figure 7b, where the non-wetting phase got disconnected from the non-wetting phase reservoir.

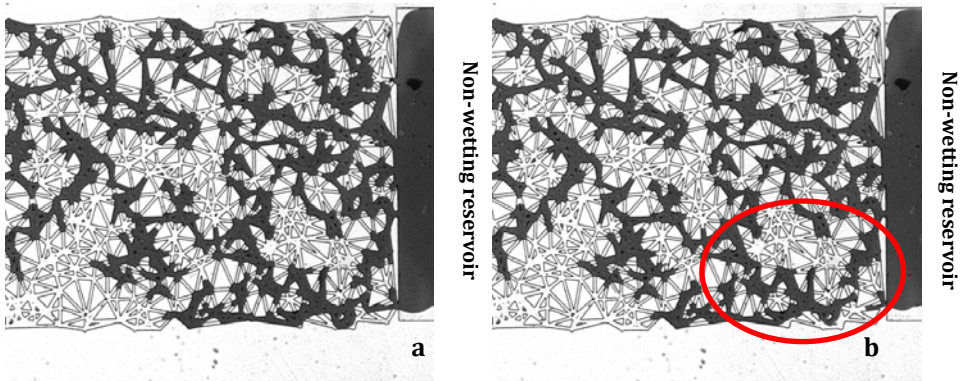


Figure 7. Picture (a) was taken exactly when the external non-wetting phase pressure was dropped to zero. In picture (d), the non-wetting phase gets locally disconnected from the reservoir, leaving a residual saturation of the non-wetting phase in the flow network.

8.4.4 Local drainage

Local drainage was observed near the wetting phase reservoir, at the start of imbibition after drainage. This is evident in images shown in Figure 8. In the left image, there are

some non-wetting phase pores, at the bottom of the image, that are still connected to the outflow reservoir. But, there are also disconnected clusters of the non-wetting phase. As the wetting enters the network, it pushes the disconnected clusters of non-wetting phase. This causes local drainage of pores in the downstream end of the cluster. This effect can usually be seen for capillary numbers larger than $4 \cdot 10^{-5}$.

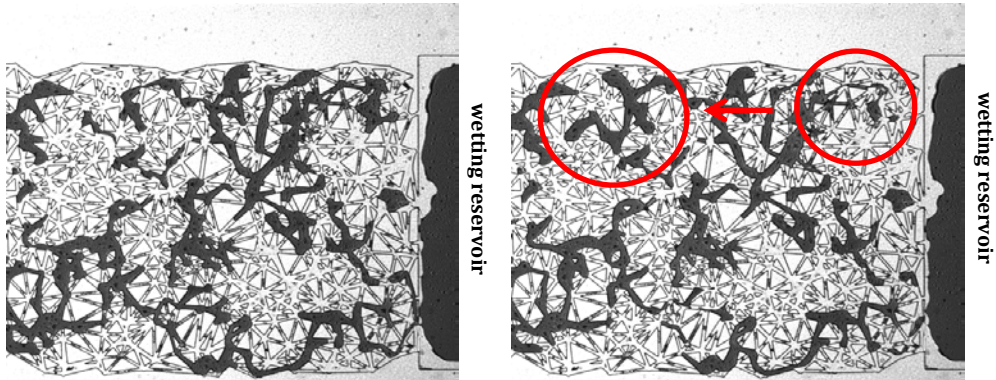


Figure 8. Pictures taken from the same part of the flow network during imbibition. The disconnected cluster of non-wetting-filled pores is pushed forward, as indicate in red circles.

8.5 Relative permeability

One of the major constitutive parameters of two-phase flow is relative permeability. The direct measurement of relative permeability of the two phases, for our micro-model, as a function of saturation was performed as follows.

For the measurement of relative permeability of the wetting phase, first the micro-model was fully saturated with the non-wetting phase. In order to make sure that no air remains trapped, the micro-model was first fully saturated with CO_2 , which displaced all the air out of the network. Then, the non-wetting phase (water) was injected into the flow network with the use of a syringe. Water dissolved CO_2 completely and the flow network became fully saturated with it. We then connected the micro-model to the two external reservoirs, which were both filled with the wetting phase. A syringe filled with the wetting phase was mounted on a syringe pump and connected to the inflow reservoir. The wetting phase was injected into the flow network at a fixed flow rate. The pressure measured at the reservoirs was monotonically increasing, until the wetting phase broke into the outflow reservoir. Then the pressure started to drop, until

it reached a constant value. This led to steady-state flow of the wetting phase at constant saturation. The values for pressure difference and flow rates were recorded. Then, by using Darcy's law we calculated the effective relative permeability. Knowing saturated permeability of the flow network ($K_{in} = 9.27 \cdot 10^{-11} \text{ m}^2$), the relative permeability at that saturation was determined. This process was repeated, each time starting with the flow network fully saturated with the non-wetting phase. Each time a higher flow rate was established by increasing the syringe pump flow rate, and thus higher wetting phase saturation. This led to the determination of the wetting phase relative permeability as a function of saturation.

The reason that the micro-model had to be saturated with the non-wetting phase for each saturation step is that once the flow of the wetting phase was established, saturation could not be changed by changing the flow rate.

A similar procedure was followed for the determination of the non-wetting phase relative permeability as a function of saturation. The outflow and inflow reservoirs, as well as the syringe, were filled with the non-wetting phase. Each time, the micro-model was first fully saturated with the wetting phase and then the non-wetting phase was injected at a constant flow rate until steady-state flow was reached. This was repeated each time at a higher flow rate. The resulting relative permeability curve is shown in Figure 9.

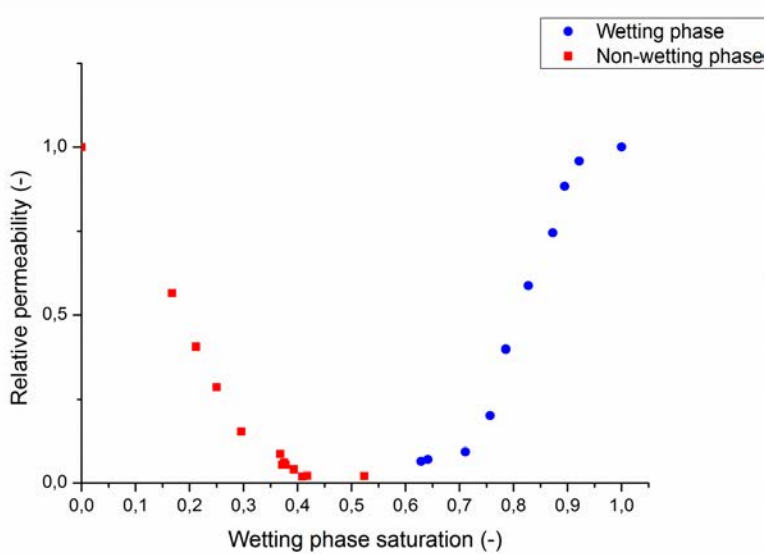


Figure 9. Relative permeability of the wetting and the non-wetting phase with respect to wetting phase saturation.

The lowest wetting phase saturation that could be reached during the measurement of the wetting phase relative permeability was close to 60%. Even when very high flow rates were applied, we could not reach a lower saturation without deforming the micro-model. This happened for a couple of reasons. First, the wetting phase was 4.7 times more viscous than the non-wetting phase. There was a distinct front moving in the flow network. This, in combination to the fact that corner flow is only limited to the side boundaries of the flow network led to low residual non-wetting phase saturation. At high flow rates, remobilization of the non-wetting phase would take place, keeping the residual saturation higher than 60%.

The highest wetting phase saturation that could be established in the measurement of the non-wetting phase relative permeability was about 53%. In other words, starting with the flow network fully saturated with the wetting phase, when we injected the non-wetting phase, even though its flow rate was very low, by the time steady-state flow was reached, the wetting phase saturation has dropped to 53%. This is because the non-wetting phase was much less viscous than the wetting phase, and it formed fingers in the flow network. Given the lack of corner flow for the wetting phase, the wetting phase could easily get disconnected, forming blobs in the flow network that blocked the flow of the non-wetting phase. For this reasons, it was impossible to have breakthrough of the non-wetting phase for higher wetting phase saturation.

In future work, it would be helpful to make use of fluids with viscosity ratios close to unity, or with the non-wetting phase being much more viscous than the wetting phase. This will allow us to compare and analyze the effect of viscosity ratio on the relative permeability of the phases.

8.6 References

Haines, W. B., (1930), Studies in the physical properties of soil, *J. Agric. Sci.*, **20**, pp. 97–116.

Wardlaw, N. C., Yu, L., (1988), Fluid topology, pore size and aspect ratio during imbibition, *Transport Porous Media*, **3**, pp. 17–34.

Ioannidis, M. A., I. Chatzis, and A. C. Payatakes (1991), A mercury porosimeter for investigating capillary phenomena and microdisplacement mechanisms in capillary networks, *J. Colloid Interface Sci.*, **143**, pp. 22– 36.

Vidales, A. M., J. L. Riccardo, and G. Zgrabli (1998), Pore-level modeling of wetting on correlated porous media, *J. Phys. D, Appl. Phys.*, **31**, pp. 2861– 2868.

Mahmud, W. M., and V. H. Nguyen (2006), Effects of snap-off in imbibition in porous media with different spatial correlations, *Transp. Porous Media*, **64**, pp. 279–300.

Joekar-Niasar, V., Hassanizadeh, S. M., Pyrak-Nolte, L. J., Berentsen, C., (2009), Simulating drainage and imbibition experiments in a high-porosity micro-model using an unstructured pore-network model, *Water Resources Research*, **45**, doi:10.1029/2007WR006641.

Chapter 9

Summary and Conclusions

9.1 Background

It is important to understand the underlying physics in two (or multi)-phase flow in porous media. There is a very wide range of applications of two-phase flow in many fields, such as hydrogeology, fuel cells and reservoir engineering.

So far, current theories of two-phase flow employ Darcy's law in its original form, where the only driving forces are the pressure gradient and gravity. The resisting force is assumed to be linearly proportional to the fluid velocity relative to the solid. It would make sense that there should be a number of other, less evident or less effective, factors that affect the balance of forces in the case of two-phase flow. Hassanizadeh and Gray (1990, 1993a), proposed a theory for two-phase flow, where specific interfacial area was introduced as a separate state variable. In this extended theory for two-phase flow, interfaces possess mass, momentum and energy. In addition to the balance equations for the two phases, they also derived balance equations for the interfaces.

The full set of equations has been studied numerically, as they do not have the physical limitations of measurement, but only some of them could be studied experimentally. For instance, so far, the significance of the inclusion of interfacial area as a separate state variable has been studied with micro-models under quasi-static conditions, but only for small domains (one REV), and not under transient conditions.

Using computational models, it has been shown that capillary pressure and saturation are related to the interfacial area between the two phases in a way that hysteresis could be removed. But in micro-model experiments, it has only been studied under quasi-static conditions, and for small domains as large as one REV.

In order to obtain experimental results on the significance of the inclusion of interfacial area as a separate state variable under any flow conditions, an elongated PDMS micro-model, in combination with optical microscopy, has been designed and constructed. From the images obtained, information on local capillary pressure, average saturation, and specific interfacial area were extracted and used to construct the relevant surfaces. Two objectives have been followed in this research.

9.2 Theory validation

The role of specific interfacial area in removing hysteresis has been numerically and experimentally investigated under quasi-static conditions. With the use of pore network modeling, a network of pore bodies and pore throats was generated, as a representation of a natural porous medium. The pore bodies were chosen to be cylinders, and the pore throats parallelepipeds. The mean pore width and the flow network depth were set to 40 microns. The size of the flow network was $5 \times 30 \text{ mm}^2$, and it was approximately equal to four REV. The size of an REV was calculated with porosity measurements, and that was also numerically and experimentally verified with the comparison of P^c-S^w curves for every individual REV and the total flow network. From the numerical model it was shown that under quasi-static conditions the inclusion of specific interfacial area as a separate state variable could eliminate the hysteretic behavior. For every pair of values for capillary pressure and saturation, a single value for specific interfacial area could be calculated under drainage or imbibition. Also, the relationship between relative permeability of each phase with respect to the wetting phase saturation was numerically studied, during drainage.

The same design for the flow network was converted to a mask to be used for the photo-lithographic step in the production of silicon, glass, or PDMS micro-models. Processes involved in oil recovery were studied with the use of a silicon micro-model. The model was sealed with a glass plate, so as to be able to visualize flow in the pores. Since glass and silicon have different wetting properties, the micro-model was not the optimal choice for two-phase flow studies, where a uniform wettability is desired.

For this reason, an all-glass micro-model was manufactured, with uniform wetting properties. The micro-model was manufactured with the use of Deep Reactive Ion Etching technique. This technique can give excellent results in reproducing the geometry of the pore bodies and throats (vertical walls and little deviation from the original design), but only if the depth is small, namely less than 30 microns. In our glass micro-model, the depth was 43.5 microns, the first to be so deep and used in two-phase flow studies. As expected, the cross sections of the pore bodies and throats were not rectangular, but trapezoidal. We obtained the P^c-S^w curve for drainage and it was compared to the result of the numerical model. After making corrections for the cross section of the micro-model, there was a very good match between numerical and experimental curves. The phases used for the experiments in the silicon-glass and all-glass micro-models were water, as the wetting phase, and fluorinert as the non-wetting phase.

Because of the shortcoming of the glass micro-models, we chose for the use of PDMS micro-models. After following the process of making micro-models with soft lithography, PDMS micro-models were manufactured. A number of experiments were performed for drainage and imbibition under quasi-static conditions. The images obtained from the experiments were processed, and information on local capillary pressure, average saturation, and specific interfacial area were extracted, for every individual REV, and for the whole flow network. By plotting average capillary pressure versus wetting phase saturation, the hysteretic behavior of the system was made evident. However, when the surface for average capillary pressure, wetting phase saturation, and specific interfacial area was plotted, the hysteretic behavior was not present anymore. For every pair of average capillary pressure and saturation, a single value for specific interfacial area was calculated. In this way, we validated that the inclusion of specific interfacial area as a state variable can help to eliminate or reduce hysteresis. After comparing the surfaces obtained from every individual REV among them, and in comparison to the total flow network, we verified that the flow network was homogeneous, since we surfaces obtained diverged for less than 8% from the total network.

The same type of PDMS micro-model was used to test the validity of the proposed theory under transient conditions. Again, for a number of drainage and imbibition experiments under dynamic conditions, images from the flow network were taken at a rate of 3 frames per second. After processing the images, the behavior of the system was depicted on a P^c-S^w graph. It was observed again that the relationship was hysteretic, but less hysteretic than in the quasi-static case. The reason was that, as the non-wetting phase is propagating inside the flow network, interfaces are formed that do not belong to the front. All these interfaces that are behind the front had lower curvatures which corresponded to lower capillary pressures.

During main imbibition, the interfaces that were located at the invading front could relax, while the interfaces which were located away from the front could not yet feel this change since the high viscous forces would not let them reach relaxation. Eventually, parts of the non-wetting phase became disconnected, and formed interfaces which were under higher capillary pressure than the ones at the moving interfaces. This led to an average capillary pressure under main imbibition which was higher than the one under equilibrium conditions.

During the subsequent to the main imbibition drainage steps, the disconnected non-wetting phase reconnected quite fast, decreasing the wetting phase saturation. Because of reconnection, the non-wetting phase propagated into the flow network and was

growing in volume, but the reconnection was faster than the volume growth. So, the non-wetting phase was present and connected in the pores and throats without having to overcome the entry pressures. In a short time, it reached the wetting phase reservoir, and then there was no reason for the average capillary pressure to build up anymore, since there was a connecting path to an area many times bigger than the size of the throats. For this reason, the average capillary pressure was lower than this during primary drainage.

After plotting the data points obtained for average capillary pressure-wetting phase saturation and specific interfacial area for drainage, imbibition, and the scanning curves for all REV, and for the total flow network, we observed that hysteresis was eliminated. When comparing surfaces from all REV to each other, and to the whole network, we did not observe a discrepancy of more than 10%. This validated the claim that specific interfacial area should be included as a separate state variable under transient conditions too.

The comparison between the surfaces obtained under quasi-static and transient conditions, for the same flow network led to the following conclusions. The highest value of specific interfacial area under dynamic conditions is lower than the value in the quasi-static case. Overall, the difference between the surfaces obtained under dynamic and quasi-static conditions was found to vary up to nearly 30%.

9.3 Innovation - Technical developments

Given the elongated nature of the micro-model, it was impossible to visualize flow through it with the conventional means of optical microscopy. For this reason, a custom “microscope” which could visualize elongated samples was designed and materialized. With the use of such a “microscope”, it was made possible to visualize flow through the micro-models at a resolution of 2.8 microns per pixel. In theory, such a setup can visualize any sample with any width-over-length ratio. In practice, the resolution of the visualization setup is limited by the diffraction limit of the light. The visualized ratio between width and length at the highest possible resolution is limited by the cost of the magnifying lens(es) and the number of cameras to be used. Such an optical microscope can have application in any field where microscopy for elongated samples is needed, as long as through-sample illumination is used.

A fully functional micro-model was manufactured from PDMS. The process was relatively easy, given that the master wafer was already prepared. The only part of the process where a clean room environment was needed was the preparation of the

master wafer. And as soon as the master wafer was ready, it could be used to manufacture multiple identical micro-models. These micro-models had very well controlled geometrical features, so as to be comparable to the numerical model. The successful salinization of PDMS micro-models, without any flakes (which could potentially block the flow network) and without any corrosion, was a big step towards the wider use of PDMS as a suitable material for the manufacture of micro-models. To our knowledge, the salinization method developed here is the fastest and safest for the user to follow, also without the need for a clean room environment.

9.4 Suggestions for future work

In our experiments, the viscosity ratio was fixed. It would be important to perform more experiments under dynamic conditions, for different capillary numbers, and different viscosity ratios. In this way, it would be possible to identify the factors which affect the capillary pressure-saturation-specific interfacial area surface, under transient conditions. This would be of value to other research field and/or industrial applications.

It will be of great significance to investigate experimentally the full set of equations proposed by Hassanizadeh and Gray. The verification of the validity of the full set of equations will drastically change the way that two-phase flow is being modeled. We have already shown under any flow conditions that specific interfacial area should be included as a separate state variable. The reason why the full set of equations was not studied in this research project was the experimental inability to measure pore-scale phase pressures in the flow network of a micro-model. This is not an easy task, because conventional pressure transducers of micro-scale dimensions don't exist yet. A possible solution to this problem would be the use of selective nano-particles, embedded in PDMS. The technology exists for particles which are selective in terms of the chemical properties of a fluid, which give an electrical signal depending on the local fluid pressure. The signal from the particles could be mapped, and in correlation to optical images, phase pressures could be identified.

Because of the two-dimensional nature of the micro-model, corner flow was not present in our experiments, except along the upper and lower boundaries of the micro-model. For this reason, the capillary pressure-saturation curve was highly hysteretic, and the residual saturation of the wetting phase was relatively high. A solution to this problem would be the use of three-dimensional micro-models. These micro-models should offer the ability to be optically monitored. But this is impossible with optical

microscopy, so far. An alternative to optical microscopy would be the use of the PVI technique introduced and employed by Montemagno and Gray (1995). This technique could be employed under quasi-static or dynamic with low capillary number conditions. The three-dimensionality of a micro-model could allow connectivity for the wetting phase, so as to be able to fully drain the micro-model, and get experimental data at lower saturations. Such micro-models can either be manufactured by performing several steps of photolithography in combination with soft lithography, or with the use of 3D printers. The refractive indices should be matched, so as for the technique proposed by Montemagno and Gray to be applicable.

Finally, it would be of great help if an optimized, integrated software package was commercially available for image processing. We managed to extract information on the curvature, position of the apex, chord length, arc length, etc. of all individual interfaces present in an image representing an REV. To get information for the whole flow network, additional programming had to be performed for averaging various quantities. The problems that came up had to do with the background illumination, the alignment of the images, identification of the time tag of each image, etc. Out of experience, we may say that an integrated software package, which could perform this corrections semi- automatically, will increase the effectiveness of the analysis of experimental work, and would be commercially successful.

Samenvatting

Het doel van dit onderzoek is meer fysica te brengen in de theorie van twee-fasen stroming. Het belang van het betrekken van de grenszone als afzonderlijke variabele in tweefase stromingsexperimenten en transportmodellen is onderzocht.

Het proefschrift heeft vier hoofdpunten. Het eerste deel beschrijft het ontwerp van een porienetwerk dat afdoende tweefase stroming beschrijft onder quasis staische condities. Dit model is gebruikt om de benodigde parameters, zoals stroomsnelheid, capillaire druk en relatieve doorlatendheid per fase te leveren.

Het tweede deel beschrijft het maken van verschillende typen micro-modellen met een gegeven geometrie en relatieve oppervlakte spanning (wetting capability). Dit houdt tevens in het optimaliseren van bestaande technieken om deze beter bruikbaar te maken voor het gestelde doel. Een voorbeeld hiervan is de verbetering van de oppervlakte behandeling (salination process) van het substraat van PDMS teneinde dit uniform hydrofoob te maken.

Het derde deel behandelt het gebruik van deze modellen in tweefasen stromingsstudies. De uitgebreide theorieën met betrekking tot twee fasenstroming, waarin het grensvlak een aparte variabele is zijn experimenteel geverifiëerd onder quasistatische condities.

Ten slotte zijn enige experimentele waarnemingen gedaan zoals blokkering van porieën, onderlinge verdringing van fasen gedurende invoer van de ene fase ten opzichte van de andere en de capillaire effecten aan de einden van het network die in numerieke modellen verondersteld worden maar nog niet waren waargenomen. Dit levert gegevens voor vervolgonderzoek.

List of publications (in chronological order)

1. Karadimitriou, N. K., Hassanizadeh, S. M., Kleingeld, P. J., (2010), Visualization setup for the investigation of interfacial area for two-phase flow in a micro-model', conference proceedings, First International Conference on Frontiers in Shallow Subsurface Technology, TU Delft.
2. Bera, B., Gunda, N. S., Karadimitriou, N. K., Mitra, S., Hassanizadeh, S. M., (2011), Fabrication of glass micro-model to perform multi-phase flow in a pore network structure, Conference Proceedings of the "ASME -JASME- KSME Joint Fluids Engineering Conference 2011", Hamamatsu, Japan.
3. Naga Siva, G., Bera, B., Karadimitriou, N. K., Mitra, S. K., and Majid Hassanizadeh, S. M., (2011), Reservoir-on-a-Chip (ROC): A new paradigm in Reservoir Engineering, Lab Chip, DOI:10.1039/C1LC20556K (Cover Article).
4. Karadimitriou, N. K., and Hassanizadeh, S. M., (2012), A Review of Micro-models and their Use in Two-Phase Flow Studies, Vadose Zone Journal, doi:10.2136/vzj2011.0072.
5. Karadimitriou, N.K., Joekar-Niasar, V., Hassanizadeh, S. M., Kleingeld, P. J., and Pyrak-Nolte, L. J., (2012), A novel deep reactive ion etched (DRIE) glass micro-model for two-phase flow experiments, Lab on a Chip, DOI: 10.1039/C2LC40530J.
6. Zhang, Q., Karadimitriou, N. K., Hassanizadeh, S. M., Kleingeld, P. J., Imhof, A., (2013), Study of Colloids Transport during Two-Phase Flow using a Novel Polydimethylsiloxane Micro-model, JGIS, <http://dx.doi.org/10.1016/j.jcis.2013.02.041>.
7. Karadimitriou, N. K., Musterd, M., Kleingeld, P. J., Kreutzer, M. T., Hassanizadeh, S. M., and Joekar-Niasar, V., (2013), On the fabrication of PDMS micro-models by rapid prototyping, and their use in two-phase flow studies, Water Resources Research, DOI: 10.1002/wrcr.20196.
8. Karadimitriou, N. K., Xiarchos, I. Hassanizadeh, S. M., Surface treatment of PDMS to enhance natural hydrophobicity, submitted to Surface and Coatings Technology.